

Salt damage in porous materials: an RH-XRD investigation

Dissertation

zur Erlangung des Doktorgrades
vorgelegt im
Department Chemie
der Fakultät für Mathematik, Informatik und Naturwissenschaften
Universität Hamburg

von

Kirsten Linnow
aus Hamburg

Februar 2007

1. Gutachter: Prof. Dr. W. Dannecker

2. Gutachter: Prof. Dr. J. Heck

Tag der Disputation: 27.4.2007

Acknowledgement

The present work has been carried out between Juli 2000 and February 2007 under the supervision of Prof. Dr. W. Dannecker and Dr. Michael Steiger at the Institute of Inorganic and Applied Chemistry, University of Hamburg.

Sincere thanks are given to Prof. Dr. W. Dannecker for the encouragement and for the confidence he has shown. Foremost I express my gratitude to Dr. Michael Steiger for his inspiring motivation and discussions and for his constant engagement throughout this work. He encouraged self-reliance, creativity, quality and conscientiousness with his invaluable advice.

This work benefited a lot from collaboration and helpful discussions with Dr. Lorraine Gibson (University of Strathclyde) and Lieve Halsberghe (Independent Ceramic Conservator, Luxembourg).

I am grateful to Dr. Herbert Juling (Institute of Material Science, Bremen), Dr. Gerd Gülker and Dr. Akram El Jarad (Department of Physics, University of Oldenburg) as well as Dr. Stefan Brüggerhoff and Dirk Kirchner (Deutsches Bergbaumuseum, Bochum) for meaningful discussions and good collaboration within the interdisciplinary research project; “Verhalten von Salzen in porösen Systemen”.

Sincere thanks to my colleagues at the University Hamburg and especially to Dr. Kathrin Hofmann, Marc Bollmann and Sarah Höxter for helpful discussions. Special thanks to the technical staff in particular to Torborg Krugmann and Angela Schlencker and to the students Karen Wilbrandt, Stephan Born, Anne Huesmann and Claudia Worthmann for help in the lab.

I am grateful to the Deutsche Forschungsgemeinschaft (DFG) for funding part of this work.

Finally, I like to thank my parents for their confidence and patience. Their help and financial support enabled me to realize both, scientific research and the education of my child.

Contents

1	Introduction.....	1
2	Investigation of sodium sulfate phase transitions in a porous material using humidity and temperature controlled X-Ray diffraction.....	9
3	Determination of equilibrium humidities using temperature and humidity controlled X-ray diffraction (RH-XRD).....	30
4	Investigation of NaCl deliquescence in porous substrates using RH-XRD.....	42
5	Hydration of $\text{MgSO}_4 \cdot \text{H}_2\text{O}$ and generation of stress in porous materials.....	63
6	Analysis of calcium acetate efflorescences formed on ceramic tiles in a museum environment.....	86
7	Phase diagram of the quaternary system $\text{Ca}(\text{CH}_3\text{COO})_2\text{--CaCl}_2\text{--Ca}(\text{NO}_3)_2\text{--H}_2\text{O}$ at 25°C	107
8	Deliquescence behavior of the incongruently soluble triple salt thecotrichite.....	133
9	Summary.....	157

Chapter 1

Introduction: Salt damage in porous materials

Salt damage in porous materials is a widespread problem and is known since centuries.[1–5]. Natural rocks, ceramics and mineral building materials such as stone, brick and concrete are porous materials that are subject to salt decay. Typically the porous materials are burdened with salts, which may be derived from different sources including the material itself, mortar, soil water, wet and dry deposition of atmospheric pollutants, de-icing materials and cleaning agents or conservation treatments [2,6]. One of the most invidious sources is the reaction between acidic air pollutants and calcareous materials such as limestone and marble. The damage caused by the presence of salts in porous building materials is due to the interaction of the salts with the environmental climatic conditions, i.e. humidity and temperature. Depending on temperature and relative humidity the salts may deliquesce, crystallize, hydrate or dehydrate. Visible damage in porous materials is caused by multiple phase transitions. Typical manifestations of damage are powdering and granular disintegration in turn leading to gradual loss of the surface and deterioration of original details whether carved or painted and in some cases leads to such severe loss that structural collapse of an object becomes inevitable. Given the severity of the problem, it is surprising that the mechanisms are not yet fully understood. Little is known about the reasons why some crystals grow on the surface as efflorescence, whilst others grow inside the porous structure as subflorescence. One point on which there is little doubt is that the real harmful process is the generation of pressure by crystals growing from supersaturated solution or during hydration in confined pore spaces [7,8].

Damage in building materials occurs if crystal growth is induced by cyclic changes of relative humidity and temperature across the equilibrium values of the respective phase transition reactions, i.e. deliquescence–crystallization and hydration–dehydration. However, the behavior of salt mixtures commonly found in building materials is more complicated and cannot be simply deduced from the behavior of the single salts. For instance, it was predicted [9,10] that crystallization of one salt from a mixture does not occur at a specific value but rather across a range of relative humidities. In agreement with the salt behavior observed at monuments [2] it was also predicted [9,10] that crystallization from a salt mixture occurs at lower humidities than expected for pure salts.

Attempts have been made over many years to model the behavior of mixed salt solutions. During the past decade the Pitzer ion interaction model has achieved wide acceptance, and has been applied in a number of important areas in the chemistry of the natural environment [11].

Equilibria in concentrated brines including the solubilities of both solid salts and atmospheric gases are closely related to the salt damage problem. It has been shown recently [12,13] that the properties of mixed pore solutions in building materials can be successfully modeled using the Pitzer ion interaction approach.

Whilst the Pitzer model is a powerful tool to predict equilibrium behavior of mixed salt solutions, there is a limitation related to non-equilibrium conditions. The harmful processes, crystal growth caused by crystallization from supersaturated solution or hydration in the confined pore spaces are non-equilibrium states. To investigate the relevant non-equilibrium states in situ measurements are required. Appropriate experimental techniques are rare. Environmental scanning electron microscopy (ESEM) offers the feasibility as well as temperature and humidity controlled X-ray diffraction (RH-XRD). Both techniques were used to study the phase changes of salts relevant to salt decay [14,15]. In contrast to ESEM, RH-XRD provides for observations to be made not only on the surface of a porous material, but also within the pore space of the material.

The major objective of the present thesis was the combined use of an equilibrium model and experimental work on both the thermodynamics and the kinetics of phase equilibria relevant to the salt decay of building materials and museum artifacts. The Pitzer model was used to calculate equilibrium conditions, i.e. concentration, temperature and humidity, under which phase transitions take place and to construct the phase diagrams of salt systems that were investigated. The experimental work largely focused on the use of RH-XRD for the in situ observation of phase transition reactions, deliquescence, crystallization, hydration and dehydration. The salt systems investigated include several single salts that are frequently found in building materials and that are commonly used in laboratory simulation studies of salt damage [16].

A special humidity chamber for a conventional X-ray diffractometer was designed by ZEUNERT [17]. The application of this method for the direct observation of phase transition reactions such as hydration–dehydration and deliquescence–crystallization not only in bulk samples but also, for the first time, within confined spaces of a porous material was a major objective of the present thesis (cf. chapters 2–5). Glass frits with pore sizes similar to common building materials, e.g. natural stone or brick, were used for the direct observation of

phase transitions of sodium sulfate, magnesium sulfate and sodium chloride within narrow pores.

In these experiments RH-XRD was used to study both the rates of the respective phase transition reactions and the characterization of the corresponding equilibrium states. Another objective of the work was to prove the capability of RH-XRD for an accurate determination of equilibrium humidities of hydration and deliquescence reactions of salt crystals. For that purpose, a new procedure was adopted for the determination of equilibrium humidities that is based on kinetic measurements. This procedure was used to determine the deliquescence humidities of NaCl and $\text{Ca}(\text{NO}_3)_2 \cdot 4\text{H}_2\text{O}$ and the equilibrium humidity of the $\text{Ca}(\text{NO}_3)_2$ – $\text{Ca}(\text{NO}_3)_2 \cdot 2\text{H}_2\text{O}$ transition. Comparison with commonly accepted literature data for these phase equilibria confirmed the accuracy of the method, which also offers good precision. The same technique was then applied to investigate the NaCl deliquescence in the confined pore space of glass frits with median pore diameters in the range of 1.4–70 μm .

The investigation of phase transitions of magnesium sulfate hydrates were subject of an interdisciplinary collaboration within a research project funded by Deutsche Forschungsgemeinschaft DFG (Verhalten von Salzen in porösen Systemen – Thermodynamische Modellierung und experimentelle Untersuchungen von Phasenumwandlungen). Magnesium sulfate is one of the salts recommended for use with the ASTM aggregate sound test [18]. Magnesium sulfate hydrates are often found in building materials and there are numerous examples where severe damage is attributed to the action of magnesium sulfate hydrates. However, compared to other salts much less is known about the behavior of magnesium sulfate in laboratory tests and under field conditions. Due to a large number of different hydrated forms the phase behavior in the system $\text{MgSO}_4 + \text{H}_2\text{O}$ is quite complex. The direct observation of the hydration of $\text{MgSO}_4 \cdot \text{H}_2\text{O}$ within a porous substrate was another objective of the present work. The RH-XRD observations of the $\text{MgSO}_4 \cdot \text{H}_2\text{O}$ hydrations in the pores of a glass frit at varying humidities are compared to calculated equilibrium humidities, the latter derived from a phase diagram of the $\text{MgSO}_4 \cdot \text{H}_2\text{O}$ system evaluated from the thermodynamic data available in the literature. The RH-XRD measurements were supplemented by the visualization of morphological changes with scanning electron microscopy (carried out at the Institute of Materials Science, Bremen) and measurements of the mechanical response of the glass frits during crystal growth (carried out

at the Department of Physik, University of Oldenburg and Deutsches Bergbaumuseum, Bochum). The results of this interdisciplinary collaboration are summarized in chapter 5.

Efflorescences containing acetate in the display cases of museums, first found by Byne [19] in 1899, are a special case of salt deterioration. Since that time, several efflorescences, consisting of Ca^{2+} and CH_3COO^- in combination with NO_3^- and/or Cl^- , were found on calcareous objects [20–25] stored in wooden show cases emitting acetic acid vapor [26,27]. The conditions, i.e. temperature, relative humidity and the nature of salts present in the objects, affecting the formation of the various efflorescences are not known up to now. In particular, the formation of the unusual and ubiquitous triple salt thecotrichite, $\text{Ca}_3(\text{CH}_3\text{COO})_3\text{Cl}(\text{NO}_3)_2 \cdot 7\text{H}_2\text{O}$ [28,29], caused attention. An explanation of the mode of formation of this triple salt on museum artifacts was another major objective of this thesis (chapters 6–8). In an analytical case study the efflorescences on seriously damaged tiles in a museum environment are examined (chapter 6). The ionic composition of the salt mixture in the tiles is deduced from the analysis of wash solutions and direct sampling and analysis revealed the composition and nature of the efflorescences. Thecotrichite is found to be the main species of the ionic constituents by using least squares and powder diffraction analysis.

Thecotrichite appears in the phase diagram of the quaternary system $\text{Ca}(\text{CH}_3\text{COO})_2$ – CaCl_2 – $\text{Ca}(\text{NO}_3)_2$ – H_2O . The phase diagram of this system was constructed to understand the formation of this efflorescent salt (chapter 6). Therefore the Pitzer model [30], applied successfully in previous work by STEIGER [13,31] to complex salt systems consisting of the ions Na^+ , K^+ , Mg^{2+} , Ca^{2+} , Cl^- , NO_3^- , and SO_4^{2-} , which are relevant to damage of building materials, was used. As a semi-empirical approach, the Pitzer model has to be parameterized using experimental data, but up to now there is a lack of available experimental data for salt systems containing CH_3COO^- . This gap was partially closed by BEYER [32] and DORN [33] who carried out vapor pressure and solubility measurements, respectively. Their work had to be continued in the present thesis in order to determine the still lacking parameters. Solubility measurements in the ternary system $\text{Ca}(\text{CH}_3\text{COO})_2$ – $\text{Ca}(\text{NO}_3)_2$ – H_2O , as well as in the quaternary system $\text{Ca}(\text{CH}_3\text{COO})_2$ – CaCl_2 – $\text{Ca}(\text{NO}_3)_2$ – H_2O were necessary to complete the parameterization of the quaternary system (chapter 8).

The final objective was the characterization and prediction of the formation and the behavior of thecotrichite under typical museum conditions. Various crystallization pathways of

thecotrichite had to be deduced from the phase diagram and the deliquescence behavior of thecotrichite is predicted. Finally, RH-XRD measurements had to be carried out to verify the predicted deliquescence and crystallization behavior of thecotrichite efflorescences and to assess the damage potential of such deliquescences to museum artifacts.

1.1 REFERENCES

- [1] EVANS I.S., Salt crystallisation and rock weathering: a review, *Rev. Géomorph. dyn.* **1970**, 4, 153–177.
- [2] ARNOLD A., ZEHNDER K., Salt weathering on monuments. In: Zezza F. (ed.), *The conservation of monuments in the Mediterranean Basin. Proceedings of the 1st international symposium, Bari*, **1989**, 31–58.
- [3] DUTTLINGER W., KNÖFEL D., Salzkristallisation und Salzsadensmechanismus, in: Snethlage R. (ed.), *Jahresberichte aus dem Forschungsprogramm Steinerfall–Steinkonservierung Band 3 – 1991*, Verlag Ernst & Sohn, Berlin, **1993**, 197–213.
- [4] STEIGER M., NEUMANN H-H., ULRICH A., DANNECKER W., Chemische Zusammensetzung und Verteilung löslicher Salze in Natursteinmauerwerk, In: Snethlage R. (ed.), *Jahresberichte aus dem Forschungsprogramm Steinerfall–Steinkonservierung Band 3 – 1991*, Verlag Ernst & Sohn, Berlin, **1993**, 21–33.
- [5] STEIGER M., NEUMANN H-H., GRODTEN T., WITTENBURG C., DANNECKER W., Salze in Natursteinmauerwerk – Probenahme, Messung und Interpretation, In: Snethlage R. (ed.), *Denkmalpflege und Naturwissenschaft, Natursteinkonservierung II*, Fraunhofer IRB Verlag, Stuttgart, **1998**, 61–91.
- [6] ZEHNDER K., ARNOLD A., Stone damage due to formate salts, *Stud. Conserv.* **1984**, 29, 32–34.
- [7] STEIGER M., Crystal growth in porous materials–1: The crystallization pressure of large crystals, *J. Crys. Growth* **2005**, 282, 455–469.
- [8] WINKLER E.M., WILHELM E.J., Salt burst by hydration pressures in architectural stone in urban atmosphere, *Geol. Soc. Am. Bull.* **1970**, 81, 567–572.
- [9] STEIGER M., DANNECKER W., Hygroskopische Eigenschaften und Kristallisationsverhalten von Salzgemischen. In: Snethlage R. (ed.): *Jahresberichte aus dem Forschungsprogramm Steinerfall–Steinkonservierung Band 5 – 1993*, Ernst & Sohn, Berlin **1995**, 115–128.
- [10] PRICE C.A., BRIMBLECOMBE, P., Preventing salt damage in porous materials. In: *Preventive conservation: Practice, theory and research*. International Institute for Conservation, **1994**, 90–93.
- [11] CLEGG S.L., WHITFIELD M., Activity coefficients in natural waters. In: Pitzer K.S. (ed.), *Activity Coefficients in Electrolyte Solutions*. CRC Press, Boca Raton, **1991**, 279–434.
- [12] PRICE C. (ed.), An expert chemical model for determining the environmental conditions needed to prevent salt damage in porous materials, European Commission project ENV4-CT95-0135, Final Report **2000**, Research Report 11, 45–52.

-
- [13] STEIGER M., Salts in porous materials: Thermodynamics of phase transitions, modeling and preventive conservation. *Restor. Build. Monum.* **2005**, 11, 419–431.
- [14] DOEHNE E., In situ dynamics of sodium sulfate hydration and dehydration in stone pores: observations at high magnifications using the environmental scanning electron microscope. In: Fassina V., Ott H., Zezza F. (eds.), *The conservation of monuments in the Mediterranean Basin. Proceedings of the 3rd International Symposium. Venice, 1994.* 143–150.
- [15] STEIGER M., ZEUNERT A., Crystallization properties of salt mixtures: Comparison of experimental results and model calculations. In: Riederer J. (ed.), *International Congress on Deterioration and Conservation of Stone - Proceedings.* Möller Druck und Verlag GmbH, Berlin, **1996**, 535–544.
- [16] Goudie A., Viles H., *Salt weathering hazards*, John Wiley & Sons ; Chichester, **1997**.
- [17] ZEUNERT A., *Feuchtekонтроllierte Röntgendiffraktometrie – Entwicklung und Anwendung zur Untersuchung verwitterungsrelevanter Salze und Salzsysteme –*, Dissertation, Fachbereich Chemie, Universität Hamburg, **2000**.
- [18] ASTM C 88-90, Standard test method for soundness of aggregate by use of sodium sulfate or magnesium sulfate. *Annu. Book ASTM Stand.* **1997**, 4.2, 37–42.
- [19] BYNE S.G., The corrosion of shells in cabinets, *J. Conchol.* **1899**, 9, 172–178.
- [20] AGNEW N., The corrosion of egg shells by acetic acid vapour, *ICCM Bull.* **1981**, 7, 3–9.
- [21] FITZHUGH E.W., GETTENS R.J., Calcicite and other efflorescent salts on objects stored in wooden museum cases. In: Brill R. (ed.), *Science and Archaeology*, MIT Press, Cambridge **1971**, 91–102.
- [22] TENNENT N.H., BAIRD T., The deterioration of mollusca collections: identification of shell efflorescence, *Stud. Conserv.* **1985**, 3, 73–85.
- [23] VAN TASSEL R., Une efflorescence d'acétatochlorure de calcium sur des roches calcaires dans des collections, *Bull. Musée royal d'Histoire naturelle Belgique* **1945**, 21, 1–11.
- [24] WHEELER G.S., WYPYSKI M.T., An unusual efflorescence on Greek ceramics, *Stud. Conserv.* **1993**, 38, 55–62.
- [25] ERHARDT D., WESTLEY H., PADFIELD T., Coral brooch with white corrosion, Conservation Analytical Laboratory (CAL), Smithsonian Institution, Washington DC, Report No. 3528, **1981**.
- [26] TÉTREAU J., La mesure de l'acidité des produits volatils, *J. Internat. Inst. Conserv.–Can. Group* **1992**, 17, 17–25.
- [27] GRZYWACZ C.M., TENNENT N.H., Pollution monitoring in storage and display cabinets: Carbonyl pollutant levels in relation to artifact deterioration. In: Roy A., Smith P (eds.) *Preventive conservation: practice, theory and research*, The International Institute for Conservation, London, **1994**, 164–172.
- [28] GIBSON L.T., COOKSEY B.G., LITTLEJOHN D., TENNENT N.H., Characterisation of an unusual crystalline efflorescence on an Egyptian limestone relief, *Anal. Chim. Acta* **1997**, 337, 151–164.

-
- [29] HALSBERGHE L., Ceramics threatened by acid-induced salts. In: Townsend J.H., Eremin K., Adriaens A. (eds.), Conservation science 2002, Archetype Publications, London **2003**, 18–24.
- [30] PITZER K.S., Ion interaction approach: Theory and data correlation. In: Pitzer K.S. (ed.), Activity Coefficients in Electrolyte Solutions. CRC Press, Boca Raton, **1991**, 75–153.
- [31] STEIGER M., BEYER R., DORN J., A Thermodynamic model of the $\text{Na}^+ - \text{Ca}^{2+} - \text{Cl}^- - \text{CH}_3\text{COO}^- - \text{H}_2\text{O}$ system. In: Price C. (ed.), An expert chemical model for determining the environmental conditions needed to prevent salt damage in porous materials, European Commission project ENV4-CT95-0135, Final Report **2000**, Research Report 11, 45–52.
- [32] BEYER R., Charakterisierung von binären und ternären Elektrolytsystemen mit Anionen organischer Säuren – Wasseraktivitätsmessungen und thermodynamische Modellierung. Dissertation, Fachbereich Chemie, Universität Hamburg **2001**.
- [33] DORN J., Experimentelle Bestimmung und thermodynamische Modellierung von Löslichkeitsgleichgewichten im System $\text{Na}^+ - \text{Ca}^{2+} - \text{OAc}^- - \text{Cl}^- - \text{H}_2\text{O}$, Dissertation, Fachbereich Chemie, Universität Hamburg, **2003**.

Chapter 2

Investigation of sodium sulfate phase transitions in a porous material using humidity and temperature controlled X-Ray diffraction

Kirsten Linnow, Anke Zeunert, Michael Steiger

Institute of Inorganic and Applied Chemistry, University of Hamburg, Martin-Luther-King-Platz 6, D-20146 Hamburg

In: Analytical Chemistry **2006**, 78, 4683–4689, ([DOI:10.1021/ac0603936](https://doi.org/10.1021/ac0603936)).

Reproduced with permission from Analytical Chemistry. Copyright [2006] American Chemical Society.

2.1 INTRODUCTION

The pressure generated by crystal growth of salts in confined spaces of porous building materials such as stone, brick and concrete is generally recognized as a major cause of damage in ancient monuments and modern buildings [1,2]. Crystal growth is also considered as an important weathering mechanism of natural rocks in a variety of environments not only on earth, e.g. in deserts [3], dry Antarctic valleys [4] and tropical coastlines, but also on Mars [5]. Crystal growth in porous materials is the result of phase changes that are induced by variation of ambient temperature and relative humidity, *RH*. Unfavorable conditions of temperature and *RH* may result in repeated cycles of crystallization–deliquescence and hydration–dehydration, respectively. Under such conditions, building materials and natural rocks are subject to rapid decay.

To investigate the deleterious processes in porous materials, appropriate in situ methods under controlled conditions of temperature and *RH* are desirable. X-ray diffraction is the obvious choice for direct speciation analysis in the solid state. There is quite a number of successful applications of temperature controlled X-ray diffractometry (TXRD) in solid-state chemistry as reviewed by EPPLE [6]. However, there are comparably few applications of X-ray diffraction under controlled conditions of relative humidity, RH-XRD. An early application of RH-XRD was a study on lattice changes in hemoglobin crystals [7] where a single crystal diffractometer was used and the humidity was controlled using saturated salt solutions. Hence, only measurements under static *RH* conditions were possible. Later, RH-XRD was improved by the use of automated humidity control systems [8–11] allowing for dynamic in situ diffractometry under controlled conditions of temperature and *RH*. Applications include studies of the hydration and expansion behavior of clay minerals and related compounds [8–13], a study of the deliquescence properties of atmospheric aerosol samples [14], the in situ investigation of crystallization from supersaturated sodium carbonate solution [9] and hydration–dehydration reactions of magnesium sulfate hydrates [15].

Temperature stability is a critical parameter in RH-XRD as the relative humidity at constant water vapor partial pressure is strongly affected by temperature variation. In most previous applications of RH-XRD an environmental cell is connected to a humidity generator providing an air flow of controlled temperature and humidity through the chamber [8,9,11]. Temperatures in this air flow that are different from the ambient air temperature may result in

temperature gradients between chamber wall, sample stage and the surrounding air. Under unfavorable conditions this may cause condensation of water on colder surfaces, in the worst case on the sample stage [9,11]. Generally, temperature gradients can severely bias the *RH* control in RH-XRD. One objective of the present study was the design of an optimized environmental cell for use with RH-XRD with improved temperature stability in order to avoid temperature gradients.

The application of RH-XRD for the direct observation of phase transition reactions occurring in the pore space of a porous substrate was another major objective of the present work. Sodium sulfate was selected as the appropriate salt for this study as this salt is most widely used in accelerated weathering tests, e.g. ASTM aggregate sound test [16]. In such type of experiments sodium sulfate proved to be extremely destructive [1]. Though there is no doubt that damage is caused by crystal growth in the pore space of the materials, it is less obvious which of the various crystalline forms of sodium sulfate is responsible under particular experimental conditions. The decahydrate $\text{Na}_2\text{SO}_4 \cdot 10\text{H}_2\text{O}$ (mirabilite) and the anhydrous form $\text{Na}_2\text{SO}_4(\text{V})$ (thenardite) are the only stable phases at temperatures close to ambient. Apart from thenardite and mirabilite however, also a metastable anhydrous form, $\text{Na}_2\text{SO}_4(\text{III})$ was observed in experiments with porous materials [17]. Considering the phase diagram of the system $\text{Na}_2\text{SO}_4 + \text{H}_2\text{O}$, there is a number of possible phase transition reactions that might cause crystal growth in porous materials. It is expected that the reaction pathways strongly depend on the ambient conditions.

In this report we demonstrate the suitability of RH-XRD for the direct observation of phase transformation reactions in the $\text{Na}_2\text{SO}_4 + \text{H}_2\text{O}$ system. It is shown that RH-XRD provides not only reliable information on the equilibrium *RH* conditions of stable and metastable equilibria but also valuable information on the reaction pathways. Using glass frits of different pore size as the porous substrates, it is possible to extend the RH-XRD approach in order to investigate in situ phase transformation reactions within the pores of the substrate.

2.2 EXPERIMENTAL SECTION

2.2.1 Environmental chamber

XRD parameters were obtained on a Siemens D5000 Bragg–Brentano para-focusing powder diffractometer with a vertical θ : 2θ configuration using Cu K α -radiation and a position-sensitive detector (PSD) recording data from a 12° 2θ band at one time. As shown in Figure 1, the goniometer is equipped with a specially designed environmental cell consisting of an airtight cylindrical stainless steel chamber which is fixed by a flange to the θ -circle of the diffractometer. Figure 2 provides a side view of the chamber with flange (a), front plate (b) and thermostated wall (c). The sample is placed on a spring mounted brass holder (d) which is fixed with adjusting screws (e) in the correct height of the θ : 2θ alignment. Inlet and outlet ports for the flows of thermostated water (f) and air from the humid air generator are located at the backside of the chamber. The window for the passage of X-rays (g) is sealed with a 6 μ m Mylar film. The loss of intensity due to absorption in the Mylar film in the range of 10° – 70° 2θ was found to be negligible. The front cover is equipped with drillings for the temperature and humidity sensors (h). Due to the sensitivity of the relative humidity to temperature variation it is particularly important that the temperature is constant over the whole chamber volume. To minimize temperature gradients in our chamber, not only the air flow from the humidity generator but also the chamber wall and the brass holder are thermostated. Small channels machined in the cylindrical chamber wall allowed the connection to a thermostat (F25-MH, Julabo, Germany), thus, ensuring that the whole chamber is kept at the same temperature. A Pt-100 sensor positioned in the ambient air close to the surface of the sample and connected to the thermostat is used for temperature control. The capacitive humidity sensor (HMP 233, Vaisala, Finland) is placed directly above the temperature probe and is connected to the humid air generator.



Figure 1: Front view of the open environmental chamber fixed to the θ -circle of the D5000 diffractometer: (1) X-ray tube, (2) goniometer, (3) position sensitive detector, (4) flange (5) chamber wall (thermostated), (6) spring mounted sample holder (thermostated), (7) adjusting screws.

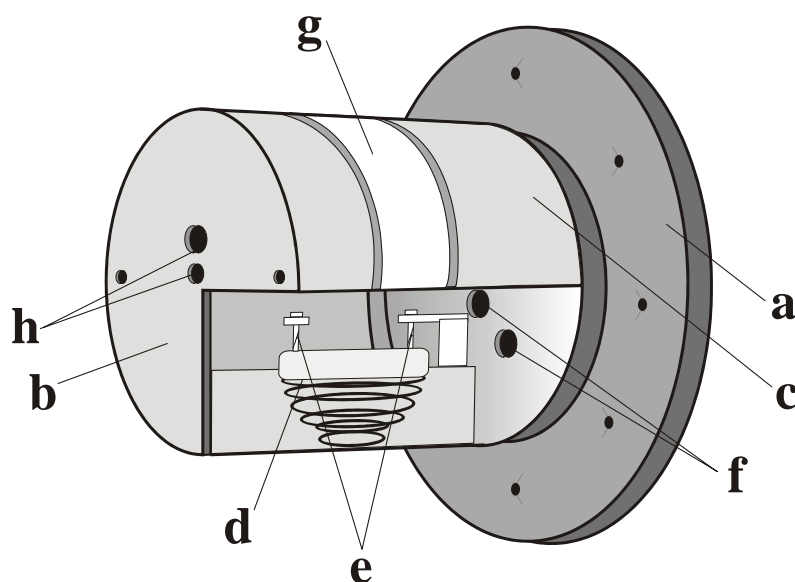


Figure 2: Side view of the environmental chamber: (a) flange, (b) front plate, (c) thermostated wall, (d) spring mounted brass holder (thermostated), (e) adjusting screws, (f) inlet and outlet ports for air and water, (g) X-ray window, (h) holes for insertion of temperature and humidity sensors.

2.2.2 Humid air generator

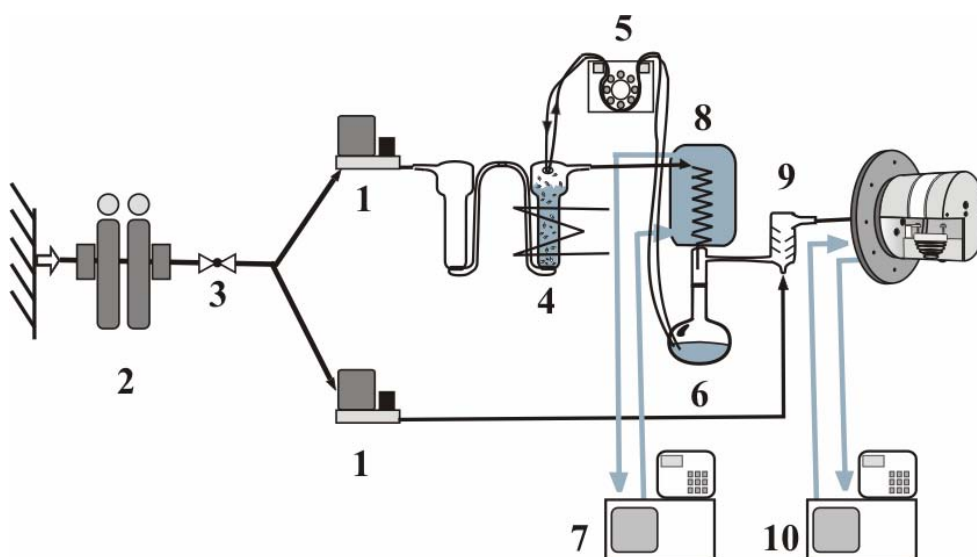


Figure 3: Schematic drawing of the humidity control system: (1) mass-flow controller, (2) adsorption dryer, (3) pressure regulator, (4) heated bubbler, (5) peristaltic pump, (6) water reservoir, (7) thermostat, (8) condensation trap, (9) mixing chamber, (10) thermostat.

A schematic drawing of the humidity control system is shown in Figure 3. Humidity control is accomplished by appropriate mixing of dry and water-saturated air using automated mass-flow controllers (1) (Brooks Instruments, Veenendaal, The Netherlands). After passing an adsorption dryer (2) and a pressure regulator (3), compressed air is saturated with water vapor in a bubbler (4) heated to about 80 °C. Using a peristaltic pump (5) the bubbler is supplied with water from a reservoir (6). To avoid condensation effects, the wet air passes a thermostated (7) condensation trap (8) at a temperature approximately 0.5 K lower than the desired final temperature, and is then mixed with the dry air in a mixing chamber (9). The temperature of the wall and the brass holder of the environmental chamber are controlled with a second thermostat (10). A computer program is used to control the humidity in the environmental chamber by appropriate mixing ratios of the wet and dry air flows. The software allows stepwise changes in humidity by defining the starting and final values, the step sizes, and the time intervals of a humidity scan. Typically, the relative humidity in the chamber can be maintained at a constant value for several days with fluctuations not exceeding $\pm 0.4\%$ RH. It is important to note, however, that the overall accuracy of the

humidity generation system is limited by the absolute accuracy of the Vaisala sensor. An overall error of $\pm 2.5\%$ *RH* was estimated from independent measurements of equilibrium humidities above saturated salt solutions. In the temperature range 10–50°C the humid air generator can be used to adjust any desired humidity within a range of 3–97% *RH*.

2.2.3 Sample preparation

Equilibration of salt and water vapor can be time-consuming. Hence, small sample sizes are desirable to avoid long equilibration times. Two different techniques were used to prepare the sodium sulfate samples. Quartz fiber filters (MK 360, Munktell Filter, Grycksbo, Sweden) were selected as a nonporous substrate. Filters were loaded with sodium sulfate using an aerosol generator [18]. A conventional cross-flow nebulizer is used to generate an aerosol of salt solution droplets of known concentration which were subsequently dried and collected on the quartz fiber filters yielding a homogeneous distribution of relatively small crystals and small amounts of sodium sulfate (10–30 mg) on the filter surface. These filters were directly used for the RH-XRD measurements.

Glass frits (VitraPOR, ROBU Glasfilter-Geräte GmbH, Germany) of porosity classes P1.6 and P16 with nominal pore sizes of 1.0–1.6 μm and 10–16 μm , respectively, were selected as porous substrates. The amorphous glass frits did not interfere with the X-ray patterns of the sodium sulfate phases. The glass frits were impregnated with a solution of Na_2SO_4 (10% w/w) and subsequently freeze-dried in order to obtain a homogeneous distribution of sodium sulfate in the frits avoiding efflorescences on the surface. This preparation yields amounts of 39 and 95 mg sodium sulfate taken up in the pores of the P16 and P1.6 frits, respectively. Semi quantitative profiles of the sodium concentration in cross sections of the glass frits were measured by laser ablation inductively coupled plasma mass spectrometry (LA-ICP-MS). The profiles showed a reasonably even salt distribution over the whole depth of the glass frits.

2.2.4 Measurements

An *RH–T* phase diagram of the stable phases in the $\text{Na}_2\text{SO}_4 + \text{H}_2\text{O}$ system at near ambient temperatures is depicted in Figure 4. It is based on a careful evaluation of the available thermodynamic data of aqueous Na_2SO_4 and the various crystalline phases. In the present work we have studied the deliquescence–crystallization equilibrium of $\text{Na}_2\text{SO}_4 \cdot 10\text{H}_2\text{O}$

(curve a in Figure 4) and the hydration–dehydration equilibrium of $\text{Na}_2\text{SO}_4 \cdot 10\text{H}_2\text{O}$ and $\text{Na}_2\text{SO}_4(\text{V})$, i.e., thenardite (curve b in Figure 4).

A summary of the experiments that were carried out is provided in Table 1, and the temperature and RH induced reaction pathways are also illustrated in Figure 4. The anhydrous Na_2SO_4 aerosol collected on the quartz fiber filters after drying the solution droplets was subjected to a stepwise increase in RH in order to induce the hydration reaction, i.e., the formation of $\text{Na}_2\text{SO}_4 \cdot 10\text{H}_2\text{O}$ and, subsequently, the deliquescence of the hydrate and the formation of a solution. RH was increased in steps of 0.5% and the samples were equilibrated for 60 min at each humidity. The crystallization from the sodium sulfate solution was induced by stepwise decreasing RH using the same step size but an increased equilibration time of 120 min. These experiments were carried out under isothermal conditions at 25°C . XRD patterns were recorded from 10° – 70° 2θ and were assigned to the respective RH in the chamber. Phase transformations were easily detected by sudden changes in the XRD patterns, i.e., the appearance or disappearance of characteristic peaks.

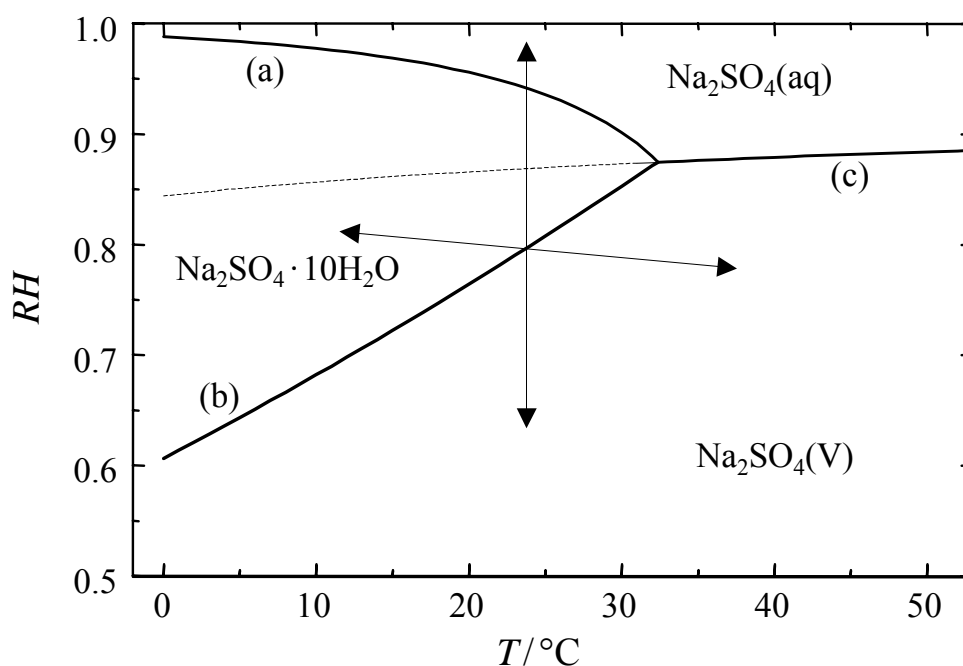


Figure 4: RH/T phase diagram of $\text{Na}_2\text{SO}_4 + \text{H}_2\text{O}$ with (a) deliquescence–crystallization equilibrium of $\text{Na}_2\text{SO}_4 \cdot 10\text{H}_2\text{O}$, (b) hydration–dehydration equilibrium, (c) deliquescence–crystallization equilibrium of $\text{Na}_2\text{SO}_4(\text{V})$ with metastable branch (dotted) and RH and temperature induced reaction pathways (arrows).

Exactly the same procedure was also used to study the hydration, deliquescence and crystallization in the glass frits P16 and P1.6, respectively. Additional experiments at approximately constant *RH* were carried out with the P1.6 frit. In these experiments the hydration of $\text{Na}_2\text{SO}_4(\text{V})$ and the subsequent dehydration of $\text{Na}_2\text{SO}_4 \cdot 10\text{H}_2\text{O}$ were induced by a change in temperature as indicated in Figure 4.

Table 1: Phase transformation reactions investigated by RH-XRD.

substrate	phase transition induced by	reaction
quartz fiber filter	<i>RH</i> scans	hydration, deliquescence, crystallization
glass frit P16	<i>RH</i> scans	hydration, deliquescence, crystallization
glass frit P1.6	<i>RH</i> scans	hydration, deliquescence, crystallization
	temperature scans	hydration/dehydration

2.3 RESULTS

2.3.1 *RH* induced phase transitions on quartz fiber filters

Evaporation drying of solution droplets in the drying tower yielded particles of anhydrous sodium sulfate that were collected on the quartz fiber filters. The initial XRD pattern of the dry filters revealed the presence of a mixture of two different anhydrous forms, $\text{Na}_2\text{SO}_4(\text{V})$ (thenardite) and $\text{Na}_2\text{SO}_4(\text{III})$ (phase III). Upon stepwise increasing *RH* the line intensities of thenardite continuously increased while the intensities of phase III decreased. Total absence of phase III peaks indicated that the conversion into thenardite was complete at 80% *RH*. Hydration of $\text{Na}_2\text{SO}_4(\text{V})$ and formation of $\text{Na}_2\text{SO}_4 \cdot 10\text{H}_2\text{O}$ was observed at 82% *RH*. Successively recorded diffraction patterns did not indicate the presence of an amorphous phase at any time during the hydration. Upon further increasing the relative humidity, the deliquescence of $\text{Na}_2\text{SO}_4 \cdot 10\text{H}_2\text{O}$ (mirabilite) occurred at 91% *RH*. After complete dissolution of mirabilite, stepwise decreases in the relative humidity resulted in the crystallization of $\text{Na}_2\text{SO}_4(\text{V})$ at 84% *RH*. Crystallization of $\text{Na}_2\text{SO}_4 \cdot 10\text{H}_2\text{O}$ was not observed.

2.3.2 RH induced phase transitions in glass frits

In contrast to evaporation drying, freeze-drying did not yield crystals of $\text{Na}_2\text{SO}_4(\text{III})$ but rather phase V was identified in the dry glass frits. The diffraction patterns of $\text{Na}_2\text{SO}_4(\text{V})$ in the pore space of the glass frits are depicted in Figure 5 together with the JCPDS (Joint Committee on Diffraction Pattern) standard 36-0397. While the pattern in the P16 glass frit compares nicely to the JCPDS standard, there are some deviations in the case of the P1.6 glass frit. Though the peaks observed at 22.5° , 23.6° , 25.5° , 37.9° , 46.3° and 48.9° 2θ are all peaks of $\text{Na}_2\text{SO}_4(\text{V})$, their intensity should be less than 3% of the intensity of the strongest peak.

Obviously, the orientation of the individual crystals in the limited pore space of the P1.6 frit is not entirely random resulting in preferred orientations which are responsible for the deviations in the XRD pattern. Nonetheless, the unambiguous identification of the pattern is possible. In contrast, the arrangement of individual crystallites in the P16 frit is obviously completely random. The identification of mirabilite in the glass frits did not pose problems as well.

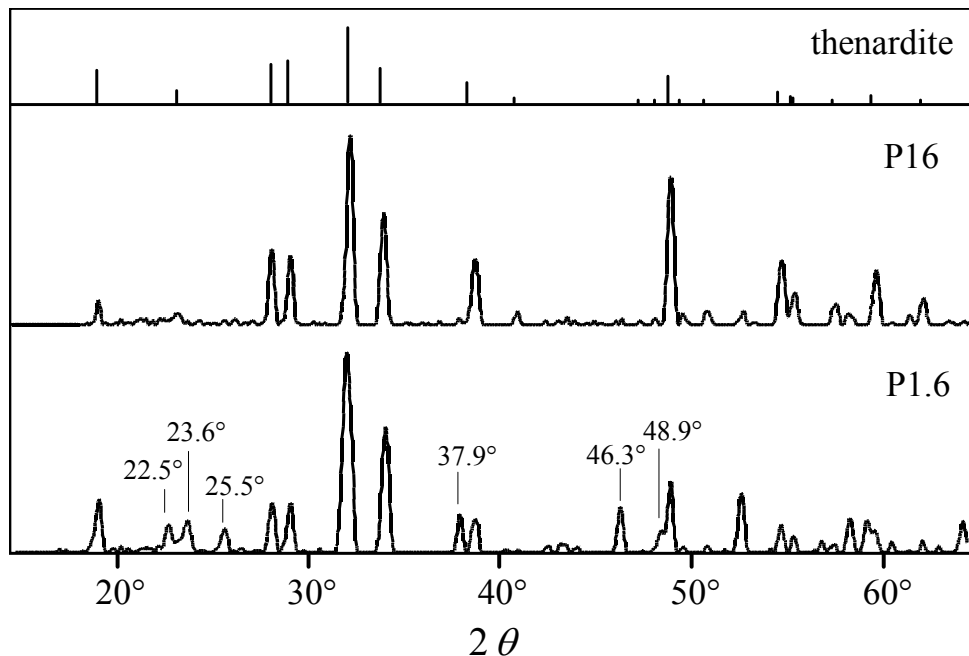


Figure 5: Diffraction pattern of $\text{Na}_2\text{SO}_4(\text{V})$ in the pore space of VitraPOR glass frits P16 and P1.6, respectively, and comparison with JCPDS standard 36-0397 of thenardite.

Diffraction patterns obtained during a scan of increasing humidity in the P16 frit are shown in Figure 6 at 1% *RH* intervals. Similar results were obtained with the P1.6 frit. In both glass frits the hydration of $\text{Na}_2\text{SO}_4(\text{V})$ to $\text{Na}_2\text{SO}_4 \cdot 10\text{H}_2\text{O}$ is observed at 83% *RH*. Like the hydration on the quartz fiber filter an amorphous phase was not observed at any time during the hydration, i.e., the decrease in thenardite peak intensities and the occurrence of mirabilite happened at the same time. The deliquescence of mirabilite started at 91% *RH* in both frits. The peaks, however, did not disappear abruptly, but the line intensities decreased over a range of relative humidity.

Dissolution of mirabilite was complete in both glass frits after five hours at 93% *RH*. In this case, the equilibration times of one hour, determined for salts in a nonporous environment, were obviously insufficient to achieve full equilibrium in the glass frits. During the subsequent decrease in *RH*, the crystallization of mirabilite did not occur, even at 75% *RH*, i.e., far below its saturation humidity (cf. Figure 4). While the crystallization of thenardite was observed at 84% *RH* on the quartz filters, i.e., slightly below its saturation humidity, no crystallization occurred in the glass frits during the humidity scans. Subsequent drying at 0% *RH* revealed the crystallization of $\text{Na}_2\text{SO}_4(\text{V})$ within a few minutes. However, the intensity of the strongest line was less than 10% of the intensity in the initial $\text{Na}_2\text{SO}_4(\text{V})$ pattern. Intensities remained constant over a period of 24 hours, indicating that the crystallization process was complete.

2.3.3 Temperature induced hydration and dehydration.

A change in temperature reveals rapid hydration and dehydration of thenardite and mirabilite, respectively. Decreasing the temperature from 25°C to 15°C at a rate of $0.2 \text{ K} \cdot \text{min}^{-1}$ and at $74.7 \pm 0.7\%$ *RH* yields the complete hydration of thenardite within 26 min, i.e., slightly below 20°C in reasonable agreement with the phase diagram (Figure 4). Subsequently, increasing the temperature from 15°C at a rate of $0.4 \text{ K} \cdot \text{min}^{-1}$ and at $\text{RH} < 87\%$ yields the complete dehydration of mirabilite within 26 min. In the latter experiment the standard deviation of the *RH* in the chamber was increased (8%) due to the rapid heating rate. It was difficult, therefore, to determine the transition temperature of the dehydration exactly. However, considering both the changes in temperature and *RH*, it appears that there is agreement with the theoretically expected values also in the case of the dehydration. It should be noted that in both

experiments the deliquescence humidities of the respective educt phases were not exceeded at any time.

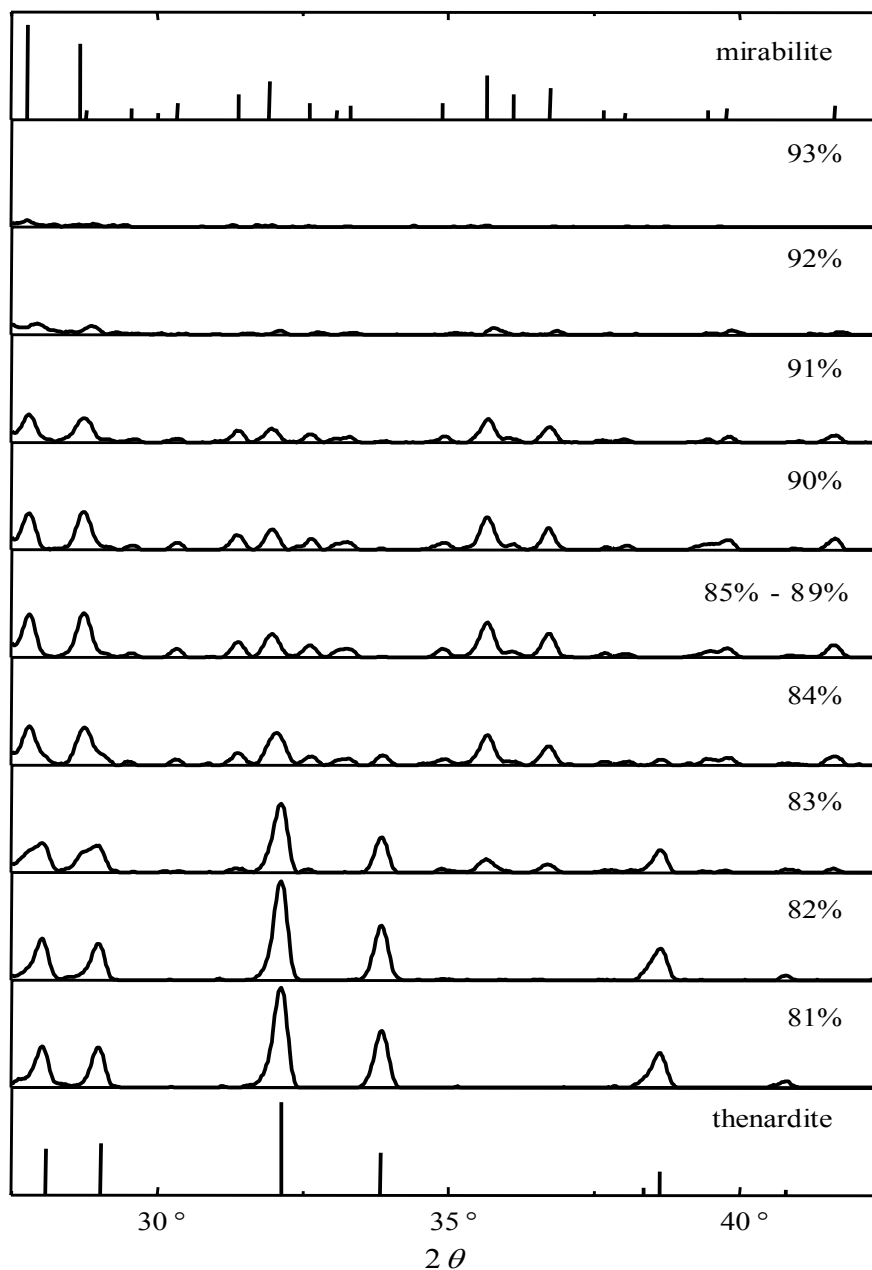


Figure 6: Diffraction patterns at 1% *RH* intervals in P16 glass frit obtained during a scan of increasing relative humidity.

2.4 DISCUSSION

2.4.1 Performance of RH-XRD

$\text{Na}_2\text{SO}_4(\text{V})$, thenardite, and $\text{Na}_2\text{SO}_4 \cdot 10\text{H}_2\text{O}$, mirabilite, are the only stable phases in the $\text{Na}_2\text{SO}_4 + \text{H}_2\text{O}$ system at near ambient temperatures (cf. Figure 4). Table 2 lists the equilibrium relative humidities, RH_{eq} , for the stable and the metastable equilibria as deduced from the available thermodynamic data. Thenardite is the stable form below 80.7% RH , while mirabilite can only exist at 25°C within the limited range of relative humidity from 80.7% RH to its deliquescence humidity at 93.6% RH . Table 2 also provides a summary of our experimental results. In the case of the hydration–dehydration equilibrium of thenardite and mirabilite, and the deliquescence of mirabilite, our values agree to within the stated uncertainty of 2.5% RH with the available literature data. It is concluded that RH-XRD provides a powerful tool for the study of such type of equilibria and the determination of equilibrium humidities.

It is particularly helpful that RH-XRD allows for the direct in situ investigation of phase transformations within the void spaces of porous materials. Though some minor bias of the XRD pattern was observed in the P1.6 glass frit due to preferred orientation, the identification of the pattern was still unambiguous. Additional problems may be expected in materials with nanometer size pores due to line broadening effects. However, the glass frits used represent typical pore sizes of many building materials such as natural stone and brick. It should be noted that there is a limited penetration depth of X-rays into the substrate used in the present study. With a mass attenuation coefficient of $31.6 \text{ cm}^2 \cdot \text{g}^{-1}$ for the glass frits, a penetration depth, normal to the sample surface, of 20–120 μm is estimated for Cu $K\alpha$ -radiation in the 2θ band 10° – 70° . Therefore, using RH-XRD only the phase transitions in the pores very close to the surface can be observed. This however, is not a severe disadvantage. Crystallization damage in porous materials induced by fluctuations in ambient temperature and RH will always start in the outermost pores of the material. For the remaining phase equilibria listed in Table 2, the equilibrium RH values could not be accurately determined due to kinetic influences which are discussed in more detail below. However, this is not a peculiarity of RH-XRD, but is rather a shortcoming of all experimental techniques used for the investigation of phase equilibria largely affected by kinetic influences. On the contrary, RH-XRD may offer excellent possibilities in kinetic studies as well.

Table 2: Equilibrium humidities RH_{eq} of $Na_2SO_4 + H_2O$ at 25°C.

phase change reactions	RH_{eq}	$RH_{eq}(exp)$	$RH_{eq}(exp)$
		quartz filter	glass frits
deliquescence of $Na_2SO_4(III)$	83.5%	(1)	(1)
hydration of $Na_2SO_4(V)$	80.7%	82%	83%
deliquescence of $Na_2SO_4 \cdot 10H_2O$	93.6%	91%	91%
crystallization of $Na_2SO_4 \cdot 10H_2O$	93.6%	(2)	(2)
crystallization of $Na_2SO_4(V)$	86.9%	84%	< 75%

(1) Not observed (formation of $Na_2SO_4(V)$ at RH below the $Na_2SO_4(III)$ RH_{eq})

(2) Crystallization of $Na_2SO_4 \cdot 10H_2O$ was not observed

2.4.2 $Na_2SO_4(III)$ – $Na_2SO_4(V)$ transition

Anhydrous sodium sulfate exists in a number of different forms commonly referred to as phases I–V. The stable phase at low temperature and low RH is the naturally occurring mineral thenardite which is also known as phase V, $Na_2SO_4(V)$. In contrast, phase III is metastable. Nonetheless, the formation of $Na_2SO_4(III)$ is frequently observed upon evaporation of sodium sulfate solutions at near ambient temperatures [17,19,20]. $Na_2SO_4(III)$ was also detected as the solid residue after evaporation of single levitated droplets [21], i.e., under similar conditions as in our drying tower. Hence, the detection of phase III in the aerosol collected on the quartz fiber filters was not surprising.

Though $Na_2SO_4(III)$ is metastable, it is known that this anhydrous form resists the transition to phase V due to the slow reaction rate and can be kept indefinitely at room temperature under absolutely dry conditions [22]. However, the presence of small amounts of water can cause the complete conversion of $Na_2SO_4(III)$ to $Na_2SO_4(V)$. This transition was investigated using in situ Raman spectroscopy by XU and SCHWEIGER [21]. They observed rapid conversion during deliquescence of anhydrous sodium sulfate, suggesting a dissolution–reprecipitation mechanism. However, no information about the deliquescence humidity was provided. In our own experiments the conversion of $Na_2SO_4(III)$ was complete at 80% RH without any indication of the presence of a liquid phase. Hence, we assume that deliquescence did not yet occur. The deliquescence humidity of $Na_2SO_4(III)$ may be estimated from existing

thermodynamic data. As $\text{Na}_2\text{SO}_4(\text{III})$ is metastable at room temperature, its solubility must be greater than that of $\text{Na}_2\text{SO}_4(\text{V})$. Consequently, its deliquescence humidity is lower than that of the more stable phase V. Using the thermodynamic data of the two solids tabulated by BRODALE and GIAUQUE [22] and the thermodynamic properties of $\text{Na}_2\text{SO}_4(\text{aq})$ [23] a solubility of $4.3 \text{ mol}\cdot\text{kg}^{-1}$ at 25°C is estimated for $\text{Na}_2\text{SO}_4(\text{III})$. This yields a deliquescence humidity of 83.5% obtained from the water activities of concentrated Na_2SO_4 solutions. Hence, the present measurements provide evidence that $\text{Na}_2\text{SO}_4(\text{III})$ rapidly converts into $\text{Na}_2\text{SO}_4(\text{V})$ below the deliquescence humidity of either of the two solids. It is concluded that the reaction proceeds as a true solid state reaction in the absence of liquid water, at relative humidities $<80\%$. However, there is no doubt that in the presence of small amounts of water vapor, the conversion is substantially accelerated. Most likely, the number of $\text{Na}_2\text{SO}_4(\text{V})$ nuclei is substantially increased in the presence of small amounts of water.

2.4.3 Hydration of $\text{Na}_2\text{SO}_4(\text{V})$

The hydration–dehydration transition of thenardite and mirabilite was previously investigated with light microscopy (LM), thermogravimetry (TG) and environmental scanning electron microscopy (ESEM). Using TG, HAMAD [24] found that both the hydration of thenardite and the dehydration of mirabilite proceed fairly rapidly at about the same rates. Also, in both cases, the product was directly formed in a single step reaction. While other authors also found that the dehydration proceeds rapidly, the formation of a layer of decahydrate during the hydration of large thenardite crystals was observed by CHAROLA and DOEHNE [25,26]. This product layer prevented the hydration of the bulk crystal. Most likely, the reaction rate is then limited by the diffusion of water vapor across the barrier product layer. In the presence of liquid water, however, rapid hydration was observed as a two-step process involving dissolution followed by recrystallization [25,26].

In our experiments at 25°C we observed the complete hydration of thenardite on the quartz fiber filter at 82% *RH*, which agrees to within our experimental uncertainty with the commonly accepted value of 80.7% *RH* (cf. Table 2). Similarly, the hydration proceeded smoothly in the pores of the glass frits and was complete at 83% *RH*. Hence, in all cases, the hydration was complete at $\leq 83\%$ *RH* which is clearly below the deliquescence humidity of 86.9% *RH* at 25°C . Furthermore, complete and rapid hydration and dehydration were achieved in the glass frit P1.6 by temperature variation at humidities below the deliquescence

humidity. In all these experiments, the diffraction patterns did not indicate the presence of an amorphous phase at any time during the reaction. Again we conclude that the hydration reaction proceeds as a true solid state reaction if the relative humidity does not exceed the deliquescence humidity of anhydrous Na_2SO_4 .

The question arises why in our experiments the initial formation of a surface layer of mirabilite did not hinder the further hydration of bulk thenardite crystals. Most likely, this is due to the small sizes of the thenardite crystals used in our experiments. Scanning electron microscopy of the loaded quartz fiber filters revealed an average crystal size of the anhydrous Na_2SO_4 crystals of about 1–2 μm (cf. Figure 7). In the glass frits, an upper crystal size limit is given by the pore geometry, i.e., the median pore diameters of 1.3 and 13 μm , respectively. Considering however, that there is a substantial reduction in total volume upon the sublimation of water vapor from the freeze-dried solutions, considerably smaller crystal sizes might be expected. In contrast, the crystal size of commercially available thenardite is usually in the order of 30–40 μm . Also DOEHNE [26] found significantly increased hydration rates of very small thenardite crystals.

2.4.4 Mirabilite deliquescence

The observed value of the mirabilite deliquescence at 91% *RH*, both on the quartz filter and in the pores of the glass frits, agrees reasonably well with the theoretical value (cf. Table 2). Hence, there is no significant influence of the substrate on the equilibrium deliquescence humidity. In contrast, the kinetics of the deliquescence is significantly slower, in the porous substrates than on the quartz fiber filter.

The rate of deliquescence of a crystalline solid is affected by (1) the rate of dissolution of the crystalline core in the solution film, and (2) the transfer of water vapor from the surrounding gas phase into the solution. The transfer of water vapor into the liquid phase is expected to depend on the available area of the gas–liquid interface. In the case of a free droplet which is formed during the deliquescence of a crystal adhered on the surface of the fiber filter, no particular hindrance of the water vapor transfer is expected. However, if the solution is formed in a pore, the available area of the gas–liquid interface is limited as a large part of the total surface area of the liquid phase is in direct contact with the pore wall. In effect, it appears that the water vapor transfer is considerably lower in a porous material than for free droplets resulting in the slower rate of the deliquescence.

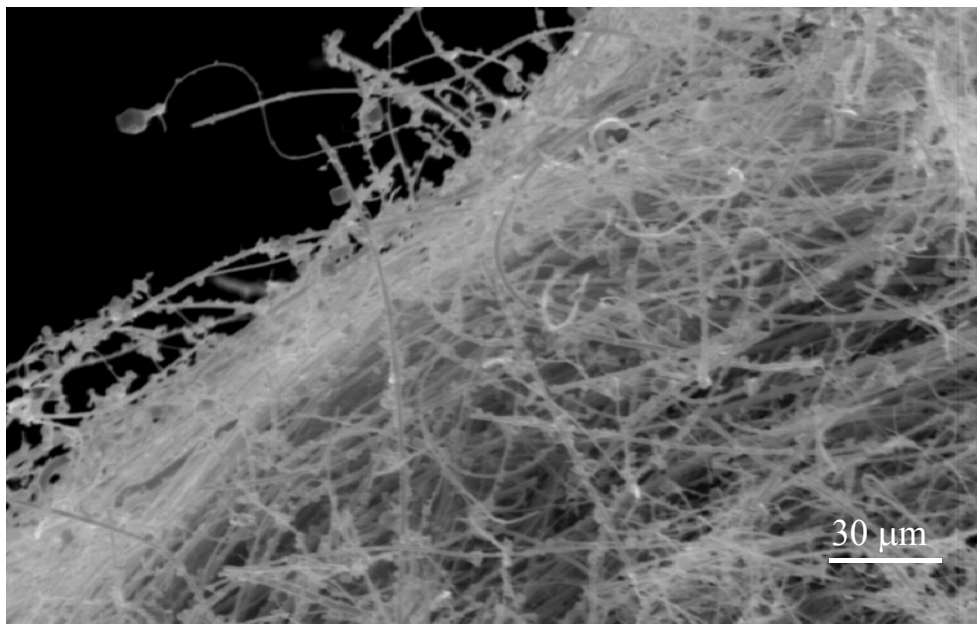


Figure 7: $\text{Na}_2\text{SO}_4(\text{III})$ crystals collected on quartz fiber filter after evaporation drying of 1% (w/w) aqueous Na_2SO_4 solution droplets; note that the average crystal sizes does not exceed about 1–2 μm .

2.4.5 Crystallization

In all reactions discussed so far, the experimentally observed relative humidities at which a particular reaction started agreed to within our stated experimental uncertainty with the available thermodynamic data. In other words, the procedure of stepwise changing relative humidity (or temperature) with equilibration times of one or two hours was sufficient to investigate true equilibrium situations. This was not so in the case of the isothermal crystallization of sodium sulfate from solution. Decreasing the relative humidity in the chamber causes the evaporation of water and the solution becomes more and more concentrated. Finally, the solution is saturated with respect to mirabilite, $\text{Na}_2\text{SO}_4 \cdot 10\text{H}_2\text{O}$, at the deliquescence point of 93.6% *RH*. However, crystallization of the decahydrate on the quartz fiber filter was not observed as the relative humidity was further decreased. Even at 87% *RH*, the deliquescence or saturation humidity of metastable $\text{Na}_2\text{SO}_4(\text{V})$, the mirabilite did not crystallize. Finally, thenardite crystallization started at 84% *RH*, where the solution is slightly supersaturated with phase V but strongly supersaturated with respect to $\text{Na}_2\text{SO}_4 \cdot 10\text{H}_2\text{O}$.

Similar results were obtained in the glass frits. No crystallization of either thenardite or mirabilite occurred at relative humidities above 75%. Under such conditions the pore solution

is far supersaturated with respect to both solids. Finally, rapid evaporation under a continuous flow of dry air through the chamber revealed the occurrence of the thenardite XRD pattern, however, with quite small intensities of the thenardite peaks. Most likely, the reduced intensities are the result of the transport of the pore solution during evaporation. As water evaporates the drying front moves from the surface of the frits into the interior. As a result of the limited supply with supersaturated solution, the outermost pores are only partly filled with growing thenardite crystals. Due to the limited penetration depth of the X-rays this leads to a reduction of the peak intensities.

Also other authors observed that sodium sulfate solutions can be easily supersaturated. Under conditions of rapid evaporation, RODRIGUEZ-NAVARRO and DOEHNE [17] obtained all three solids in a porous limestone, the two anhydrous forms III and V, and the decahydrate. Even higher supersaturations at about 57% *RH* were observed in evaporating droplets [27]. The present measurements confirm that it is possible to achieve substantial supersaturation also in narrow pores without spontaneous heterogeneous nucleation occurring. This tendency of sodium sulfate solutions to supersaturate is an important property of the salt which is closely related to its ability to generate high stresses and damage in porous materials [28].

There is no obvious explanation why thenardite crystallization occurred at lower *RH* in the glass frits than on the quartz filter and additional experiments including a systematic investigation of kinetic influences are required to clarify this behavior. RH-XRD will be a very helpful tool in future work for an improved understanding of the behavior of sodium sulfate in porous materials. In the present work the evaporation from the pore solutions and resulting supersaturation were only determined under conditions of comparably slow scans of stepwise changes in *RH*. In future studies, however, it is possible to use entirely different conditions to study evaporation and crystallization in situ. It should be possible to determine the critical conditions under which evaporation of sodium sulfate leads to particularly high supersaturations, thus, generating large stresses to porous materials.

2.5 CONCLUSIONS

RH-XRD is an appropriate method for the in situ investigation of phase transformations and crystal growth. Reactions that cause crystal growth within confined spaces are major causes of damage in porous building materials such as natural stone, brick, ceramics etc. Typically,

the deleterious phase transition reactions are initiated by changes in temperature and relative humidity. In the present paper it is demonstrated that RH-XRD can also be successfully applied to investigate such phase transformation reactions in situ within the void spaces of a porous material. Glass frits with pore sizes similar to common building materials, e.g. natural stone or brick, proved to be an appropriate substrate for the direct observation of crystal growth within narrow pores.

This work was focused on sodium sulfate which is generally considered as a particularly deleterious salt in building materials. RH-XRD proved to be very useful in understanding the various phase transformation reactions of sodium sulfate. The equilibrium humidity of the hydration–dehydration reaction ($\text{Na}_2\text{SO}_4(\text{V})\text{--}\text{Na}_2\text{SO}_4 \cdot 10\text{H}_2\text{O}$) and the deliquescence humidity of $\text{Na}_2\text{SO}_4 \cdot 10\text{H}_2\text{O}$ determined by RH-XRD agree within the stated experimental uncertainty with theoretical values derived from the available thermodynamic data. In situ observation with RH-XRD yields additional information about the reaction pathways of both, the hydration of $\text{Na}_2\text{SO}_4(\text{V})$ and the solid–solid transition of metastable $\text{Na}_2\text{SO}_4(\text{III})$ and formation of $\text{Na}_2\text{SO}_4(\text{V})$. Both reactions proceed as true solid state reactions at enhanced relative humidity but still below the deliquescence *RH* of the respective educt phase, i.e., $\text{Na}_2\text{SO}_4(\text{V})$ or $\text{Na}_2\text{SO}_4(\text{III})$, thus, without the formation of a solution phase. Similarly, hydration of $\text{Na}_2\text{SO}_4(\text{V})$ and dehydration of $\text{Na}_2\text{SO}_4 \cdot 10\text{H}_2\text{O}$ can be easily initiated by temperature variation with *RH* continuously below the deliquescence humidity of $\text{Na}_2\text{SO}_4(\text{V})$. While these solid state reactions proceed fairly rapidly, crystal growth of sodium sulfate from an aqueous solution is found to be substantially hindered and requires remarkable supersaturations.

There are important implications of these findings concerning the behavior of sodium sulfate in porous building materials. Quite short-term variation of temperature or relative humidity, e.g. typical daily climatic cycles, are sufficient to cause continuous changes of the hydration state of sodium sulfate within the pore space of a building material. In contrast, on the same time scale, fluctuations of the ambient humidity around the deliquescence *RH* of $\text{Na}_2\text{SO}_4 \cdot 10\text{H}_2\text{O}$ might not be sufficient to induce crystal growth within the pores. However, during longer periods of low ambient *RH*, crystal growth of either mirabilite, or preferably, thenardite from highly supersaturated pore solutions is very likely. Under such conditions substantial stresses generated by the growing crystals confined in the pore space are to be expected.

Acknowledgements

The authors are grateful to Angela Schlenker for LA-ICP-MS measurements and Dr. Herbert Juling for the freeze-drying of the glass frits. This work benefited a lot from helpful discussions with Dr. Kathrin Hofmann. Part of this work was funded by the European Commission, grant No. ENV4–CT95–0135.

2.6 REFERENCES

- [1] GOUDIE A., VILES H., *Salt Weathering Hazards*, John Wiley & Sons, Chichester, **1997**.
- [2] DOEHNE E., *Natural Stone, Weathering Phenomena, conservation strategies and case studies*, Geol. Soc. Spec. Publ. **2002**, 205, 51–64.
- [3] COOKE R. U., SMALLEY I. J., Salt weathering in deserts, *Nature* **1968**, 220, 1226–1227.
- [4] JOHNSTON J. H., Salt weathering processes in the McMurdo dry valley regions of South Victoria Land, Antarctica, *NZ J. Geol. Geophys.* **1973**, 16, 221–224.
- [5] MALIN M. C., Salt weathering on Mars, *J. Geophys. Res.* **1974**, 79, 3888–3894.
- [6] EPPLE M., Applications of temperature-resolved diffraction methods in thermal analysis, *J. Therm. Anal.* **1994**, 42, 559–593.
- [7] HUXLEY H. E., KENDREW J. C., Discontinuous lattice changes in haemoglobin crystals, *Acta Cryst.* **1953**, 6, 76–80.
- [8] WATANABE T., SATO T., Expansion characteristics of montmorillonite and saponite under various relative humidity conditions, *Clay Sci.*, **1988**, 7, 129–138.
- [9] KÜHNEL R., VAN DER GAAST S. J., Humidity controlled diffractometry and its applications, *Adv. X-Ray Anal.* **1993**, 36, 439–449.
- [10] HASHIZUME H., SHIMOMURA S., YAMADA H., FUJITA T., NAKAZAWA H., AKUTSO O., An X-ray diffraction system with controlled relative humidity and temperature, *Powder Diffr.* **1996**, 11, 288–289.
- [11] CHIPERA S. J., CAREY J. W., BISH D. L., Controlled humidity XRD analysis: Application to the study of smectite expansion/contraction, *Adv. X-Ray Anal.* **1997**, 39, 713–722.
- [12] HASHIZUME H., Basal spacing of montmorillonite/amono acid complexes at different relative humidity, *Clay Sci.* **2002**, 11, 565–574.
- [13] HOU X., BISH D. L., WANG S., JOHNSTON C. T., KIRKPATRICK R. J. Hydration, expansion, structure, and dynamics of layered double hydroxides, *Am. Mineral.* **2003**, 88, 167–179.
- [14] KLAUE B., DANNECKER W. J., Humidity dependent X-ray diffraction—A new way to investigate deliquescence properties of hygroscopic salts in ambient aerosol samples, *Aerosol Sci.* **1994**, 5, S297–S298.
- [15] VANIMAN D. T., BISH D. L., CHIPERA S. J., FIALIPS C. I., CAREY J. W., FELDMAN W. C., Magnesium sulphate salts and the history of water on Mars, *Nature* **2004**, 431, 663–665.

- [16] ASTM C 88-90, Standard test method for soundness of aggregate by use of sodium sulfate or magnesium sulfate, Annu Book ASTM Stand **1997**, 4.2, 37–42.
- [17] RODRIGUEZ-NAVARRO C., DOEHNE E., SEBASTIAN E., How does sodium sulfate crystallize? Implications for the decay and testing of building materials, *Cem. Concr. Res.* **2000**, 30, 1527–1534.
- [18] HAUPT O., SCHÄFER C., STRAUSS S., DANNECKER W., Production of calibration standards for x-ray fluorescence analysis of aerosol particles, *Fres. J. Anal. Chem.* **1996**, 355, 375–378.
- [19] AMIRTHALINGAM V., KARKHANAVALA M. D., RAO U. R. K., Topotaxial phase change in Na_2SO_4 , *Acta Cryst.* **1977**, A33, 522.
- [20] GROSSI C. M., ESBERT R. M., SUÁREZ DEL RIO L. M., MONTATO M., LAURENZI-TABASSO M., Acoustic emission monitoring to study sodium sulphate crystallization in monumental porous carbonate stones, *Stud. Conserv.* **1997**, 42, 115–125.
- [21] XU B., SCHWEIGER G. J., In-situ Raman observation of phase transformation of Na_2SO_4 during the hydration/dehydration cycles on single levitated microparticle, *Aerosol Sci.* **1999**, 30, 379–380.
- [22] BRODALE G. E., GIAUQUE, W. F., The relationship of crystalline forms I, III, IV, and V of anhydrous sodium sulfate as determined by the third law of thermodynamics, *J. Phys. Chem.* **1972**, 76, 737–743.
- [23] RARD J. A., CLEGG S. L., PALMER D. A., Isopiestic determination of the osmotic coefficients of $\text{Na}_2\text{SO}_4(\text{aq})$ at 25 and 50°C, and representation with ion-interaction (Pitzer) and mole fraction thermodynamic models, *J. Solution Chem.* **2000**, 29, 1–49.
- [24] HAMAD S. EL D., A study of the reaction $\text{Na}_2\text{SO}_4 \cdot 10\text{H}_2\text{O} \rightarrow \text{Na}_2\text{SO}_4 + 10 \text{H}_2\text{O}$ in the temperature range 0 to 25°C, *Thermochim. Acta* **1976**, 17, 85–96.
- [25] CHAROLA A. E., WEBER J., The hydration-dehydration mechanism of sodium sulphate, In: Delgado Rodrigues J., Henriques F., Jeremias F.T. (eds.), *Proceedings of the 7th International Congress on Deterioration and Conservation of Stone Vol. 2, Lisbon* **1992**, 581–590.
- [26] DOEHNE E., In situ dynamics of sodium sulphate hydration and dehydration in stone pores: observations at high magnification using the environmental SEM, In: Zezza F., Ott H., Fascina V. (eds.), *The conservation of monuments in the Mediterranean Basin. Proceedings of the 3rd International Symposium, Venice* **1994**, 143–150.
- [27] TANG I. N., MUNKELWITZ H.R., Water activities, densities, and refractive indices of aqueous sulfates and sodium nitrate droplets of atmospheric importance, *J. Geophys. Res.* **1994**, 99, 18801–18808.
- [28] STEIGER M., Crystal Growth in porous materials. I: The crystallization pressure of large crystals, *J. Crystal Growth* **2005**, 282, 455–469.

Chapter 3

Determination of equilibrium humidities using temperature and humidity controlled X-ray diffraction (RH-XRD)

Kirsten Linnow, Michael Steiger

Institute of Inorganic and Applied Chemistry, University of Hamburg, Martin-Luther-King-Platz 6, D-20146 Hamburg

In: *Analytica Chimica Acta* **2007**, 583, 197–201, ([DOI:10.1016/j.aca.2006.09.054](https://doi.org/10.1016/j.aca.2006.09.054)).

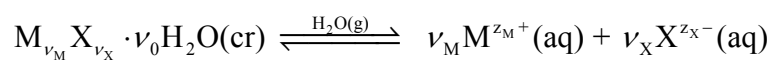
3.1 INTRODUCTION

Crystal growth in the pores of natural rocks or porous building materials such as stone, brick, concrete etc. is a major weathering mechanism [1,2]. Damage in such materials is caused by the pressure generated if growing crystals become confined. Crystal growth of salts and salt hydrates is the result of phase transition reactions that are usually induced by changes in ambient relative humidity (*RH*) and temperature. Relevant processes include crystal growth from solution or in the course of a hydration reaction. Under unfavorable climatic conditions repeated cycles of humidity and temperature can cause the rapid decay of building materials attacked by this process. X-ray diffraction is an appropriate method for the investigation of phase transition reactions. It has been shown recently [3] that deleterious reactions such as crystallization from solution or during a hydration reaction can be studied in situ using X-ray diffraction under controlled conditions of temperature and relative humidity (RH–XRD).

For the conservation of building materials it is very important to know critical environmental conditions that have to be avoided to prevent crystal growth. Therefore, the knowledge of deliquescence humidities and equilibrium humidities of hydration–dehydration reactions is particularly important [4]. In previous work [3] we have shown that it is possible to determine equilibrium humidities by using RH–XRD. In the present work, we extend our previous approach and improve the capability of RH–XRD for an accurate determination of both equilibrium humidities of hydration reactions and the deliquescence humidity of salt crystals. The procedure adopted for the determination of equilibrium humidities involves kinetic measurements. The procedure is used to determine the deliquescence humidities of NaCl and $\text{Ca}(\text{NO}_3)_2 \cdot 4\text{H}_2\text{O}$ and the equilibrium humidity of the $\text{Ca}(\text{NO}_3)_2$ – $\text{Ca}(\text{NO}_3)_2 \cdot 2\text{H}_2\text{O}$ transition. Comparison with available literature data confirms the accuracy of the method, which also offers good precision.

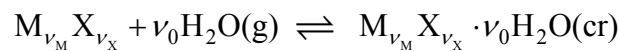
3.2 METHODOLOGY

A salt with general composition $\text{M}_{\nu_M} \text{X}_{\nu_X} \cdot \nu_0 \text{H}_2\text{O}$ consists of ν_M positive ions, M, of charge z_M , ν_X negative ions, X, of charge z_X , and ν_0 molecules of water. In a deliquescence reaction of a salt



the crystalline solid picks up water vapor and forms a saturated solution. At relative humidities above RH_{eq} , i.e. the deliquescence humidity, the solution continues to pick up water and a more dilute solution is formed. If the relative humidity drops below the deliquescence humidity, water evaporates to dryness and the crystalline solid is formed again. At equilibrium however, according to the Gibbs phase rule, the crystalline solid and the saturated solution can coexist indefinitely. Consequently, the net reaction rate at $RH = RH_{eq}$ is zero. Approaching RH_{eq} , the rate of the transformation reaction continuously decreases.

Considering a hydration reaction,



the situation is quite similar. At RH_{eq} , the two solid phases coexist in equilibrium with water vapor and the net reaction rate is equal to zero. At relative humidities either above or below RH_{eq} the hydrated and the anhydrous forms, respectively, are the only stable solids that can exist.

Several methods have been described in the literature for determining equilibrium humidities of phase transition reactions. One approach is water vapor pressure measurements at equilibrium. Methods for the determination of vapor pressure have been reviewed by Greenspan [5]. For instance, the vapor pressure over a saturated salt solution yields the deliquescence humidity of the salt at that temperature. Such experimental data exist in the literature for many salts; however, the data are usually quite scattered, particularly in the case of hydration–dehydration equilibria.

Another approach for the determination of equilibrium humidities is based on dynamic measurements. Such methods involve the measurement of a property of a condensed phase, i.e. a solid or a solution, at different relative humidities. These methods have been summarized by YANG et al. [6]. We have shown recently that X-ray diffraction, if conducted in a humidity chamber (RH–XRD), is also an appropriate technique for that purpose [3]. In that work, the equilibrium humidities RH_{eq} of phase transformation reactions were determined by a stepwise procedure. A sample of the educt phase was subjected to a stepwise increase in RH under isothermal conditions. Samples were equilibrated for one or two hours at each humidity. Phase transformations induced by a change in RH were detected by sudden changes in the XRD patterns, i.e. the appearance or disappearance of characteristic peaks of the educt

or the product phase. This approach requires very small step-sizes in RH variation in order to improve the uncertainty in the determination of RH_{eq} . A major problem with this approach arises from the kinetics of the transformation reaction. Usually the reaction rate strongly decreases as one approaches the equilibrium humidity of the transformation reaction. This results in very long equilibration times close to RH_{eq} . Unacceptable increases in equilibration times severely limit the applicability of the stepwise method. This problem resulted in an increased uncertainty of $\pm 2.5\%$ RH in the determination of the deliquescence humidity of $\text{Na}_2\text{SO}_4 \cdot 10\text{H}_2\text{O}$ in our previous work [3].

In the present work we present an improved dynamic method for more accurate determination of equilibrium humidities with RH-XRD. It is shown below how analysis of the rates of phase transition reactions can be successfully applied for the determination of RH_{eq} . The procedure is based on the evaluation of the total reaction time that is required until a phase transition reaction is complete. If a reaction, induced by an RH change, is carried out at different relative humidities, the total reaction times should increase as one approaches RH_{eq} . If an appropriate functional form of the RH dependence of the total reaction time can be established, the equilibrium RH can be determined by extrapolation to infinite reaction time. It is shown below that this approach can be successfully applied to determine the equilibrium humidities of deliquescence and hydration reactions.

3.3 EXPERIMENTAL SECTION

3.3.1 Instrumentation

Diffraction patterns were recorded on a Bragg-Brentano parafocusing reflection diffractometer (D 5000, Siemens, Germany) providing a horizontal $\theta:2\theta$ configuration using Cu $K\alpha$ -radiation and a position-sensitive detector (PSD). The goniometer is equipped with an environmental cell consisting of an air-tight cylindrical stainless steel chamber which is fixed to the θ -circle of the diffractometer. The window for passage of X-rays is sealed with a 6 μm Mylar film. The sample stage in the chamber is fixed with adjusting screws in the correct height of the $\theta:2\theta$ alignment. A uniform temperature distribution in the chamber is achieved by circulating water through channels in both the cylindrical chamber wall and the sample stage. The front cover is equipped with drillings for temperature and humidity sensors. Inlet

and outlet ports for the flows of thermostated water and air from a humid air generator are located on the backside of the chamber.

In the humid air generator compressed air is saturated with water vapor in a thermostated bubbler and passes a condensation trap at a temperature approximately 0.5 K below the final temperature. The desired relative humidity is maintained by accurately mixing dry and water-saturated air flows using automated mass-flow controllers. Appropriate mixing ratios of the wet and dry air flows are controlled by a computer program. A Pt-100 sensor and a capacitive humidity sensor (HMP 233, Vaisala, Finland) are positioned closed to the sample stage and give feedback of temperature and humidity in the chamber. The humidity control system allows variation of the relative humidity in the chamber between 3% *RH*–97% *RH*. A more detailed description of the environmental chamber and the humidity control system is provided in reference [3].

3.3.2 Sample preparation and measurements

NaCl and $\text{Ca}(\text{NO}_3)_2 \cdot 4\text{H}_2\text{O}$ (analytical grade, Merck) were used without further purification. Anhydrous $\text{Ca}(\text{NO}_3)_2$ was obtained by drying the tetrahydrate to constant weight. The weight loss corresponded to a nonideal composition, $\text{Ca}(\text{NO}_3)_2 \cdot 4.2\text{H}_2\text{O}$, of the tetrahydrate. The dry salt was identified as the anhydrous phase by comparison of the diffraction pattern with the JCPDS Standard 7-0204 for anhydrous $\text{Ca}(\text{NO}_3)_2$.

All experiments were carried out at 25°C. Constant weights of the educt phases were equilibrated in the environmental chamber of the XRD for 24 h at relative humidities considerably lower than the expected equilibrium values, i.e. at 41% *RH* (NaCl), close to 0% *RH* ($\text{Ca}(\text{NO}_3)_2$), and at 42% *RH* ($\text{Ca}(\text{NO}_3)_2 \cdot 4\text{H}_2\text{O}$), respectively. The phase transitions were induced by a sudden increase in the relative humidity to the desired value above the expected RH_{eq} . Subsequently, the humidity was kept constant until the reaction was complete. Each transformation reaction was carried out at different relative humidities as listed in Table 1. Progress of the transformation reactions was observed by successively recorded diffraction patterns. In most experiments, the XRD patterns were recorded in the range of 10°–70° 2θ . The time required for the collection of the patterns was 24 min, a new measurement was started every hour. In some cases, in order to improve the time resolution, XRD patterns were collected in the range 25°–55° 2θ and measurements were started every 15 min.

Relative humidity and temperature in the environmental chamber were continuously monitored. Care was taken to check the performance of the humidity sensor. The capacitive sensor was regularly calibrated using saturated solutions of LiCl and NaCl. Saturation humidities of these salts were taken from GREENSPAN [5]. The accuracy of the *RH* determinations with the calibrated sensor was tested by repeated measurements on different days of the equilibrium humidity of saturated solutions of LiCl, NaCl, $\text{MgCl}_2 \cdot 6\text{H}_2\text{O}$, and KCl at room temperature. No systematic deviation of the average saturation humidities of these salts from the tabulated reference values [5] could be observed. Moreover, the standard deviations of these *RH* measurements were no larger than 0.2–0.6% *RH* in the humidity range 11–84%, i.e. relevant to the present study. Typical fluctuations of *RH* in the chamber did not exceed $\pm 0.4\%$ during all experiments. This value represents the combined influences of the humidity generation system and the precision of the sensor over the time scale of the measurements (see Table 1).

3.4 RESULTS AND DISCUSSION

Selected XRD patterns measured during the hydration of $\text{Ca}(\text{NO}_3)_2$ are depicted in Figure 1. The reaction was induced by a humidity jump to 10.9% *RH*. Subsequently, XRD patterns were recorded every hour. In the initial XRD pattern only peaks of the anhydrous educt $\text{Ca}(\text{NO}_3)_2$ were present and there were no significant changes during the initial 13 h. First peaks of the product phase $\text{Ca}(\text{NO}_3)_2 \cdot 2\text{H}_2\text{O}$ were noticeable after 14.6 h (see Figure 1) and the subsequent patterns revealed the presence of both phases. Decreasing educt peak intensities and increasing product peak intensities showed the progress of hydration. Major $\text{Ca}(\text{NO}_3)_2$ peaks are still detectable in the XRD pattern collected at 24.6–25.0 h. Complete absence of the $\text{Ca}(\text{NO}_3)_2$ peaks was visually detected in the pattern recorded from 25.6 h to 26.0 h. Subsequently, no further changes could be detected in the XRD patterns and constancy in the $\text{Ca}(\text{NO}_3)_2 \cdot 2\text{H}_2\text{O}$ peak intensities indicated that the hydration reaction was complete. Hence, the end of the reaction was reached after 25.0–25.6 h, i.e. corresponding to $t_c = 25.3 \pm 0.3$ h where the uncertainty reflects the limited time resolution of the XRD measurements. Due to the difficulties in the unambiguous detection of peak disappearance in the XRD patterns the true uncertainty is somewhat larger. A maximum error of ± 1 h in the determination of t_c is estimated for the reactions studied in the present work. In both hydration and deliquescence reactions the disappearance of the respective educt phase peaks in the XRD

patterns was used as the criterion for the determination of the total reaction time t_c . Reaction times for the deliquescence of NaCl and $\text{Ca(NO}_3)_2 \cdot 4\text{H}_2\text{O}$ and the hydration of $\text{Ca(NO}_3)_2$ are listed in Table 1. As expected, the conversion times decrease with increasing RH .

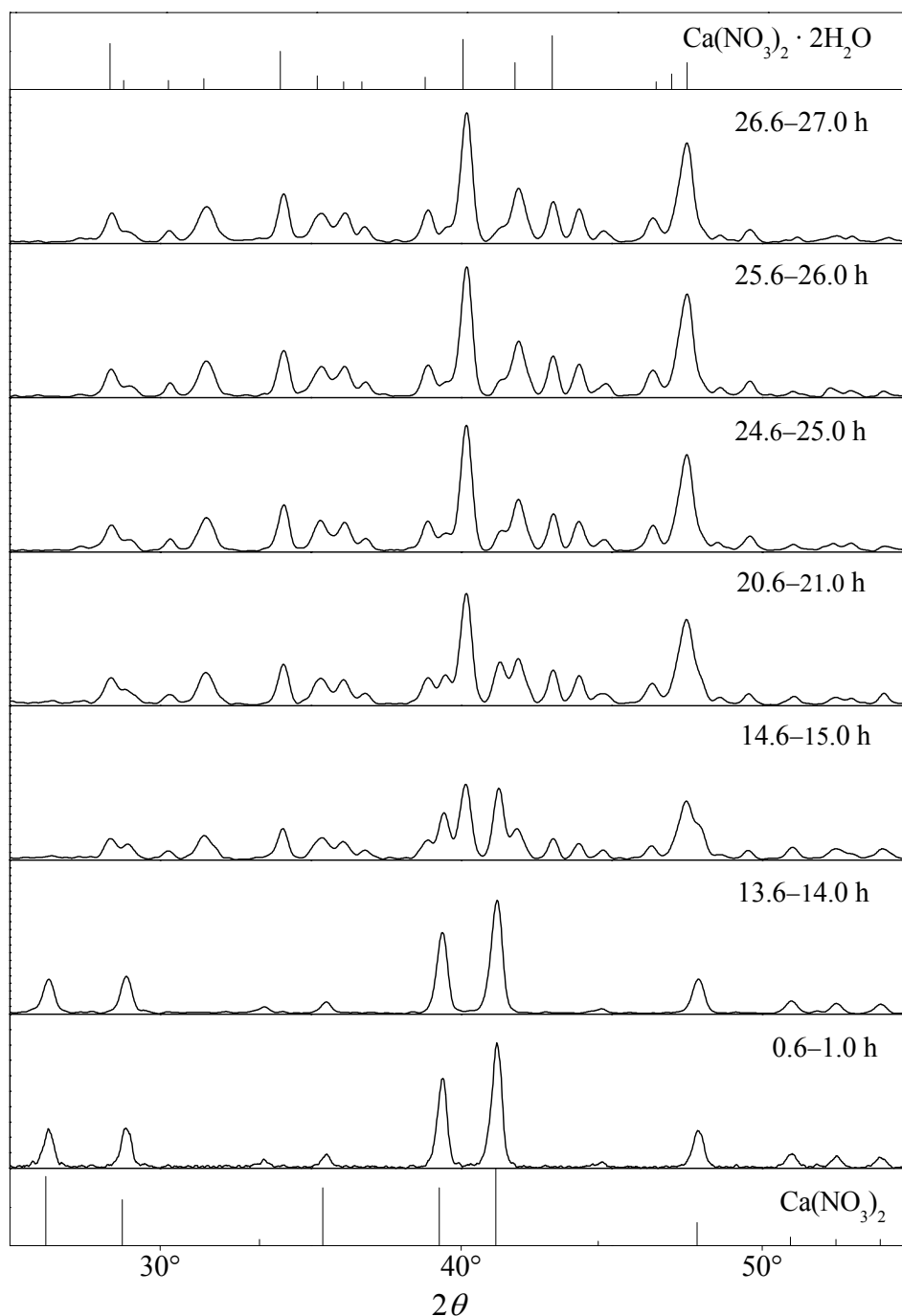


Figure 1: Evolution of the XRD patterns of $\text{Ca(NO}_3)_2$ and $\text{Ca(NO}_3)_2 \cdot 2\text{H}_2\text{O}$ during the hydration reaction at 25°C and $10.9\% RH$.

Table 1: Relative humidities and complete reaction times t_c of the observed phase transition reactions at 25°C.

NaCl deliquescence		Ca(NO ₃) ₂ · 4H ₂ O deliquescence		Ca(NO ₃) ₂ hydration	
<i>RH</i> /%	t_c /h	<i>RH</i> /%	t_c /h	<i>RH</i> /%	t_c /h
82.3	7.0	60.1	2.3	16.1	3.3
81.4	9.0	57.5	3.3	14.2	4.3
79.1	12.7	55.5	4.3	12.1	8.3
78.5	17.5	53.0	10.3	11.3	14.3
77.6	22.7	52.5	11.3	10.9	25.3
76.7	31.7				
76.5	44.7				

The results for the deliquescence of NaCl are shown in Figure 2. The vertical error bars in Figure 2 represent the uncertainty of the *RH* measurement. Horizontal error bars represent the uncertainties in the determination of the reaction times as discussed before. The experimental values can be represented to within their uncertainties by an exponential function of the form

$$RH = A \cdot \exp(B/t_c) \quad (1)$$

Linearization of Equation (1) yields:

$$\ln RH = \ln A + B/t_c \quad (2)$$

Equation (2) is now suitable for the determination of the deliquescence humidity of NaCl as illustrated in Figure 3. As discussed before, crystalline NaCl, the saturated NaCl solution and water vapor coexist at equilibrium and the net reaction rate is zero. In effect, the conversion time t_c approaches infinity as the relative humidity approaches RH_{eq} . Hence, extrapolation to $B/t_c = 0$ yields $\ln A = \ln RH_{eq}$. Using Eq. (2), the slope B and the intercept $\ln A$ were calculated by linear least squares analysis. The results for the deliquescence of NaCl are listed in Table 2. The resulting deliquescence humidity RH_{eq} of $75.4 \pm 0.5\%$ at 25°C is in excellent agreement with the commonly accepted value of 75.3% [5,7,8]. Our estimated uncertainty is based on the standard error of the regression estimate on the 95% confidence level.

The same procedure was used to determine equilibrium humidities for the deliquescence of $\text{Ca}(\text{NO}_3)_2 \cdot 4\text{H}_2\text{O}$ and for the hydration of $\text{Ca}(\text{NO}_3)_2$. Results of these calculations are also listed in Table 2. Our deliquescence humidity of $50.8 \pm 0.7\%$ at 25°C agrees well with the value of $50.5 \pm 0.4\%$ reported by EWING [9] derived from static vapor pressure measurements over saturated solutions of $\text{Ca}(\text{NO}_3)_2 \cdot 4\text{H}_2\text{O}$. EWING [9] also reported vapor pressures for the hydration equilibrium $\text{Ca}(\text{NO}_3)_2\text{--Ca}(\text{NO}_3)_2 \cdot 2\text{H}_2\text{O}$. His equilibrium humidity of $9.3 \pm 0.4\%$ is somewhat lower than our value of $10.2 \pm 0.3\%$. In this case, the deviation slightly exceeds the combined uncertainties of the two methods. Nonetheless, the agreement between RH-XRD and the vapor pressure measurements is still considered as satisfactory.

Considering both the coefficients of determination R^2 listed in Table 2 and the excellent agreement of our equilibrium humidities with literature data, it is concluded that the extrapolation approach based on the total reaction times together with Equation (2) leads to accurate values of equilibrium humidities. Furthermore, using an optimized environmental chamber as in the present work and after careful calibration of the sensor in the chamber, the precision of such measurements with RH-XRD is very satisfactory.

Table 2: Coefficients of Equation (2) and equilibrium humidities RH_{eq} of phase transition reactions.

Reaction	$\ln A$	B/sec	R^2	$RH_{eq}/\%$
NaCl deliquescence	4.323 ± 0.007	2287 ± 124	0.985	75.4 ± 0.5
$\text{Ca}(\text{NO}_3)_2 \cdot 4\text{H}_2\text{O}$ deliquescence	3.928 ± 0.004	1416 ± 58	0.995	50.8 ± 0.7
$\text{Ca}(\text{NO}_3)_2$ hydration	2.321 ± 0.009	5382 ± 170	0.997	10.2 ± 0.3

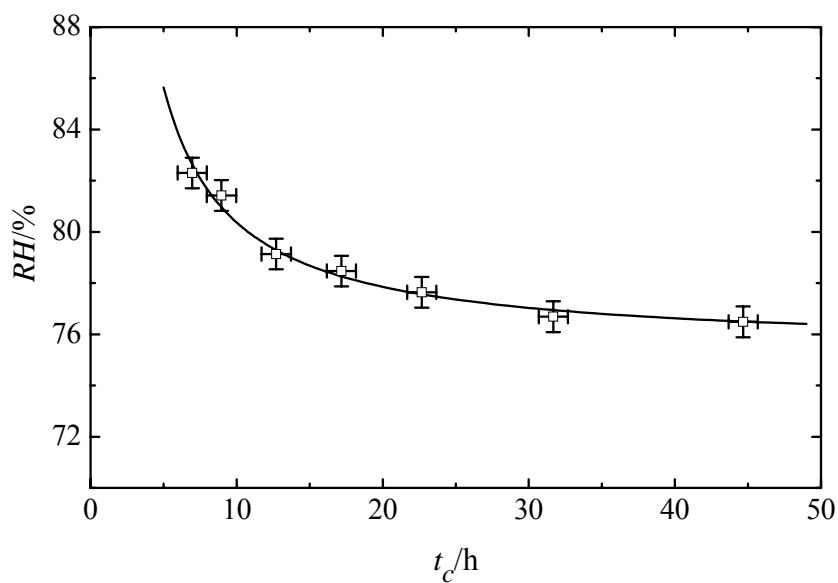


Figure 2: Relative humidities vs. total reaction times during the NaCl deliquescence at 25°C; vertical error bars correspond to the uncertainty of the RH measurements (one standard deviation on either side), horizontal error bars reflect the maximum uncertainty in the determination of t_c from the XRD patterns.

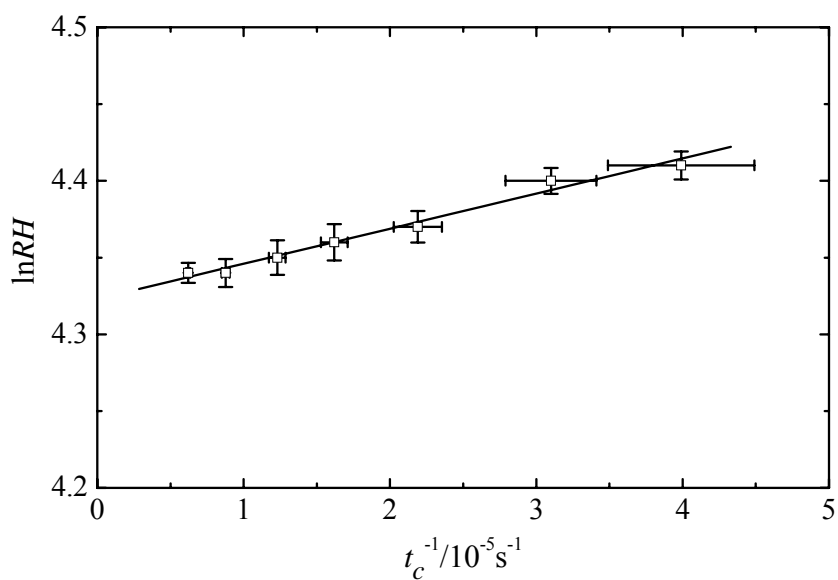


Figure 3: Plot of $\ln RH$ vs. t_c^{-1} for the NaCl deliquescence at 25°C, error bars as in Figure 2.

3.5 CONCLUSIONS

Dynamic XRD measurement is an appropriate method for the accurate and precise determination of equilibrium humidities. The extrapolation technique proposed here proved to be simple and robust and permits a number of possible future applications. RH-XRD measurements are particularly helpful in cases where the application of other techniques, e.g. vapor pressure measurements, is inconvenient or impossible. For example, RH-XRD might be used for the determination of deliquescence humidities of incongruently soluble double salts. Another potential future application includes the investigation of phase transition reactions within porous materials. It was shown recently [3] that RH-XRD can be successfully applied for direct observation of phase transition reactions in the pore space of glass filter frits. By using this X-ray amorphous substrate problems with interfering XRD patterns are avoided. Nominal pore sizes of glass filter frits are representative for many building materials such as natural stone and brick and the penetration depth of X-rays is sufficient to investigate phase transition reactions within pores close to the surface of the material. Using appropriate porous substrates and the extrapolation approach of the present study, it will be possible to determine the equilibrium humidities of phase transition reactions in confined geometries and to study the influence of the pore size and the pore geometry.

Acknowledgements

Part of this work was funded by the Deutsche Forschungsgemeinschaft (DFG).

3.6 REFERENCES

- [1] GOUDIE A., VILES H., Salt Weathering Hazards, John Wiley & Sons, Chichester, **1997**.
- [2] DOEHNE E., Natural Stone, Weathering Phenomena, conservation strategies and case studies, Geol. Soc. Spec. Publ. **2002**, 205, 51–64.
- [3] LINNOW K., ZEUNERT A., STEIGER M., Investigation of sodium sulfate phase transitions in a porous material using humidity- and temperature-controlled X-ray diffraction, Anal. Chem. **2006**, 13, 4683–4689.
- [4] STEIGER M., Salts in porous materials: Thermodynamics of phase transitions, modeling and preventive conservation, Restorat. Build. Monum. **2005**, 11, 419–431.
- [5] GREENSPAN L., Humidity fixed points of binary saturated aqueous solutions, J. Res. Nat. Bur. Stand. **1977**, 81A, 89–96.

-
- [6] YANG L., PABALAN R.T., JUCKETT M.R., Deliquescence Relative Humidity Measurements Using an Electrical Conductivity Method, *J. Solution Chem.* **2006**, 35, 583–604.
 - [7] STOKES R.H., ROBINSON R.A., Standard solutions for humidity control at 25°C, *Ind. Eng. Chem.* **1949**, 41, 2013.
 - [8] STOLOFF L., Calibration of water activity measuring instruments and devices: Collaborative study, *J. Assoc. Off. Anal. Chem.* **1978**, 61, 1166–1178.
 - [9] EWING W.W., Calcium nitrate. II. The vapor pressure-temperature relations of the binary system calcium nitrate-water, *J. Am. Chem. Soc.* **1927**, 49, 1963–1973.

Chapter 4

Investigation of NaCl deliquescence in porous substrates using RH-XRD

Kirsten Linnow¹, Herbert Juling², Michael Steiger¹

¹Institute of Inorganic and Applied Chemistry, University of Hamburg, Martin-Luther-King-Platz 6, D-20146 Hamburg

²Institute of Materials Science (IWT), Paul Feller Straße 1, D-28199 Bremen

In: *Environmental Geology* **2007**, 52, 317–327, ([DOI:10.1007/s00254-006-0590-9](https://doi.org/10.1007/s00254-006-0590-9)).

The original publication is available at www.springerlink.com.

4.1 INTRODUCTION

The pressure generated during crystal growth in confined spaces of porous materials is generally accepted as a major cause of damage of such materials [1,2]. Crystal growth damage not only affects porous building materials such as stone, brick, concrete etc., it is also an important weathering mechanism of natural rocks in hot and cold deserts [3,4] and even on Mars [5,6]. Crystal growth in a porous material is always the result of a phase transition reaction usually induced by a change in ambient temperature or relative humidity. Unfavorable environmental conditions may cause repeated cycles of deliquescence–crystallization or hydration–dehydration, which lead to the rapid decay of building materials or natural rocks. The identification of critical environmental conditions requires the knowledge of the thermodynamics of the relevant phase transition reactions [7]. In addition, the rates at which these processes take place in porous materials are extremely important in order to determine the critical levels of environmental fluctuations [8]. The overall kinetics of phase transition reactions in porous materials is affected by a number of different influences including the rates of chemical reactions, the moisture transport in a porous material and the rate of moisture exchange between the material and the environment.

The investigation of the deleterious processes in porous materials requires suitable experimental techniques. In previous work, we have shown that X-ray diffraction under controlled conditions of relative humidity and temperature (RH-XRD) is an appropriate experimental technique for the investigation of phase transitions. LINNOW [9] used RH-XRD for the investigation of sodium sulfate phase transitions in porous substrates. They demonstrated that hydration–dehydration and deliquescence–crystallization equilibria can be directly observed within confined spaces of a porous material. Subsequently, it was shown that dynamic RH-XRD is also a very useful experimental technique for the quantitative determination of equilibrium humidities of relevant phase transition reactions, e.g. deliquescence and hydration humidities [10].

In this study we extend our previous applications of RH-XRD. The method is used in the present work for the direct observation of the deliquescence of sodium chloride (NaCl) within the pore space of glass frits with different pore diameters. One objective of the study was to test the use of RH-XRD as a potential technique for the direct observation of the kinetics of the deliquescence reaction of a salt confined in a porous substrate. The second objective was

to test whether dynamic XRD measurements are also an appropriate method for the accurate and precise determination of equilibrium humidities of crystals present in small pores. The paper describes both the potential and the limitations of such applications of RH-XRD.

4.2 MATERIALS AND METHODS

4.2.1 Instrumentation

RH-XRD measurements were carried out on a Bragg-Brentano parafocusing powder diffractometer (D 5000, Siemens, Germany) with a θ - 2θ configuration, using Cu K α -radiation (generated at 25 kV and 20 mA) and a position sensitive detector recording data from a $12^\circ 2\theta$ band at one time. The diffractometer is equipped with an environmental cell [9] consisting of an air-tight cylindrical stainless steel chamber which is fixed to the goniometer. In order to avoid temperature gradients in the chamber, not only the air flow from the humidity generator but also the chamber walls and the sample stage are thermostated. A Pt-100 sensor and a capacitive humidity sensor (HMP 233, Vaisala, Finland) are used for temperature and humidity control in the chamber. They are placed close to the surface of the samples. The window for the passage of X-rays is sealed with a 6 μ m Mylar film.

The humidity sensor is connected to the humid air generator. In the temperature range 10–50 °C the humidity control system allows the variation of the relative humidity (*RH*) in the chamber within a range of 3–97% *RH*. Humidity control is accomplished by mixing of dry and water-saturated air using automated mass-flow controllers. Appropriate mixing ratios of the wet and dry air flows are controlled by a computer program. A more detailed description of the humidity control system is provided by LINNOW [9].

A Hitachi S 4004 scanning electron microscope (SEM) was used to determine crystal size and shape and the distribution of NaCl in the glass frits that were used for the XRD measurements.

4.2.2 Sample preparation

Analytical grade NaCl (Merck, Germany) was directly used throughout the study. The size distribution of the crystals was determined by mechanical sieving and yielded the following weight percentage distribution in the respective crystal size ranges: 94% (>125 μ m), 5% (63–

125 μm), 0.2% (40–63 μm), and 0.03% (<40 μm). The deliquescence of a bulk sample of NaCl (146 mg) was investigated at 78% *RH* and 25°C.

Disks of glass frits (VitraPOR, ROBU Glasfilter-Geräte GmbH, Germany) of four different porosity classes (P2–P5) with a diameter of 20 mm and varying heights between 2.4–3.2 mm were used as porous substrates. Porosity classes P4 and P5 of the same glass frits were already successfully applied in a previous study with sodium sulfate [9]. The amorphous material did not significantly interfere with the X-ray pattern of crystalline NaCl. Median pore diameters d_m of 70 μm (P2), 28 μm (P3), 11.1 μm (P4), and 1.44 μm (P5) are provided by the manufacturer and are based on mercury intrusion porosimetry. These median pore sizes are typical for many building materials such as natural stone and brick. In contrast to such materials however, the pore size distribution of the glass filters is very narrow, thus, the filter frits are well suited for an investigation of pore size influences.

Glass frits of each porosity class were washed, dried and immersed in a NaCl solution at room temperature. Preliminary tests showed that evaporative drying of the glass frits in dry air lead to the formation of a salt crust on the surface of the frits. However, since XRD patterns of efflorescences and NaCl crystals within the pore space of the glass frits are nearly indistinguishable, it is absolutely essential that the formation of efflorescences during the drying procedure is avoided. Otherwise, an unambiguous determination of the deliquescence humidity of NaCl crystals within the pores is impossible. In order to avoid efflorescences during the sample preparation, freeze-drying was used. The impregnated glass frits were subjected to rapid cooling rates by placing the impregnated sample into melting nitrogen (slush nitrogen) such that the NaCl solution forms a glassy solid matrix. Subsequent sublimation of water and crystallization of NaCl were carried out under applied vacuum until the whole nitrogen is evaporated.

Two glass frits of each porosity class were impregnated with a 10%w/w solution. After cryo-preparation the glass frits did neither show visible efflorescences nor any discoloration of the surfaces that would indicate the presence of crystalline surface deposits. One specimen of each porosity class was selected to determine the crystal sizes and distributions of crystalline NaCl by using scanning electron microscopy (SEM). The frits were broken in the center and their cross sections were examined. The SEM observations confirmed that there were practically no efflorescences present on the surfaces. The remaining specimens were used to

observe the deliquescence reaction at constant humidity of 78% RH and at 25°C. The total weights of NaCl in these glass frits after the impregnation and drying procedure were 222.3 mg ($d_m = 1.44 \mu\text{m}$), 70.3 mg ($d_m = 11.1 \mu\text{m}$), 21.8 mg ($d_m = 28 \mu\text{m}$), and 55.2 mg ($d_m = 70 \mu\text{m}$), respectively.

The X-ray intensities in the initial experiments with glass frits that were impregnated with a 10%w/w NaCl solution were relatively low. In order to improve the sensitivity for the subsequent determination of the deliquescence humidities of NaCl in the porous substrates, several glass frits of each porosity class were immersed in a saturated NaCl solution. After freeze-drying these specimens appeared slightly brighter on their surfaces, thus, indicating the presence of NaCl crystals. To remove these efflorescences the surfaces were carefully brushed. Thereby, glass particles flaked off, such that the weight fraction of NaCl in each specimen could not be determined. The deliquescence of NaCl in these specimens was observed at different relative humidities in order to determine the equilibrium deliquescence humidity as discussed below.

4.2.3 Measurement procedure

An improved dynamic method for the quantitative determination of equilibrium humidities of phase transition reactions was recently proposed by LINNOW and STEIGER [10]. The method is based on kinetic measurements, namely on the evaluation of total reaction times required until the reaction is complete. If a phase transition reaction induced by a sudden change in relative humidity, e.g. a deliquescence reaction is carried out at different humidities, the total reaction time t_c increases as one approaches the equilibrium value of the relative humidity, i.e. the deliquescence humidity. At equilibrium, according to the phase rule, the crystalline solid and the saturated solution coexist indefinitely, thus, the reaction rate vanishes. As shown recently [10], an exponential function of the form

$$RH = RH_{\text{eq}} \exp(Bt_c^{-1}) \quad (1)$$

provides an accurate representation of the RH dependence of the total reaction times of phase transition reactions such as hydration or deliquescence of a solid. In Equation (1) RH_{eq} is the equilibrium relative humidity of the respective reaction. In the case of a deliquescence reaction, the equilibrium humidity corresponds to the deliquescence humidity RH_{del} . Both

RH_{del} and B are treated as adjustable parameters. For a deliquescence reaction, linearization of Equation (1) yields:

$$\ln RH = \ln RH_{\text{del}} + Bt_c^{-1} \quad (2)$$

Values of RH_{del} and B can be determined by linear least squares analysis from experimental measurements of t_c at different relative humidities. It was shown in our previous work that the extrapolation to $t_c^{-1} = 0$ allows for the accurate determination of RH_{del} from Equation (2). This method was also adopted in the present work.

All experiments were carried out at 25°C in the environmental chamber of the diffractometer. Samples were equilibrated in the chamber at 40% RH until the reaction was induced by a sudden increase in the relative humidity to the desired value. Subsequently, the humidity was kept constant until the absence of sodium chloride peaks in the diffraction pattern indicated that the reaction was complete. Progress of the deliquescence reaction was observed by successively recorded diffraction patterns. For the determination of the deliquescence humidities, diffraction patterns were recorded in the range 25°–70° 2θ . The time required for the collection of the patterns was 19 min. Relative humidity and temperature in the chamber were continuously monitored during all experiments. Typical fluctuations were less than 0.4% RH . The accuracy of the RH determinations with the calibrated Vaisala sensor was tested by repeated measurements on different days of the equilibrium humidity of saturated solutions of various salts [10]. No systematic deviations from tabulated reference values [11] could be observed and the standard deviation of these measurements did not exceed 0.6% RH .

All kinetic experiments were carried out at 78% RH . These experiments included a bulk sample and the glass frits impregnated with 10%w/w NaCl solution in order to compare the kinetics of the deliquescence reaction and to assess the influence of confinement on the rate of the deliquescence reaction. The XRD patterns of the bulk sample and the P3 specimen were recorded in the range 10°–70° 2θ , which required 24 min. A new measurement was started every 30 min. In order to improve the time resolution, XRD patterns in the subsequent measurements with the P2, P4 and P5 specimens were recorded in the range 25°–55° 2θ such that a new measurement could be started every 15 min.

4.3 RESULTS AND DISCUSSION

4.3.1 SEM observations

SEM images of the cross sections of the glass frits are shown in Figure 1. Salt crystals appear brighter than the glass matrix in the backscattered electron image due to the higher average atomic number of NaCl compared to the borosilicate material. An even distribution of crystalline NaCl over the whole cross section was found in the P2 ($d_m = 70\ \mu\text{m}$) and P4 ($d_m = 11.1\ \mu\text{m}$) glass frits. In contrast, there is an accumulation of NaCl close to the surface into a depth of about 300–500 μm in the P3 glass frit ($d_m = 28\ \mu\text{m}$). Only minor amounts of NaCl are obviously present in the interior of this specimen. Though it appears that the salt is also evenly distributed in the P5 glass frit ($d_m = 1.4\ \mu\text{m}$), there are two narrow zones of high salt enrichment in depths of about 150 μm on the upper side and about 300–450 μm on the opposite side of the specimen. These enrichment zones indicate the presence of cracks in the fabric of the P5 frit.

Figure 2 shows crystal sizes and morphologies in the freeze-dried glass frits. In the pore space of the P2 glass frit ($d_m = 70\ \mu\text{m}$) agglomerates of euhedral NaCl crystals of about 1–3 μm edge length are found. Similar crystal sizes are observed in the P3 ($d_m = 28\ \mu\text{m}$) and P4 ($d_m = 11.1\ \mu\text{m}$) frits. However, in these specimens the crystals are less well-formed and show rounded edges. The SEM image of the enrichment zone in the P5 frit ($d_m = 1.4\ \mu\text{m}$) confirms that the pore space is nearly entirely filled with a compact aggregate of NaCl crystals of different sizes. The size of the largest crystals (6 μm , see arrow in Figure 2) exceeds the median pore size by far and, thus, confirms the presence of a crack in the P5 frit. Though evenly distributed (see Figure 1) only small amounts of NaCl were found in the interior pore space of the P5 specimen. This result is in contradiction with the substantial weight increase of 222 mg determined for another P5 specimen which was treated in the same way and was used for the determination of the deliquescence rate at 78% *RH*. It is concluded that the cracks parallel to the surface in the P5 specimen shown in Figure 1 did also affect the sample preparation procedure. Therefore, it is likely that the cracks already existed prior to the imbibition and freeze-drying procedure. Though it could be suspected that the cracks were also caused by the rapid freezing of the samples, it should be noted that we have never observed damage to glass filter frits upon freeze-drying including previous work on Na_2SO_4 [9] and in experiments with the freeze-drying of MgSO_4 solutions in filter frits [12].

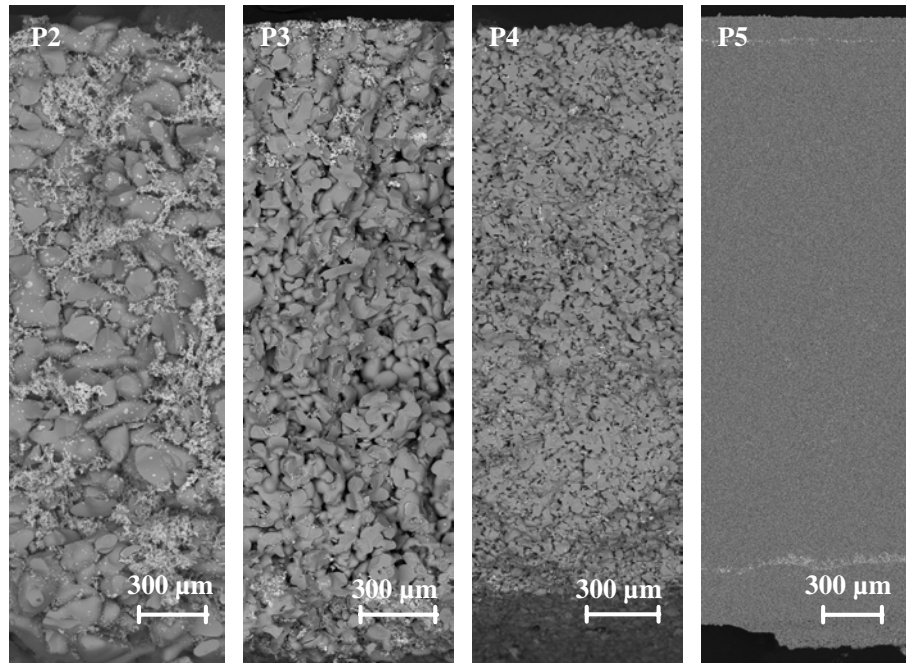


Figure 1: SEM micrographs of NaCl distribution in the glass frits P2 ($d_m = 70 \mu\text{m}$), P3 ($d_m = 28 \mu\text{m}$), P4 ($d_m = 11.1 \mu\text{m}$), and P5 ($d_m = 1.44 \mu\text{m}$) [BSE-images, 20 kV].

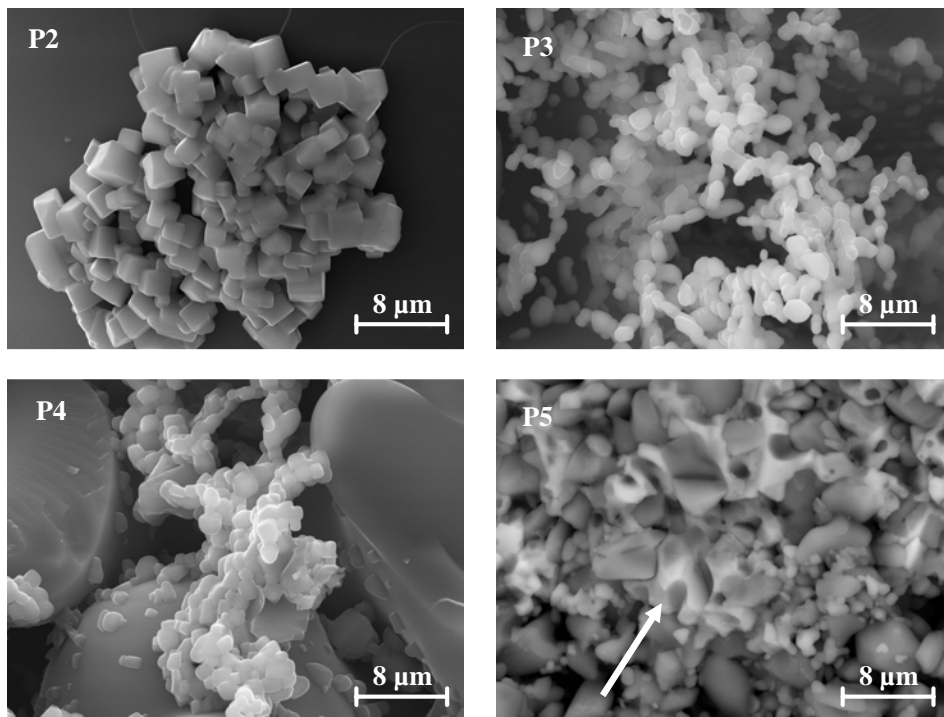


Figure 2: SEM micrographs of NaCl crystals in the glass frits P2 ($d_m = 70 \mu\text{m}$), P3 ($d_m = 28 \mu\text{m}$), P4 ($d_m = 11.1 \mu\text{m}$), and P5 ($d_m = 1.44 \mu\text{m}$) [SE-images, 20 kV].

The morphologies of the NaCl crystals observed after the freeze-drying of the porous substrates show more or less significant deviations from the cubic equilibrium shape of halite crystals (Figure 2). Nonetheless, the morphologies of salt crystals growing from evaporating solutions in porous substrates are known to show a whole variety of different morphologies including isometric shapes and forms far from the equilibrium shape of the respective salt [13,14]. For instance, depending on the conditions during crystal growth, ZEHNDER and ARNOLD [13] observed both isometric forms, sometimes with rounded edges, and acicular forms like columnar crystals, whiskers or fibrous aggregates. They also report on aggregates of euhedral crystals with rounded edges comparable with those shown in Figure 2. It is concluded therefore, that freeze-drying does not yield unrealistic crystal morphologies, which would restrict the interpretation of the results.

4.3.2 Kinetics of deliquescence

Diffraction patterns, recorded successively during one of the experiments, are shown in Figure 3 together with the JCPDS (Joint Committee on Diffraction Pattern) standard 5-0628 for NaCl. Apart from an obvious increase in background intensities in the range of 18° – 30° 2θ which is caused by the amorphous glass matrix, the diffraction patterns of NaCl in the glass frit compare nicely to the JCPDS standard and the identification did not pose any problems. The peak area intensities of the peaks at 31.7° , 45.4° , 53.8° , 56.5° and 66.3° 2θ , respectively, were used for the evaluation of the diffraction patterns during the course of the deliquescence reactions. The highest peak intensities were observed at the beginning of the experiment during the equilibration of the glass frit at 40% *RH* (cf. Figure 3). At $t = 0$ the deliquescence reaction was induced by a sudden increase in relative humidity to the desired value, i.e. 78% *RH* in the case of the experiment shown in Figure 3. In the subsequent XRD patterns, the peak intensities continuously decrease during the course of the deliquescence reaction.

The experiment with the bulk NaCl sample was evaluated in the same way, though of course, there was no increased background intensities caused by the glass matrix such that the peak at 27.3° 2θ could be used for the evaluation of the peak intensities as well. The change in peak intensities during the experiment at 78% *RH* is shown in Figure 4. The values plotted are averaged relative intensities I/I_0 of the different NaCl peaks where I is the peak intensity at

time t and I_0 is the intensity of the respective peak at the very beginning of the experiment ($t = 0$).

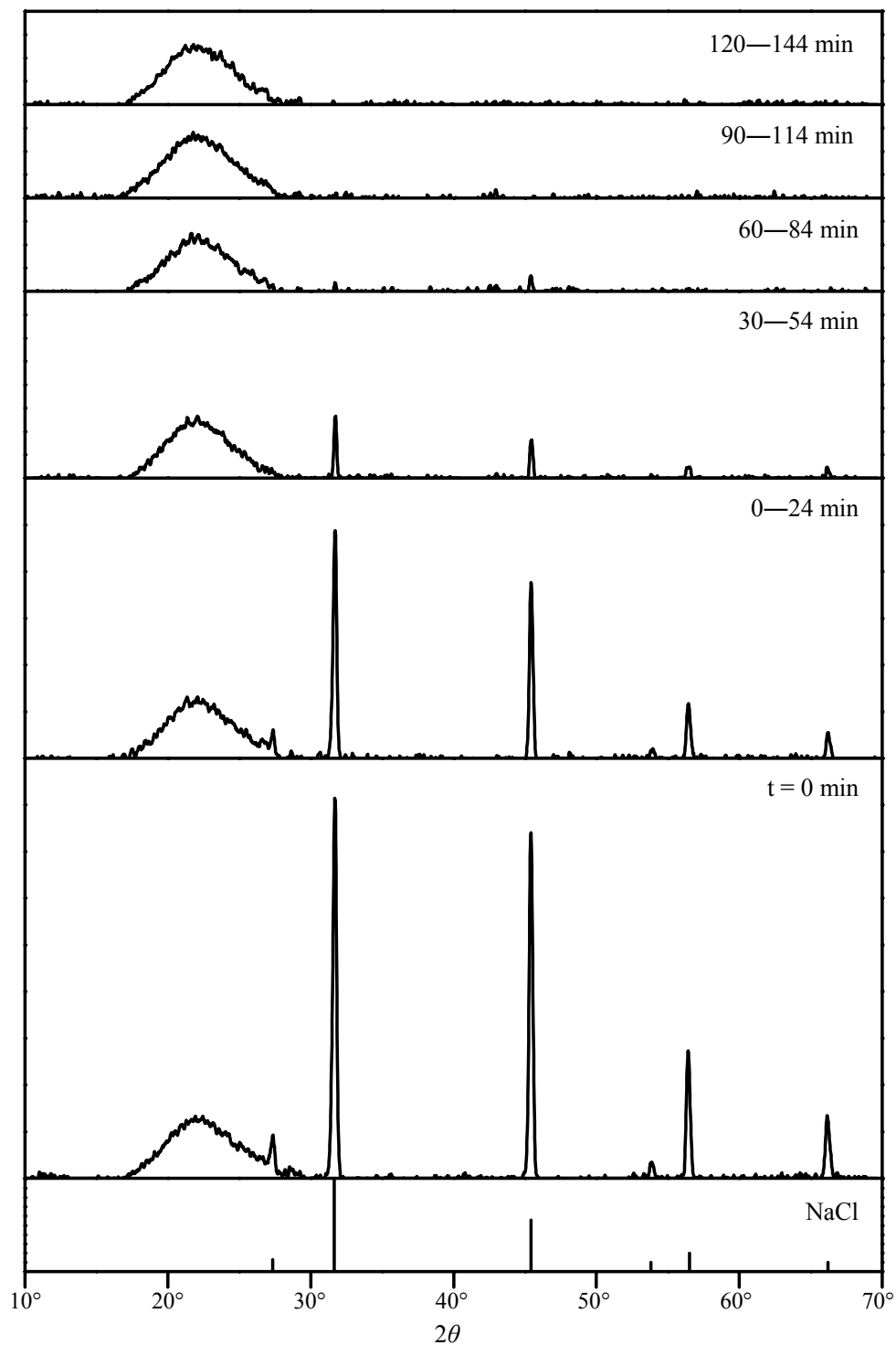


Figure 3: Successively recorded diffraction patterns during deliquescence of NaCl in the pore space of glass frit P3 ($d_m = 28 \mu\text{m}$) at 78% RH and 25°C and comparison with JCPDS standard 5-0628 of NaCl.

During the course of the reaction the relative intensities continuously decrease approaching the final value $I/I_0 = 0$. In the case of the bulk sample however, the deliquescence reaction was still not complete, even after 25 h when the measurements were terminated. The measured intensities were fitted to an exponential function of the form

$$I/I_0 = \exp(-kt^n) \quad (3)$$

in order to represent the experimental data in intensity versus time curves (Figure 4). In Equation (3) k and n are treated as empirical adjustable parameters that are not meant to be related to a particular reaction mechanism.

The peak intensities during the deliquescence of NaCl in the glass frits at the same relative humidity (i.e. 78% RH) are also shown in Figure 4. It is obvious that the reaction times are smaller in the case of the porous substrates compared to the bulk sample. However, in the case of the porous substrates, the relative intensities have to be interpreted in a different way. Due to the limited penetration depth of the X-rays in the glass frits, the total loss of intensity does not indicate that the deliquescence reaction in the whole specimen is complete. It rather means that no more crystalline NaCl can be detected in a layer close to the surface of the substrate. The thickness of this layer depends on the penetration depth of the X-rays. For Cu K α -radiation and the substrate used in this work, it can be estimated from the absorption law that the penetration of the X-rays for different angles θ would hardly exceed about 100–200 μm .

Due to the limited penetration depth of X-rays in the salt loaded glass frits, only a fraction of the total amount of NaCl present in the specimens is observable by XRD. In principle it should be possible to assess this fraction, if the total mass load of the specimens and the penetration depth are known. However, the heterogeneous distribution of crystalline NaCl at least in some of the glass frits does not permit an accurate assessment of the NaCl fraction in the outer pore space. Transport processes across the layer penetrated by the X-rays may further affect the measured intensities. In the case of a deliquescence reaction, the solution that is initially formed might be transported by capillary action into greater depth. This results in a reduced attenuation of the X-ray intensities in the outermost layer and, eventually, increases the penetration depth slightly. In effect, the intensity vs. time plots shown in Figure 4 may also be affected by solution transport.

For the reasons given, the intensity curves obtained during the deliquescence of the bulk samples and the glass substrates are not directly comparable. Nonetheless, despite of the difficulties in the interpretation of the reaction curves, the measurements of the deliquescence kinetics in the porous substrates clearly indicate that in the pore space close to the surface the reaction proceeds on a time-scale of a few hours. It is concluded that quite short-time variations of relative humidity, e.g. the typical daily variation of ambient relative humidity, may be sufficient to cause dissolution of crystalline salts in the pore space close to the surface of building materials. A subsequent decrease in relative humidity may then cause crystallization and the generation of stress in the material. However, much longer reaction times may be required for the deliquescence of salt crystals in greater depth of a porous material.

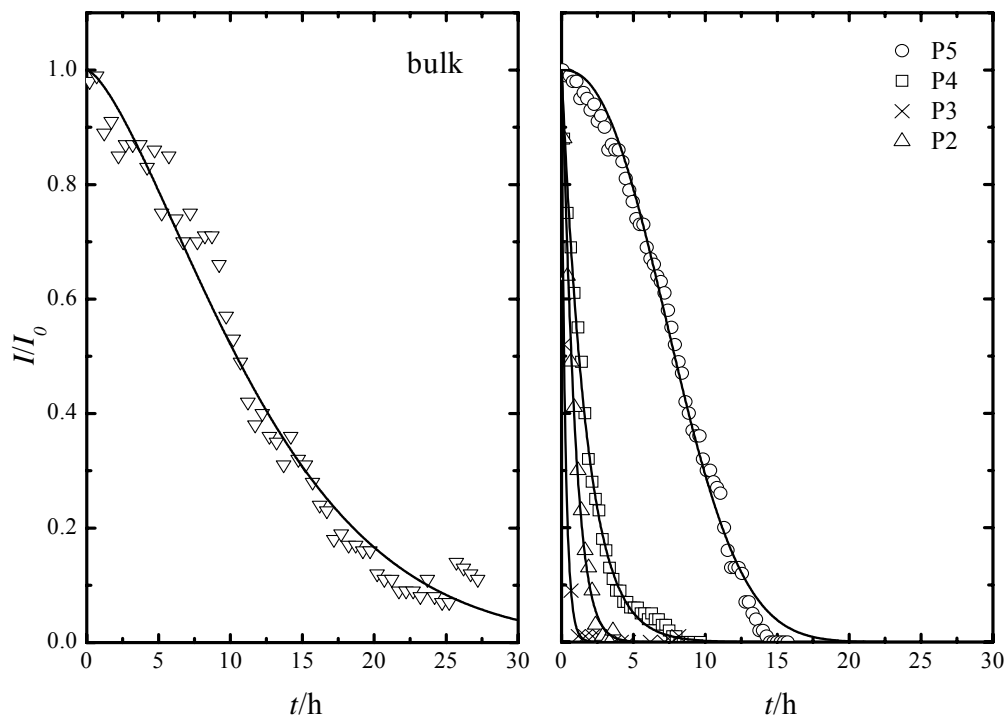


Figure 4: Course of the deliquescence of NaCl at 78% *RH* (25°C) in bulk samples and in the glass frits P2 ($d_m = 70 \mu\text{m}$), P3 ($d_m = 28 \mu\text{m}$), P4 ($d_m = 11.1 \mu\text{m}$), and P5 ($d_m = 1.44 \mu\text{m}$).

In general, the rate of deliquescence of a crystalline solid is affected by (1) the rate of dissolution of the crystalline core in the solution film that is initially formed on the particle surface and (2) the transfer of water vapor from the surrounding gas phase into the solution.

The rate of water vapor transfer depends on the available surface area of the gas–liquid interface. Considering the deliquescence of a confined crystal, e.g. a crystal in a pore, the available surface area of the gas–liquid interface is limited as a large part of the total surface area of the liquid phase is in direct contact with the pore wall. Similar arguments apply to the deliquescence of powders or crystal agglomerates. In this case, the solution formed during the initial phase of the deliquescence reaction fills the free space in the aggregate but is not necessarily accessible to water vapor transfer from the surrounding atmosphere.

This implies that the rate of deliquescence of crystal aggregates or crystals confined in a pore should be lower than for single crystals that form free droplets upon deliquescence. In fact, this was confirmed by LINNOW [9] for the deliquescence of small crystals of mirabilite ($\text{Na}_2\text{SO}_4 \cdot 10\text{H}_2\text{O}$) adhered to the surface of a fiber filter. In the present work however, the experiments with bulk NaCl were carried out with a powder of rather coarse grained material with a median crystal size of $>125 \mu\text{m}$. Furthermore, the total sample weights were considerably larger than in our previous experiments with mirabilite. Therefore, the significantly lower reaction rate observed in the present study for the bulk NaCl sample appears to be plausible.

The deliquescence of a bulk sample may correspond to the situation of a salt efflorescence on a building. The time required for the complete deliquescence of a salt efflorescence strongly depends on its morphology. The deliquescence of the bulk NaCl sample may correspond to the situation of a fluffy or powdery efflorescence on a building. However, efflorescences may also form compact crusts as sometimes found on heavily contaminated building materials. The more compact a crust is, the longer will the deliquescence reaction take. It is well known that dense salt crusts on buildings in some instances require quite a long time, i.e. days or even weeks, until their deliquescence is complete. For example, ARNOLD and ZEHNDER [15] reported that sodium nitrate efflorescences in the crypt of Grossmünster Zurich disappeared about one or two months after the ambient *RH* exceeded the deliquescence humidity of the salt. DIAZ GONÇALVES [16] obtained similar reaction times in laboratory experiments with different salts.

The relative intensity curves for the deliquescence in the glass frits shown in Figure 4 reveal considerable differences between the specimens. In particular, the deliquescence rate in the P5 glass frit ($d_m = 1.44 \mu\text{m}$) is significantly lower than in the glass frits P2–P4. As shown in

Figure 2 the NaCl in the pore space of these latter specimens forms small agglomerates of individual crystals about 2 μm in size. The agglomerates do not entirely fill the pore space of the specimens, thus, leaving sufficient space for the transfer of water vapor from the surrounding gas phase. This is also in agreement with the moderate load of these specimens with NaCl, i.e. 55.2 mg (P2), 21.8 mg (P3) and 70.3 mg (P4), respectively. In contrast, the mass load of the P5 glass frit used for the deliquescence measurements was much higher (222 mg). Unfortunately, the P5 glass frit used for the microscopic examinations does not appear to be representative due to the presence of cracks as discussed before. Hence, we do not have representative SEM micrographs of the NaCl distribution in the pore space of the P5 specimen. However, NaCl agglomerates with similar morphology to those found in the other specimens should be also present in the P5 specimen. Considering the much higher concentration of NaCl together with the smaller pore size, it is then very likely that a much larger fraction of the pores in the P5 frit was filled with NaCl resulting in the considerably slower deliquescence rate observed.

The discussion so far indicates that the kinetics of the deliquescence in porous building materials is strongly affected by a number of different influences including pore size and geometry, crystal morphology and the volume fraction of the available pore space that is filled with the crystalline salt. Finally, the relative humidity itself strongly influences the deliquescence rate. As mentioned before and discussed in more detail below, this influence of the ambient humidity on the deliquescence kinetics can be utilized for the determination of the equilibrium deliquescence humidity of a salt in a porous material.

4.3.3 Deliquescence humidities

The method proposed by LINNOW and STEIGER [10] was used for the determination of the equilibrium deliquescence humidities (RH_{del}) of NaCl in the pore space of the glass frits. This method is based on the use of Equation (2) for the determination of RH_{del} and requires the measurement of total reaction times t_c at different relative humidities. For maximum accuracy, it is important to measure t_c close to the equilibrium humidity. While measurements at high relative humidity are helpful to fix the parameter B in Equation (2), such measurements are less important for the accurate determination of RH_{del} . For that reason, most of the measurements were carried out at relative humidities close to the expected RH_{del} (Table 1).

Table 1: Relative humidities and total reaction times t_c of the NaCl deliquescence in glass frits P2–P5 with different median pore diameters d_m at 25°C.

$d_m/\mu\text{m}$	$RH/\%$	t_c/h	$d_m/\mu\text{m}$	$RH/\%$	t_c/h
70	75.8	23.4	11.1	75.8	25.2
	76.0	15.7		76.0	22.8
	76.3	11.2		76.2	33.6
	76.7	13.3		76.5	9.2
	77.0	10.2		76.8	20.0
				77.0	11.7
$d_m/\mu\text{m}$	$RH/\%$	t_c/h	$d_m/\mu\text{m}$	$RH/\%$	t_c/h
28	75.9	26.3	1.44	76.5	33.7
	76.0	18.7		77.0	26.3
	76.5	19.2		77.7	19.7
	76.2	4.9		78.5	12.5
	77.9	1.2		78.8	15.0

In contrast to the previous study, total reaction times t_c were not determined by visual inspection of the diffraction patterns in the present work. The fits of the experimental intensities to Equation (3) were used instead by taking t_c as the time corresponding to a decrease in the intensity to 0.1% of its initial value, i.e. $I/I_0 = 0.001$. The resulting values of t_c are listed in Table 1. As discussed before, approaching the deliquescence humidity, the reaction rate decreases. Hence, the total reaction times in Table 1 increase with decreasing RH . The experimental data were used together with Equation (2) to determine $\ln RH_{\text{del}}$ and the coefficient B by linear least squares analysis. The results are summarized in Table 2. As an example, the results for the glass frit P4 are depicted in Figure 5. The error bars represent both the uncertainty in the control of the relative humidity in the XRD chamber and the uncertainty in the determination of t_c . In comparison to our previous study with bulk samples, the present measurements are more scattered resulting in increased standard errors of $\ln RH_{\text{del}}$ and B , and less satisfactory coefficients of determination R^2 . In part, the increased experimental error is caused by the loss of intensity in the measurements with the glass frits and the resulting difficulties in the determination of t_c . Other important sources of error include material inhomogeneities of the glass frits and the limited reproducibility of the sample preparation resulting in an inhomogeneous distribution of the NaCl in the pore space of the specimens.

Table 2: Coefficients $\ln RH_{\text{del}}$ and B of Equation (2) and coefficient of determination R^2 in the glass frits with different median pore sizes d_m .

$d_m/\mu\text{m}$	$\ln RH_{\text{del}}$	B/sec	R^2
70	4.317 ± 0.007	897 ± 327	0.715
28	4.330 ± 0.002	99 ± 18	0.911
11.1	4.329 ± 0.005	416 ± 291	0.337
1.44	4.322 ± 0.006	2043 ± 361	0.911

Despite of the increased experimental error, Equation (2) provides a satisfactory representation of the experimental data to within their stated uncertainty (Figure 5) while the standard error of the RH_{del} is still acceptable. This is illustrated in Figure 6 where the deliquescence humidities of NaCl in the glass frits and their standard errors are plotted as a function of the median pore diameter. The deliquescence humidities in the glass frits compare nicely with the value of $75.4 \pm 0.5\%$ determined in our previous work for bulk NaCl [10], which was in excellent agreement with the commonly accepted reference value of 75.3% [11, 17]. Within the combined experimental uncertainties there are no significant deviations of the deliquescence humidities in the porous substrates and the bulk sample. This is in agreement with theoretical considerations according to which a significant increase in the chemical potentials of small crystals is not expected at crystal sizes above about $0.1 \mu\text{m}$ [18]. According to Figure 2 the crystal sizes in the porous specimens that were investigated in the present work are hardly smaller than about $1 \mu\text{m}$. The results of the present measurements confirm that there is no crystal size influence on the deliquescence humidity of such large NaCl crystals that are deposited in the pore space of glass frits.

The results listed in Table 1 also confirm that the deliquescence rates are lower in the P5 glass frit. As discussed before, this is most likely the result of a higher load of the P5 frit with NaCl. Considering the scatter in the experimental data, the differences in the deliquescence rates in the P2–P4 specimens are less obvious and not significant. Finally, it is important to note that there is a strong influence of the relative humidity on the deliquescence rate. Most measurements in the present work were carried out at $<80\% RH$, i.e. only slightly above the deliquescence humidity of NaCl. However, according to Equation (1) and as shown by LINNOW and STEIGER [10], there is a substantial increase in the reaction rates at high humidity.

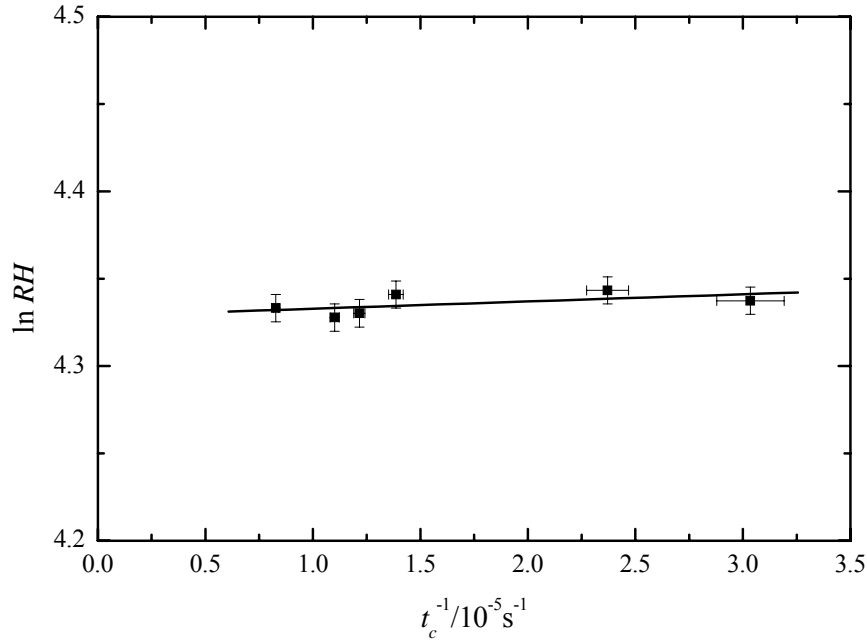


Figure 5: Plot of $\ln RH$ vs. t_c^{-1} for the deliquescence of NaCl in the pore space of the glass frit P4 ($d_m = 11.1 \mu\text{m}$) at 25°C ; vertical error bars represent uncertainties in the measurement and control of RH in the XRD-chamber, horizontal error bars represent uncertainties in the determination of t_c from the XRD patterns.

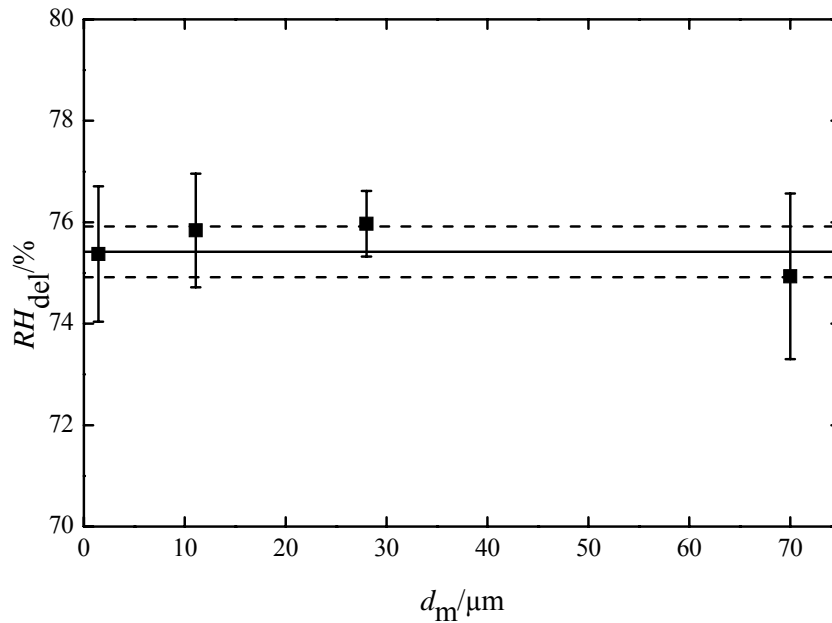


Figure 6: Deliquescence humidity RH_{del} of NaCl in porous glass frits at 25°C as a function of median pore diameter d_m . Error bars represent the uncertainties in the determination of RH_{del} from experimental data by least squares analysis. Solid and dashed lines are the RH_{del} and the range of experimental uncertainty for bulk NaCl as reported by LINNOW and STEIGER [10].

The present work largely focused on the low to intermediate *RH* range, which is most important for the accurate determination of the deliquescence humidity. In future studies, it might be useful to carry out measurements at high *RH* in order to evaluate the effects of short-term *RH* maxima. This however, will require an optimization of the measurement conditions to improve the limited time resolution of the RH-XRD method.

4.4 CONCLUSIONS

The present study confirms that RH-XRD is an appropriate experimental technique for the in situ investigation of phase transformations in confined spaces of porous materials. By using an X-ray amorphous substrate such as glass frits problems with interfering XRD patterns are avoided, however, the technique might also be successfully applied in future studies with materials of simple mineralogical composition, e.g. limestones or quartzitic sandstones.

Due to the limited penetration depth of X-rays the diffraction measurements are limited to a narrow zone close to the surface of the porous material under investigation. Moreover, the penetration depth is not defined sharply but follows the exponential absorption law and, in addition, depends on the Bragg angle. It follows that the distribution of the salt under investigation within the porous substrate is critical in direct XRD studies with porous substrates. The sample preparation procedure used in the present work including impregnation with salt solution and subsequent freeze-drying did not always yield a homogeneous salt distribution in the porous substrates. Therefore, additional characterization of the samples using scanning electron microscopy is recommended in RH-XRD studies with porous substrates. Also, future studies should aim at an optimization of the sample preparation.

The kinetic measurements that were carried out in the present work show that the deliquescence of NaCl in the pore space close to the surface of a porous substrate proceeds on a time scale of a few hours. Since our measurements were all carried out at comparably low relative humidity (< 80%) even shorter reaction times are to be expected at high *RH* as predicted by Equation (1). This implies that the dynamics of deliquescence–crystallization cycles in building materials is strongly affected by both frequency and amplitude of the ambient humidity variation. There appears to be no doubt however, that quite short-term variation of ambient relative humidity, e.g. typical daily fluctuations, might induce damaging deliquescence–crystallization cycles within the pore space of building materials.

RH-XRD measurements do not provide information on the deliquescence in greater depth, i.e. beyond the X-ray penetration depth. With increasing depth, the overall rate of the deliquescence process is not only affected by the reaction kinetics and the supply with water vapor, but is increasingly limited by transport processes, i.e. water vapor diffusion and capillary transport of the solution initially formed by the dissolution of the salt crystals in the pore space near the surface. At a given depth, the deliquescence kinetics in the porous building material is expected to follow a considerably more complex rate law and a number of different parameters need to be taken into consideration, including porosity and pore size distribution, the nature of the salt, crystal morphology and the ambient *RH*. In order to investigate the kinetics of deliquescence in building materials, it will be useful in future studies to combine different experimental techniques. For instance, RH-XRD appears to be very useful to study the deliquescence in the pores close to the surface, while bulk measurement techniques such as gravimetric sorption measurements reveal additional information on the rates in greater depth. For example, SAWDY [8] carefully measured the rates of moisture uptake and loss in salt-contaminated samples and identified the major rate controlling influences. NMR measurements could provide further insight as this technique allows for the simultaneous determination of moisture and ion transport [19].

The limited penetration depth of X-rays in porous materials does not pose any particular problems in the determination of equilibrium humidities of confined crystals. The present work shows that the dynamic approach for the determination of equilibrium humidities that was successfully used with bulk samples [10] can also be applied for the determination of the deliquescence humidity of NaCl in glass frits without significant loss of accuracy. In agreement with theoretical considerations, the present measurements confirm that the deliquescence humidity of NaCl crystals of about 1–3 μm in size is not affected by the confinement in the pore space of glass frits with median pore diameters in the range of 1.4–70 μm . The ability of RH-XRD for the direct determination of equilibrium humidities within pores offers the possibility in future studies to apply the technique to mesoporous materials in order to determine the influence of confinement of very small ($< 0.1 \mu\text{m}$) crystals on the deliquescence humidity.

Acknowledgments

This work was funded by the Deutsche Forschungsgemeinschaft (DFG).

4.5 REFERENCES

- [1] GOUDIE A., VILES H., Salt Weathering Hazards, Wiley, Chichester, **1997**.
- [2] DOEHNE E., Natural Stone, Weathering Phenomena, conservation strategies and case studies, Geol. Soc. Spec. Publ. **2002**, 205, 51–64.
- [3] COOKE R.U., SMALLEY I.J., Salt weathering in deserts, Nature **1968**, 220, 1226–1227.
- [4] JOHNSTON J.H., Salt weathering processes in the McMurdo dry valley regions of South Victoria Land, Antarctica. N.Z., J. Geol. Geophys. **1973**, 16, 221–224.
- [5] MALIN M.C., Salt weathering on Mars, J. Geophys. Res. **1974**, 79, 3888–3894.
- [6] RODRIGUEZ-NAVARRO C., Evidence of honeycomb weathering on Mars, Geophys. Res. Lett. **1998**, 25, 3249–3252.
- [7] STEIGER M., Salts in porous materials: thermodynamics of phase transitions, modelling and preventive conservation, Restor. Build. Monum. **2005**, 11, 419–431.
- [8] SAWDY A., The kinetics of salt weathering of porous materials: stone monuments and wall paintings. PhD Thesis, University College London **2001**.
- [9] LINNOW K., ZEUNERT A., STEIGER M., Investigation of sodium sulfate phase transitions in a porous material using humidity- and temperature-controlled X-ray diffraction, Anal. Chem., **2006**, 78, 4683–4689.
- [10] LINNOW K., STEIGER M., Determination of equilibrium humidities using temperature- and humidity-controlled X-ray diffraction (RH-XRD), Anal. Chim. Acta. **2007**, 583, 197–201.
- [11] GREENSPAN L., Humidity fixed points of binary saturated aqueous solutions, J. Res. Natl. Bur. Stand. **1977**, 81A, 89–96.
- [12] JULING H., KIRCHNER D., BRÜGGERHOFF S., LINNOW K., STEIGER M., EL JARAD A., GÜLKER G., Salt damage of porous materials: a combined theoretical and experimental approach, in: Kwiatkowski D., Löfvendahl R. (eds), Proceedings of the 10th International Congress on Deterioration and Conservation of Stone, ICOMOS, Stockholm **2004**, 187–194.
- [13] ZEHNDER K., ARNOLD A., Crystal growth in salt efflorescence, J. Cryst Growth **1989**, 97, 513–521.
- [14] RODRIGUEZ-NAVARRO C., DOEHNE E., Salt weathering: influence of evaporation rate, supersaturation and crystallization pattern, Earth Surf. Process Landforms **1999**, 24, 191–209.
- [15] ARNOLD A., ZEHNDER K., Monitoring wall paintings affected by soluble salts, in: Cather S. (ed.), The conservation of wall paintings, The Getty Conservation Institute, Los Angeles, **1991**, 103–135.
- [16] DIAZ GONÇALVES T., DELGADO RODRIGUES J., MARINHO ABREU M., Evaluating the salt content of salt-contaminated samples on the basis of their hygroscopic behaviour: Part II: experiments with nine common soluble salts, J. Cult. Herit. **2006**, 7, 193–200.
- [17] STOKES R.H., ROBINSON R.A., Standard solutions for humidity control at 25° C. Ind. Eng. Chem. **1949**, 41, 2013.

-
- [18] STEIGER M., Crystal growth in porous materials—II: Influence of crystal size on the crystallization pressure, *J. Cryst. Growth* **2005**, 282, 470–481.
- [19] PEL L., HUININK H., KOPINGA K., Ion transport and crystallization in inorganic building materials as studied by nuclear magnetic resonance, *Appl. Phys. Lett.* **2002**, 81, 2893–2895.

Chapter 5

Hydration of $\text{MgSO}_4 \cdot \text{H}_2\text{O}$ and generation of stress in porous materials

Michael Steiger¹, Kirsten Linnow¹, Herbert Juling², Gerd Gülker³, Akram El Jarad³, Stefan Brüggerhoff⁴, Dirk Kirchner⁴

¹Institute of Inorganic and Applied Chemistry, University of Hamburg, Martin-Luther-King-Platz 6, D-20146 Hamburg

²Institute of Materials Science (IWT), Badgasteiner Str. 3, D-28359 Bremen

³Carl von Ossietzky University, Institute of Physics, D-26111 Oldenburg,

⁴German Mining Museum Bochum, Preservation of Monuments and Material Sciences, Herner Strasse 45, D-44787 Bochum

In: Journal of Crystal Growth and Design **2007**, (DOI:[10.1021/cg060688c](https://doi.org/10.1021/cg060688c)).

Reproduced with permission from Journal of Crystal Growth and Design. Copyright [2007] American Chemical Society.

5.1 INTRODUCTION

Crystal growth in pores is not only a major cause of damage in building materials such as stone, brick and concrete, but is also considered as an important weathering mechanism of natural rocks [1,2]. Crystal growth in void spaces of porous materials occurs as the result of phase changes induced by variation of ambient temperature or relative humidity, RH . Under unfavorable conditions cycles of repeated crystallization–deliquescence and hydration–dehydration can cause rapid decay of a porous substrate. The pressures generated by growing crystals are usually classified as either crystallization pressure, for growth from a solution, or hydration pressure, for crystal growth during a hydration reaction. The crystallization pressure is related to the supersaturation of the solution [3], while hydration pressure is often attributed to the volume expansion during hydration reactions [1,4].

Magnesium sulfate is often used in laboratory tests and is one of the salts recommended for use with the ASTM (American Society for Testing and Materials) aggregate sound test [5]. Furthermore, this salt is frequently found as contaminant in building materials and there are numerous examples where severe damage is attributed to the action of magnesium sulfate. Compared to other salts, however, much less is known about the behavior of magnesium sulfate in laboratory tests and under field conditions. Due to a large number of different hydrated forms the phase behavior in the system $\text{MgSO}_4 + \text{H}_2\text{O}$ is quite complex and it is difficult to predict which phase crystallizes under given experimental conditions.

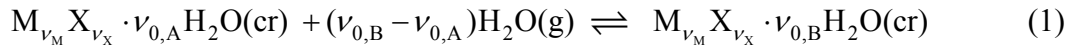
A better understanding of the action of magnesium sulfate, i.e. the phase transitions that occur within pores and the mechanism responsible for the generation of stress in porous materials, requires appropriate experimental techniques for the *in situ* investigation of the relevant processes in the pore space. In the present work we have studied the hydration of $\text{MgSO}_4 \cdot \text{H}_2\text{O}$ within confined spaces of a porous material by using a combined experimental approach. Dynamic diffractometry under controlled conditions of temperature and relative humidity was used for the direct observation of the hydration reaction within the pores. Scanning electron microscopy after cryo-fixation of the samples was used to visualize morphological changes during the course of the reaction. Finally, strain and deformation as the macroscopic manifestation of stresses generated during crystal growth, were analyzed using electronic speckle pattern interferometry. Based on the phase diagram of $\text{MgSO}_4 + \text{H}_2\text{O}$ derived from a careful evaluation of the available thermodynamic data, all experiments were carried out under appropriate conditions in a controlled environment. First results of this study were reported re-

cently [6]. This paper reports additional data and results including a conclusive discussion on the pathway of the hydration reaction and the mechanisms that are responsible for the generation of stress.

5.2 THEORETICAL CONSIDERATIONS

5.2.1 Growth Pressure

For a salt of general composition $\text{M}_{\nu_M} \text{X}_{\nu_X} \cdot \nu_0 \text{H}_2\text{O}$ consisting of ν_M positive ions M, ν_X negative ions X, and ν_0 molecules of water, the equilibrium constant K_{AB} of the hydration reaction



is given by:

$$K_{AB} = p_w^\circ / p_{w,AB} = 1 / RH_{AB} \quad (2)$$

where $p_{w,AB}$ is the equilibrium water vapor partial pressure, p_w° is the saturation water vapor pressure and RH_{AB} is the equilibrium relative humidity for the hydration–dehydration equilibrium of the two hydrates with $\nu_{0,A}$ and $\nu_{0,B}$ molecules of water. If the lower hydrated form is confined in void spaces of a porous material, pressure can be generated during the hydration reaction. This hydration pressure Δp_{Hydr} is given by:

$$\Delta p_{\text{hydr}} = \frac{\Delta \nu_0 RT}{\Delta V_m} \ln \frac{p_w}{p_{w,AB}} \quad (3)$$

where R is the gas constant, T is the absolute temperature, $\Delta V_m = V_{m,B} - V_{m,A}$ is the difference in the molar volumes of the two solids, and $\Delta \nu_0 = \nu_{0,B} - \nu_{0,A}$. The hydration pressure is the pressure that would have to be exerted to the hydrated crystal to prevent its growth. In other words, p_w is the equilibrium water vapor partial pressure of the hydration–dehydration equilibrium, if the vapor phase is under ambient pressure p_a and the solid phases are under the enhanced pressure p_c , thus, $\Delta p_{\text{hydr}} = p_c - p_a$. It is important to note that the driving force for the hydration pressure is supersaturation. While the supersaturation of a solution is the driving force for the crystallization pressure [3], it is the water vapor supersaturation of the ambient air in respect to the equilibrium water vapor pressure of the hydrated salt which is responsible for the generation of hydration pressure.

Eq. (3) was first derived by MORTENSEN [7], later it was misused by calculating very high hydration pressures at relative humidities close to 100% (e.g. reference [4]). In these calculations it was overlooked however, that there is an upper limit of the ambient RH due to the deliquescence of both, the educt and the product phases [8]. Above the deliquescence humidity, RH_{del} , of the product phase, i.e. the higher hydrated form, a solid cannot exist anymore and, consequently, there is no hydration pressure at all. If the RH_{del} of the educt phase is exceeded, a solution supersaturated with respect to the product phase is formed and the hydration reaction follows a different reaction pathway, namely a dissolution–recrystallization pathway [8]. In this case, the pressure generated is more realistically described as a crystallization pressure Δp_{crys} which can be calculated from the degree of supersaturation of the solution according to

$$\Delta p_{\text{crys}} = \frac{RT}{V_m} \ln \frac{a}{a_0} \quad (4)$$

where V_m is the molar volume of the hydrated phase, a and a_0 are the activity products of the supersaturated and the saturated solutions, respectively [3].

5.2.2 Phase Diagram of $\text{MgSO}_4 + \text{H}_2\text{O}$

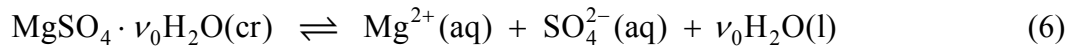
Figure 1 depicts an RH – T phase diagram of the stable phases in the $\text{MgSO}_4 + \text{H}_2\text{O}$ system from 0–80°C. It is based on an evaluation of the available thermodynamic data of aqueous MgSO_4 and the various crystalline phases, i.e. $\text{MgSO}_4 \cdot 7\text{H}_2\text{O}$ (epsomite), $\text{MgSO}_4 \cdot 6\text{H}_2\text{O}$ (hexahydrate), and $\text{MgSO}_4 \cdot \text{H}_2\text{O}$ (kieserite). The deliquescence humidities of $\text{MgSO}_4 \cdot 7\text{H}_2\text{O}$ and $\text{MgSO}_4 \cdot 6\text{H}_2\text{O}$ (curves a and b in Figure 1) were obtained from the commonly accepted solubilities of these solids in the respective temperature ranges and the water activities of the saturated solutions. The latter were taken from ARCHER AND RARD [9]. Available solubilities of kieserite are much more scattered. For the present treatment the values of SMITS et al. [10] and ROBSON [11] were accepted and used to fix the deliquescence humidities of the monohydrate above the hexahydrate–kieserite transition temperature (curve c).

Curve d in Figure 1 is a representation of the available experimental data of equilibrium humidities for the epsomite–hexahydrate transition [12–15]. No such data are available for the kieserite–hexahydrate equilibrium, hence, the equilibrium humidities were calculated from solubility data. The equilibrium humidity for a particular hydration–dehydration equilibrium

is related to the thermodynamic solubility products of the two hydrates under consideration. This leads to the following equation for RH_{AB} :

$$\ln RH_{AB} = \frac{\ln K_B - \ln K_A}{\Delta \nu_0} = \frac{1}{\ln K_{AB}} \quad (5)$$

where K_A and K_B are the standard solubility products of the lower and the higher hydrated solids, respectively. The reaction describing the equilibrium between the magnesium sulfate hydrates and their respective saturated solutions is



The solubility product is thus given by

$$K = m_{\text{sat}}^2 \gamma_{\pm, \text{sat}}^2 a_{\text{w}, \text{sat}}^{\nu_0} \quad (7)$$

where m_{sat} , $\gamma_{\pm, \text{sat}}$ and $a_{\text{w}, \text{sat}}$ are the molality, mean activity coefficient and water activity of the saturated solution. Using Eq. (7), values of the solubility product of epsomite, K_{eps} , were calculated from solubility data using the activity coefficients and water activities of the saturated solutions from reference [9]. These values of K_{eps} were then used together with the experimental equilibrium humidities for the hexahydrate–epsomite equilibrium to calculate the solubility product of $\text{MgSO}_4 \cdot 6\text{H}_2\text{O}$ at low temperatures, i.e. below the epsomite–hexahydrate transition. From the hexahydrate solubility products the water activities of the metastable equilibrium between hexahydrate and its saturated solution could be calculated, i.e. the deliquescence humidities of metastable $\text{MgSO}_4 \cdot 6\text{H}_2\text{O}$ (curve h in Figure 1). The solubility products of kieserite, K_{kies} , above the hexahydrate–kieserite transition temperature were calculated from the solubility data [10,11] as described before. At low temperatures the solubility product was calculated from kieserite solubilities in the ternary system $\text{MgSO}_4\text{--MgCl}_2\text{--H}_2\text{O}$. Finally, the values of K_{kies} were used to calculate both, the equilibrium humidities of the kieserite–hexahydrate and the kieserite–epsomite transition (curves e and f), and the deliquescence humidities of metastable kieserite (curve g).

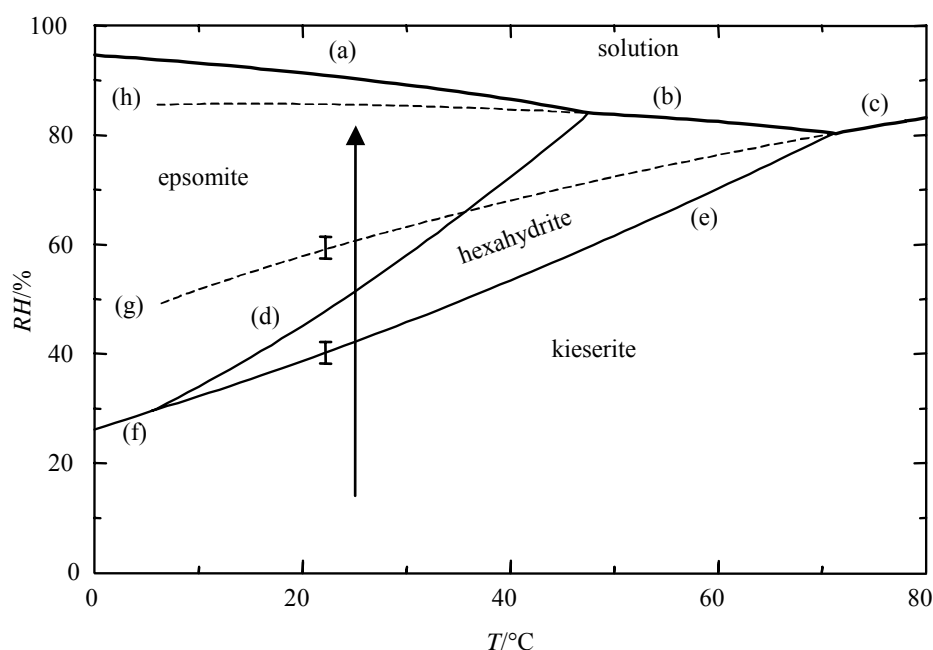


Figure 1: RH/T phase diagram of $\text{MgSO}_4 + \text{H}_2\text{O}$ with deliquescence–crystallization equilibria of (a) epsomite, (b) hexahydrate and (c) kieselrite, and hydration–dehydration equilibria of (d) hexahydrate–epsomite, (e) kieselrite–hexahydrate and (f) kieselrite–epsomite; dashed curves represent metastable deliquescence humidities of (g) kieselrite and (h) hexahydrate; the error bars are estimated uncertainties and the arrow indicates the experimental conditions for the humidity induced hydration of kieselrite.

While the existing thermodynamic data are consistent and quite confidential in the case of epsomite and hexahydrate, there remains some uncertainty in the calculated equilibrium humidities for the phase equilibria involving kieselrite. An error estimate of the calculated values is indicated in Figure 1 for the deliquescence humidities of kieselrite and the equilibrium humidities for the kieselrite–hexahydrate equilibrium close to room temperature.

5.3 EXPERIMENTAL SECTION

5.3.1 Samples

Glass filter frits were used as the porous substrate in all experiments. This amorphous material offers several advantages including a simple chemical composition and well defined porosities and pore size distributions. Moreover, this substrate does not show moisture induced swelling and shrinking, thus, does not interfere with the deformation measurements. Mercury

intrusion porosimetry revealed a median pore radius of 6 μm , and a narrow pore size distribution for glass filters of porosity class 4 supplied by Schott (Mainz) which were used throughout the study. A porosity of 18% was determined by optical microscopy, mercury intrusion measurements yielded a porosity of 20%. Hence, the glass frits used represent typical pore sizes and porosities of many building materials such as natural stone and brick.

The glass frits were impregnated with a solution of MgSO_4 (19% w/w) and subsequently freeze-dried in order to avoid an inhomogeneous distribution of the magnesium sulfate and the formation of efflorescences on the surface as result of transport processes during evaporation drying. The freeze-dried samples proved to be quite hygroscopic and after rapid moisture uptake in laboratory atmosphere, hexahydrate was identified as the major species by X-ray diffraction. The subsequent dehydration of hexahydrate to obtain kieserite, $\text{MgSO}_4 \cdot \text{H}_2\text{O}$, as the educt phase of the intended investigation of a hydration reaction turned out to be difficult as a mixture of different metastable lower hydrates including $\text{MgSO}_4 \cdot 3\text{H}_2\text{O}$, $\text{MgSO}_4 \cdot 2\text{H}_2\text{O}$ and $\text{MgSO}_4 \cdot 5/4\text{H}_2\text{O}$ was observed. In order to obtain kieserite as a definite educt phase, the specimens were dried at 200 °C for three weeks until X-ray diffraction measurements confirmed that no other hydrates except kieserite were present. We have also tried to obtain kieserite by direct crystallization from solution at enhanced temperature (100 °C) as suggested by the phase diagram. However, this treatment of the samples also yielded a mixture of different hydrates, i.e. $\text{MgSO}_4 \cdot 3\text{H}_2\text{O}$, $\text{MgSO}_4 \cdot 1.25\text{H}_2\text{O}$ and $\text{MgSO}_4 \cdot 1\text{H}_2\text{O}$. In addition, the evaporation drying procedure caused severe problems by the formation of efflorescences on the surfaces of the specimens which would strongly interfere with the intended investigation of the hydration of crystals confined in pores. The morphology of kieserite in the pores of the glass filters is shown in Figure 2. The kieserite is evenly distributed in the porous matrix and forms highly porous aggregates. Their morphology indicates that they are formed by the decomposition of large single crystals of a higher hydrated phase, most likely hexahydrate.

5.3.2 Scanning Electron Microscopy with Cryo-preparation

Sample preparation is a critical step in conventional scanning electron microscopy (SEM) of water containing samples as evaporation of solutions and precipitation of dissolved species may occur under the applied vacuum. Such drying artifacts severely hamper the ability of conventional SEM to study phase transition reactions involving salt solutions. Cryo-preparation is a powerful tool in scanning electron microscopy in order to avoid such prepara-

tion artifacts. In cryo-preparation samples eventually containing liquid water are subjected to rapid cooling at rates of about $1000 \text{ K} \cdot \text{s}^{-1}$ such that solutions form a glassy solid matrix. Such high rates are obtained when placing the sample into melting nitrogen (slush nitrogen). The frozen samples are subsequently fixed on a cooling tablet and further manipulations of the sample, e.g. cutting and crushing, and the microscopic examination are carried out at -150°C , hence, avoiding preparation artifacts. The method is described in more detail in reference [16]. In the present work a Hitachi S 4004 scanning electron microscope with a Balzers SCU 020 cryo unit was used for the Cryo-SEM investigations.

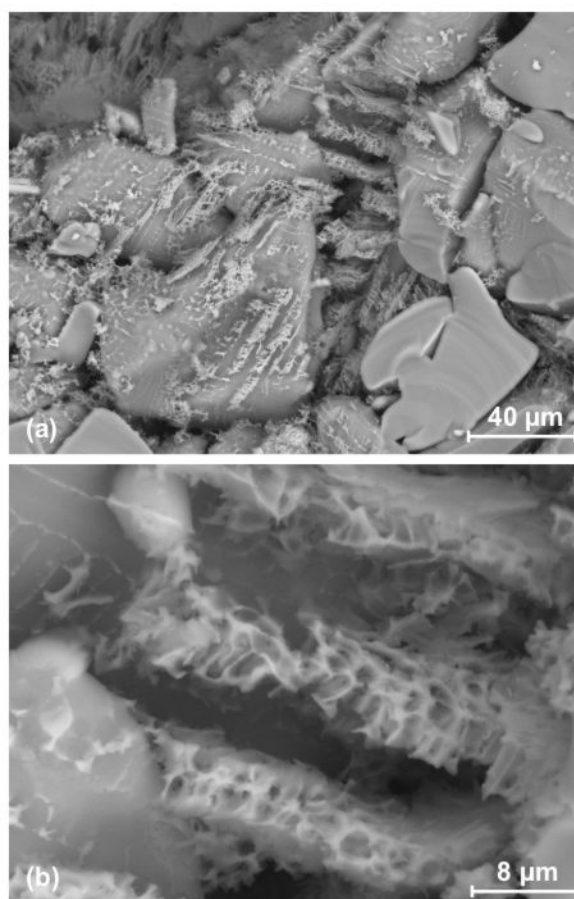


Figure 2: SEM micrographs of kieserite in dried glass filters formed after dehydration of higher hydrated forms, mainly hexahydrate [BSE image, 20 kV].

5.3.3 X-ray Diffractometry under Controlled RH

X-ray diffractometry (XRD) is the obvious choice for the direct in situ investigation of phase transformations and crystal growth. Typically, deleterious phase transition reactions in porous

materials are initiated by changes in temperature and relative humidity. Hence, XRD under controlled conditions of temperature and relative humidity (RH-XRD) is an appropriate method to study such processes. It has been shown recently that RH-XRD can also be successfully applied to investigate phase transformation reactions within the void spaces of a porous material [17]. In the present work, RH-XRD was used for the direct observation of the hydration of kieserite in the glass filters at different humidities. Diffraction patterns were recorded on a Bragg-Brentano parafocusing reflection diffractometer (D 5000, Siemens) providing a horizontal θ - 2θ configuration using Cu $K\alpha$ -radiation and a position-sensitive detector (PSD). The diffractometer is equipped with an environmental chamber allowing for dynamic diffractometry under controlled conditions of temperature and *RH*. Details of the environmental chamber and the humidity control system may be found in reference [17]. Filter disks with a diameter of 20 mm and a height of 2 mm were prepared as described before and were placed on the sample holder of the diffractometer without further treatment.

5.3.4 Electronic Speckle Pattern Interferometry

One approach to study the formation of salt-induced stress is to measure micro-deformations and surface micro-structure changes of a porous substrate during crystal growth. For this purpose electronic speckle pattern interferometry (ESPI) was used. ESPI is a non-contact and full-field optical method, which is able to detect submicron deformations within the field of view spatially resolved and in video real-time. The underlying principles of ESPI are widely known and comprehensively described in the literature (e.g. [18]). This technique has been used successfully for a long time to investigate deterioration processes in works of art and to develop procedures for their preservation [19]. The use of this full-field method offers the big advantage that deforming parts of the object's surface can be immediately identified and further examined in detail, e.g. applying Cryo-SEM, which is extremely important in cases where the surface deforms inhomogeneously. During the measurements the objects under investigation were placed in a small computer controlled climatic chamber where they could be exposed to well defined ambient temperature and relative humidity. To improve the sensitivity and spatial resolution of the method a HeCd-laser (442 nm) was used for the illumination of the test specimen. A CCD-camera Adimec MX12P with standard objectives or, in cases where the investigation of microscopic areas turned out to be appropriate a Mitutoyo

objective M Plan APO 20 were used to create the image of the object. Further details of the ESPI-setup may be found in reference [6].

To detect salt-induced deformations by ESPI, cubes of fritted glass with dimensions of 1 cm^3 were used in most of the experiments. The sample treatment for the ESPI measurements was modified as follows. Prior to the impregnation and drying procedure described before, one surface of the specimens was coated with a thin layer of platinum with thickness of about 20 nm. This coating has two important effects: On the one hand it avoids the penetration of the illuminating laser light into the bulk material since the glass specimens are semi-transparent. Light from deeper regions within the material could suffer from multiple scattering leading to unwanted changes in the backscattered light field resulting in an undesired de-correlation of the speckle pattern. On the other hand the surface of the specimens was made hydrophobic to some extent by this method of treatment thus preventing the transport of salt solution to the surface. The formation of a solution film would change the micro-topography of the surface and the light field scattered by the object would be significantly altered, leading to a de-correlation of the underlying speckle patterns impairing the method. With this modified procedure speckle de-correlations were nearly completely avoided and deformation measurements could be performed over the entire range of RH variation.

5.3.5 Measurements

The humidity induced hydration of kieserite was investigated at constant temperature as indicated by the arrow in Figure 1. According to the phase diagram of the $\text{MgSO}_4 + \text{H}_2\text{O}$ system at 25°C kieserite and epsomite are the stable phases at $RH < 42\%$ and $RH > 51\%$, respectively. In between there is a relatively small range of stable existence of hexahydrate from 42% – $51\% RH$. Hence, it was expected that the hydration of kieserite starts at $RH > 42\%$ with the formation of hexahydrate, while epsomite should be the hydration product at $RH > 51\%$. In the RH -XRD measurements glass filter specimens prepared as described before were placed in the environmental chamber and equilibrated at $29\% RH$ and 25°C . Subsequently, the RH was adjusted in a single step to the desired final value at constant temperature and the diffraction patterns were continuously recorded for several hours. Measurements were carried out at humidities 45% , 50% , 55% , 58% , 65% , 70% , 75% and 80% , typical fluctuations did not exceed $0.4\% RH$. To detect deformations of the glass filter specimens during the hydration reaction continuous ESPI measurements at 21°C were carried out while stepwise increas-

ing the relative humidity, typically, from nearly 0% to about 80% *RH*. Cryo-SEM was used to observe the morphological changes during the hydration reaction. Glass filter specimens that were exposed in the climatic chamber of the ESPI setup were removed from the chamber and immediately prepared for the SEM with flush nitrogen. In particular, several samples were prepared directly after they were used for the ESPI measurements. Hence, it was possible to correlate the deformation of the samples as determined by ESPI with the morphological changes in the pore space of the glass filters.

5.4 RESULTS AND DISCUSSION

RH-XRD Measurements Kieserite, hexahydrite and epsomite in the glass filters were identified by comparison of the XRD patterns with the standards JCPDS (Joint Committee on Diffraction Standards) 33-0882, 24-0719 and 36-0419. In the beginning and at the end of the hydration reactions XRD patterns were recorded from 10° – 70° 2θ . This was necessary for an unambiguous identification of educt and product phases and to rule out the presence of additional metastable phases. During the course of the hydration reaction a smaller range, 19° – 29° 2θ , was recorded in order to increase the time resolution, i.e. the number of consecutive patterns. Figure 3 depicts the diffraction patterns of the three hydrates in bulk samples and in the glass filters. It is obvious that there is a considerable loss of intensity in the glass filters compared to the bulk samples. This is largely due to the small content of magnesium sulfate in the specimens. Nonetheless, the unambiguous identification of the patterns is possible.

While the phase diagram predicts the formation of epsomite at $RH > 51\%$, the hydration of kieserite always led to the formation of hexahydrite at $RH \leq 75\%$. Only at 80% *RH* the initial hydration product, hexahydrite, was subject to subsequent hydration and formation of epsomite. Hence, the direct hydration of kieserite to epsomite did not occur at any humidity. At *RH* values of 45%, 50%, 55% and 58% the transition from kieserite to hexahydrite was incomplete as indicated by the presence of kieserite peaks of significant intensity even after several hours. In contrast, the complete conversion to hexahydrite was rapidly achieved at 65%, 70%, 75% and 80% *RH*. In order to understand these surprising results it proved helpful to evaluate quantitatively the reaction extent during the hydration process at different *RH*. The quantitative evaluation of the educt phase kieserite was not possible due to the low peak intensities. For the quantitative evaluation of the product phase formation, intensities measured

as the areas of nearly undisturbed peaks of hexahydrate and epsomite at $20.2^\circ 2\theta$ and $22.0^\circ 2\theta$, respectively, were used. As a result of the low intensities and due to peak overlap and an increased background caused by the amorphous matrix, the data obtained for hexahydrate are somewhat more scattered than for epsomite. Nonetheless, the course of the hydration reactions can be followed reasonably well. Figure 4 depicts the lapse of reaction time in terms of relative intensities I/I_0 , where I_0 is the constant hexahydrate intensity at the end of the reaction, i.e. when the absence of kieserite peaks indicated that the hydration was complete. In the case of the incomplete hydrations of kieserite at low RH , I_0 was determined at the end of an experiment by a short increase of RH to $> 65\%$ which was sufficient to achieve rapid and complete hydration thus yielding the intensities I_0 of hexahydrate. It can be seen from Figure 4 that rapid and complete hydration is observed at $RH \geq 65\%$.

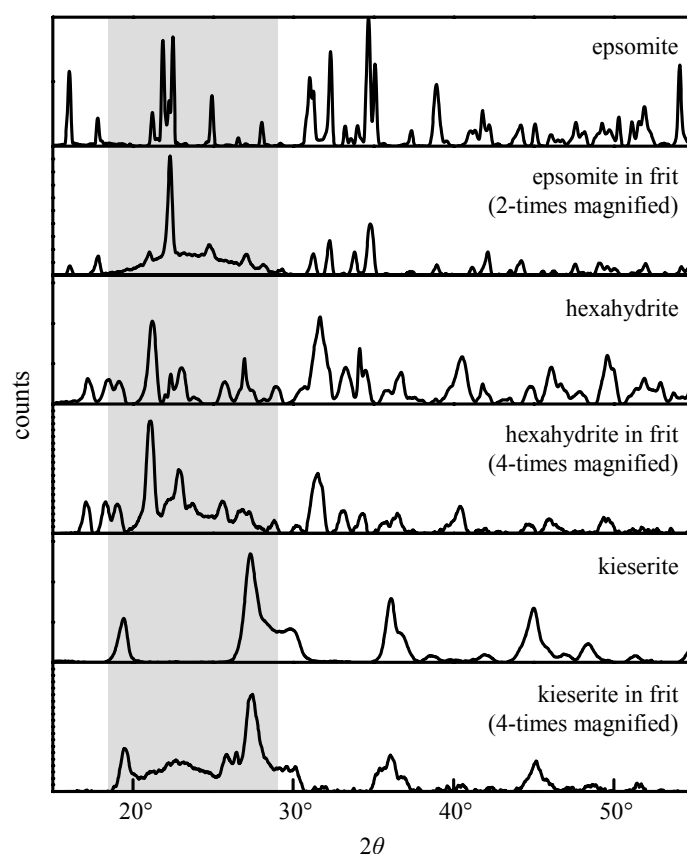


Figure 3: Diffraction patterns of epsomite, hexahydrate and kieserite in bulk samples and in the pore space of the glass filters; note the reduced intensities in glass filters; the hatched area indicates the range of 2θ continuously recorded during the hydration experiments.

In contrast, at $\leq 58\%$ *RH* the reactions are incomplete and less rapid. For example, at 58% the diffraction patterns of both kieserite and hexahydrate did not reveal any significant changes, even after 63 hours. Only after a short increase in *RH* the reaction continued and the kieserite intensities vanished. The experimental findings are consistent with the assumption of two different reaction pathways for the kieserite hydration. At humidities below the deliquescence humidity of kieserite, i.e. below about 60% *RH* at 25°C (cf. Figure 1), the reaction proceeds as a true solid state reaction according to Eq. (1). Obviously however, this reaction is kinetically hindered. Though not yet fully understood, it appears plausible that the formation of a barrier product layer of hexahydrate prevents the hydration of a bulk kieserite crystal. In addition, due to the considerable volume expansion during the hydration in the confined spaces of the porous glass filters, the accessibility of kieserite to the water vapor may be further reduced.

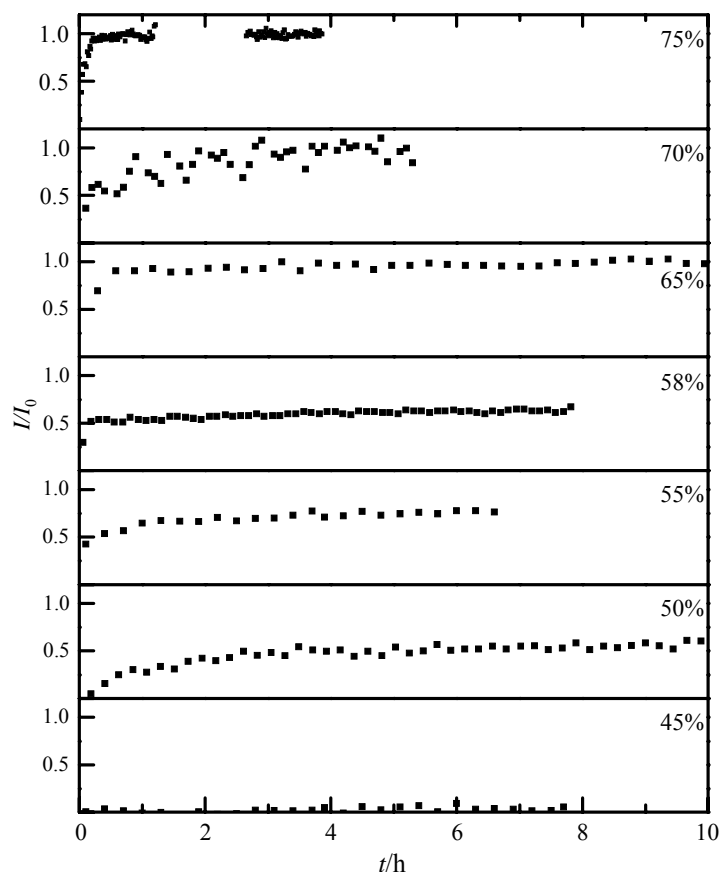


Figure 4: Course of the hydration of kieserite and formation of hexahydrate at different humidities; reaction extent given as relative intensities I/I_0 of hexahydrate with I_0 the maximum intensity after complete hydration.

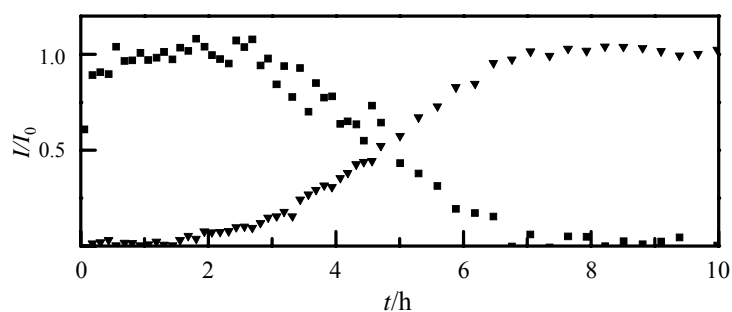


Figure 5: Relative Intensities I/I_0 of hexahydrate (\blacklozenge) and epsomite (\blacktriangledown) during the hydration of kieserite at 80% RH .

At humidities above the deliquescence humidity of kieserite, a two-step process involving dissolution of kieserite followed by crystallization of hexahydrate is suggested. The deliquescence of kieserite leads to a very concentrated MgSO_4 solution. The maximum possible concentration is given by the solubility of kieserite, i.e. $m_{\text{sat}} = 6 \text{ mol} \cdot \text{kg}^{-1}$ at 25°C . At the same temperature, the solubilities of hexahydrate and epsomite are $m_{\text{sat}} = 3.7 \text{ mol} \cdot \text{kg}^{-1}$ and $m_{\text{sat}} = 3.0 \text{ mol} \cdot \text{kg}^{-1}$, respectively. Thus, the solution formed is far supersaturated with respect to both hydrates and rapid crystallization is to be expected. Though the formation of epsomite should be expected on pure thermodynamic grounds, hexahydrate precipitation is obviously kinetically favored. There is also an obvious kinetic hindrance of the epsomite formation by hydration of hexahydrate, which is expected at $RH > 51\%$ but is only observed at 80% RH . For instance, at 75% RH no significant change in the hexahydrate peak intensity could be observed after 20 hours nor could epsomite peaks be identified. In contrast, the hydration of hexahydrate proceeds smoothly at 80% RH . Figure 5 depicts the course of the hydration of kieserite at 80% RH . Initially, hexahydrate is rapidly formed and the hydration of kieserite is complete within 30 minutes. Hexahydrate intensities remain constant for at least another hour before epsomite peaks appear for the first time. Subsequently, the epsomite intensities continuously increase and hexahydrate peaks continuously decrease until the reaction is complete after 7–8 hours. Though there is no obvious explanation for the kinetic hindrance of the hexahydrate hydration at 75% RH and below, it is important to note that 80% RH is still well below the deliquescence humidity of 85.6% of hexahydrate. Hence, a two step reaction mechanism as for the kieserite hydration can be ruled out in this case.

5.4.1 Cryo-SEM Examinations

Samples for the Cryo-SEM examinations were taken from specimens that were exposed in the climatic chamber of the ESPI-setup. One specimen, subjected to a stepwise increase in relative humidity to 81%, was immediately removed from the chamber and samples were prepared for the Cryo-SEM with melting nitrogen. Figure 6 shows SEM images of the pore space close to the surface of the specimen. In comparison to the situation prior to the hydration reaction (cf. Figure 2) it is obvious that the pore space close to the surface is entirely filled with hydrated magnesium sulfate (Figure 6a and 6b). According to the results of the RH-XRD measurements the hydrated solid is most likely hexahydrate, though some secondary formation of epsomite cannot be ruled out as the specimen was subjected for nearly three hours to an increased *RH* of 80–82%. Obviously the volume expansion during the hydration reaction led to confinement and, therefore, it is very likely that stress was generated during the growth of the hydrated crystals.

The cryo-fixation of the samples also allows for the detection of liquid water in backscattering images due to the differences in atomic numbers. In Figure 6c the dark color of the material in the groove on the surface compared to the surrounding glass particles indicates the presence of a solution. Similarly, solution inclusions can be also identified below the surface (see arrow in Figure 6b), thus, the Cryo-SEM results confirm the deliquescence–crystallization mechanism of the hydration at enhanced humidity as discussed before. It is important to note that the concentration of the solution saturated with kieserite, i.e. $m_{\text{sat}} = 6 \text{ mol} \cdot \text{kg}^{-1}$, contains 9 moles of water per mole of MgSO_4 . Hence, a large fraction of the liquid water that is formed upon deliquescence is rapidly consumed again, if the higher hydrates, $\text{MgSO}_4 \cdot 6\text{H}_2\text{O}$ or $\text{MgSO}_4 \cdot 7\text{H}_2\text{O}$, crystallize out. Provided that the precipitation of the hydrates proceeds at a reasonable rate, it can be easily understood that the deliquescence of kieserite cannot lead to bulk solutions filling the pores but rather to solution films that occur during the hydration just as observed in the SEM.

5.4.2 ESPI Measurements

Kieserite hydration was investigated by continuous ESPI measurements while stepwise increasing the relative humidity. As a first result an immediate deformation of the sample surface due to the humidity change was observed. In addition, the rate of deformation and thus the dynamics of hydration seemed to depend on the relative humidity.

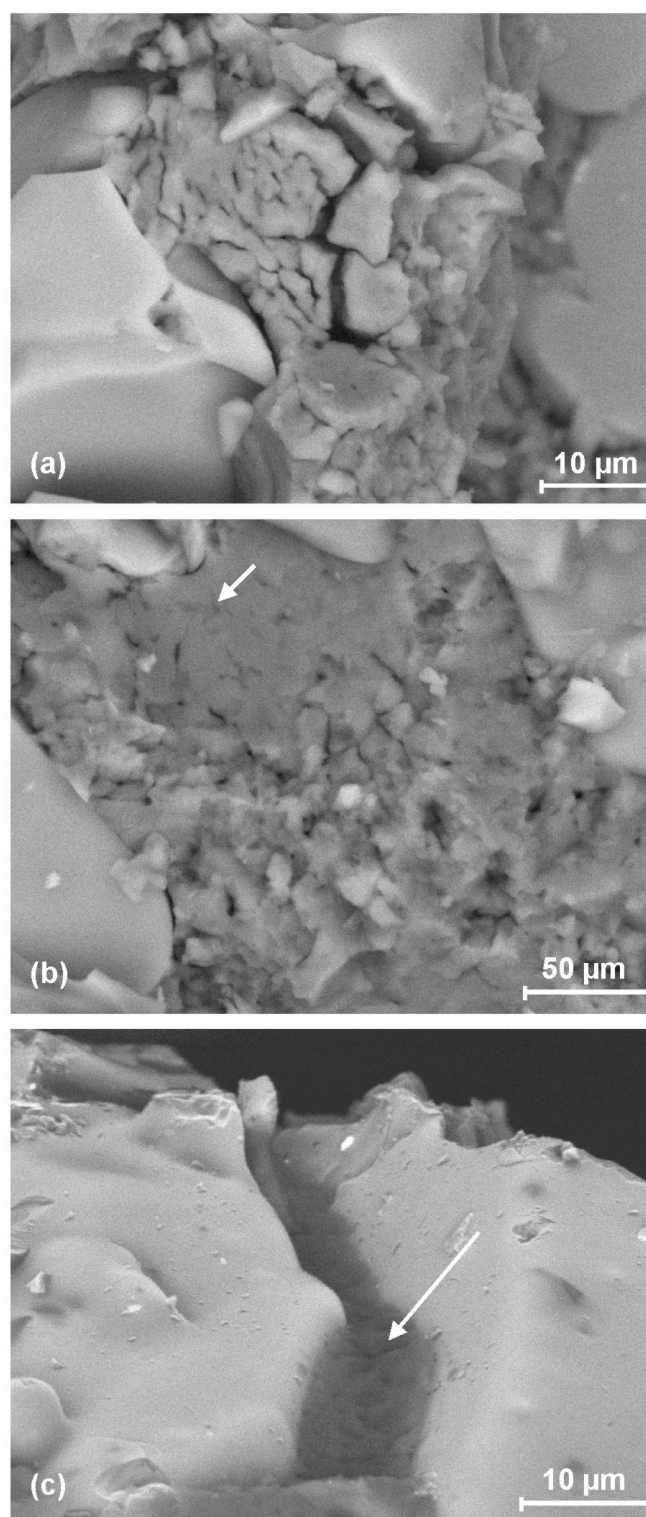


Figure 6: Cryo-SEM images of the pore space close to the surface (a and b) and on the surface (c) of a specimen exposed to stepwise increasing RH , arrows indicate the presence of solutions [BSE image, 20 kV].

To get better insight into the hydration process the ESPI results were used to evaluate the local strain of the center of the specimen. This was possible because a non-contaminated control specimen was placed in the same climatic chamber and was simultaneously measured by ESPI. By comparing the resulting ESPI data from the contaminated and the control specimen and by temporal phase unwrapping [20] the absolute deformation of the contaminated sample and thus the strain was determined.

In Figure 7 the measured strain for the sample that was subsequently examined by Cryo-SEM (cf. Figure 6) is plotted vs. time and *RH*. It can be seen that immediately after increasing the *RH* to about 30% the sample started to deform significantly. This was not expected theoretically since no phase changes should occur below 42% *RH*. In the further course of the experiment, the increase of *RH* was associated with a nearly linear increase of the strain. These results verify that hydration of kieserite leads to the formation of pressure and to an amount of strain which can be measured by ESPI. Above about 60% *RH* the strain rate changed significantly and increased considerably. Hence, the ESPI measurements confirm that there are two different reaction pathways for the kieserite hydration as discussed before. Furthermore, the strain measurements by ESPI yield information about the efficiency of the reaction pathways in generating stress. At low humidities, pressure is generated during the direct hydration of kieserite and is best treated as a hydration pressure according to Eq. (3). At humidities above the deliquescence humidity of kieserite, stress is generated by hexahydrate crystals growing from highly supersaturated solutions leading to pronounced dilatations. Hence, the reason for the mechanical response of the sample at this stage of the experiment has to be assigned to crystallization pressure.

The occurrence of a solution during hydration was also verified in an additional experiment. A contaminated specimen was placed in the climatic chamber at room temperature and low *RH* of about 30%. The preparation of this specimen was slightly modified just to make the surface under investigation less hydrophobic and thus to allow some salt enrichment directly on the surface. This was achieved by coating the specimen with platinum not prior to the contamination and drying procedure but afterwards. While increasing the humidity in a single step to about 70% *RH*, ESPI images were recorded and the deformation of the surface was observed right from the beginning. However, after a while a de-correlated region could be clearly observed in the resulting ESPI images. This means that the light field scattered from this part of the surface changed considerably indicating significant alterations in the micro-

topography of the surface, possibly due to the formation of a solution film. For clarification the experiment was stopped at that moment in time where the de-correlated area covered about half of the surface area. The sample was immediately removed from the climatic chamber and prepared for the Cryo-SEM.

The frozen sample was cut inside the microscope along the transition line separating the correlated and the de-correlated surface areas. In Figure 8 an SEM micrograph is presented showing a cross section exactly from the region where the de-correlation stopped. In fact, the backscattered image reveals the presence of liquid films on and directly beneath the surface (see arrows in Figure 8). This experiment provides further evidence that the transition from kieserite to hexahydrite above the deliquescence humidity of kieserite mainly occurs via dissolution and recrystallization.

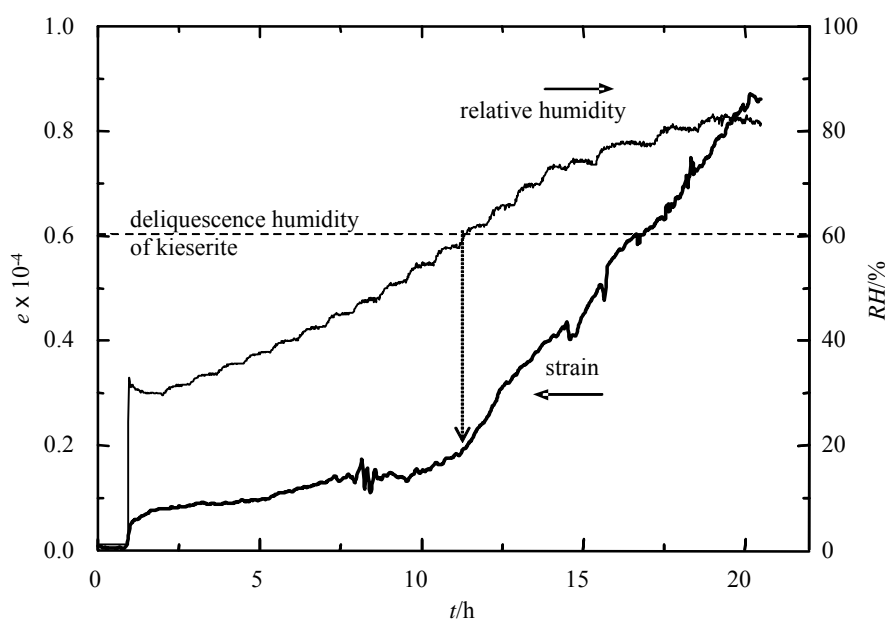


Figure 7: Local strain ε at the center of the specimen vs. measuring time and RH ; increase of strain rate at about 60% RH corresponding to the deliquescence of kieserite.

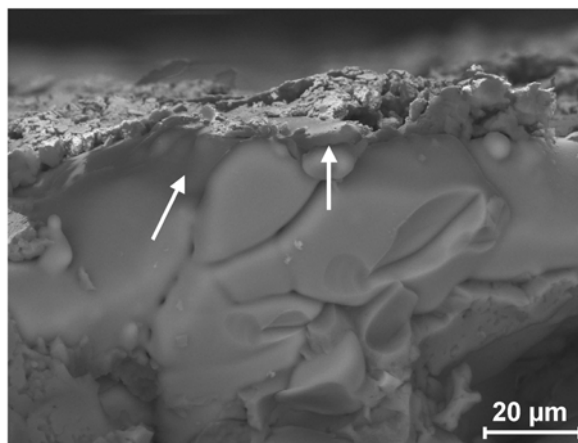


Figure 8. Cryo-SEM image of the sample surface in the transition region of correlated and de-correlated surface areas; arrows indicate solution films [BSE image, 20 kV] (from reference [6] reproduced with permission).

5.4.3 Damage Mechanism

The strain measured by ESPI provides evidence that stress is generated during both the direct solid state reaction and the two step reaction pathway of kieserite hydration. The latter reaction involves the reorganization of the crystal lattice by dissolution and subsequent crystallization. In contrast, the direct hydration in the solid state must involve an interface in the reacting solid between the reactant (i.e. kieserite) and the recrystallized product (i.e. hexahydrate). In this case, the reaction follows a more complicated mechanism with a number of different possible rate limiting steps. Nonetheless, whatever the mechanism of the hydration reaction on the molecular scale is, the thermodynamic treatment leading to Eq. (3) is valid for the direct hydration according to Eq. (1), i.e. at humidities below the deliquescence humidity of kieserite. Using Eq. (3) a hydration pressure $\Delta p_{\text{hydr}} = 57 \text{ MPa}$ is calculated for an ambient RH close to the kieserite deliquescence humidity. Considering that tensile strengths of most building materials do not exceed values of about 3–5 MPa, it is obvious that the stress generated by the direct hydration of kieserite may be sufficient to cause damage to most materials.

At humidities above the deliquescence humidity of kieserite, Eq. (3) is inappropriate and the pressure generated by the growth of hexahydrate crystals from solution can be calculated using Eq. (4). However, it is difficult to estimate the concentration in solution formed during the two step hydration reaction. Initially, a solution saturated with kieserite and supersaturated with hexahydrate is formed during deliquescence. Subsequently, the solution supersaturation

is consumed as hexahydrate precipitates. Hence, the concentration in the vicinity of the growing hexahydrate crystal is controlled by the dissolution rate of the kieserite crystal, the growth rate of the hexahydrate crystal and the diffusion rate of the ions from the surface of the kieserite crystal to the growing hexahydrate crystal. Though the actual solution concentration is not known, the upper limit of the crystallization pressure is given by the maximum concentration of $m_{\text{sat}} = 6 \text{ mol} \cdot \text{kg}^{-1}$. For hexahydrate at 25°C , this yields a crystallization pressure of $\Delta p_{\text{crys}} = 26 \text{ MPa}$ [3], a value also sufficient to damage nearly every building material.

There appears to be an apparent contradiction as the calculated pressures predict that the direct hydration of kieserite may be more efficient in generating stress, while the deformation measurements suggest that crystallization from solution is more efficient. It has to be considered in the case of the hydration pressure that the calculated pressure is a maximum pressure that can be generated, provided that the growing crystal is confined. However, considering the highly porous aggregates of kieserite crystals present in the pore space of the glass filters (Figure 2) it is questionable if the volume increase during the initial phase of the hydration is sufficient to confine the growing hexahydrate crystals. Though there is an increase in total volume by a factor of 2.46 for the kieserite–hexahydrate transition, the dead space present in the porous kieserite aggregates may compensate for much of the volume increase. This is particularly important at low RH where the hydration reaction is incomplete. Hence, it appears very likely that several of the growing crystals may not become confined during the initial stage of the hydration reaction at low RH . For the same reasons, it was suggested that the hydration of anhydrous sodium sulfate may be less damaging than the crystallization from solution [21]. In the case of the dissolution–recrystallization transition, the reaction is rapid and complete and the pore space is entirely filled with hexahydrate while still in contact with supersaturated solution films (cf. Figure 6). Therefore, the conditions for the generation of substantial stress due to crystallization pressure are fulfilled. Based on these considerations it is possible to define a critical volume fraction of a porous material that has to be filled with kieserite crystals in order that a growing hydrated crystal becomes confined and can build up pressure. In the case of the formation of hexahydrate, the critical volume fraction is 41%. In building materials or natural rocks such a high degree of pore space filling might evolve during rapid evaporation of a pore solution if there is a continuous supply with solution due to capillary transport. Under such conditions an anhydrous or lower hydrated salt accumulates

and a subsequent hydration reaction, particularly at high relative humidity, clearly is a relevant damage process.

Finally, it is important to note that also the hydration of hexahydrate may be an important cause of damage. In the present work this hydration was observed at 80% *RH* still below the deliquescence humidity of hexahydrate. In this case, Eq. (3) is appropriate to calculate the hydration pressure yielding an extremely high pressure of $\Delta p_{\text{hydr}} = 77 \text{ MPa}$ at 80% *RH*. It is the observed kinetic hindrance of the hexahydrate hydration at low *RH* which is the cause of the large supersaturation leading to such a remarkable hydration pressure. This calculation also shows that it is the supersaturation and not the volume expansion which is the driving force for the generation of stress during a hydration reaction.

5.5 CONCLUSIONS

The combined approach using in situ experimental techniques for the investigation of the hydration of $\text{MgSO}_4 \cdot \text{H}_2\text{O}$ proved to be very useful and led to consistent results. *RH*-XRD allows for the direct observation of the phase transformation within the pore space of the substrate. Cryo-fixation is a very useful technique for the artifact free visualization of morphological changes in the SEM. In particular it is possible to detect the formation of solutions. Finally, the deformations occurring as the result of crystal growth in confined spaces and the generation of stress can be reliably measured using ESPI.

The hydration of $\text{MgSO}_4 \cdot \text{H}_2\text{O}$ (kieserite) and the formation of $\text{MgSO}_4 \cdot 6\text{H}_2\text{O}$ (hexahydrate) is a true solid state reaction at humidities below the deliquescence humidity of kieserite (i.e. 60% *RH* at 25°C). This reaction, however, is kinetically hindered. Above the deliquescence humidity of kieserite the reaction proceeds via a two stage reaction pathway involving the dissolution of kieserite and the subsequent crystallization of hexahydrate from a highly supersaturated solution. While according to the phase diagram the hydration of hexahydrate and formation of $\text{MgSO}_4 \cdot 7\text{H}_2\text{O}$ (epsomite) is expected at humidities just above 51% at room temperature, it is not observed at humidities $\leq 75\%$. The hydration of kieserite in confined spaces generates substantial stresses resulting in considerable deformations of the glass filters that were used as porous substrate. The deformation measurements confirm that the deliquescence–recrystallization pathway is more efficient in generating stress. Theoretical considerations confirm that the stress generated during the hydration is sufficient to damage nearly

every building material. While the present study focused on the hydration of kieserite as a model system, other hydration reactions in the system $\text{MgSO}_4 + \text{H}_2\text{O}$ might be important in the weathering of building materials or natural rocks. As discussed before, kieserite is the only product obtained by thermal dehydration of hexahydrate at high temperature. Under typical ambient conditions however, a mixture of several hydrates including $\text{MgSO}_4 \cdot 4\text{H}_2\text{O}$, $\text{MgSO}_4 \cdot 3\text{H}_2\text{O}$, $\text{MgSO}_4 \cdot 5/4\text{H}_2\text{O}$ and kieserite is expected to occur in materials contaminated with magnesium sulfate. If exposed to an increasing relative humidity, each of these phases will be subject to hydration with hexahydrate as the most likely reaction product. The equilibrium humidities for the respective equilibria and the deliquescence humidities of the educt phases are not known with sufficient accuracy to predict the behavior of a mixture of lower hydrated magnesium sulfates. Nonetheless, it is concluded from the results of the present study that the generation of stress during the hydration reactions is very likely, in particular, if the deliquescence humidity of the respective educt phases is exceeded. In future research the conditions for the formation of metastable hydrates under ambient conditions and their hydration and deliquescence equilibria will be investigated in more detail.

Acknowledgement. The authors gratefully acknowledge financial support from the Deutsche Forschungsgemeinschaft (DFG).

5.6 REFERENCES

- [1] GOUDIE A., VILES H., Salt Weathering Hazards, John Wiley & Sons, Chichester, **1997**.
- [2] DOEHNE E., Natural Stone, Weathering Phenomena, conservation strategies and case studies, Geol. Soc. Spec. Publ. **2002**, 205, 51–64.
- [3] STEIGER M., Crystal Growth in porous materials. I: The crystallization pressure of large crystals, J. Crystal Growth **2005**, 282, 455–469.
- [4] WINKLER E. M., Stone in architecture: Properties, durability., 3rd ed., Springer-Verlag, Berlin **1994**.
- [5] ASTM C 88-90, Standard test method for soundness of aggregate by use of sodium sulfate or magnesium sulfate. Annu. Book ASTM Stand. **1997**, 4.2, 37–42.
- [6] GÜLKER G., EL JARAD A., HINSCH K. D., JULING H., LINNOW K., STEIGER M., BRÜGGERHOFF S., KIRCHNER D., Monitoring of deformations induced by crystal growth of salts in porous systems using microscopic speckle pattern interferometry, In: Proceedings of LACONA VI, Lasers in the Conservation of Artwork, Vienna, 21–26 September 2005, Springer-Verlag, Berlin (in press).

- [7] MORTENSEN H., Die "Salzsprengrung" und ihre Bedeutung für die regionalklimatische Gliederung der Wüsten, *Petermans Mitteilungen aus Justus Perthes geographischer Anstalt* **1933**, 79, 130–135.
- [8] STEIGER M., In: Brimblecombe P. (ed.), *Air Pollution Reviews – Vol. 2: The Effects of Air Pollution on the Built Environment*, Imperial College Press, London **2003**, 133–181.
- [9] ARCHER D. A., RARD J. A., Isopiestic investigation of the osmotic and activity coefficients of aqueous MgSO_4 and the solubility of $\text{MgSO}_4 \cdot 7\text{H}_2\text{O}(\text{cr})$ at 298.15 K: Thermodynamic properties of the $\text{MgSO}_4 + \text{H}_2\text{O}$ System to 440 K, *J. Chem. Eng. Data* **1998**, 43, 791–806.
- [10] SMITS A., RINSE J., LOUWE KOOYMANS L. H., Das System Wasser-Magnesiumsulfat, *Z. Phys. Chem.* **1928**, 135, 78–84.
- [11] ROBSON H. L., The system $\text{MgSO}_4 - \text{H}_2\text{O}$ from 68°C to 240°C, *J. Am. Chem. Soc.* **1927**, 49, 2772–2783.
- [12] SCHUMB W. C., The dissociation pressures of certain salt hydrates by the gas-current saturation method, *J. Am. Chem. Soc.* **1923**, 45, 342–354.
- [13] CARPENTER C. D., JETTE E. R., The vapor pressures of certain hydrated metal sulfates, *J. Am. Chem. Soc.* **1923**, 45, 578–590.
- [14] BONNELL D. G., BURRIDGE L. W., The dissociation pressures of some salt hydrates, *Trans. Faraday Soc.* **1935**, 31, 473–478.
- [15] CHOU I.-M., SEAL R. R., Evaporates, water, and life, part I. Determination of epsomite-hexahydrate equilibria by the humidity-buffer technique at 0.1 MPa with implications for phase equilibria in the system $\text{MgSO}_4 - \text{H}_2\text{O}$, *Astrobiol.* **2003**, 3, 619–630.
- [16] LANGENFELD M., JULING H., BLASCHKE R., Kryo-Untersuchungen zum Feuchtigkeits- und Salztransport in porösen Baustoffen, *Wiss. Z. Hochsch. Architektur Bauwesen Weimar* **1994**, 40, 23–26.
- [17] LINNOW K., ZEUNERT A., STEIGER M., Investigation of sodium sulfate phase transitions in a porous material using humidity- and temperature-controlled X-ray diffraction, *Anal. Chem.* **2006**, 78, 4683–4689.
- [18] SIROHI R.S., *Speckle Metrology*, Marcel Dekker, New York **1993**.
- [19] HINSCH K. D., GÜLKER G., Lasers in art conservation, *Phys. World* **2001**, 14, 37–42.
- [20] HUNTLEY J., SALDNER H., Temporal phase-unwrapping algorithm for automated interferogram analysis, *Appl. Opt.* **1993**, 32, 3047–3052.
- [21] DOEHNE E., In situ dynamics of sodium sulphate hydration and dehydration in stone pores: observations at high magnification using the environmental SEM, In: Zezza F., Ott H., Fascina V. (eds.), *The conservation of monuments in the Mediterranean Basin. Proceedings of the 3rd International Symposium, Venice* **1994**, 143–150.

Chapter 6

Analysis of calcium acetate efflorescences formed on ceramic tiles in a museum environment

Kirsten Linnow¹, Lieve Halsberghe², Michael Steiger¹

¹Institute of Inorganic and Applied Chemistry, University of Hamburg, Martin-Luther-King-Platz 6, D-20146 Hamburg

²Ceramic Conservator, 15 rue de Bivange, L-3395 Roeser

In: Journal of Cultural Heritage **2007**, 8, 44–52, ([DOI:10.1016/j.culher.2006.09.004](https://doi.org/10.1016/j.culher.2006.09.004)).

6.1 INTRODUCTION

Salt crystallization in porous building materials not only limits the durability of the world's architectural heritage but is also a major cause of damage in porous museum artifacts. Damage is caused by the growth of salt crystals in the porous structures of materials such as stone or ceramics. Acetate salts are frequently observed in efflorescences on calcareous objects in museum cabinets. Their formation is the result of the attack of acetic acid which is emitted by wood [1,2] and a number of other materials such as paints, resins or silicone-based sealants that are used for the construction of display cases [3]. The low air exchange rates in typical display cases and storage cabinets provide favourable conditions for the enrichment of volatile pollutants liberated by these materials. GRZYWACZ AND TENNENT [4] measured acetic acid concentrations in display and storage cabinets of several European museums and confirmed very high concentrations in wooden cabinets. They also observed high concentrations in very old cabinets, i.e. up to 120 years. Hence, acetic acid attack is not only the result of a high exposure in the past, but is an ongoing process leading to the continuous formation of acetate salts.

A number of different acetate salts were identified in efflorescences on museum objects. Pure calcium acetate was found on collections of egg-shells [5] and molluscs [6], a double salt, calcium acetate chloride pentahydrate, $\text{Ca}(\text{CH}_3\text{COO})\text{Cl} \cdot 5\text{H}_2\text{O}$ [7], was found on both calcareous stone [8] and on ceramics [9]. An acetate nitrate double salt that was first identified on a coral brooch [10] was later characterized as dicalcium triacetate nitrate dihydrate, $\text{Ca}_2(\text{CH}_3\text{COO})_3(\text{NO}_3) \cdot 2\text{H}_2\text{O}$ [11]. Finally, another widespread but initially unidentified efflorescence [12] was later characterized as the triple salt $\text{Ca}_3(\text{CH}_3\text{COO})_3\text{Cl}(\text{NO}_3)_2 \cdot 7\text{H}_2\text{O}$, which was named thecotrichite [13,14].

Recently, the phase diagram of the quaternary thecotrichite system $\text{Ca}^{2+}-\text{CH}_3\text{COO}^{-}-\text{Cl}^{-}-\text{NO}_3^{-}-\text{H}_2\text{O}$ was established to understand the formation of the various double and triple salts mentioned before [15]. A total of nine different solid phases can exist in stable equilibrium with saturated solutions at 298 K. Both, calcium chloride and calcium nitrate can exist in two different hydrated forms, hence, there are five different solids representing the pure salts, i.e. $\text{CaCl}_2 \cdot 6\text{H}_2\text{O}$, $\text{CaCl}_2 \cdot 4\text{H}_2\text{O}$, $\text{Ca}(\text{NO}_3)_2 \cdot 4\text{H}_2\text{O}$, $\text{Ca}(\text{NO}_3)_2 \cdot 3\text{H}_2\text{O}$, and $\text{Ca}(\text{CH}_3\text{COO})_2 \cdot \text{H}_2\text{O}$. In addition, there are three double and a triple salt that can crystallize from mixed solutions, i.e. $\text{Ca}_3(\text{CH}_3\text{COO})_3\text{Cl}(\text{NO}_3)_2 \cdot 7\text{H}_2\text{O}$, $\text{CaCl}(\text{NO}_3) \cdot 2\text{H}_2\text{O}$, $\text{Ca}(\text{CH}_3\text{COO})\text{Cl} \cdot 5\text{H}_2\text{O}$ and

$\text{Ca}_2(\text{CH}_3\text{COO})_3(\text{NO}_3) \cdot 2\text{H}_2\text{O}$. Which of these solids is formed depends on the mixture composition and the ambient conditions, i.e. temperature and relative humidity. Hence, in order to assess the damage potential in a contaminated material it is important to know concentration and composition of the salt mixture present in the pore space and the environmental conditions as well. In the case of museum artifacts, the analysis of salts is usually problematic as the normal procedures of sampling and analysis cause unacceptable damage to the objects. In such cases, the analysis of wash solutions that are obtained during a desalination measure is an appropriate means for the determination of the soluble salt contents of an object.

In the present paper we report results of an analytical study on Dutch tiles of glazed ceramics that are seriously damaged by acetate salt crystallization. In previous papers [16,17] preliminary results were provided and discussed in the context of the conservation of the tiles and other ceramic objects from the same museum. Here, we focus on the analytical characterization of the salt system present in selected tiles and the formation of acetate containing phases. The ionic composition of the salt mixture in the tiles was deduced from the analysis of wash solutions. Direct sampling and analysis revealed the composition and nature of the efflorescences. It is shown that the quantitative speciation of the ionic constituents in the efflorescences is possible using least squares analysis. Based on the available information on the phase equilibria in the system comprising of the main constituents chloride, nitrate, acetate, calcium and sodium, the crystallization pathways of the various solid phases are traced. In particular, it is shown that the formation of thecotrichite efflorescences can be understood with the help of the phase diagram. Finally, the possibilities of preventive conservation of salt contaminated ceramics in typical museum environments are discussed.

6.2 EXPERIMENTAL SECTION

6.2.1 Tiles and salt concentration reduction

In previous centuries glazed tiles, attached to damp walls of houses were often used to keep the humidity out. But as evaporation of the rising ground water did take place, through tiny cracks in the glaze, soluble salts, such as chlorides, nitrates and sulfates, accumulated in the tiles. In a previous study thecotrichite ($\text{Ca}_3(\text{CH}_3\text{COO})_3\text{Cl}(\text{NO}_3)_2 \cdot 7\text{H}_2\text{O}$) was identified along with halite (NaCl), calcite (CaCO_3) and quartz (SiO_2) in efflorescences on lead-glazed

ceramic tiles of the collection of the Stedelijke Musea in Kortrijk, Belgium in early 2001 [16]. End of 2001 further damage and efflorescences were noted on some 160 ceramic objects in the same museum. The present study is concerned with 72 tiles with biblical scenes executed in manganese on tin-glazed earthenware that are on display in a show-case on the same tile-panel. The tiles all measure $130 \times 130 \text{ mm}^2$ and are about 8 mm thick. The tiles of this group were badly damaged by salt crystallization as shown in Figure 1. The unglazed backsides of most tiles were covered with a thick layer of fluffy needles of salt, in which tiny bits of earthenware were hidden. Some tiles had a badly pitted backside, some large cracks evolved and much debris was found on the bottom of the shelves. To conserve the tiles it was necessary to reduce the concentration of the salt by washing the tiles in different baths of demineralized water. Five tiles from this group were selected to determine the salt content in the efflorescences and in the wash solutions.

6.2.2 Sampling

Efflorescences were collected by careful brushing and weighed. Sample sizes varied from 120 mg to 274 mg. Known weights of the efflorescences were dissolved in doubly distilled water and the solutions were filtered to remove insoluble particles consisting mainly of grains of ceramic material lifted off during the growth of the efflorescences.

After removal of the efflorescences, the tiles were washed in a bath of 2 L of demineralized water. The tiles remained in the bath for several days and the procedure was repeated six times. The efficiency of the salt concentration reduction was monitored by measurements of the conductivity of the wash solutions at regular intervals. To accelerate the diffusion process, the water was changed every 24 h during the first two days (bath 1 and bath 2, respectively). Subsequently, the water bath was changed if the increase in conductivity indicated a significant slow-down of the salt mobilization. The extraction times for baths 3, 4, 5 and 6 were 9, 25, 12 and 21 days respectively. About 20 mL of all wash solutions were stored in a refrigerator in HDPE bottles until they were used for the final measurement of the conductivity at constant temperature and the determination of the ion concentrations.



Figure 1: Dutch tin glazed tiles (18th century) in the display case: efflorescences and damage.

6.2.3 Instrumentation

Conductivity in the baths was measured by a multi-parameter instrument and conductivity cell (pH/Cond 340i and TetraCon 325, WTW, Weilheim, Germany). All conductivities were measured at 19°C. XRD parameters were obtained on a Bragg-Brentano parafocusing reflection diffractometer (D 5000, Siemens, Germany) using Cu K α -radiation and a position-sensitive detector (PSD) recording data from a 12° 2θ band at one time. The scan was from 10° 2θ to 70° 2θ stepping at 0.02° every 20 sec. Cations in the aqueous solutions were determined by atomic spectrometry (AAS 5000 and AAS 300 Perkin Elmer, Überlingen, Germany). Sodium and potassium were analyzed by flame emission spectrometry, while atomic absorption was used for the determination of calcium and magnesium. Isocratic ion chromatography was used to determine the concentrations of acetate, chloride, nitrate and sulfate in the aqueous solutions. The chromatographic system consisted of an isocratic pump

P 1000, an automated sampler Spectra Series AS 100 (Thermo Separation Products, San Jose, CA, USA) and an ion chromatograph 2000i with conductivity detector CDM-I (Dionex, Sunnyvale, CA, USA). An ASRS-Ultra suppressor with SRS controller (Dionex) in the autosuppression recycle mode was employed for electrochemical suppression. Separation of the anions was achieved using a guard column AG 14 and a separation column AS 14 using a $9.5 \text{ mmol}\cdot\text{L}^{-1} \text{ Na}_2\text{CO}_3 / 1 \text{ mmol}\cdot\text{L}^{-1} \text{ NaHCO}_3$ eluent at a flow rate of $1.2 \text{ mL}\cdot\text{min}^{-1}$.

6.3 RESULTS

6.3.1 Efflorescences

Thecotrichite, halite, calcite and quartz were found in each of the efflorescence samples by XRD. As an example, a diffraction pattern is depicted in Figure 2. Halite, calcite and quartz were identified by the JCPDS (Joint committee on diffraction pattern) standards 5-0628, 5-0586 and 33-1161, respectively. Due to missing JCPDS standard and structural data, thecotrichite was identified by comparison with the diffraction pattern of a sample of synthetic thecotrichite which was prepared by precipitation and careful separation from a solution of appropriate composition upon evaporation. The XRD pattern of synthetic thecotrichite agrees nicely with the diffraction pattern reported by Gibson et al. [13] obtained from efflorescences on an Egyptian limestone relief.

The analysis of the content of the soluble cations and anions in the efflorescences revealed that the total amount of the soluble ions accounts for 30–47% of the total mass of the samples. The remaining fraction largely consists of ceramic particles trapped between the growing salt crystals. The disaggregation of these ceramic particles is the result of crystal growth in the pore space close to the surface of the tiles. The results are listed in Table 1 where the content of each ion i is given as charge equivalent content e_i according to

$$e_i = w_i |z_i| / M_i \quad (1)$$

where e_i is given in units of $\text{meq}\cdot\text{g}^{-1}$, w_i is the content of an ion of charge z_i in the efflorescence samples (in $\text{mg}\cdot\text{g}^{-1}$) and M_i is the molar mass of the ion. The main components of the soluble fraction are calcium, sodium, acetate, chloride and nitrate. The contribution of the minor constituents magnesium, potassium and sulfate is less than 3% of the total amount

of soluble salts in all samples. The total equivalent content of positive and negative charges in the efflorescence (in $\text{meq}\cdot\text{g}^{-1}$) is then given as

$$E_c = \sum_c e_c \text{ and } E_a = \sum_a e_a \quad (2)$$

where the subscripts c and a refer to cations and anions, respectively. The charge imbalance B_z may then be expressed as [14]

$$B_z = 2(E_c - E_a)/(E_c + E_a) \quad (3)$$

Values of E_c , E_a and B_z are also listed in Table 1. The imbalance does not reveal any significant deviation on either side suggesting that the charge imbalance was due to random measurement error and not due to omission of an ion.

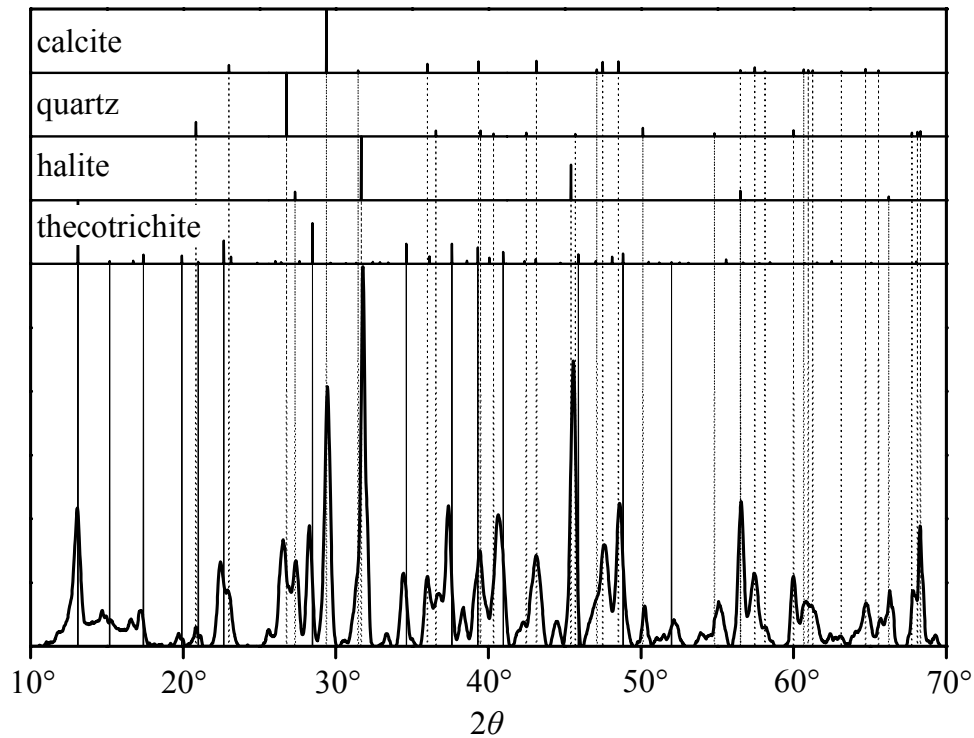


Figure 2: Diffraction pattern of the efflorescences collected from tile 5 and comparison with JCPDS standards 5-0586 (calcite), 33-1161 (quartz) and 5-0628 (halite) and the pattern of synthetic thecotrichite.

Table 1: Content e_i of soluble ions (units are $\text{meq}\cdot\text{g}^{-1}$), total charge equivalent concentrations E_c and E_a (units are $\text{meq}\cdot\text{g}^{-1}$) and charge imbalances B_z in efflorescence samples collected from five tiles.

	1	2	3	4	5
acetate	2.38	1.93	1.52	2.76	2.74
chloride	1.66	1.44	1.53	1.43	2.11
nitrate	1.79	1.33	1.10	2.03	1.62
sulfate	0.22	<0.10	< 0.10	0.13	< 0.10
calcium	5.06	3.71	3.24	5.56	4.51
sodium	0.82	1.10	0.80	0.54	1.57
potassium	0.06	0.03	0.04	0.05	0.04
magnesium	0.06	< 0.06	< 0.06	< 0.06	< 0.06
E_c	5.99	4.83	4.07	6.15	6.12
E_a	6.05	4.69	4.15	6.35	6.47
B_z	-0.01	0.03	-0.02	-0.03	-0.06

6.3.2 Wash solutions

The analysis of the wash solutions revealed high concentrations of soluble salts during the initial phase of the desalination. The concentrations continuously decreased with every change of the bath. In all cases, the extraction of the soluble salts was practically complete after about three to four washings. For example, less than 2% of the total amount of soluble salts is found in wash solutions 5 and 6. A typical result is depicted in Figure 3. Using expressions analogous to Equations 1–3, equivalent concentrations and charge imbalances were calculated for each solution.

In this case, w_i refers to the mass concentration of the ions in the wash solutions (in $\text{mg}\cdot\text{L}^{-1}$) yielding the charge equivalent concentrations e_i in $\text{meq}\cdot\text{L}^{-1}$ according to Equation (1). Then, E_c and E_a (in $\text{meq}\cdot\text{L}^{-1}$) are the molar concentrations of positive or negative charges. In contrast to the efflorescence samples, the values of B_z reveal significant anion deficiencies in several wash solutions indicating the omission of an anion with significant contribution to the total anion concentration (Figure 4).

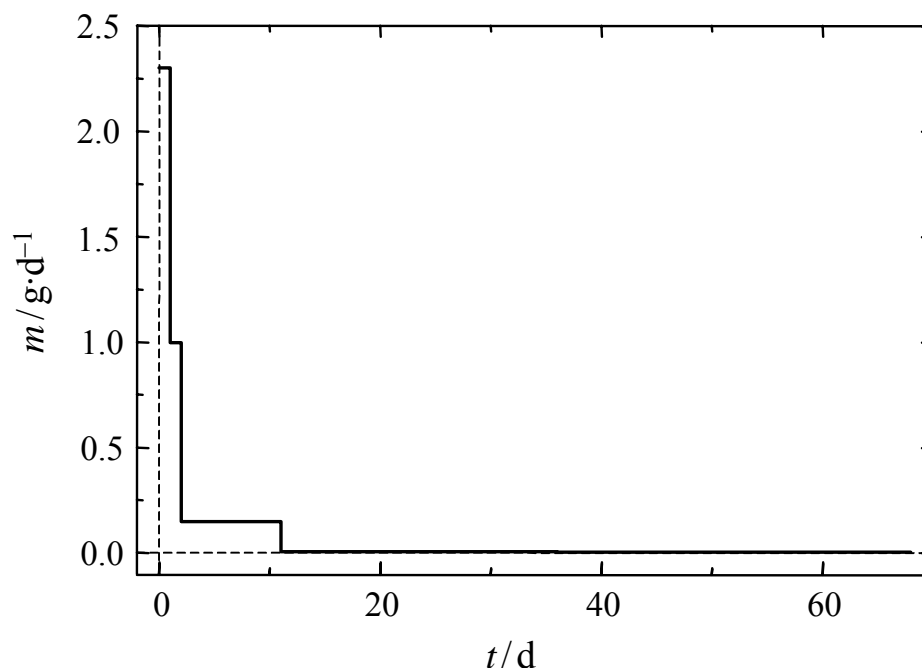


Figure 3: Rate of total salt removal m from tile 1 versus time t in 6 subsequent washings.

Most likely, the missing anion is bicarbonate (HCO_3^-) as all tiles contain calcite. Due to the limited solubility of calcite we expect a small but approximately constant concentration of bicarbonate in the wash solutions. The anion deficit is much less severe in the most concentrated wash solutions, i.e. solutions 1–3. In contrast, the total cation charges are approaching a constant value of about $0.5\text{--}1\text{ meq}\cdot\text{L}^{-1}$ with decreasing concentrations of acetate, chloride, nitrate and sulfate. Hence, there appears to be a constant anion deficiency of $0.5\text{--}1\text{ meq}\cdot\text{L}^{-1}$. The solubility of calcite in pure water at room temperature and under atmospheric pressure is $0.55\text{ mmol}\cdot\text{L}^{-1}$ corresponding to a charge equivalent calcium concentration of $1.1\text{ meq}\cdot\text{L}^{-1}$.

Therefore, it is very likely that the missing anion is bicarbonate resulting from the partial dissolution of calcite. An enhanced solubility of calcite is expected with increasing concentration of other salts which might cause a slightly higher contribution of bicarbonate in the more concentrated wash solutions. Another possible source for an anion deficiency, particularly in the more concentrated wash solutions, might be seen in the fact that acetate could not be determined in the present study due to its relatively high limits of quantitation (LOQ) in the wash solutions (LOQ = $0.5\text{ meq}\cdot\text{L}^{-1}$ in solutions 1 and 2, and LOQ = $0.05\text{ meq}\cdot\text{L}^{-1}$ in solutions 3–6). The capacity and selectivity of the IC column in

combination with high chloride and small acetate concentrations leads to the unfavourable LOQ values for acetate. Considering the composition of the efflorescences, it is somewhat surprising that acetate was not detected. Hence, additional attempts to detect acetate qualitatively were carried out. The dry residues of the first wash solution of each tile were put on paper-strips that were impregnated with a $0.5 \text{ mol}\cdot\text{L}^{-1}$ FeCl_3 solution. Red coloration of the yellow paper-strips indicated the presence of acetates due to the formation of a basic iron acetate $[\text{Fe}_3(\text{O})(\text{OAc})_6(\text{H}_2\text{O})_3]^+$ [18]. Hence, there might also be a minor contribution to the anion deficiency resulting from the missing acetate values. However, considering the LOQ values in the more dilute solutions, i.e. wash solutions 5 and 6, cf. Figure 4, the contribution of acetate does not exceed $0.05 \text{ meq}\cdot\text{L}^{-1}$ which is negligible.

The results of the conductivity measurements are shown in Figure 5. As could be expected the conductivities agree nicely with the total equivalent concentrations, $E_t = E_c + E_a$, of the wash solutions ($r = 0.9994$). Hence, conductivity measurement is an appropriate and simple method to control the efficiency of a desalination measure in the conservation lab as long as there is no substantial change in the composition of the wash solutions. This is not generally the case however, as depending on the particular material investigated and the composition of the salt mixture conductivity measurements might be severely affected by pH changes.

Calcium, sodium, chloride and nitrate were found to be the main ionic constituents in the wash solutions, the contribution of the minor ions potassium, magnesium and sulfate is slightly greater than in the efflorescences but does not exceed 10% of the total ion concentrations. For the purpose of the present study, we are largely interested in the total amount of soluble salts in the tiles. Hence, Table 2 lists the total charge equivalents of the respective ions released from the tiles during the six subsequent washings. The major anions chloride and nitrate account for 97.7–99.6% of the total equivalents of negative charge in the wash solutions. On the cation side, calcium and sodium account for 84.0–88.1% of the total positive charge. For comparison, the total charge equivalents in the efflorescences are also shown in Table 2. With the exception of acetate only a very small fraction (0.6–1.6% by mass) of the soluble salts is found in the efflorescences, i.e., most ions are predominantly present in the interior pore space of the tiles. In contrast, acetate is mainly found in the efflorescences, though there remains some uncertainty concerning the concentrations in the wash solutions as discussed before.

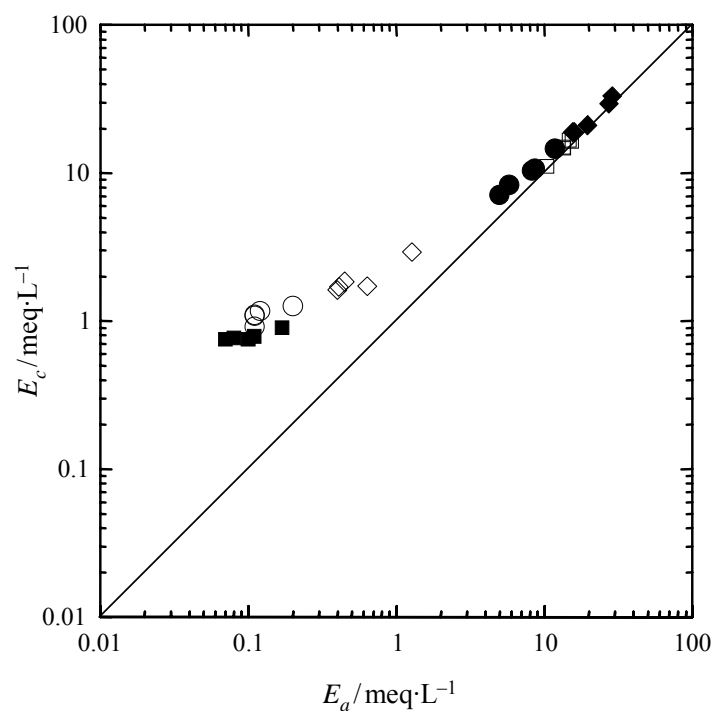


Figure 4: Ion balances in wash solutions 1–5, the line represents the ideal case of balanced cation and anion charges, the meaning of the symbols is: (◆) solution 1, (□) solution 2, (●) solution 3, (◇) solution 4, (■) solution 5, and (○) solution 6.

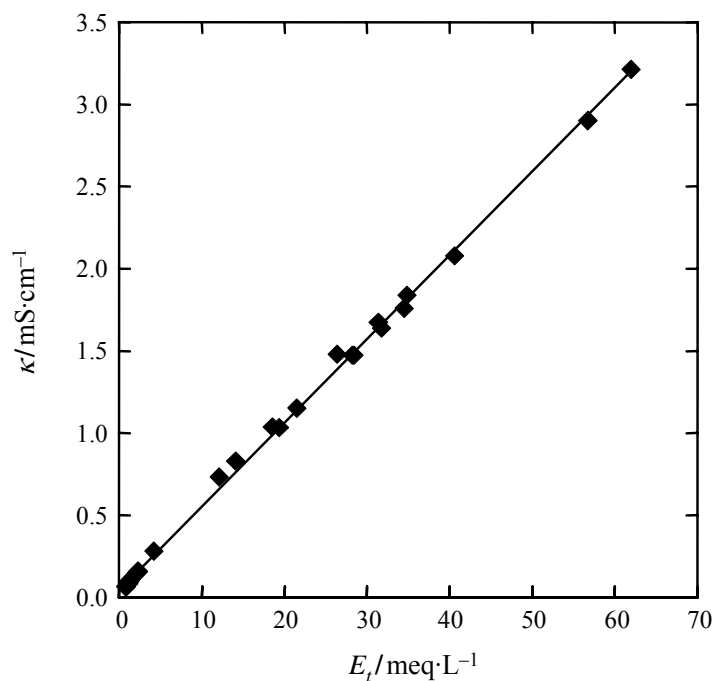


Figure 5: Comparison of conductivities κ and total salt concentrations E_t in the wash solutions.

Table 2: Total amounts in wash solutions and efflorescences (units are meq)

tile	acetate	chloride	nitrate	sulfate	sodium	potassium	magnesium	calcium
<i>wash solutions:</i>								
1	< 2.4	37.3	38.1	1.43	22.4	7.07	7.13	60.1
2	< 2.4	42.4	35.8	1.13	24.0	6.45	5.35	63.8
3	< 2.4	43.1	43.7	1.24	23.4	8.65	5.57	64.7
4	< 2.4	46.1	47.8	1.58	26.3	10.7	7.26	68.8
5	< 2.4	48.8	46.3	2.35	27.4	10.9	7.09	74.0
<i>efflorescences:</i>								
1	0.285	0.200	0.215	0.027	0.098	0.007	0.006	0.608
2	0.254	0.189	0.175	< 0.002	0.145	0.004	0.003	0.489
3	0.218	0.218	0.158	< 0.004	0.114	0.006	0.004	0.463
4	0.617	0.319	0.454	0.029	0.119	0.011	0.007	1.243
5	0.751	0.577	0.444	< 0.007	0.429	0.012	0.007	1.235

6.4 DISCUSSION

To understand the formation of acetate salts on salt contaminated objects the phase diagram of the salt system of the main components is an appropriate means that allows tracing the crystallization pathway of the salts in the tiles. Neglecting the minor contributions of sulfate, potassium and magnesium (cf. Table 2), a salt mixture consisting of the ions acetate, chloride, nitrate, sodium and calcium is obtained. The phase diagram of the system $\text{Na}^+ - \text{Ca}^{2+} - \text{CH}_3\text{COO}^- - \text{Cl}^- - \text{NO}_3^- - \text{H}_2\text{O}$, consisting of three anions and two cations, is a five component system and can be constructed in the form of a prism as shown in Figure 6. All mixture compositions are expressed in terms of the charge equivalent fractions of the anions ($f_a = e_a/E_a$) and cations ($f_c = e_c/E_c$), respectively. The anion equivalent fractions are represented in triangular diagrams and the two base triangles of the prism in Figure 6 represent the two quaternary subsystems with $f_{\text{Na}} = 1$ and $f_{\text{Ca}} = 1$, respectively. If both cations are present, the position of the triangle in the interior of the prism is given by the cation equivalent fraction as shown for the wash solutions in Figure 6. In the wash solutions, nearly constant cation charge fractions of $f_{\text{Ca}} = 0.729 \pm 0.004$ and $f_{\text{Na}} = 0.271 \pm 0.004$ were found. In the efflorescences the cation charge fractions are more scattered yielding $f_{\text{Ca}} = 0.82 \pm 0.06$ and $f_{\text{Na}} = 0.18 \pm 0.06$.

For clearness, a two-dimensional projection can be used to investigate the crystallization pathways of thecotrichite. Figure 7 depicts the anion mole fractions as projections on the quaternary phase diagram of the thecotrichite system $\text{Ca}^{2+}\text{--CH}_3\text{COO}^-\text{--Cl}^-\text{--NO}_3^-\text{--H}_2\text{O}$ ($f_{\text{Ca}} = 1$). The composition of the wash solutions and the efflorescences are represented by squares and triangles, respectively.

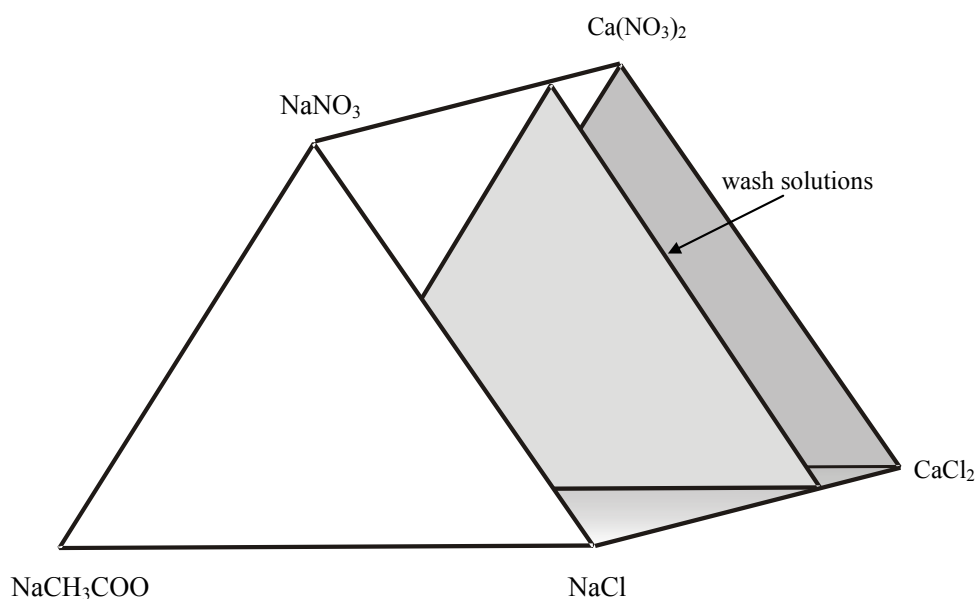


Figure 6: Representation of the quinary system $\text{Na}^+\text{--Ca}^{2+}\text{--CH}_3\text{COO}^-\text{--Cl}^-\text{--NO}_3^-\text{--H}_2\text{O}$.

The composition of pure thecotrichite is given by point T. Drawing a straight line from point T to the chloride corner of the projection in Figure 7 reveals that the efflorescences are enriched in chloride compared to the composition of pure thecotrichite. Since there is a significant contribution of sodium also in the efflorescences and considering the extreme hygroscopicity of calcium chlorides, i.e. $\text{CaCl}_2 \cdot 6\text{H}_2\text{O}$ and $\text{CaCl}_2 \cdot 4\text{H}_2\text{O}$, it is very unlikely that chloride is present in the form of a calcium salt. Hence, in accordance with the XRD results, it is concluded that thecotrichite and halite are the major constituents of the water soluble fraction of the efflorescences. A quantitative speciation of the constituents in the efflorescences from the XRD measurements was impossible. However, using a simple mass balance approach, the concentration c_i of each ion i in the efflorescences (in $\text{mmol} \cdot \text{g}^{-1}$) can be

expressed in terms of the concentrations a_s of the different solid phases s present in the efflorescences and containing the ions of interest. In the present study there are only two solid phases, thecotrichite and halite, which account for the concentrations of the five ions in the efflorescences. Therefore, the mass balance takes the form

$$c_i = a_{th}V_{i,th} + a_{ha}V_{i,ha} \quad (4)$$

where a_{th} and a_{ha} represent the content of thecotrichite and halite in the efflorescences (in $\text{mmol}\cdot\text{g}^{-1}$) and $v_{i,th}$ and $v_{i,ha}$ are the stoichiometric numbers of the ions i in the formula of the solid phases thecotrichite and halite. In the case of five ions, this yields five equations in the two unknowns a_{th} and a_{ha} which can be determined by ordinary least squares analysis. Results are listed in Table 3.

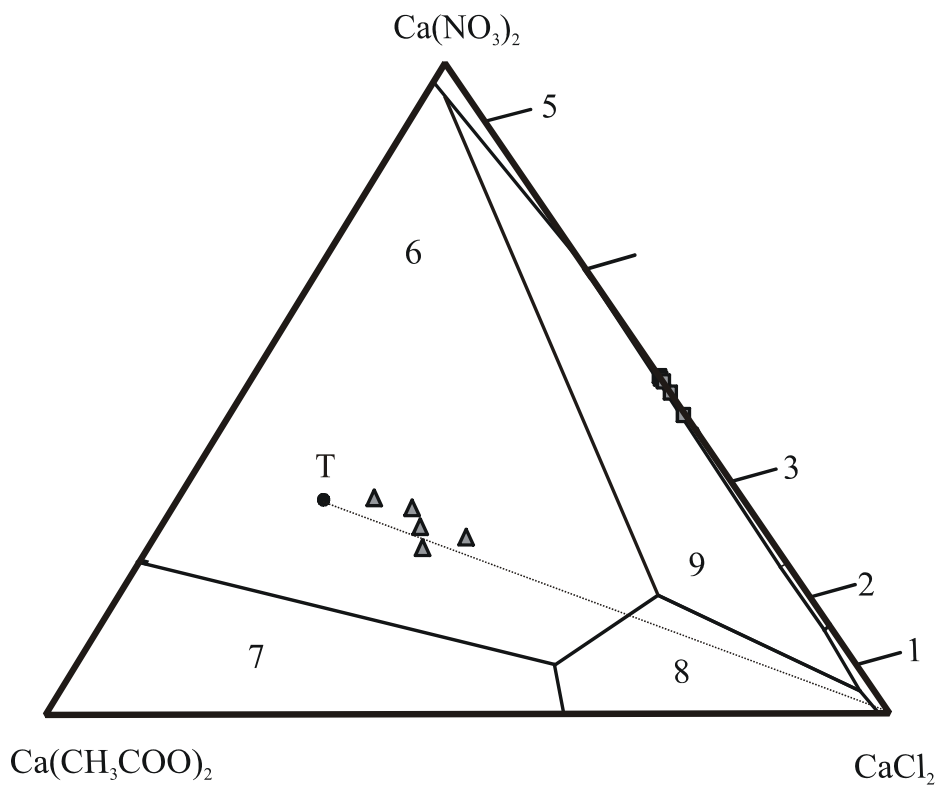


Figure 7: Projection of the composition of efflorescences (triangles) and wash solutions (squares) to the phase diagram of the quaternary system $\text{Ca}^{2+}\text{--CH}_3\text{COO}^-\text{--Cl}^-\text{--NO}_3^-\text{--H}_2\text{O}$ at 25°C [15]; point T represents the stoichiometric composition of thecotrichite, numbers refer to the following stability fields: (1) $\text{CaCl}_2 \cdot 6\text{H}_2\text{O}$, (2) $\text{CaCl}_2 \cdot 4\text{H}_2\text{O}$, (3) $\text{CaCl}(\text{NO}_3) \cdot 2\text{H}_2\text{O}$, (4) $\text{Ca}(\text{NO}_3)_2 \cdot 3\text{H}_2\text{O}$, (5) $\text{Ca}(\text{NO}_3)_2 \cdot 4\text{H}_2\text{O}$, (6) $\text{Ca}_2(\text{CH}_3\text{COO})_3(\text{NO}_3) \cdot 2\text{H}_2\text{O}$, (7) $\text{Ca}(\text{CH}_3\text{COO})_2 \cdot \text{H}_2\text{O}$, (8) $\text{Ca}(\text{CH}_3\text{COO})\text{Cl} \cdot 5\text{H}_2\text{O}$, (9) $\text{Ca}_3(\text{CH}_3\text{COO})_3\text{Cl}(\text{NO}_3)_2 \cdot 7\text{H}_2\text{O}$.

Table 3: Content of thecotrichite (a_{th}) and halite (a_{ha}) in efflorescences as calculated by least squares analysis.

tile	$a_{th}/\text{mmol}\cdot\text{g}^{-1}$	$a_{ha}/\text{mmol}\cdot\text{g}^{-1}$
1	0.83 ± 0.02	0.83 ± 0.07
2	0.63 ± 0.03	0.95 ± 0.09
3	0.53 ± 0.02	0.89 ± 0.07
4	0.94 ± 0.02	0.51 ± 0.07
5	0.82 ± 0.05	1.43 ± 0.17

Using these values of a_{th} and a_{ha} , the concentrations of the individual ions in the efflorescences from the five tiles may be calculated and compared with the experimental concentrations. Such a comparison is depicted in Figure 8. There is very good agreement between the calculated and the measured ion concentrations. Only in two cases (out of 25) the deviation between calculated and measured concentration exceeds 10%. Hence, the calculated concentrations of thecotrichite and halite in the efflorescences are quite confidential. The combination of phase identification by XRD, quantitative determination of ion concentrations and additional information from the phase diagram of the mixture yields quantitative information on the composition of the efflorescence samples as summarized in Table 4. According to the mass balance calculations thecotrichite and halite account for 37–55% and 3.0–8.3% by mass of the efflorescences, respectively. The remaining fraction consists of insoluble debris from the tiles, mainly quartz, calcite and eventually other mineral constituents of the ceramics. It should be noted that the crystallization of thecotrichite and halite in the pore space close to the surface of the tiles causes a substantial loss of material. Considering that only a very small fraction (<1%, cf. Table 2) of the total chloride and nitrate in the tiles is found in the efflorescences, the equivalent fractions of these ions in the wash solutions are regarded as representative for the composition of the salt mixtures that were originally present in the tiles before they were exposed to an acetic acid environment.

Table 4: Composition (mass fraction) of efflorescences

tile	1	2	3	4	5
thecotrichite	0.485	0.367	0.311	0.547	0.479
halite	0.048	0.056	0.052	0.030	0.083
sum	0.533	0.423	0.363	0.577	0.563

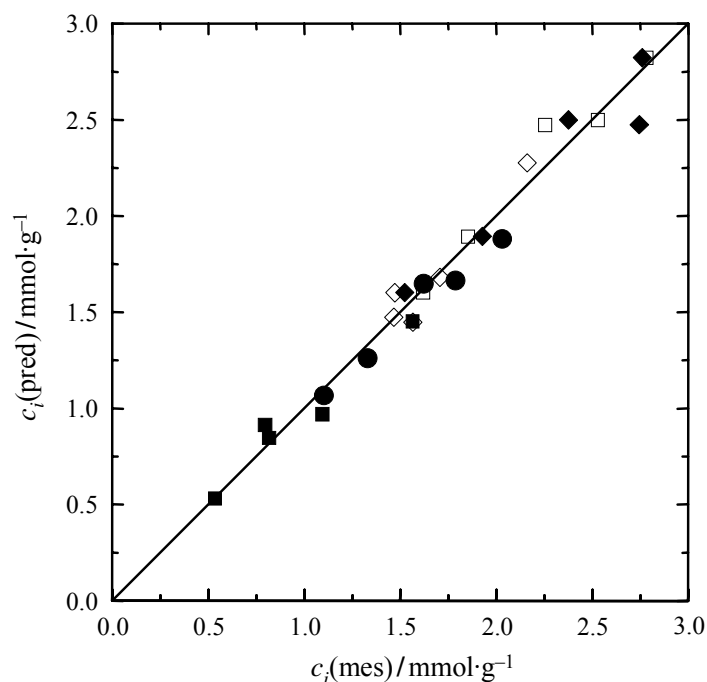


Figure 8: Calculated, $c_i(\text{pred})$, and measured, $c_i(\text{mes})$, contents in efflorescences; meaning of symbols is: (\diamond) chloride, (\bullet) nitrate, (\blacklozenge) acetate, (\blacksquare) sodium, and (\square) calcium.

The compositions of the five solutions represented by the squares in Figure 7 are located in the stability field (3) of $\text{CaCl}(\text{NO}_3) \cdot 2\text{H}_2\text{O}$. Such mixtures are extremely hygroscopic and the crystallization of the double salt $\text{CaCl}(\text{NO}_3) \cdot 2\text{H}_2\text{O}$ would occur only at relative humidities below 20%. However, as the acetate concentration increases as a result of acetic acid deposition and dissolution of calcite, the composition of the solution in the pore space close to the surface moves along the line connecting point A and the corner representing pure $\text{Ca}(\text{CH}_3\text{COO})_2$ as depicted in Figure 9. The solution composition moves into the stability field of thecotrichite ($\text{Ca}_3(\text{CH}_3\text{COO})_3\text{Cl}(\text{NO}_3)_2 \cdot 7\text{H}_2\text{O}$). Due to its much lower solubility thecotrichite may eventually precipitate in the pore space close to the surface as the solution becomes supersaturated. The exact composition of the saturated solution depends on the mixing ratio of chloride and nitrate and the concentration of the ions, i.e. the water content. For a porous material in a museum case, the latter is largely determined by the ambient relative humidity. Assuming that the solution is reaching saturation with respect to thecotrichite at point B (see Figure 9), any further deposition of acetic acid causes the precipitation of thecotrichite.

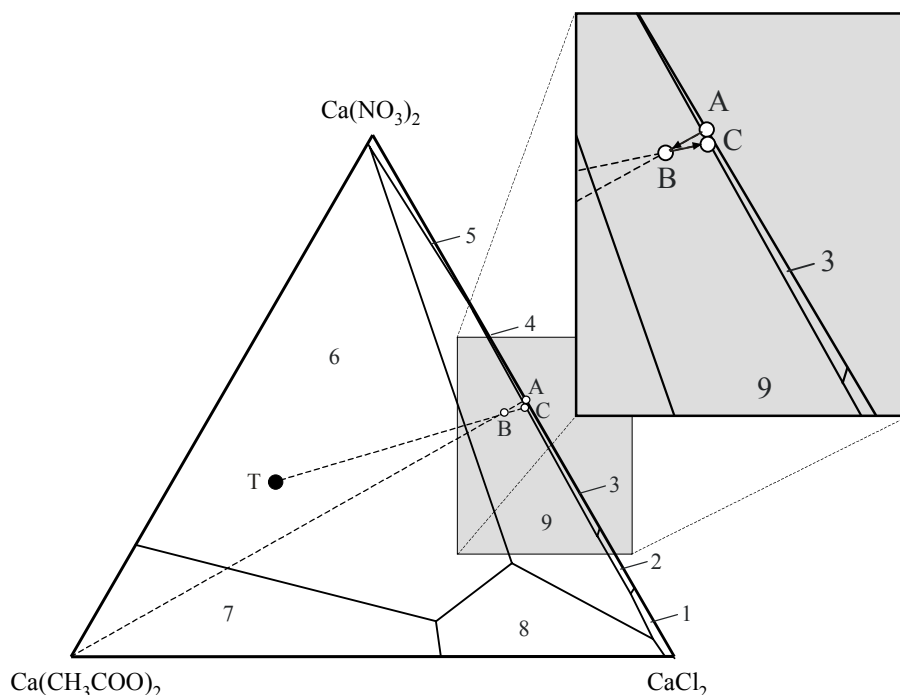


Figure 9: Schematic representation of acetate deposition and thecotrichite precipitation in the thecotrichite phase diagram; point T represents the stoichiometric composition of thecotrichite; point A represents the average composition of the salt mixture in the tiles; see text for explanation of points B and C, respectively; numbers refer to the stability fields as in Figure 6.

The dynamics of the solution composition is then controlled by two processes proceeding at the same time. Upon precipitation of thecotrichite, the composition moves along line T–B–C in the direction of the stability field of $\text{CaCl}(\text{NO}_3) \cdot 2\text{H}_2\text{O}$. Upon further deposition of acetate, the composition of the solution moves along line A–B into the direction of the calcium acetate corner of the diagram. In effect, there will only be a minor change in the solution composition due to the fact that removal of thecotrichite will cause a depletion of nitrate in respect to chloride. However, it is very likely that diffusion from the interior of the tiles might compensate for the nitrate depletion close to the surface. Hence, the deposition of acetic acid will continuously cause the crystallization of thecotrichite in the pore space close to the surface. Considering the excess of calcium nitrate and calcium chloride solution in the interior of the tiles (cf. Table 2), there is no doubt that there is sufficient supply with these ions. Hence, the damage process will continue as long as there is acetic acid available.

The first measure to prevent the tiles from further deterioration must be a considerable reduction in the acetic acid concentration in the display case by replacement of all products releasing acetic acid or by application of appropriate protective layers on the surfaces of such

materials. However, even if acetic acid attack is stopped, there remains the risk to salt contaminated objects of deterioration by salt crystallization. Chlorides, nitrates and sulfates are commonly present in the pore space of ceramics [19] and stone objects [20]. Depending on the hygroscopicity of a salt mixture at a given temperature and relative humidity (*RH*) in a display case, salts may be either present as crystalline solids or as salt solutions. Unfavorable climatic conditions may cause damage to the objects as a result of repeated cycles of dissolution and crystallization of a salt in the pore space. The ions found in the present study as the main constituents of the salt mixture in the tiles, i.e. sodium, calcium, chloride and nitrate, are also often found in ancient monuments [21]. Due to the presence of calcium nitrate and calcium chloride this salt mixture is particularly hygroscopic and, as mentioned before, the crystallization of the calcium salts is expected only at very low humidities. However, depending on the composition of the mixture, the sodium salts, NaCl and NaNO₃, may be subject to cycles of crystallization/dissolution in the range of 30–70% *RH*. For the composition of the salt mixture found in the tiles, i.e. $f_{\text{Na}} = 0.3$, $f_{\text{Ca}} = 0.7$ and $f_{\text{Cl}} = f_{\text{NO}_3} = 0.5$, a critical value of 60% *RH* below which the crystallization of halite starts can be calculated using a thermodynamic model [22]. Hence, *RH* fluctuations in the critical range 30–60% *RH* should be avoided to reduce the risk of salt damage. In case that stable climatic conditions cannot be guaranteed, a desalination of the contaminated tiles may be necessary to avoid further damage. The desalination may be carried out in water baths as described before and the progress of the desalination may be controlled by measurement of the conductivity in the baths. It is important to note however, that desalination as an interventive measure might also be the cause of further damage due to mechanical stress and loss of cohesion in the water bath. Hence, the decision whether desalination is necessary and appropriate requires an assessment of both risks, damage due to repeated cycles of dissolution and crystallization, and damage due to the desalination measure itself. The final decision lies in the responsibility of the conservator and will largely depend on the particular situation at the object under consideration.

6.5 CONCLUSIONS

The evaluation of the damage potential in salt contaminated porous objects requires the analysis of both the salts present in visible efflorescences and the salt load within the pore space of the material. The exclusive analysis of the efflorescences is clearly not sufficient and

may lead to misinterpretations. In fact, in the present study it was found that the efflorescences account for only about 1% of the total salt mass present in the tiles. Combination of qualitative XRD analysis of the phases present in the efflorescences together with a quantitative determination of the ionic composition is sufficient for the quantitative analysis of major crystalline species in the efflorescences. The concentration of the solid phases, thecotrichite and halite, which were found in the present study, is obtained from a solution of the mass balance by least squares analysis. The composition of the efflorescences does not reflect the composition of the salt mixture in the tiles. However, considering that the tiles are contaminated with a mixture of calcium chloride and calcium nitrate, the formation of thecotrichite as a result of acetic acid vapor attack is consistent with the phase diagram of the $\text{Na}^+ - \text{Ca}^{2+} - \text{CH}_3\text{COO}^- - \text{Cl}^- - \text{NO}_3^- - \text{H}_2\text{O}$ system. Due to the large reservoir of the hygroscopic salt mixture in the tiles the main damage process of thecotrichite formation will continue as long as the tiles are exposed to an acetic acid environment. If the salt mixture in the tiles contains both chloride and nitrate, thecotrichite will be always the major reaction product. In the case of a contamination with a large excess of either chloride or nitrate, the deposition of acetic acid may also lead to the formation of other acetate containing compounds, e.g. $\text{Ca}(\text{CH}_3\text{COO})\text{Cl} \cdot 5\text{H}_2\text{O}$ or $\text{Ca}_2(\text{CH}_3\text{COO})_3(\text{NO}_3) \cdot 2\text{H}_2\text{O}$. In all cases, acetic acid deposition leads to crystal growth in the pore space close to the surface of the object resulting in severe damage. Hence, the most important step in the conservation of such objects is the elimination of acetic acid emissions in show and storage cases by coating or replacement of materials, e.g. wood, that release acetic acid vapor. Such a preventive conservation measure is indispensable in order to avoid continuous crystallization of acetate containing phases in the future. However, even if there is no further input of acetic acid, the salt mixture already present in an object may still cause damage if the object is subjected to unfavourable climatic conditions, i.e. fluctuations across critical values of temperature and relative humidity that might induce salt crystallization. For a given composition of the salt mixture present in an object, the risk of crystallization-dissolution cycles may be assessed for different climatic conditions and appropriate preventive or interventive conservation measures may be selected by the conservator.

6.6 REFERENCES

- [1] ARNI P.C., COCHRANE G.C., GRAY J.D., The emission of corrosive vapours by wood. I. Survey of the acid-release properties of certain freshly felled hardwoods and softwoods, *J. of Appl. Chem.* **1965**, 15, 305–313.
- [2] ARNI P.C., COCHRANE G.C., GRAY J.D., The emission of corrosive vapours by wood. II. The analysis of the vapours emitted by certain freshly felled hardwoods and softwoods by gas chromatography and spectrophotometry, *J. Appl. Chem.* **1965**, 15, 463–468.
- [3] TETREAULT J., La mesure de l'acidité des produits volatils, *J. Internat. Inst. Conserv.–Can. Group* **1992**, 17, 17–25.
- [4] GRZYWACZ C.M., TENNENT N.H., Pollution monitoring in storage and display cabinets: Carbonyl pollutant levels in relation to artifact deterioration, In: Roy A., Smith P (eds.) *Preventive conservation: practice, theory and research*, The International Institute for Conservation, London, **1994**, 164–172.
- [5] AGNEW N., The corrosion of egg shells by acetic acid vapour, *ICCM Bulletin* **1981**, 7, 3–9.
- [6] TENNENT N.H., BAIRD T., The deterioration of mollusca collections: Identification of shell efflorescence, *Stud. Conserv.* **1985**, 30, 73–85.
- [7] VAN TASSEL R., On the crystallography of calclacite, $\text{Ca}(\text{CH}_3\text{COO})\text{Cl} \cdot 5\text{H}_2\text{O}$, *Acta Cryst.* **1958**, 11, 745–746.
- [8] VAN TASSEL R., Une efflorescence d'acétatochlorure de calcium sur des roches calcaires dans des collections, *Bull. Musée royal d'Histoire naturelle Belgique* **1945**, 21, 1–11.
- [9] WHEELER G.S., WYPYSKI M.T., An unusual efflorescence on Greek ceramics, *Stud. Conserv.* **1993**, 38, 55–62.
- [10] ERHARDT D., WESTLEY H., PADFIELD T., Coral brooch with white corrosion, Conservation Analytical Laboratory (CAL), Smithsonian Institution, Washington DC, Report No. 3528, **1981**.
- [11] COOKSEY B.G., GIBSON L.T., KENNEDY A.R., LITTLEJOHN D., STEWART L., TENNENT N.H., Dicalcium triacetate nitrate dihydrate, *Acta Cryst.* **1999**, C55, 324–326.
- [12] FITZHUGH E.W., GETTENS R.J., Calclacite and other efflorescent salts on objects stored in wooden museum cases, In: Brill R. (ed), *Science and Archaeology*, MIT Press, Cambridge **1971**, 91–102.
- [13] GIBSON L.T., COOKSEY B.G., LITTLEJOHN D., TENNENT N.H., Characterisation of an unusual crystalline efflorescence on an Egyptian limestone relief, *Anal. Chim. Acta* **1997**, 337, 151–164.
- [14] GIBSON L.T., COOKSEY B.G., LITTLEJOHN D., TENNENT N.H., Investigation of the composition of a unique efflorescence on calcareous museum artifacts, *Anal. Chim. Acta* **1997**, 337, 253–264.
- [15] GIBSON L.T., COOKSEY B.G., LITTLEJOHN D., LINNOW K., STEIGER M., TENNENT N.H., The mode of formation of thecotrichite, a widespread calcium acetate nitrate chloride efflorescence, *Stud. Conserv.* **2005**, 50, 284–294.

-
- [16] HALSBERGHE L., Ceramics threatened by acid-induced salts, In: Townsend J.H., Eremin K., Adriaens A. (eds.), *Conservation science 2002*, Archetype Publications, London **2003**, 18–24.
- [17] HALSBERGHE L., GIBSON L.T., ERHARDT D., A collection of ceramics damaged by acetate salts: conservation and investigation into the causes, In: Verger I. (ed) *ICOM–CC 14th Triennial Meeting Preprints*, James & James/Earthscan, London **2005**, 131–138.
- [18] VOGEL A.I., *Macro and semimicro qualitative inorganic analysis*, Longmans, London, **1962**.
- [19] COSTA PESSOA J.C., ANTUNES J.L.F., FIGUEIREDO M.O., FORTES M.A., Removal and analysis of soluble salts from ancient tiles, *Stud. Conserv.* **1996**, 41, 153–160.
- [20] NUNBERG S., HEYWOOD A., WHEELER G., Relative humidity control as an alternative approach to preserving an egyptian limestone relief, In: SFIIC (ed.), *Le dessalement des matériaux poreux*, Champs-sur-Marne **1996**, 127–135.
- [21] LARSEN P.K., Moisture measurement in Tirsted church, *J. Architect. Conserv.* **2004**, 10, 22–35.
- [22] STEIGER M., Salts in porous materials: Thermodynamics of phase transitions, modeling and preventive conservation. *Restorat. Build. Monum.* **2005**, 11, 419–431.

Chapter 7

Phase diagram of the quaternary system

$\text{Ca}(\text{CH}_3\text{COO})_2\text{--CaCl}_2\text{--Ca}(\text{NO}_3)_2\text{--H}_2\text{O}$ at 25°C

(to be published)

7.1 INTRODUCTION

It is widely accepted that salt crystallization is a major cause of damage of porous materials such as natural stone, brick, concrete and ceramics. Large parts of the world's architectural heritage and important artifacts in museums comprise of these materials. Various efflorescences, consisting of Ca^{2+} and CH_3COO^- in combination with NO_3^- and/or Cl^- , were found on museum objects stored in wooden show cases emitting acetic acid vapor [1,2]. The phase diagram of the quaternary system $\text{Ca}(\text{CH}_3\text{COO})_2\text{--CaCl}_2\text{--Ca}(\text{NO}_3)_2\text{--H}_2\text{O}$ was recently used by GIBSON et al. [3] and LINNOW et al. [4] to establish the mode of formation of these efflorescences, in particular of the triple salt $\text{Ca}_3(\text{CH}_3\text{COO})_3\text{Cl}(\text{NO}_3)_2 \cdot 7\text{H}_2\text{O}$, thecotrichite. The quaternary phase diagram based on three ternary systems, i.e. two salts and water, contains a total of nine different solid phases at 25°C. Apart from the single salts $\text{CaCl}_2 \cdot 6\text{H}_2\text{O}$, $\text{CaCl}_2 \cdot 4\text{H}_2\text{O}$, $\text{Ca}(\text{NO}_3)_2 \cdot 4\text{H}_2\text{O}$, $\text{Ca}(\text{NO}_3)_2 \cdot 3\text{H}_2\text{O}$ and $\text{Ca}(\text{CH}_3\text{COO})_2 \cdot \text{H}_2\text{O}$, three double salts $\text{CaCl}(\text{NO}_3) \cdot 2\text{H}_2\text{O}$, $\text{Ca}(\text{CH}_3\text{COO})\text{Cl} \cdot 5\text{H}_2\text{O}$ and $\text{Ca}_2(\text{CH}_3\text{COO})_3(\text{NO}_3) \cdot 2\text{H}_2\text{O}$ can exist in stable equilibrium with saturated solutions. In addition, there is a triple salt that can crystallize from mixed solutions of the quaternary system, i.e. $\text{Ca}_3(\text{CH}_3\text{COO})_3\text{Cl}(\text{NO}_3)_2 \cdot 7\text{H}_2\text{O}$.

The construction of the phase diagram requires the calculation of solubilities for each possible mixture composition in the quaternary system. The calculation of solubilities in mixed electrolyte solutions is one of the major applications of the Pitzer ion interaction model [5–7]. The Pitzer model is a semi-empirical model, i.e. the ion interaction equations arise from theoretical considerations, while there remain empirical parameters which have to be determined from experimental data [5]. The model accounts for interactions of pairs and triplets of each possible combination of ions. Higher order interactions between more than three ions are not considered in the basic form of the Pitzer model. The interactions are quantitatively described by binary parameters, obtained from experimental data of systems composed of one salt and water, and ternary parameters, determined from systems composed of two salts with one common ion and water. Once that all binary and ternary interaction parameters are known, the prediction of the behavior of more complex salt solutions containing more than three ions is possible.

As pointed out by STEIGER et al. [8], there is a lack of available experimental data for systems containing organic ions such as acetate and formate and their mixtures with common

inorganic salts. The treatment of the quaternary thecotrichite system requires experimental data for the three ternary subsystems $\text{CaCl}_2\text{--Ca}(\text{NO}_3)_2\text{--H}_2\text{O}$, $\text{Ca}(\text{CH}_3\text{COO})_2\text{--CaCl}_2\text{--H}_2\text{O}$ and $\text{Ca}(\text{CH}_3\text{COO})_2\text{--Ca}(\text{NO}_3)_2\text{--H}_2\text{O}$. Experimental solubility data for the $\text{CaCl}_2\text{--Ca}(\text{NO}_3)_2\text{--H}_2\text{O}$ system at 25°C are available from EHRET [9]. Solubilities in the $\text{Ca}(\text{CH}_3\text{COO})_2\text{--CaCl}_2\text{--H}_2\text{O}$ ternary system from 5°C to 35°C were recently determined by DORN [10]. However, no data were available for the $\text{Ca}(\text{CH}_3\text{COO})_2\text{--Ca}(\text{NO}_3)_2\text{--H}_2\text{O}$.

The main objective of the present work was the construction of the phase diagram of the quaternary thecotrichite system at 25°C. For that purpose, the solubilities in the ternary $\text{Ca}(\text{CH}_3\text{COO})_2\text{--Ca}(\text{NO}_3)_2\text{--H}_2\text{O}$ subsystem were measured and the missing ternary interaction parameters were determined. In addition, the equilibrium constant of the triple salt thecotrichite was evaluated from solubility measurements in the quaternary system. Finally, the isothermal invariant points and the solubility diagram of the full quaternary system at 25°C were calculated.

7.2 MODELLING APPROACH

7.2.1 Basic theory

Given a salt of composition $\text{M}_{\nu_M}\text{X}_{\nu_X} \cdot \nu_0\text{H}_2\text{O}$ consisting of ν_M positive ions M of charge z_M , ν_X negative ions X of charge z_X and ν_0 molecules of water the equilibrium constant K_{MX} of the dissolution reaction is given by

$$\ln K_{MX} = \nu_M \ln m_M + \nu_X \ln m_X + \nu_M \ln \gamma_M + \nu_X \ln \gamma_X + \nu_0 \ln a_w \quad (1)$$

where m_M , m_X , γ_M and γ_X represent the molalities and activity coefficients of the cations and anions, respectively, and a_w is the water activity defined as

$$\ln a_w = -\phi M_w \sum_i m_i \quad (2)$$

where ϕ is the osmotic coefficient and $M_w = 1.801528 \cdot 10^{-2} \text{ kg} \cdot \text{mol}^{-1}$ is the molar mass of water. The calculation of solubilities in mixed electrolyte solutions requires the knowledge of the equilibrium constants K_{MX} of all solid phases and the ability to calculate activity coefficients and water activities in mixed electrolyte solutions.

7.2.2 Ion interaction equations

One approach that has been successfully applied to the calculation of activity and osmotic coefficients is the ion interaction model of PITZER [5]. The expressions for the osmotic coefficient ϕ and the activity coefficients γ_M and γ_X of cation M and anion X in mixed electrolyte solutions are:

$$(\phi - 1) = \frac{2}{\sum_i m_i} \left[\frac{-A_\phi I^{3/2}}{(1 + bI^{1/2})} + \sum_c \sum_a m_c m_a (B_{ca}^\phi + ZC_{ca}) \right. \\ \left. + \sum_{c < c'} \sum m_c m_{c'} (\Phi_{cc'}^\phi + \sum_a m_a \psi_{cc'a}) + \sum_{a < a'} \sum m_a m_{a'} (\Phi_{aa'}^\phi + \sum_c m_c \psi_{caa'}) \right] \quad (3)$$

$$\ln \gamma_M = z_M^2 F + \sum_a m_a (2B_{Ma} + ZC_{Ma}) + \sum_c m_c (2\Phi_{Mc} + \sum_a m_a \psi_{Mca}) \\ + \sum_{a < a'} \sum m_a m_{a'} \psi_{Maa'} + z_M \sum_c \sum_a m_c m_a C_{ca} \quad (4)$$

$$\ln \gamma_X = z_X^2 F + \sum_c m_c (2B_{cX} + ZC_{cX}) + \sum_a m_a (2\Phi_{Xa} + \sum_c m_c \psi_{cXa}) \\ + \sum_{c < c'} \sum m_c m_{c'} \psi_{cc'X} + |z_X| \sum_c \sum_a m_c m_a C_{ca} \quad (5)$$

The function F is defined as:

$$F = -A_\phi \left[\frac{I^{1/2}}{(1 + bI^{1/2})} + \frac{2}{b} \ln(1 + bI^{1/2}) \right] + \sum_c \sum_a m_c m_a B'_{ca} \\ + \sum_{c < c'} \sum m_c m_{c'} \Phi'_{cc'} + \sum_{a < a'} \sum m_a m_{a'} \Phi'_{aa'} \quad (6)$$

In equations (3)–(6) the subscripts c , a and i refer to cations, anions or ions of any charge, respectively. Summation indices $c < c'$ and $a < a'$ refer to distinguishable pairs of cations and anions. A_ϕ is the Debye-Hückel parameter for the osmotic coefficient and b is a universal parameter with the value $1.2 \text{ kg}^{1/2} \text{ mol}^{-1/2}$. The value of the Debye-Hückel parameter, $A_\phi = 0.39147 \text{ kg}^{1/2} \cdot \text{mol}^{-1/2}$, was taken from ARCHER AND WANG [11]. I is the ionic strength given by

$$I = \frac{1}{2} \sum_i m_i z_i^2 \quad (7)$$

and the function Z is defined as

$$Z = \sum_i m_i |z_i| \quad (8)$$

The ionic strength dependence of the second virial coefficients B_{MX} is given as:

$$B_{\text{MX}}^\phi = \beta_{\text{MX}}^{(0)} + \beta_{\text{MX}}^{(1)} \exp(-\alpha_{\text{MX}}^{(1)} I^{1/2}) + \beta_{\text{MX}}^{(2)} \exp(-\alpha_{\text{MX}}^{(2)} I^{1/2}) + \beta_{\text{MX}}^{(3)} \exp(-\alpha_{\text{MX}}^{(3)} I^{1/2}) \quad (9)$$

$$B_{\text{MX}} = \beta_{\text{MX}}^{(0)} + \beta_{\text{MX}}^{(1)} g(\alpha_{\text{MX}}^{(1)} I^{1/2}) + \beta_{\text{MX}}^{(2)} g(\alpha_{\text{MX}}^{(2)} I^{1/2}) + \beta_{\text{MX}}^{(3)} g(\alpha_{\text{MX}}^{(3)} I^{1/2}) \quad (10)$$

$$B'_{\text{MX}} = \frac{1}{I} \left[\beta_{\text{MX}}^{(1)} g'(\alpha_{\text{MX}}^{(1)} I^{1/2}) + \beta_{\text{MX}}^{(2)} g'(\alpha_{\text{MX}}^{(2)}) + \beta_{\text{MX}}^{(3)} g'(\alpha_{\text{MX}}^{(3)}) \right] \quad (11)$$

where the functions g and g' are defined as:

$$g(x) = 2/x^2 [1 - (1+x) \exp(-x)] \quad (12)$$

$$g'(x) = -2/x^2 [1 - (1+x+x^2/2) \exp(-x)] \quad (13)$$

with $x = \alpha_{\text{MX}} I^{1/2}$ for each $\alpha_{\text{MX}}^{(i)}$ and $\beta_{\text{MX}}^{(i)}$. In the original Pitzer equations [5] the values of $\alpha_1 = 2 \text{ kg}^{1/2} \cdot \text{mol}^{-1/2}$ and $\alpha_2 = 12 \text{ kg}^{1/2} \cdot \text{mol}^{-1/2}$ are fixed and the latter is only used for 2–2 electrolytes. In the extended set of equations used here individual values of $\alpha_{\text{MX}}^{(i)}$ are assigned to each electrolyte and an additional term in $\alpha_{\text{MX}}^{(3)}$ and $\beta_{\text{MX}}^{(3)}$ is used to improve the representation of data at very high concentration.

In equations (3)–(6) the terms in Φ and ψ account for the ion interactions in mixed electrolyte solutions. The second virial coefficients Φ_{ij} account for interactions between pairs of ions of like sign. The complete expressions for Φ_{ij} are:

$$\Phi_{ij} = \theta_{ij} + {}^E\theta_{ij}(I) \quad (14)$$

$$\Phi'_{ij} = {}^E\theta'_{ij}(I) \quad (15)$$

$$\Phi_{ij}^\phi = \theta_{ij} + {}^E\theta_{ij}(I) + I {}^E\theta'_{ij}(I) \quad (16)$$

where the unsymmetrical electrostatic mixing terms ${}^E\theta_{ij}(I)$ and ${}^E\theta'_{ij}(I)$ depend only on the charges of the ions i and j , and the ionic strength, I . They account for unsymmetrical mixing effects of two ions with different charge of like sign [5]. Since there are no ion pairs of

unsymmetrical charge in the quaternary system $\text{Ca}(\text{CH}_3\text{COO})_2\text{--CaCl}_2\text{--Ca}(\text{NO}_3)_2\text{--H}_2\text{O}$, equations (14) to (16) simplify to $\Phi_{ij} = \Phi_{ij}^\phi = \theta_{ij}$ and $\Phi'_{ij} = 0$, respectively.

The parameters θ_{ij} account for interactions of pairs of ions of like sign, i.e. i and j refer to anion pairs $a\text{--}a'$ or cation pairs $c\text{--}c'$. The parameters ψ_{ijk} are the third virial coefficient mixing parameters. They account for interactions between triplets of ions, i.e. two different cations and an anion, or, two different anions and a cation, respectively.

7.2.3 Model parameters

The Pitzer equations incorporate a set of empirical interaction parameters. The binary parameters $\beta_{\text{MX}}^{(i)}$ and C_{MX} account for the interactions of each pair of cations M and anions X, respectively. They have to be determined from experimental data in binary systems. Likewise the ternary interaction parameters θ_{ij} and ψ_{ijk} that are required to predict the properties of mixed electrolyte solutions are determined from experimental data in ternary systems with one common ion. The treatment of the quaternary system $\text{Ca}(\text{CH}_3\text{COO})_2\text{--CaCl}_2\text{--Ca}(\text{NO}_3)_2\text{--H}_2\text{O}$ requires three sets of binary parameters $\beta_{\text{MX}}^{(i)}$ and C_{MX} , i.e. for $\text{Ca}(\text{CH}_3\text{COO})_2(\text{aq})$, $\text{CaCl}_2(\text{aq})$ and $\text{Ca}(\text{NO}_3)_2(\text{aq})$. In addition, the ternary parameters required include values of $\theta_{aa'}$ and $\psi_{aa'\text{Ca}}$ for the ternary subsystems corresponding to the three anion–anion pairs $\text{CH}_3\text{COO}^-\text{--Cl}^-$, $\text{Cl}^-\text{--NO}_3^-$ and $\text{CH}_3\text{COO}^-\text{--NO}_3^-$.

Several of the parameters and equilibrium constants that are required for the purpose of the present work are available from previous investigations. The binary interaction parameters were taken from BEYER [13]; the ternary parameters and all equilibrium constants of the system $\text{Ca}(\text{CH}_3\text{COO})_2\text{--CaCl}_2\text{--H}_2\text{O}$ were initially taken from DORN [8,10] but slightly adjusted. The binary parameters of $\text{Ca}(\text{NO}_3)_2(\text{aq})$ and the ternary parameters and equilibrium constants in the $\text{CaCl}_2\text{--Ca}(\text{NO}_3)_2\text{--H}_2\text{O}$ system were evaluated by STEIGER [14]. The ternary interaction parameters of the $\text{Ca}(\text{CH}_3\text{COO})_2\text{--Ca}(\text{NO}_3)_2\text{--H}_2\text{O}$ system and the equilibrium constants of the double salt $\text{Ca}_2(\text{CH}_3\text{COO})_3(\text{NO}_3) \cdot 2\text{H}_2\text{O}$ and the triple salt $\text{Ca}_3(\text{CH}_3\text{COO})_3\text{Cl}(\text{NO}_3)_2 \cdot 7\text{H}_2\text{O}$ were determined in the present work from new solubility data.

7.2.4 Solubility calculation

The calculation of phase equilibria in multicomponent systems requires numerical techniques [15]. In the present work, solubilities were calculated by the simultaneous solution of a set of mass action, i.e. Eq. (1), and mass balance equations [16]. The mass balance equations also include the total charge balance

$$\sum_c z_c m_c = \sum_a z_a m_a \quad (17)$$

where the sums are over all cations c and anions a , respectively. The mass action equations are given by Eq. (1) for the respective solid phases. The set of equations (1) and (17) can be simultaneously solved for the unknown molalities by Newton-Raphson iteration [15] yielding initial values, $m_i^{(0)}$, for the equilibrium molalities of all ions i in the solution. The ion interaction model is then used to calculate the corresponding activity coefficients and the water activity. The Newton-Raphson iteration is repeated with the activities $a_i^{(0)} = \gamma_i^{(0)} m_i^{(0)}$ and the water activity $a_w^{(0)}$ as starting values, yielding new molalities $m_i^{(1)}$ which are used to calculate $\gamma_i^{(1)}$ and $a_w^{(1)}$. The procedure is repeated until convergence in all γ_i and m_i is obtained.

7.3 EXPERIMENTAL

7.3.1 Sample preparation

The solubilities were measured by direct methods, i.e. by analysis of the composition of the liquid phase at equilibrium under isothermal-isobaric conditions. All aqueous solutions were prepared by weighing double distilled water and analytical grade salts, i.e. $\text{Ca}(\text{CH}_3\text{COO})_2$ (with 10% w/w water), $\text{CaCl}_2 \cdot 2\text{H}_2\text{O}$ and $\text{Ca}(\text{NO}_3)_2 \cdot 4\text{H}_2\text{O}$ (Merck, Darmstadt, Germany). During the course of the measurements the sample preparation, the sampling of the saturated solutions and the removal of the solid residues was modified several times in order to improve the accuracy of the analytical procedure.

In a first series of solubility measurements in the $\text{Ca}(\text{CH}_3\text{COO})_2\text{--Ca}(\text{NO}_3)_2\text{--H}_2\text{O}$ system, the samples were prepared by adding one component to a saturated solution of the second component. The solutions were stirred in round-bottom flasks at room temperature for at least two days to reach equilibrium. Three samples of each saturated solution were taken and the

wet residues were removed by filtration using a syringe-driven filter unit (Millex 0,45 μm pore size, Millipore, Billerica, USA) connected to a cannula. After flushing the cannula, the filter and the syringe with saturated solution, approximately 500 mg of the filtrate were accurately weighed into a 50 mL volumetric flask. The temperature of the saturated solutions was measured during the sampling procedure. Once the sampling procedure was complete, a new sample was prepared by addition of the next portion of the first salt to the remaining saturated solution in the round-bottom flask and subsequent equilibration. The composition of the saturated solutions was obtained by analysis of the anions CH_3COO^- and NO_3^- with high pressure ion chromatography (HPIC).

In a second set of experiments (*series 2*) particular emphasis was placed on the analysis of the composition of the precipitates in the ternary system $\text{Ca}(\text{CH}_3\text{COO})_2\text{--Ca}(\text{NO}_3)_2\text{--H}_2\text{O}$ and the quaternary system $\text{Ca}(\text{CH}_3\text{COO})_2\text{--CaCl}_2\text{--Ca}(\text{NO}_3)_2\text{--H}_2\text{O}$. Samples were prepared by weighing the components into polyethylene tubes (Sarstedt, Nümbrecht, Germany). The solutions were shaken at room temperature for a week to reach equilibrium. Liquid and solid phases were separated by water jet vacuum filtration using a glass filter G3 (SCHOTT, Mainz, Germany) with a nominal pore size of 16–40 μm . The stoichiometry of the precipitate was determined by using SCHREINEMAKER's wet residue method [17], which is based on the analysis of the mother liquor, the wet residue and a mixture of both for each sample. Approximately 0.1 g, 1 g and 0.6 g of the filtrate, the residue or the mixture were weighed into a 100 mL volumetric flask and double distilled water was added to the mark. The solution compositions were obtained by analyzing the anions CH_3COO^- , NO_3^- and Cl^- with high pressure ion chromatography (HPIC). The composition of the three samples, i.e. mother liquor, wet residue and the mixture, were drawn in the phase diagram and connected by a regression line. The intersection of these tie lines for all samples then yields the stoichiometry of the precipitate [17]. In addition to this graphical procedure, the wet residue was instantly analyzed without further preparation by powder X-ray diffraction.

In a third set (*series 3*) solutions saturated with respect to $\text{Ca}_2(\text{CH}_3\text{COO})_3(\text{NO}_3) \cdot 2\text{H}_2\text{O}$ and solutions saturated with respect to both solid phases, $\text{Ca}_3(\text{CH}_3\text{COO})_3\text{Cl}(\text{NO}_3)_2 \cdot 7\text{H}_2\text{O}$ and $\text{Ca}_2(\text{CH}_3\text{COO})_3(\text{NO}_3) \cdot 2\text{H}_2\text{O}$, were prepared by isothermal evaporation. An equimolar solution of $\text{Ca}(\text{CH}_3\text{COO})_2$, CaCl_2 and $\text{Ca}(\text{NO}_3)_2$ was prepared and water was evaporated into a continuous flow of dry air over the solution. After reaching saturation, indicated by precipitation, the first sample was taken, using a filter and a cannula as described before

(series I). $\text{Ca}_2(\text{CH}_3\text{COO})_3(\text{NO}_3) \cdot 2\text{H}_2\text{O}$ precipitates first from an equimolar solution and the solution composition continuously changes during the crystallization of the double salt due to the fact that the precipitate and the solution have different compositions. Reaching the coexisting line of both solid phases during ongoing evaporation, $\text{Ca}_3(\text{CH}_3\text{COO})_3\text{Cl}(\text{NO}_3)_2 \cdot 7\text{H}_2\text{O}$ starts to crystallize. The change in the composition of the saturated solution during the course of the evaporation was followed by daily sampling and analysis. Nine samples saturated with respect to $\text{Ca}_2(\text{CH}_3\text{COO})_3(\text{NO}_3) \cdot 2\text{H}_2\text{O}$ and seven samples saturated with respect to $\text{Ca}_3(\text{CH}_3\text{COO})_3\text{Cl}(\text{NO}_3)_2 \cdot 7\text{H}_2\text{O}$ and $\text{Ca}_2(\text{CH}_3\text{COO})_3(\text{NO}_3) \cdot 2\text{H}_2\text{O}$ were obtained. The anion concentrations in the solutions were determined as described before.

The crystallization pathway for a general quaternary system $\text{A--B--C--H}_2\text{O}$ is shown in Figure 1 as Jänecke projection. The system contains crystallization fields of a double salt with stoichiometric composition AB and an incongruently soluble triple salt of composition ABC. The initial equimolar composition D lies in the stability field of the double salt AB. With ongoing evaporation AB precipitates and the solution composition changes along a straight line between AB and D in the opposite direction of AB. Reaching the coexistence line of the compounds AB and ABC, the triple salt ABC precipitates and the solution composition would change along a straight line connecting points E and ABC in the direction of point F. Simultaneously however, AB dissolves and the solution composition changes along the straight line between F and AB in the direction of AB. As a result of the simultaneous precipitation of ABC and the dissolution of AB, the solution composition moves along a line between E and G in the direction of G, i.e. along the coexistence line of both solid phases, AB and ABC.

At last, the solubility measurement device of DORN [10] was used to determine solubilities in both the ternary and the quaternary systems. Samples were prepared by weighing the components into round-bottom flasks. The flasks were placed in a thermostat at 25°C and the saturated solutions were stirred for a week. Samples were taken by using a thermostated syringe-driven filter unit (5 µm pore size, Schleicher & Schuell, Dassel, Germany) connected to a cannula. Subsequently, the liquid and the solid phases were separated by water jet vacuum filtration using a glass filter G3 (SCHOTT, Mainz, Germany) to separate the wet residue. To avoid phase transitions in the wet residue induced by changes in temperature or relative humidity, a thermostated humidifier was used consisting of a twisted glass tube

partially filled with a portion of the saturated solution and connected to the low pressure filtration unit. An airflow equilibrated with the saturated solution in the humidifier was continuously sucked by the vacuum and forced to flow through the wet residue on the glass filter. Thus, the temperature of the air passing the wet residue during the filtration was held constant at 25°C and the humidity of the air was equal to the equilibrium humidity of the saturated solution. After filtration, the wet residue was instantly analyzed by powder X-ray diffraction and SCHREINEMAKER's method was used to determine the stoichiometry of the precipitate as described before. Solubilities of five samples were measured in the quaternary system $\text{Ca}(\text{CH}_3\text{COO})_2\text{--CaCl}_2\text{--Ca}(\text{NO}_3)_2\text{--H}_2\text{O}$ and two saturated solutions in the ternary system $\text{Ca}(\text{CH}_3\text{COO})_2\text{--Ca}(\text{NO}_3)_2\text{--H}_2\text{O}$ were analyzed. Some of the samples (*series 4*) were treated as described before for the *series 2* sample. In the case of five samples (*series 5*), wet chemical analysis methods were selected, therefore the amount of sample weighed into the volumetric flask was increased by a factor of ten. Acetate and chloride were determined by potentiometric titration and a photometric technique was used for the measurement of nitrate.

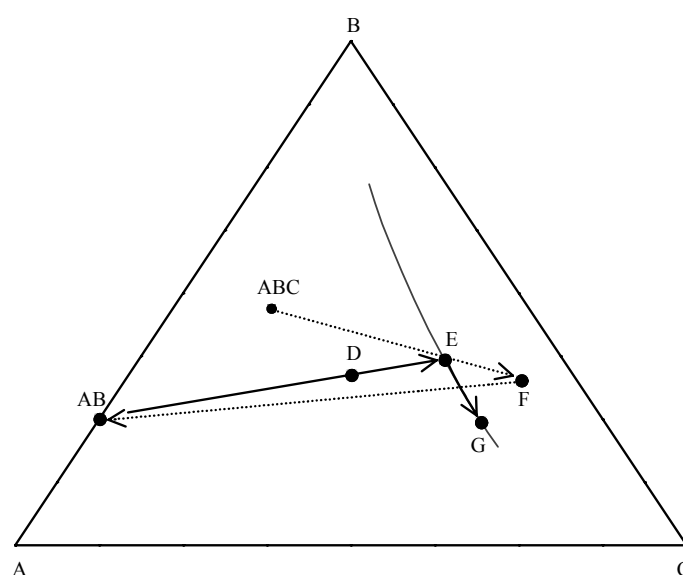


Figure 1: Crystallization pathway during isothermal evaporation, of a quaternary system $\text{A--B--C--H}_2\text{O}$, containing a double salt AB and an incongruently soluble triple salt ABC, shown as Jänecke projection.

7.4 INSTRUMENTATION

Anions were analyzed by high pressure ion chromatography (HPIC). The chromatographic system consisted of an isocratic pump P 1000 (Thermo Separation Products, San Jose, CA, USA), an automated sampler Biotronik BT7041 (Biotronik/Eppendorf, Hamburg, Germany) and an ion chromatograph 2010i with conductivity detector CDM-I (Dionex, Sunnyvale, CA, USA). An ASRS-Ultra suppressor with SRS controller (Dionex) in the autosuppression recycle mode was employed for electrochemical suppression. Separation of the anions was achieved using a guard column AG 10 and a separation column AS 10 (Dionex) with a $100 \text{ mmol}\cdot\text{L}^{-1}$ NaOH eluent (analytical grade, Merck) at a flow rate of $1.2 \text{ mL}\cdot\text{min}^{-1}$.

A SenTix 61 pH electrode (WTW, Weilheim, Germany) and an ion analyzer (EA 940; Orion Research Inc., Boston, USA) were used for the potentiometric titrations of acetate. Argentometric titration with a titro processor 672 (Metrohm, Filderstadt, Germany) was used for the determination of chloride. An UV/VIS spectrophotometer (Lambda 2, Perkin Elmer, Überlingen, Germany) was used to determine nitrate as 4-nitro-2,6-dimethylphenol at 324 nm according to DIN 38 405-D9-2.

Wet residues were characterized by X-ray powder diffraction. Diffraction patterns were obtained on a Bragg-Brentano parafocusing reflection diffractometer (D 5000, Siemens, Germany) using Cu $K\alpha$ -radiation and a position-sensitive detector (PSD) recording data from a $12^\circ 2\theta$ band at one time.

7.5 RESULTS AND DISCUSSION

7.5.1 Solubility measurements and characterization of precipitates

Solubilities are usually expressed in molal concentrations ($\text{mol}\cdot\text{kg}^{-1}$ solvent), thus, the mass concentrations ($\text{g}\cdot\text{L}^{-1}$ solution) as determined by HPIC were converted into molalities. The weight w_{MX} of an anhydrous salt in the saturated solution samples is given by:

$$w_{\text{MX}} = c_{\text{X}} \cdot V_{\text{s}} \cdot \frac{\nu_{\text{M}} M_{\text{MX}}}{\nu_{\text{X}} \cdot M_{\text{X}}} \quad (18)$$

where c_{X} is the mass concentration of anion X, V_{s} is the volume of the volumetric flask, M_{MX} and M_{X} are the molar masses ($\text{g}\cdot\text{mol}^{-1}$) of the anhydrous salt and the anion, respectively. Also,

$\nu_{\text{M}}/\nu_{\text{X}} = 1/2$ for all salts used in the present study. The molalities of the salts are then given by:

$$m_{\text{MX}} = \frac{w_{\text{MX}}}{w_{\text{H}_2\text{O}}} \frac{1000}{M_{\text{MX}}} \quad (19)$$

where $w_{\text{H}_2\text{O}}$, the weight of water in the sample, is given by:

$$w_{\text{H}_2\text{O}} = w_s - \sum w_{\text{MX}} \quad (20)$$

The summation in Eq. (20) is over all salts MX present in the solution and w_s is the total mass of the sample.

The results of the solubility determinations are listed in Tables 1 and 2 for the $\text{Ca}(\text{CH}_3\text{COO})_2\text{--Ca}(\text{NO}_3)_2\text{--H}_2\text{O}$ ternary and the $\text{Ca}(\text{CH}_3\text{COO})_2\text{--CaCl}_2\text{--Ca}(\text{NO}_3)_2\text{--H}_2\text{O}$ quaternary system, respectively. An overall error of the salt concentrations was estimated by repeated sampling and IC measurement. A saturated solution at 25°C was prepared from an equimolar mixture of $\text{Ca}(\text{CH}_3\text{COO})_2$, CaCl_2 and $\text{Ca}(\text{NO}_3)_2$. Tenfold sampling resulted in relative standard deviations of 13%, 8% and 5% for the molalities in the saturated solutions of $\text{Ca}(\text{CH}_3\text{COO})_2$, CaCl_2 and $\text{Ca}(\text{NO}_3)_2$, respectively.

Tables 1 and 2 also list the nature of the precipitate as characterized by X-ray powder diffraction and SCHREINEMAKER's method. $\text{Ca}(\text{CH}_3\text{COO})_2 \cdot \text{H}_2\text{O}$ was identified in the powder patterns of the wet residues by comparison with the JCPDS (Joint committee on diffraction pattern) standard 30-0221. Due to missing JCPDS standards, $\text{Ca}_2(\text{CH}_3\text{COO})_3(\text{NO}_3) \cdot 2\text{H}_2\text{O}$ was identified by comparison with a powder pattern, shown in Figure 2, calculated from structural data [18] of the double salt. In the case of $\text{Ca}_3(\text{CH}_3\text{COO})_3\text{Cl}(\text{NO}_3)_2 \cdot 7\text{H}_2\text{O}$, neither JCPDS standards nor structural data were available. The triple salt was identified by comparison with the diffraction pattern obtained from efflorescences of this compound on an Egyptian limestone relief [19].

The application of SCHREINEMAKER's method yielded three solid phases with different composition that were determined as the intersections of the respective regression lines. Firstly, the intersection with the binary system $\text{Ca}(\text{CH}_3\text{COO})_2\text{--H}_2\text{O}$ represents the stoichiometry of $\text{Ca}(\text{CH}_3\text{COO})_2 \cdot \text{H}_2\text{O}$. Though the second intersection corresponds to the stoichiometry $\text{Ca}_2(\text{CH}_3\text{COO})_3(\text{NO}_3) \cdot 4\text{H}_2\text{O}$, but $\text{Ca}_2(\text{CH}_3\text{COO})_3(\text{NO}_3) \cdot 2\text{H}_2\text{O}$ was

unambiguously identified in these samples by X-ray diffraction. As an example, the powder pattern of the wet residue of the solution saturated at $0.65 \text{ mol}\cdot\text{kg}^{-1}$ $\text{Ca}(\text{CH}_3\text{COO})_2$ and $3.27 \text{ mol}\cdot\text{kg}^{-1}$ $\text{Ca}(\text{NO}_3)_2$ is depicted in Figure 1. Most likely, the difference in the water content is caused by the uncertainties of the chemical analysis of the wet residue, hence, it is concluded that the precipitate is $\text{Ca}_2(\text{CH}_3\text{COO})_3(\text{NO}_3) \cdot 2\text{H}_2\text{O}$.

A third intersection corresponding to the stoichiometric composition $\text{Ca}(\text{CH}_3\text{COO})(\text{NO}_3) \cdot 3\text{H}_2\text{O}$ was found in a small region of high nitrate and low acetate content. The corresponding XRD patterns of the four wet residue samples showed very small intensities, line broadening and considerable differences in peak positions and intensity ratios. All efforts to synthesize the salt again were unsuccessful so far. Preliminary calculations have shown that the stability field of $\text{Ca}(\text{CH}_3\text{COO})(\text{NO}_3) \cdot 3\text{H}_2\text{O}$ would be very small [3]. As further evidence of the existence of this phase is still missing and due to the fact that its omission causes only very minor changes of the phase diagram, the double salt $\text{Ca}(\text{CH}_3\text{COO})(\text{NO}_3) \cdot 3\text{H}_2\text{O}$ is ignored in the present paper.

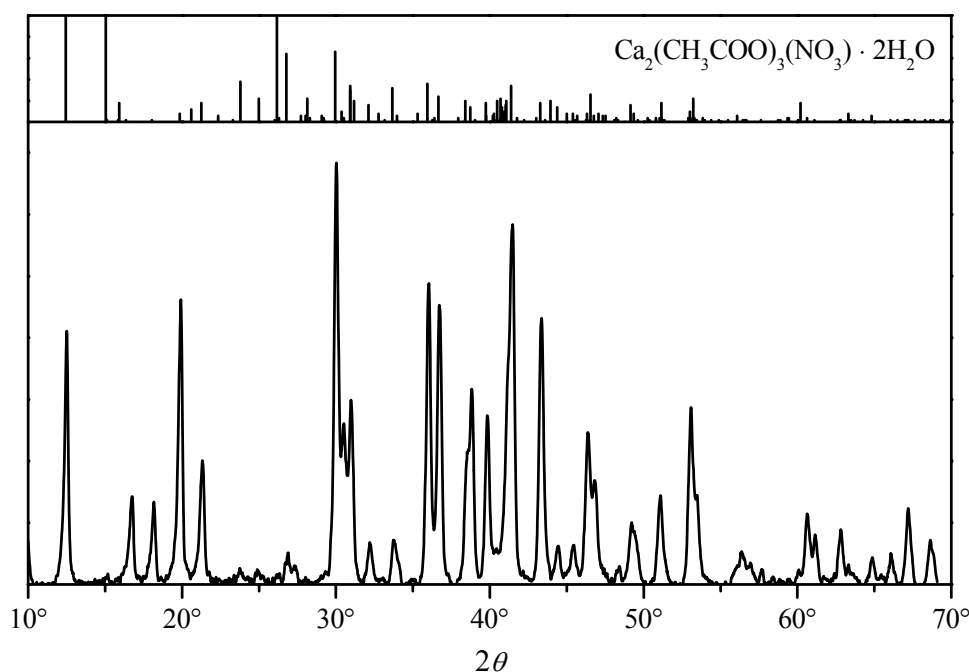


Figure 2: Powder pattern of $\text{Ca}_2(\text{CH}_3\text{COO})_3(\text{NO}_3) \cdot 2\text{H}_2\text{O}$ calculated from structural data [18] and powder pattern of the wet residue of the solution saturated at $0.65 \text{ mol}\cdot\text{kg}^{-1}$ $\text{Ca}(\text{CH}_3\text{COO})_2$ and $3.27 \text{ mol}\cdot\text{kg}^{-1}$ $\text{Ca}(\text{NO}_3)_2$.

Table 1: Solubilities in the ternary system $\text{Ca}(\text{CH}_3\text{COO})_2\text{--Ca}(\text{NO}_3)_2\text{--H}_2\text{O}$ (units are $\text{mol}\cdot\text{kg}^{-1}$) and analysis of the precipitate.

$T/^\circ\text{C}$	$\text{Ca}(\text{CH}_3\text{COO})_2$	$\text{Ca}(\text{NO}_3)_2$	precipitate
<i>series 1</i>			
25.0	2.15	0.080	na ⁽¹⁾
25.0	2.09	0.172	na
25.0	2.21	0.260	na
25.0	2.32	0.322	na
24.0	2.11	0.373	na
24.0	2.15	0.418	na
24.0	2.13	0.512	na
23.5	1.99	0.600	na
22.5	1.87	0.604	na
23.3	1.79	0.654	na
22.8	1.62	0.825	na
23.2	1.62	0.778	na
24.0	1.65	0.918	na
24.0	1.56	0.964	na
24.5	1.58	1.07	na
23.7	1.39	1.12	na
23.7	1.35	1.16	na
25.0	1.44	1.27	na
24.2	1.37	1.32	na
23.7	1.31	1.41	na
24.3	1.30	1.49	na
24.3	1.31	1.57	na
23.0	1.26	1.64	na
23.2	0.378	5.09	na
24.5	0.333	5.31	na
23.5	0.300	5.64	na
23.0	0.281	5.99	na
23.0	0.248	6.25	na
24.0	0.197	6.79	na
24.2	0.184	7.04	na

Table 1: continued

T/°C	$\text{Ca}(\text{CH}_3\text{COO})_2$	$\text{Ca}(\text{NO}_3)_2$	precipitate
<i>series 1</i>			
24.5	0.170	6.98	na
22.0	0.149	7.03	na
23.7	2.15	0.080	na
23.0	2.09	0.172	na
23.0	2.21	0.260	na
23.3	2.32	0.322	na
23.7	2.11	0.373	na
<i>series 2</i>			
RT	2.07	0.110	$\text{Ca}(\text{CH}_3\text{COO})_2 \cdot \text{H}_2\text{O}$
RT	2.19	0.226	$\text{Ca}(\text{CH}_3\text{COO})_2 \cdot \text{H}_2\text{O}$
RT	2.13	0.057	$\text{Ca}(\text{CH}_3\text{COO})_2 \cdot \text{H}_2\text{O}$
RT	1.79	0.894	ni ⁽²⁾
RT	1.07	1.72	ni
RT	0.903	2.13	$\text{Ca}_2(\text{CH}_3\text{COO})_3(\text{NO}_3) \cdot 2\text{H}_2\text{O}$
RT	0.916	2.59	$\text{Ca}_2(\text{CH}_3\text{COO})_3(\text{NO}_3) \cdot 2\text{H}_2\text{O}$
RT	0.650	3.27	$\text{Ca}_2(\text{CH}_3\text{COO})_3(\text{NO}_3) \cdot 2\text{H}_2\text{O}$
RT	0.377	5.48	$\text{Ca}_2(\text{CH}_3\text{COO})_3(\text{NO}_3) \cdot 2\text{H}_2\text{O}$
RT	0.330	4.60	ni
RT	0.270	5.88	ni
RT	0.163	6.10	ni
RT	0.168	6.93	ni
<i>series 5</i>			
25.0	0.137	7.95	ni
25.0	0.120	8.34	ni

(1) wet residue not analyzed

(2) no unambiguous identification of the precipitate possible

In several cases an explicit identification of the precipitate was impossible. In general, due to the large crystal sizes and the high moisture content the quality of the XRD patterns of the wet residue samples is not always satisfactory if compared to the patterns of ideal powdered

samples. In addition, pattern distortion might also be caused by ongoing crystallization due to evaporation during the XRD measurements. The peak intensities were not in due proportion, the intensities of some peaks were very low and peak broadening occurred. Even the wet residue of a pure calcium nitrate solution at 25°C could not be unambiguously identified as $\text{Ca}(\text{NO}_3)_2 \cdot 4\text{H}_2\text{O}$ by comparison with the JCPDS standard 26-0318, although there is no doubt that $\text{Ca}(\text{NO}_3)_2 \cdot 4\text{H}_2\text{O}$ is the stable phase at 25°C [9].

Similar problems occurred when SCHREINEMAKER's wet residue method was applied to identify the composition of the precipitates in those samples that did not yield unambiguous XRD patterns. In these cases, SCHREINEMAKER's method did not reveal an unambiguous composition of the solid phases in the residues from the intersections of the tie lines as well. Hence, the stoichiometry of these precipitates is not always known exactly.

In the quaternary system $\text{Ca}(\text{CH}_3\text{COO})_2\text{--CaCl}_2\text{--Ca}(\text{NO}_3)_2\text{--H}_2\text{O}$ all XRD results were in accordance with the results of the SCHREINEMAKER's method. The wet residues were unambiguously identified as either $\text{Ca}_2(\text{CH}_3\text{COO})_3(\text{NO}_3) \cdot 2\text{H}_2\text{O}$ or $\text{Ca}_3(\text{CH}_3\text{COO})_3\text{Cl}(\text{NO}_3)_2 \cdot 7\text{H}_2\text{O}$.

Table 2: Solubilities in the quaternary system $\text{Ca}(\text{CH}_3\text{COO})_2\text{--CaCl}_2\text{--Ca}(\text{NO}_3)_2\text{--H}_2\text{O}$ (units are $\text{mol}\cdot\text{kg}^{-1}$) and analysis of the precipitates.

$T/^\circ\text{C}$	$\text{Ca}(\text{CH}_3\text{COO})_2$	CaCl_2	$\text{Ca}(\text{NO}_3)_2$	precipitate ⁽¹⁾
<i>series 2</i>				
RT	0.607	1.29	1.44	tri
RT	0.816	0.932	1.12	tri
RT	0.913	0.873	0.971	tri
RT	1.44	0.769	0.499	tri
RT	0.495	1.92	1.18	th
RT	0.562	1.15	2.35	th
RT	0.195	2.10	2.02	th
RT	0.217	2.06	1.96	th
RT	0.382	1.73	1.53	th
<i>series 3⁽³⁾</i>				
25.0	0.890	1.15	1.24	tri
25.0	0.963	1.11	1.22	tri

Table 2: continued

$T/^\circ\text{C}$	$\text{Ca}(\text{CH}_3\text{COO})_2$	CaCl_2	$\text{Ca}(\text{NO}_3)_2$	precipitate ⁽¹⁾
<i>series 3⁽³⁾</i>				
25.0	0.954	1.17	1.25	tri
22.5	0.798	1.19	1.22	tri
23.7	0.762	1.37	1.28	tri
23.7	0.792	1.27	1.30	tri
24.7	0.808	1.28	1.38	tri
23.8	0.701	1.31	1.29	tri
24.2	0.686	1.34	1.31	tri
23.0	0.681	1.59	1.44	th/tri
22.7	0.567	1.56	1.35	th/tri
24.0	0.627	1.69	1.35	th/tri
24.5	0.591	1.63	1.31	th/tri
24.0	0.608	1.72	1.32	th/tri
24.2	0.624	1.59	1.18	th/tri
23.5	0.649	1.77	1.18	th/tri
<i>series 4</i>				
25.0	0.557	1.32	2.09	tri
25.0	0.486	2.22	1.24	th
<i>series 5</i>				
25.0	0.396	2.18	1.32	th
25.0	0.150	3.39	1.27	th
25.0	0.231	2.81	1.35	th
<i>Strathclyde⁽⁴⁾</i>				
RT	0.207	3.64	1.10	th
RT	0.229	2.46	1.33	th
RT	0.430	1.51	1.62	th
RT	0.308	1.12	2.30	th

(1) RT: room temperature

(2) th: $\text{Ca}_3(\text{CH}_3\text{COO})_3\text{Cl}(\text{NO}_3)_2 \cdot 7\text{H}_2\text{O}$; tri: $\text{Ca}_2(\text{CH}_3\text{COO})_3(\text{NO}_3) \cdot 2\text{H}_2\text{O}$

(3) wet residue not analyzed (evaporation experiment, see text)

(4) Values provided by GIBSON and COOKSEY [20] (not used to calculate the equilibrium constant $\ln K$ of $\text{Ca}_3(\text{CH}_3\text{COO})_3\text{Cl}(\text{NO}_3)_2 \cdot 7\text{H}_2\text{O}$); composition of the solid phase deduced from phase diagram.

7.5.2 Model parameters

All model parameters that are required for the prediction of solubilities in the quaternary $\text{Ca}(\text{CH}_3\text{COO})_2\text{--CaCl}_2\text{--Ca}(\text{NO}_3)_2\text{--H}_2\text{O}$ system are listed in Tables 3–5. Table 1 lists the values of the single salt parameters for $\text{Ca}(\text{CH}_3\text{COO})_2(\text{aq})$, $\text{Ca}(\text{NO}_3)_2(\text{aq})$ and $\text{CaCl}_2(\text{aq})$ used in the calculations [13,14]. Table 4 provides a summary of the mixed electrolyte parameters and Table 5 lists all equilibrium constants required for the calculation of the complete solubility diagram of the system at 25°C. Several of these model parameters were taken from previous investigations as indicated in Tables 3–5. The ternary interaction parameters of DORN [10] for the system $\text{Ca}(\text{CH}_3\text{COO})_2\text{--CaCl}_2\text{--H}_2\text{O}$ were re-evaluated to improve the model predictions in the quaternary system.

The mixing parameters for the $\text{Ca}(\text{CH}_3\text{COO})_2\text{--Ca}(\text{NO}_3)_2\text{--H}_2\text{O}$ ternary system were determined together with the equilibrium constant of $\text{Ca}_2(\text{CH}_3\text{COO})_3(\text{NO}_3) \cdot 2\text{H}_2\text{O}$ using the solubility data of the present work listed in Table 1. Calculated solubilities using these parameters and experimental values are depicted in Figure 3. Considering the estimated overall errors of 13% and 5% of the acetate and nitrate concentrations, the fitted curve is in very good agreement with the experimental data.

Table 3: Binary interaction parameters at 25°C.

Parameter	$\text{Ca--CH}_3\text{COO}^-$ ^(a)	$\text{Ca}^{2+}\text{--Cl}^-$ ^(b)	$\text{Ca}^{2+}\text{--NO}_3^-$ ^(b)
$\beta_{\text{MX}}^{(0)}$	0.0438	−4.9228	0.0330
$\beta_{\text{MX}}^{(1)}$	1.1845	4.9689	1.4672
$\beta_{\text{MX}}^{(2)}$	0	−5.5975	0.1435
$\beta_{\text{MX}}^{(3)}$	0	8.4191	0
C_{MX}	0.0028	0.0155	−0.0006
$\alpha_{\text{MX}}^{(1)}$	1.4	1.4	1.7
$\alpha_{\text{MX}}^{(2)}$	1.0	0.5	0.1
$\alpha_{\text{MX}}^{(3)}$	0	0.1	0

(a) Parameters of BEYER [13]

(b) Parameters of STEIGER [14]

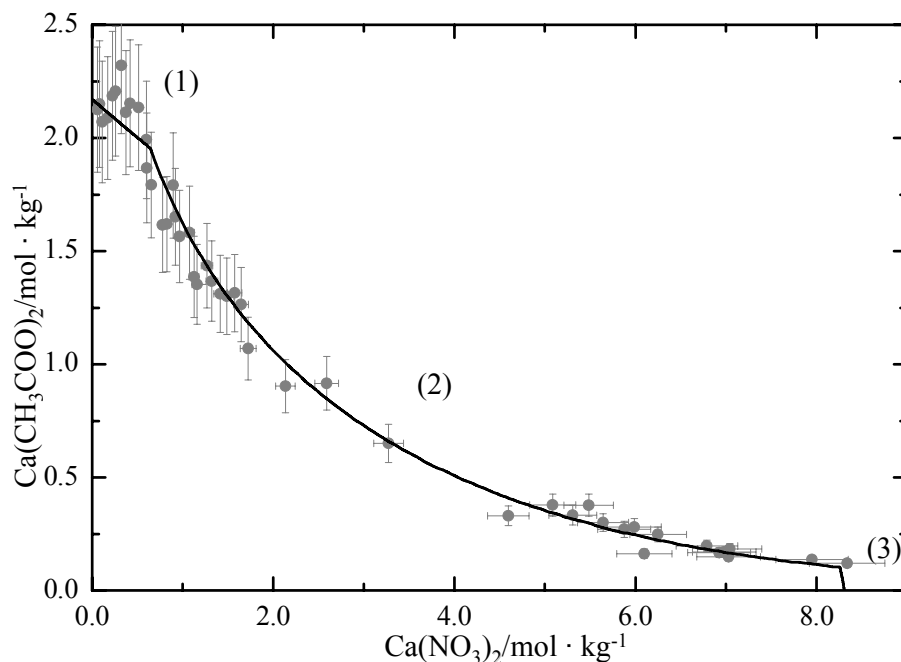


Figure 3: Solubilities in the ternary system $\text{Ca}(\text{CH}_3\text{COO})_2\text{--Ca}(\text{NO}_3)_2\text{--H}_2\text{O}$ at 25°C. Lines represent the calculated solubilities of: (1) $\text{Ca}(\text{CH}_3\text{COO})_2 \cdot \text{H}_2\text{O}$, (2) $\text{Ca}_2(\text{CH}_3\text{COO})_3(\text{NO}_3) \cdot 2\text{H}_2\text{O}$ and (3) $\text{Ca}(\text{NO}_3)_2 \cdot 4\text{H}_2\text{O}$. Points represent the measured solubilities, horizontal and vertical error bars represent the estimated overall errors for the $\text{Ca}(\text{NO}_3)_2$ and $\text{Ca}(\text{CH}_3\text{COO})_2$ molalities.

Table 4: Ternary interaction parameters at 25°C.

Parameter	$\text{CH}_3\text{COO}^- \text{--} \text{Cl}^-$	$\text{CH}_3\text{COO}^- \text{--} \text{NO}_3^-$	$\text{Cl}^- \text{--} \text{NO}_3^-$ ^(a)
$\theta_{aa'}$	−0.03	−0.02	−0.01874
$\Psi_{aa'\text{Ca}}$	−0.015	0.003	0.00198

(a) Parameters of STEIGER [14]

The equilibrium constant K_{th} of thecotrichite, $\text{Ca}_3(\text{CH}_3\text{COO})_3\text{Cl}(\text{NO}_3)_2 \cdot 7\text{H}_2\text{O}$, was calculated using the molalities of the saturated solutions listed in Table 2 except the values provided by COOKSEY and GIBSON [20] and the molalities of the solutions saturated with both $\text{Ca}_3(\text{CH}_3\text{COO})_3\text{Cl}(\text{NO}_3)_2 \cdot 7\text{H}_2\text{O}$ and $\text{Ca}_2(\text{CH}_3\text{COO})_3(\text{NO}_3) \cdot 2\text{H}_2\text{O}$ (th/tri). This calculation yields $\ln K_{\text{th}} = -0.53$.

Table 5: Equilibrium constants of the solid phases in the quaternary system $\text{Ca}(\text{CH}_3\text{COO})_2\text{--CaCl}_2\text{--Ca}(\text{NO}_3)_2\text{--H}_2\text{O}$ at 25°C.

Solid phase	$\ln K$
$\text{CaCl}_2 \cdot 6\text{H}_2\text{O}^{(a)}$	9.052
$\text{CaCl}_2 \cdot 4\text{H}_2\text{O}^{(a)}$	12.245
$\text{CaCl}(\text{NO}_3) \cdot 2\text{H}_2\text{O}^{(a)}$	10.817
$\text{Ca}(\text{NO}_3)_2 \cdot 3\text{H}_2\text{O}^{(a)}$	6.081
$\text{Ca}(\text{NO}_3)_2 \cdot 4\text{H}_2\text{O}^{(a)}$	4.556
$\text{Ca}_2(\text{CH}_3\text{COO})_3(\text{NO}_3) \cdot 2\text{H}_2\text{O}$	−1.95
$\text{Ca}(\text{CH}_3\text{COO})_2 \cdot \text{H}_2\text{O}^{(b)}$	−0.5734
$\text{Ca}(\text{CH}_3\text{COO})\text{Cl} \cdot 5\text{H}_2\text{O}$	0.50
$\text{Ca}_3(\text{CH}_3\text{COO})_3\text{Cl}(\text{NO}_3)_2 \cdot 7\text{H}_2\text{O}$	−0.53

^(a) Equilibrium constants of STEIGER [14]^(b) Equilibrium constants of DORN [10]

7.5.3 Solubilities in the quaternary system

Presentation of a quaternary system in a three dimensional diagram would be confusing; therefore, the calculated phase diagram of the quaternary system is depicted as the frequently employed Jänecke projection in Figure 4. All possible solution compositions are expressed as mole fractions of $\text{Ca}(\text{CH}_3\text{COO})_2$, CaCl_2 , and $\text{Ca}(\text{NO}_3)_2$ in the triangular diagram. The corners represent the pure salts, the sides represent the three ternary systems $\text{CaCl}_2\text{--Ca}(\text{NO}_3)_2\text{--H}_2\text{O}$, $\text{Ca}(\text{CH}_3\text{COO})_2\text{--CaCl}_2\text{--H}_2\text{O}$ and $\text{Ca}(\text{CH}_3\text{COO})_2\text{--Ca}(\text{NO}_3)_2\text{--H}_2\text{O}$ and the interior represents compositions of salt mixtures containing all three salts. The stability fields between the lines in the interior represent the composition of solutions saturated with respect to only one solid phase. The lines represent saturated solution compositions coexisting with two solid phases. According to the phase rule a maximum of three solid phases can coexist with a saturated solution in a quaternary system at constant temperature. Hence, for each possible combination of three solid phases, there exists only one composition of a saturated solution. These solution compositions are the intersections of the univariant lines.

The experimental data of the quaternary system, listed in Table 2, are also shown in Figure 4. Triangles and diamonds, respectively, represent solution compositions saturated with respect to either $\text{Ca}_2(\text{CH}_3\text{COO})_3(\text{NO}_3) \cdot 2\text{H}_2\text{O}$ or $\text{Ca}_3(\text{CH}_3\text{COO})_3\text{Cl}(\text{NO}_3)_2 \cdot 7\text{H}_2\text{O}$. Filled diamonds

represent four solution compositions saturated with $\text{Ca}_3(\text{CH}_3\text{COO})_3\text{Cl}(\text{NO}_3)_2 \cdot 7\text{H}_2\text{O}$ measured at the University of Strathclyde and kindly provided by COOKSEY and GIBSON [20]. Filled triangles and filled squares represent solutions prepared by isothermal evaporation (*series 3*). The filled squares represent solution compositions saturated with respect to, both, $\text{Ca}_2(\text{CH}_3\text{COO})_3(\text{NO}_3) \cdot 2\text{H}_2\text{O}$ and $\text{Ca}_3(\text{CH}_3\text{COO})_3\text{Cl}(\text{NO}_3)_2 \cdot 7\text{H}_2\text{O}$. It is obvious that the experimental data agree nicely with the calculated stability fields.

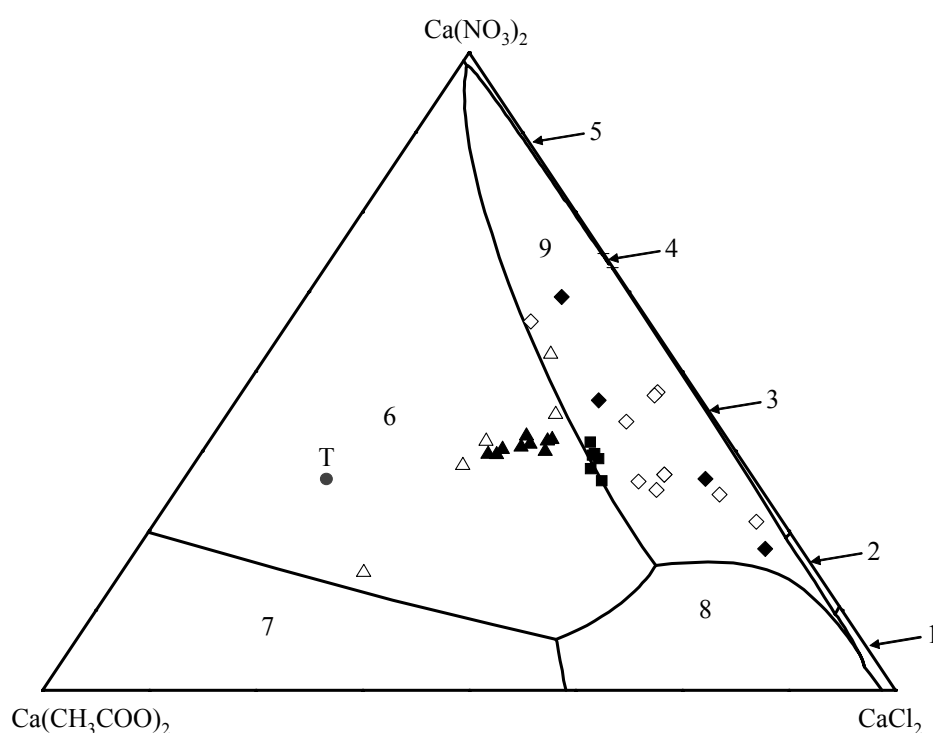


Figure 4: Phase diagram of the quaternary system $\text{Ca}^{2+}\text{--CH}_3\text{COO}^-\text{--Cl}^-\text{--NO}_3^-\text{--H}_2\text{O}$ at 25°C; point T represents the stoichiometric composition of thecotrichite, numbers refer to the following stability fields:

(1) $\text{CaCl}_2 \cdot 6\text{H}_2\text{O}$, (2) $\text{CaCl}_2 \cdot 4\text{H}_2\text{O}$, (3) $\text{CaCl}(\text{NO}_3) \cdot 2\text{H}_2\text{O}$, (4) $\text{Ca}(\text{NO}_3)_2 \cdot 3\text{H}_2\text{O}$, (5) $\text{Ca}(\text{NO}_3)_2 \cdot 4\text{H}_2\text{O}$, (6) $\text{Ca}_2(\text{CH}_3\text{COO})_3(\text{NO}_3) \cdot 2\text{H}_2\text{O}$, (7) $\text{Ca}(\text{CH}_3\text{COO})_2 \cdot \text{H}_2\text{O}$, (8) $\text{Ca}(\text{CH}_3\text{COO})\text{Cl} \cdot 5\text{H}_2\text{O}$, (9) $\text{Ca}_3(\text{CH}_3\text{COO})_3\text{Cl}(\text{NO}_3)_2 \cdot 7\text{H}_2\text{O}$. The meaning of the symbols representing experimental data is as follows: triangles, solutions saturated with respect to (6); diamonds, solutions saturated with respect to (9); squares, solutions saturated with respect to both, (6) and (9); filled triangles and filled squares, solutions prepared by isothermal evaporation (*series 3*); filled diamonds, data provided by COOKSEY [20].

Information about the molalities and water activities of the saturated solutions is not provided by the Jänecke projection of Figure 4. Therefore, the concentrations and water activities of the saturated solutions are depicted in Figure 5 along a cross section in the quaternary diagram corresponding to equimolar mixtures of chloride and nitrate with varying acetate

concentrations. This cross section in the quaternary diagram is shown in the inset in Figure 5. The lower curve represents the total molality expressed as Ca^{2+} concentration of the saturated solutions (m_{Ca}) and the dotted curve represents the corresponding water activities a_w of these solutions. Depending on the mole fraction of acetate, x_{ac} , the solutions are saturated with respect to four different solid phases. At very low acetate mole fractions, $x_{\text{ac}} < 0.0026$ (next to the right y-axis), there exists a very small range of highly concentrated solutions saturated with $\text{CaCl}(\text{NO}_3) \cdot 2\text{H}_2\text{O}$. With increasing acetate mole fraction, thecotrichite ($0.0026 < x_{\text{ac}} < 0.17$) and the double salt $\text{Ca}_2(\text{CH}_3\text{COO})_3(\text{NO}_3) \cdot 2\text{H}_2\text{O}$ ($0.17 < x_{\text{ac}} < 0.63$) are the stable solid phases in contact with the respective saturated solutions. At $x_{\text{ac}} > 0.63$ the pure binary compound $\text{Ca}(\text{CH}_3\text{COO})_2 \cdot \text{H}_2\text{O}$ is the stable solid. Vertical lines mark the compositions of solutions coexisting with two solids in Figure 5. For clarity, no line is drawn for the solution saturated with respect to $\text{CaCl}(\text{NO}_3) \cdot 2\text{H}_2\text{O}$ and $\text{Ca}_3(\text{CH}_3\text{COO})_3\text{Cl}(\text{NO}_3)_2 \cdot 7\text{H}_2\text{O}$. Noticeable is the stability field of thecotrichite (field 9 in Figure 4) covering a strikingly broad range of total molalities from 12.1–3.6 $\text{mol}\cdot\text{kg}^{-1}$ and the corresponding water activities a_w from 0.20–0.76.

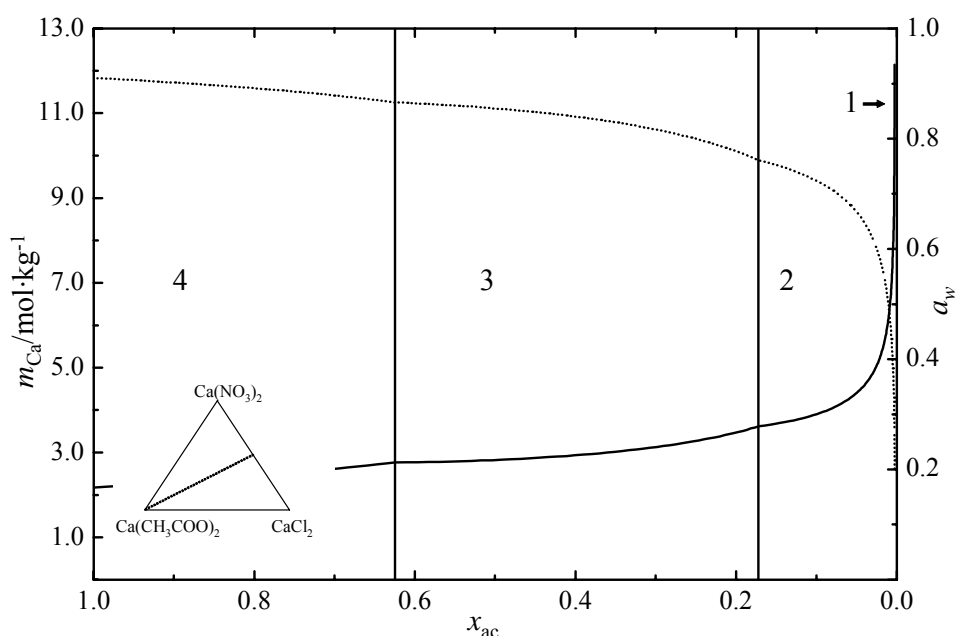


Figure 5: Total molalities, expressed as m_{Ca} , (solid line, left axis) and water activities (dotted line, right axis) of equimolar solutions of chloride and nitrate at 25°C. The solutions are saturated with respect to the salts: (1) $\text{CaCl}(\text{NO}_3) \cdot 2\text{H}_2\text{O}$, (2) $\text{Ca}(\text{CH}_3\text{COO})_3\text{Cl}(\text{NO}_3)_2 \cdot 7\text{H}_2\text{O}$, (3) $\text{Ca}(\text{CH}_3\text{COO})_3(\text{NO}_3) \cdot 2\text{H}_2\text{O}$, (4) $\text{Ca}(\text{CH}_3\text{COO})_2 \cdot \text{H}_2\text{O}$.

A comparison of the calculated solubilities and the experimental data is depicted in Figure 6. Using the molar ratios of the saturated solutions given in Table 2, the total molalities, expressed as $m_{\text{Ca}}(\text{calc})$, of the saturated solutions were calculated. Using the overall experimental errors of 13%, 8% and 5% of the acetate, chloride and nitrate concentrations, the uncertainties of the total molalities $m_{\text{Ca}}(\text{meas})$ were calculated by error propagation. There is a good agreement between the calculated and the measured molalities within these errors. Only in three cases (out of 34) the deviation between calculated and measured concentration exceeds 10% with a maximum deviation of 13.7%. Furthermore, the correct prediction of the $\text{Ca}_2(\text{CH}_3\text{COO})_3(\text{NO}_3) \cdot 2\text{H}_2\text{O}$ solubilities in the full quaternary system (squares and filled squares in Figure 6) is a validation of the model parameters.

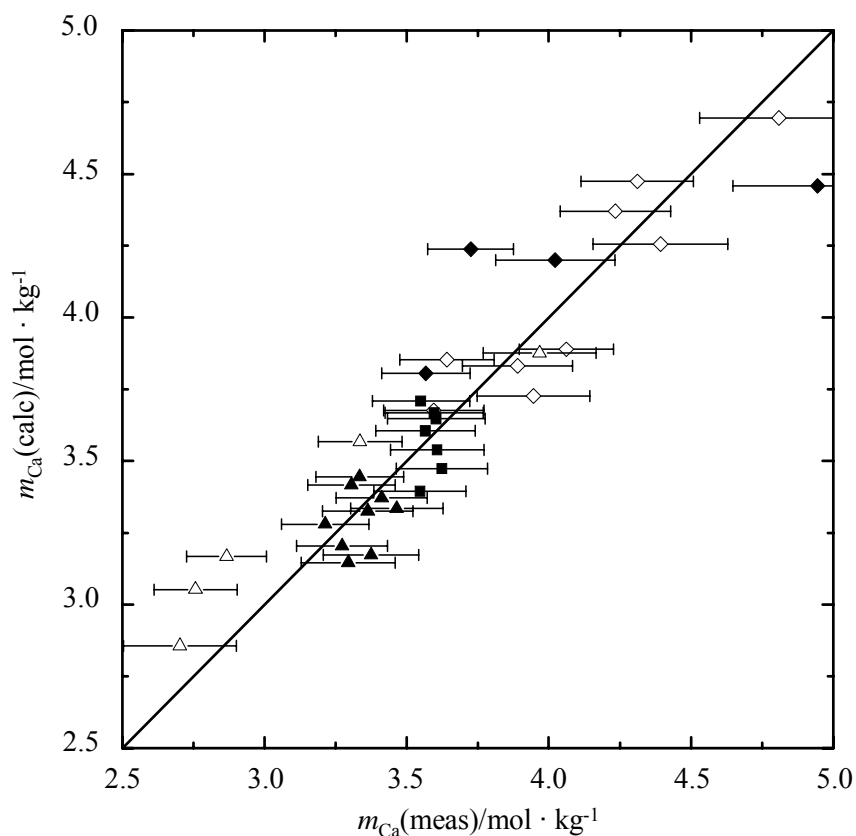


Figure 6: Comparison of calculated, $m_{\text{Ca}}(\text{calc})$, and measured, $m_{\text{Ca}}(\text{meas})$, solubilities at 25°C. Triangles and squares represents solutions saturated with respect to $\text{Ca}(\text{CH}_3\text{COO})_3\text{Cl}(\text{NO}_3)_2 \cdot 7\text{H}_2\text{O}$ and/or $\text{Ca}_2(\text{CH}_3\text{COO})_3(\text{NO}_3) \cdot 2\text{H}_2\text{O}$; meaning of symbols as in Figure 4.

7.6 CONCLUSIONS

Solubilities of the ternary system $\text{Ca}(\text{CH}_3\text{COO})_2\text{--Ca}(\text{NO}_3)_2\text{--H}_2\text{O}$ were used to parameterize the Pitzer model and to determine the equilibrium constant of thecotrichite and the double salt $\text{Ca}_2(\text{CH}_3\text{COO})_3(\text{NO}_3) \cdot 2\text{H}_2\text{O}$. The interaction parameters and the equilibrium constants of the respective solid phases allow for calculating the molalities and water activities of the saturated solution of each possible solution composition and for constructing the solubility diagram of the quaternary system $\text{Ca}(\text{CH}_3\text{COO})_2\text{--CaCl}_2\text{--Ca}(\text{NO}_3)_2\text{--H}_2\text{O}$. Calculated solubilities and location of the stability fields in the Jänecke diagram agree with the experimental data to within the experimental error. This agreement confirms the consistency of the model parameters and the model's ability to predict the real behavior of the $\text{Ca}(\text{CH}_3\text{COO})_2\text{--CaCl}_2\text{--Ca}(\text{NO}_3)_2\text{--H}_2\text{O}$ system.

A lot of information on the crystallization properties of salt mixtures can be readily derived from the phase diagram as discussed above and in previous work [3,4]. Usually, if the solution composition is not equal to composition of the solid phase, the evaporation of water from a mixed salt solution leads to the initial precipitation of only one solid. Saturation with respect to a second solid is reached when a sufficient quantity of water has been removed. Now two salts are in equilibrium with the solution. Hence, the presence of two different phases in salt efflorescence is not surprising. However, there are restrictions. For example, according to the phase diagram there are solutions coexisting with thecotrichite and either one of the two double salts $\text{Ca}_2(\text{CH}_3\text{COO})_3(\text{NO}_3) \cdot 2\text{H}_2\text{O}$ and $\text{Ca}(\text{CH}_3\text{COO})\text{Cl} \cdot 5\text{H}_2\text{O}$ (calclacite) but not with $\text{Ca}(\text{CH}_3\text{COO})_2 \cdot \text{H}_2\text{O}$ (calcium acetate hydrate). Hence, the occurrence of both thecotrichite and calcium acetate hydrate as simultaneous efflorescence products is not possible, whilst the presence of thecotrichite and calclacite may be expected, and has been observed [21].

The ubiquity of the formation of thecotrichite efflorescences on museum objects is easily explained by using the phase diagram. The thecotrichite stability field covers a strikingly broad range of $\text{Cl}^-/\text{NO}_3^-$ ratios and extends closely to the $\text{CaCl}_2\text{--Ca}(\text{NO}_3)_2$ side of the diagram. Hence, adding only a small amount of acetate to a mixed solution of chloride and nitrate is sufficient to reach the stability field of thecotrichite. Only at very high $\text{Cl}^-/\text{NO}_3^-$ ratios (>0.96) leads the acetate deposition to the formation of $\text{Ca}(\text{CH}_3\text{COO})\text{Cl} \cdot 5\text{H}_2\text{O}$ in an object and the formation of $\text{Ca}_2(\text{CH}_3\text{COO})_3(\text{NO}_3) \cdot 2\text{H}_2\text{O}$ only occurs at extremely small Cl^-

/ NO_3^- ratios (<0.008). This is the main reason for the widespread occurrence of thecotrichite efflorescences on museum artifacts.

Acknowledgement

The author is grateful to Brian Cooksey and Lorraine Gibson for providing solubility data.

7.7 REFERENCES

- [1] FITZHUGH E.W., GETTENS R.J., Calclacite and other efflorescent salts on objects stored in wooden museum cases. In: Brill R. (ed.), *Science and Archaeology*, MIT Press Cambridge, **1971**, 91–102.
- [2] TENNENT N.H., BAIRD T., The deterioration of mollusca collections: identification of shell efflorescence, *Stud. Conserv.* **1985**, 3, 73–85.
- [3] GIBSON L.T., COOKSEY B.G., LITTLEJOHN D., LINNOW K., STEIGER M., TENNENT, N.H., The mode of formation of thecotrichite, a widespread calcium acetate chloride nitrate efflorescence. *Stud. Conserv.* **2005**, 50, 284–294.
- [4] LINNOW K., HALSBERGHE L., STEIGER M., Analysis of calcium acetate efflorescences formed on ceramic tiles in a museum environment, *J. Cult. Heritage* **2007**, doi:10.1016/j.culher.2006.09.004
- [5] PITZER K.S., Ion interaction approach: Theory and data correlation. In: Pitzer K.S. (ed.), *Activity Coefficients in Electrolyte Solutions*. CRC Press, Boca Raton, **1991**, 75–153.
- [6] HARVIE C.E., WEARE J.H., The prediction of mineral solubilities in natural waters: the Na–K–Mg–Ca–Cl– SO_4 – H_2O system at 25°C. *Geochim. Cosmochim. Acta* **1980**, 44, 981–997.
- [7] PABALAN R., PITZER K.S., Thermodynamics of concentrated electrolyte mixtures and the prediction of mineral solubilities to high temperatures for mixtures in the system Na–K–Mg–Cl– SO_4 –OH– H_2O . *Geochim. Cosmochim. Acta* **1987**, 51, 2429–2443.
- [8] STEIGER M., BEYER R., DORN J., A Thermodynamic model of the $\text{Na}^+\text{--Ca}^{2+}\text{--Cl}^-\text{--CH}_3\text{COO}^-\text{--H}_2\text{O}$ system. In: Price C. (ed.), *An expert chemical model for determining the environmental conditions needed to prevent salt damage in porous materials*, European Commission project ENV4-CT95-0135, Final Report **2000**, Research Report 11, 45–52.
- [9] EHRET W.F., Ternary Systems, *J. Am. Chem. Soc.* **1932**, 54, 3126–3134.
- [10] DORN J., Experimentelle Bestimmung und thermodynamische Modellierung von Löslichkeitsgleichgewichten im System $\text{Na}^+\text{--Ca}^{2+}\text{--OAc}^-\text{--Cl}^-\text{--H}_2\text{O}$. Dissertation, Fachbereich Chemie, Universität Hamburg, **2003**.
- [11] ARCHER D.G., WANG P., The dielectric constant of water and Debye-Hückel limiting law slopes, *J. Phys. Chem. Ref. Data* **1990**, 19, 371–411.

- [12] PITZER K.S., MAYORGA G., Thermodynamics of electrolytes. II. Activity and osmotic coefficients for strong electrolytes with one or both ions univalent, *J. Phys. Chem.* **1973**, 77, 2300–2308.
- [13] BEYER R., Charakterisierung von binären und ternären Elektrolytsystemen mit Anionen organischer Säuren – Wasseraktivitätsmessungen und thermodynamische Modellierung. Dissertation, Fachbereich Chemie, Universität Hamburg, **2001**.
- [14] STEIGER M., unpublished results.
- [15] VAN ZEGGEREN F., STOREY S.H., The computation of chemical equilibria, Cambridge: University Press, 1970.
- [16] STEIGER M. Salts in porous materials: Thermodynamics of phase transitions, modeling and preventive conservation, *Restor. Build. Monum.* **2005**, 11, 419–431.
- [17] SCHREINEMAKERS F.A.H., Graphische Ableitungen aus den Lösungs-Isothermen eines Doppelsalzes und seiner Komponenten und mögliche Formen der Umwandlungskurven, *Z. Phys. Chem.* **1893**, 11, 75–109.
- [18] COOKSEY B.G., GIBSON L.T., KENNEDY A.R., LITTLEJOHN D., STEWART L., TENNENT N.H., Dicalcium triacetate nitrate dihydrate, *Acta Cryst.* **1999**, C55, 324–326.
- [19] GIBSON L.T., COOKSEY B.G., LITTLEJOHN D., TENNENT N.H., Characterisation of an unusual crystalline efflorescence on an Egyptian limestone relief, *Anal. Chim. Acta* **1997**, 337, 151–164.
- [20] COOKSEY B.G., GIBSON L.T., The synthesis of thecotrichite. Unpublished report, University of Strathclyde, Glasgow, **2000**.
- [21] HALSBERGHE L., Ceramics threatened by acid-induced salts, In: Townsend J.H., Eremin K., Adriaens A. (eds.), *Conservation science 2002*, Archetype Publications, London **2003**, 18–24.

Chapter 8

Deliquescence behavior of the incongruently soluble triple salt thecotrichite

(to be published)

8.1 INTRODUCTION

Single salts pick up water vapor from the surrounding air to form a saturated aqueous solution at a specific humidity, generally referred to as deliquescence humidity RH_{del} . In a multicomponent salt system the deliquescence behavior is much more complicated. Initially, upon water uptake a saturated solution of a composition different from the original salt mixture composition is formed. Further increasing the RH there exists a relative humidity at which the salt mixture dissolves completely. This upper limiting values of RH during the deliquescence of a salt mixture is best referred to as the crystallization humidity, as the precipitation from a salt solution starts if the relative humidity drops below this value. The lower limit of RH , i.e. the humidity at which the mixture starts to pick up moisture and forms a solution is referred to as the mutual deliquescence humidity RH_{mdel} .

Formation of thecotrichite, $\text{Ca}_3(\text{CH}_3\text{COO})_3\text{Cl}(\text{NO}_3)_2 \cdot 7\text{H}_2\text{O}$, is a deleterious process to calcareous museum artifacts [1]. The phase diagram of the underlying quaternary system was constructed by using the Pitzer ion interaction model (see Chapter 7). Using the phase diagram, an understanding of the mode of formation of thecotrichite and the ubiquity of its presence in efflorescences is achieved [2,3]. Thecotrichite is an incongruently soluble salt, which precipitates from solutions with compositions different from its own composition. There exist no unique values for the conditions of deliquescence and crystallization of the salt, i.e. solution composition, concentration and water activity. The conditions for the crystallization of thecotrichite are well known and can be deduced from the phase diagram of the thecotrichite system. The stability field of the compound extends over a broad range of solution compositions and corresponding water activities.

Thecotrichite in contact with a solution of its own composition represents a metastable state, i.e. such a solution is supersaturated with respect to the less soluble double salt $\text{Ca}_2(\text{CH}_3\text{COO})_3(\text{NO}_3) \cdot 2\text{H}_2\text{O}$. The crystallization pathway of the solution can be derived from the phase diagram. The equilibrium pathway of the deliquescence process simply corresponds to the crystallization pathway in reverse direction. In the present chapter the crystallization or deliquescence pathways of three different mixture compositions are investigated in more detail. The solid mixtures that were studied are pure thecotrichite, thecotrichite enriched with acetate and either nitrate or chloride. These mixtures correspond to typical efflorescences of thecotrichite on real museum objects which hardly consist of pure thecotrichite but usually also contain minor amounts of other salts. The deliquescence and crystallization pathways for

the three mixture compositions are calculated based on the quaternary phase diagram and using the same equilibrium model as described in Chapter 7. In addition, the results of an experimental study of the deliquescence pathway of a synthetic thecotrichite sample enriched with acetate and chloride by using humidity and temperature controlled X-ray diffraction (RH-XRD) are presented and compared to the calculated deliquescence pathway.

8.2 EXPERIMENTAL

8.2.1 Synthesis of thecotrichite, $\text{Ca}_3(\text{CH}_3\text{COO})_3\text{Cl}(\text{NO}_3)_2 \cdot 7\text{H}_2\text{O}$

Analytical grade CaCO_3 , $\text{CaCl}_2 \cdot 2\text{H}_2\text{O}$ and $\text{Ca}(\text{NO}_3)_2 \cdot 4\text{H}_2\text{O}$ (Merck, Darmstadt, Germany) were weighed into a mortar in the molar ratio of about 3:1:2. After intimate mixing the sticky mass was filled in a beaker such that the bottom was covered. The beaker was stored in a desiccator above a 50% v/v acetic acid solution saturated with sodium chloride, i.e. in a controlled acetic acid environment at constant relative humidity, so that the humidity was somewhat lower than the equilibrium humidity of a saturated NaCl solution (75.4% RH). The actual RH was not measured with hygrometers due to the high corrosiveness of the environment. The additional lowering of the water vapor pressure of the NaCl solution, caused by acetic acid, could be neglected as the intention was to synthesize thecotrichite, which is known to be formed at a broad range of humidities between 20–76% RH.

White fibrous crystals grew from the mixture during a period of several months. After 18 months the crystals were immersed in acetone three times, filtrated and dried with compressed air to constant weight. To reach an equilibrium state under room conditions, the product was intimately mixed in a mortar.

8.2.2 Instrumentation

Diffraction patterns were obtained on a Bragg-Brentano parafocusing reflection diffractometer (D 5000, Siemens, Germany) using Cu K α -radiation and a position-sensitive detector (PSD) recording data from a 12° 2 θ band at one time. The diffractometer is equipped with an environmental cell consisting of an air-tight cylindrical stainless steel chamber which is fixed to the goniometer. In order to avoid temperature gradients in the chamber, not only the air flow from the humidity generator but also the chamber walls and the sample stage are

thermostated. A Pt-100 sensor and a capacitive humidity sensor (HMP 233, Vaisala, Finland) are used for temperature and humidity control in the chamber. They are placed close to the surface of the samples. The window for the passage of X-rays is sealed with a 6 μm Mylar film. The humidity sensor is connected to the humid air generator. In the temperature range 10–50 °C the humidity control system allows for the variation of the relative humidity (*RH*) in the chamber within a range of 3–97% *RH*. Humidity control is accomplished by mixing of dry and water-saturated air using automated mass-flow controllers. Appropriate mixing ratios of the wet and dry air flows are controlled by a computer program. A more detailed description of the environmental cell and the humidity control system is provided by LINNOW et al. [4].

A SenTix 61 pH electrode (WTW, Weilheim, Germany) and an ion analyzer (EA 940; Orion Research Inc., Boston, USA) were used for the potentiometric titrations of acetate. Argentometric titration with a titro processor 672 (Metrohm, Filderstadt, Germany) was used for the determination of chloride. An UV/VIS spectrophotometer (Lambda 2, Perkin Elmer, Überlingen, Germany) was used to determine nitrate as 4-nitro-2,6-dimethylphenol at 324 nm according to DIN 38 405-D9-2. The calcium concentration was determined by complexometric titration with NaEDTA.

8.2.3 RH-XRD measurement procedure

Equilibration of salt and water vapor can be time-consuming. Hence, small sample sizes are desirable to avoid long equilibration times. Therefore, samples of 100 mg were placed in the humidity chamber in a first series of measurements, despite of the low intensities and the broad peaks in the XRD pattern caused by the small sample thickness. Deliquescence was induced by a sudden increase in the relative humidity to the desired value. Experiments were carried out in the range of 73.7%–88.4% *RH* at 25°C. Subsequently, the humidity was kept constant for at least 60 h to ensure that there was sufficient time for the reaction to complete and to arrive at an equilibrium state. Progress of the transformation reactions was observed by successively recorded diffraction patterns. The XRD patterns were recorded in the range of 10°–70° 2θ . The time required for the collection of the patterns was 24 min, a new measurement was started every hour.

In a second set of measurements the crystallization pathway of one sample of about 100 mg was followed by stepwise decreasing the relative humidity down to 72.7% *RH* at 25°C. The

sample was equilibrated at 83.3% *RH* to ensure that $\text{Ca}(\text{CH}_3\text{COO})_3(\text{NO}_3) \cdot 2\text{H}_2\text{O}$ was present as the sole solid phase. In the first step the humidity was lowered to 76.9%, subsequently, the *RH* was stepwise decreased by increments of about 1% and then kept constant for at least 3 or 4 days. Though the progress of the reaction was also observed during the crystallization, the main purpose of these measurements was the identification of the solid phases present at the end of the reaction.

Care was taken to check the performance of the humidity sensor. Relevant to the present study are high humidities between 74% and 87% *RH*. Therefore, the capacitive sensor was calibrated using saturated solutions of NaCl and K_2SO_4 and their tabulated reference values [5]. The accuracy of the *RH* determinations with the calibrated sensor was tested by repeated measurements on different days of the equilibrium humidity of saturated solutions of NaCl and K_2SO_4 at room temperature. The standard deviations of these *RH* measurements were no larger than 0.9% *RH*.

8.3 RESULTS AND DISCUSSION

8.3.1 Phase analysis and purity

Due to a missing JCPD (Joint committee on diffraction pattern) standard the pattern of the product was identified by comparison with a diffraction pattern of the salt $\text{Ca}_3(\text{CH}_3\text{COO})_3\text{Cl}(\text{NO}_3)_2 \cdot 7\text{H}_2\text{O}$ reported by GIBSON et al. [1]. The diffraction pattern does not provide evidence for the presence of another solid phase except thecotrichite. However, the results of the analysis of the ionic composition of the synthetic sample revealed a significant deviation from the stoichiometric composition of pure thecotrichite. Table 1 lists the contents c_i of each ion i in the sample in $\text{mmol} \cdot \text{g}^{-1}$ according to

$$c_i = w_i / M_i \quad (1)$$

where w_i is the weight fraction of the ions in mg g^{-1} and M_i is the molar mass of the ion. The total equivalent contents of positive and negative charges in $\text{meq} \cdot \text{g}^{-1}$ is then given as

$$E_c = \sum_c c_c \cdot z_{ca} \text{ and } E_a = \sum_a c_a \cdot |z_a| \quad (2)$$

where the subscripts c and a refer to cations and anions, respectively. The charge imbalance B_z may then be expressed as [6]

$$B_z = 2(E_c - E_a)/(E_c + E_a) \quad (3)$$

Values of E_c , E_a and B_z are also listed in Table 1. The imbalance does not reveal any significant deviation on either side.

Figure 1 shows the composition of the synthesized thecotrichite as point E and the composition of pure thecotrichite as point T in the quaternary phase diagram. The synthetic sample is enriched in CH_3COO^- and Cl^- compared to the composition of pure thecotrichite. All possible combinations of solid phases in equilibrium with thecotrichite can be deduced from the phase diagram. Most likely there are $\text{Ca}(\text{CH}_3\text{COO})\text{Cl} \cdot 5\text{H}_2\text{O}$, calclacite, and the double salt $\text{Ca}(\text{CH}_3\text{COO})_3(\text{NO}_3) \cdot 2\text{H}_2\text{O}$ present in the sample. Using a simple mass balance approach, the concentration c_i of each ion i in the efflorescences (in $\text{mmol} \cdot \text{g}^{-1}$) can be expressed in terms of the concentrations a_s of the different solid phases s present in the efflorescences and containing the ions of interest. The mass balance takes the form

$$c_i = a_{th}v_{i,th} + a_{ca}v_{i,ca} + a_d v_{i,d} \quad (4)$$

where a_{th} , a_{ca} and a_d represent the content of thecotrichite, calclacite and the double salt $\text{Ca}(\text{CH}_3\text{COO})_3(\text{NO}_3) \cdot 2\text{H}_2\text{O}$ in the efflorescences (in $\text{mmol} \cdot \text{g}^{-1}$) and $v_{i,th}$, $v_{i,ca}$ and $v_{i,d}$ are the stoichiometric numbers of the ions i in the formula of the solid phases. In the case of five ions, this yields five equations in the three unknowns a_{th} , a_{ca} and a_d which can be determined by ordinary least squares analysis. Results are listed in Table 2 corresponding to a composition of 85.3% w/w thecotrichite, 13.4% w/w calclacite and 1.3% w/w $\text{Ca}(\text{CH}_3\text{COO})_3(\text{NO}_3) \cdot 2\text{H}_2\text{O}$.

Table 1: Measured and calculated ion concentrations c_i (units are $\text{mmol} \cdot \text{g}^{-1}$) and total charge equivalent concentrations E_c and E_a (units are $\text{meq} \cdot \text{g}^{-1}$) and charge imbalances B_z in the synthesized thecotrichite.

	Ca^{2+}	CH_3COO^-	Cl^-	NO_3^-	E_a	E_c	B_z
measured	5.29	5.34	2.16	3.10	10.59	10.60	0.001
calculated	5.30	5.33	2.16	3.10	10.59	10.59	0.000

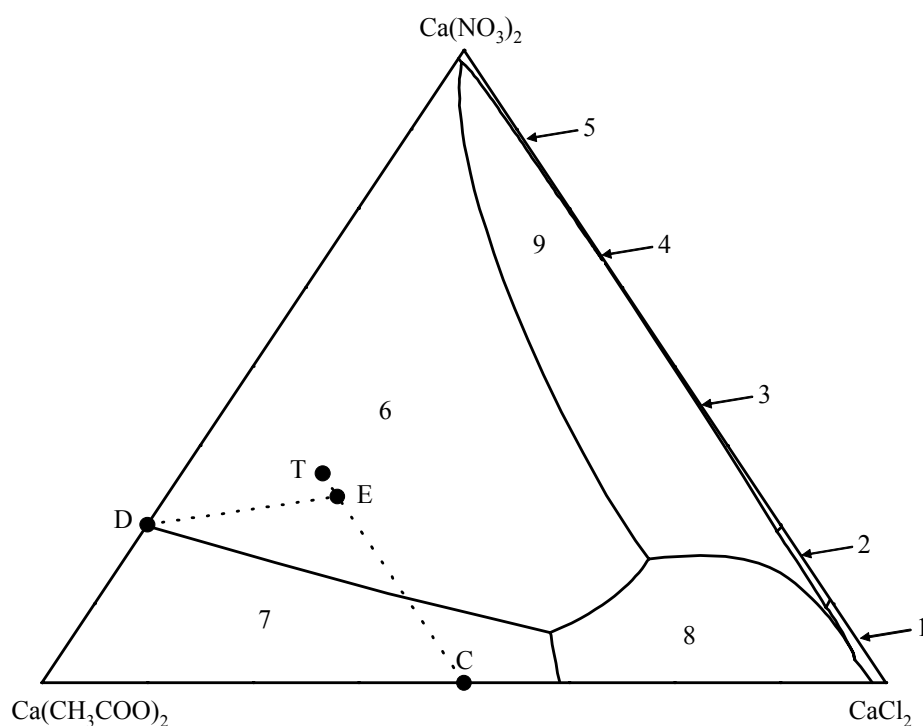


Figure 1: Jänecke projection of the quaternary system $\text{Ca}^{2+}\text{--CH}_3\text{COO}^-\text{--Cl}^-\text{--NO}_3^-\text{--H}_2\text{O}$ at 25°C ; numbers refer to the following stability fields: (1) $\text{CaCl}_2 \cdot 6\text{H}_2\text{O}$, (2) $\text{CaCl}_2 \cdot 4\text{H}_2\text{O}$, (3) $\text{CaCl}(\text{NO}_3) \cdot 2\text{H}_2\text{O}$, (4) $\text{Ca}(\text{NO}_3)_2 \cdot 3\text{H}_2\text{O}$, (5) $\text{Ca}(\text{NO}_3)_2 \cdot 4\text{H}_2\text{O}$, (6) $\text{Ca}_2(\text{CH}_3\text{COO})_3(\text{NO}_3) \cdot 2\text{H}_2\text{O}$, (7) $\text{Ca}(\text{CH}_3\text{COO})_2 \cdot \text{H}_2\text{O}$, (8) $\text{Ca}(\text{CH}_3\text{COO})\text{Cl} \cdot 5\text{H}_2\text{O}$, (9) $\text{Ca}_3(\text{CH}_3\text{COO})_3\text{Cl}(\text{NO}_3)_2 \cdot 7\text{H}_2\text{O}$. Points D, T and C represent the composition of $\text{Ca}_2(\text{CH}_3\text{COO})_3(\text{NO}_3) \cdot 2\text{H}_2\text{O}(\text{cr})$, $\text{Ca}_3(\text{CH}_3\text{COO})_3\text{Cl}(\text{NO}_3)_2 \cdot 7\text{H}_2\text{O}(\text{cr})$, $\text{Ca}(\text{CH}_3\text{COO})\text{Cl} \cdot 5\text{H}_2\text{O}(\text{cr})$, point E represents the composition of the synthetic thecotrichite sample.

Table 2: Concentrations a_s (units are $\text{mmol}\cdot\text{g}^{-1}$) and c_s (units are $\text{mg}\cdot\text{g}^{-1}$) of the solid phases s ; thecotrichite, calclacite and $\text{Ca}(\text{CH}_3\text{COO})_3(\text{NO}_3) \cdot 2\text{H}_2\text{O}$ in the synthetic thecotrichite sample.

	a_s	c_s
$\text{Ca}_3(\text{CH}_3\text{COO})_3\text{Cl}(\text{NO}_3)_2 \cdot 7\text{H}_2\text{O}$	1.532	853
$\text{Ca}(\text{CH}_3\text{COO})\text{Cl} \cdot 5\text{H}_2\text{O}$	0.6267	134
$\text{Ca}_2(\text{CH}_3\text{COO})_3(\text{NO}_3) \cdot 2\text{H}_2\text{O}$	0.0374	13.0

The X-ray powder pattern of the product is compared in Figure 2 to the diffraction patterns of the potential solids in the quaternary system. A diffraction pattern for $\text{Ca}_3(\text{CH}_3\text{COO})_3\text{Cl}(\text{NO}_3)_2 \cdot 7\text{H}_2\text{O}$ was obtained by GIBSON et al. from efflorescences on an Egyptian limestone relief [1]. The pattern for $\text{Ca}_2(\text{CH}_3\text{COO})_3(\text{NO}_3) \cdot 2\text{H}_2\text{O}$ was calculated from the structural data reported by COOKSEY et al. [8] and the pattern for $\text{Ca}(\text{CH}_3\text{COO})\text{Cl} \cdot 5\text{H}_2\text{O}$ (calclacite) is available as JCPDS standard 12-0869. Considering the detection limits of XRD, it is not surprising that the small amount of 1.3 %w/w $\text{Ca}_2(\text{CH}_3\text{COO})_3(\text{NO}_3) \cdot 2\text{H}_2\text{O}$ cannot be identified. An explicit identification of calclacite was also not possible, most likely due to poor crystallinity of the sample and some degree of peak overlap. However, the presence of calclacite in the sample cannot be entirely ruled out from the powder pattern.

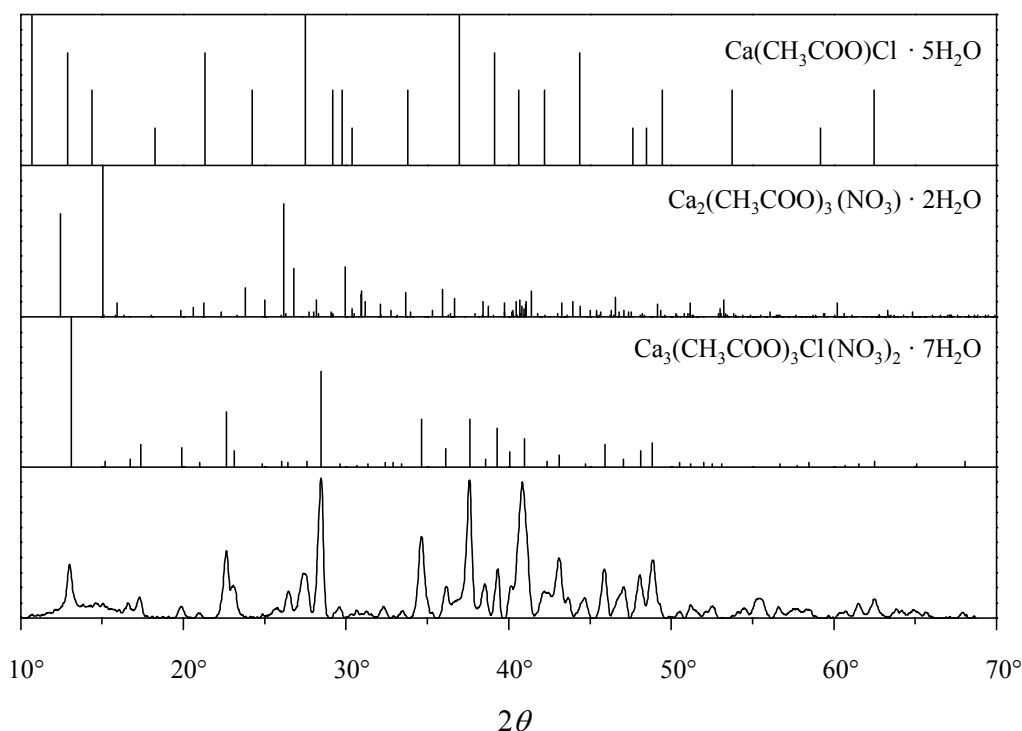


Figure 2: X-ray powder pattern of the synthetic thecotrichite at 40% RH and 25°C compared to the diffraction patterns of $\text{Ca}_3(\text{CH}_3\text{COO})_3\text{Cl}(\text{NO}_3)_2 \cdot 7\text{H}_2\text{O}$ (taken from reference [1]), $\text{Ca}_2(\text{CH}_3\text{COO})_3(\text{NO}_3) \cdot 2\text{H}_2\text{O}$ (pattern calculated from structural data reported in reference [8]) and $\text{Ca}(\text{CH}_3\text{COO})\text{Cl} \cdot 5\text{H}_2\text{O}$ (JCPDS standard 12-0869).

Despite of the impurities, the thecotrichite sample is suitable to investigate the deliquescence behavior of the incongruently soluble triple salt. On the one hand is the product composition located in the stability field of $\text{Ca}_2(\text{CH}_3\text{COO})_3(\text{NO}_3) \cdot 2\text{H}_2\text{O}$ very close to the composition of pure thecotrichite, i.e. a very similar reaction pathway is expected after deliquescence. On the other hand, it is very unlikely that the formation of thecotrichite on a museum object yields exactly the pure salt. Up to now, the pure compound was never found in efflorescences [2,6] but impurities comprising of the salts present in the objects from former usage or treatments were always found [3]. Hence, the synthesized thecotrichite is appropriate to act in place of typical efflorescences on museum objects throughout the investigation of the deliquescence behavior.

8.3.2 Calculated crystallization-deliqescence pathways

Investigations of the deliquescence behavior of incongruent salts are rare. KLAUE [7] used humidity controlled X-ray powder diffraction (RH-XRD) to observe the deliquescence of the incongruently soluble salts $(\text{NH}_4)_4(\text{NO}_3)_2(\text{SO}_4)$ and $(\text{NH}_4)_5(\text{NO}_3)_3(\text{SO}_4)$ in the ternary system NH_4NO_3 – $(\text{NH}_4)_2\text{SO}_4$ – H_2O . He observed complete dissolution of $(\text{NH}_4)_4(\text{NO}_3)_2\text{SO}_4$ with simultaneous crystallization of $(\text{NH}_4)_2\text{SO}_4$ at humidities above 68% RH corresponding to the water activity of a solution saturated with respect to both, $(\text{NH}_4)_4(\text{NO}_3)_2\text{SO}_4$ and $(\text{NH}_4)_2\text{SO}_4$. Similarly, the complete dissolution of $(\text{NH}_4)_5(\text{NO}_3)_3\text{SO}_4$ with simultaneous crystallization of $(\text{NH}_4)_4(\text{NO}_3)_2\text{SO}_4$ occurred at humidities above 64% RH corresponding to the water activity of a solution saturated with respect to both, $(\text{NH}_4)_5(\text{NO}_3)_3\text{SO}_4$ and $(\text{NH}_4)_4(\text{NO}_3)_2\text{SO}_4$.

According to the phase rule, there are invariant points for the coexistence of two solid phases in a ternary system like NH_4NO_3 – $(\text{NH}_4)_2\text{SO}_4$ – H_2O . A quaternary system is more complex, univariant lines represent the coexistence of two solid phases and invariant points represent the coexistence of three solid phases. Point T in phase diagram of the quaternary system Ca^{2+} – CH_3COO^- – Cl^- – NO_3^- – H_2O at 25°C (Figure 1) represents the composition of pure thecotrichite. In contrast, a solution saturated with thecotrichite is metastable, i.e. it is supersaturated with the double salt (cf. Chapter 7). Therefore, the first solid that crystallizes out from a mixed solution of pure thecotrichite upon evaporation is $\text{Ca}_2(\text{CH}_3\text{COO})_3(\text{NO}_3) \cdot 2\text{H}_2\text{O}$. The relative humidity in equilibrium with the corresponding saturated solution is the crystallization humidity of that mixture composition.

For any mixture composition the dissolution and crystallization behavior can be predicted using the phase diagram of the system and the corresponding crystallization humidity can be calculated using an equilibrium model such as the one presented in Chapter 7. In order to predict the behavior of thecotrichite efflorescences as typically found on museum artifacts, calculations of the crystallization pathways were carried out using the model parameters of Chapter 7. Three mixture compositions were studied, i.e. pure thecotrichite and thecotrichite enriched with acetate and either nitrate or chloride. The crystallization pathway of a solution of pure thecotrichite composition is drawn in Figure 3. The amount of solid phases present in the system as a function of RH is expressed as weight fraction $x_{w/w}$ of the total amount of the salts. For a solution of initial composition T, i.e. pure thecotrichite, saturation with $\text{Ca}_2(\text{CH}_3\text{COO})_3(\text{NO}_3) \cdot 2\text{H}_2\text{O}$ is reached at 86.3% RH . Further evaporation causes the continuous crystallization of the double salt whilst the composition of the saturated solution moves along the line shown in the inset of Figure 3. Finally, at 76.1% RH the solution composition reaches the coexistence line of both solid phases, $\text{Ca}_2(\text{CH}_3\text{COO})_3(\text{NO}_3) \cdot 2\text{H}_2\text{O}$ and thecotrichite. This point is the crystallization endpoint or drying point of a solution of that composition. With ongoing evaporation, $\text{Ca}_2(\text{CH}_3\text{COO})_3(\text{NO}_3) \cdot 2\text{H}_2\text{O}$ already precipitated dissolves completely while thecotrichite crystallizes out.

The equilibrium pathway of the deliquescence process of pure thecotrichite corresponds to the crystallization pathway but in reverse direction. Increasing the relative humidity, the formation of a solution starts at 76.1% RH and thecotrichite dissolves completely. Hence, in the particular case of pure thecotrichite, the mutual deliquescence humidity of thecotrichite at 76.1% RH is equal to the equilibrium relative humidity for the complete dissolution of the salt. Nonetheless, due to the fact, that the dissolution of thecotrichite leads to the formation of a solution supersaturated with the double salt $\text{Ca}_2(\text{CH}_3\text{COO})_3(\text{NO}_3) \cdot 2\text{H}_2\text{O}$ the latter salt crystallizes out instead. Only if the RH is further increased the double salt dissolves continuously and the complete dissolution of the salt requires a relative humidity of at least 86.3%.

The crystallization pathway of a solution of composition E as obtained after complete dissolution of the synthetic thecotrichite sample is depicted in Figure 4. The solution of this composition is saturated with $\text{Ca}_2(\text{CH}_3\text{COO})_3(\text{NO}_3) \cdot 2\text{H}_2\text{O}$ at the crystallization humidity $RH_{\text{cr}} = 86.0\%$. Further evaporation causes the continuous crystallization of the double salt whilst the composition of the saturated solution moves along the line shown in the inset of

Figure 4, reaching the univariant coexistence curve of both solid phases, i.e. $\text{Ca}_2(\text{CH}_3\text{COO})_3(\text{NO}_3) \cdot 2\text{H}_2\text{O}$ and thecotrichite, at 75.8% *RH*. In contrast to the crystallization pathway of pure thecotrichite however, this is not the crystallization endpoint of solution E. Further evaporation causes the continuous dissolution of $\text{Ca}_2(\text{CH}_3\text{COO})_3(\text{NO}_3) \cdot 2\text{H}_2\text{O}$ and the simultaneous crystallization of thecotrichite, whilst the composition of the saturated solution moves along the univariant coexistence line of $\text{Ca}_2(\text{CH}_3\text{COO})_3(\text{NO}_3) \cdot 2\text{H}_2\text{O}$ and thecotrichite (see inset of Figure 4). Finally, at 73.7% *RH* the solution composition reaches the coexistence point of the three solid phases $\text{Ca}_2(\text{CH}_3\text{COO})_3(\text{NO}_3) \cdot 2\text{H}_2\text{O}$, thecotrichite and calclacite, which is the drying point of solution E. Water evaporates completely while $\text{Ca}_2(\text{CH}_3\text{COO})_3(\text{NO}_3) \cdot 2\text{H}_2\text{O}$ dissolves and calclacite and thecotrichite crystallize out. The dry residue then consists of 85.3% w/w thecotrichite, 13.4% w/w calclacite and 1.3% w/w $\text{Ca}_2(\text{CH}_3\text{COO})_3(\text{NO}_3) \cdot 2\text{H}_2\text{O}$.

The equilibrium pathway of the deliquescence process of the latter salt mixture can be derived accordingly. Increasing the relative humidity, the deliquescence starts with the complete dissolution of calclacite at 73.7% *RH*, referred to as the mutual deliquescence humidity of a salt mixture of composition E. Thecotrichite continuously dissolves in the range of 73.7%–75.8% *RH*, whilst $\text{Ca}_2(\text{CH}_3\text{COO})_3(\text{NO}_3) \cdot 2\text{H}_2\text{O}$ precipitates. Thecotrichite dissolution is complete at 75.8% *RH*, referred to as the crystallization humidity RH_{cr} of the salt for the mixture composition E. At this point the initial crystallization of $\text{Ca}_2(\text{CH}_3\text{COO})_3(\text{NO}_3) \cdot 2\text{H}_2\text{O}$ is finished and further increasing the humidity leads to the continuous dissolution of the double salt. Finally, reaching the crystallization humidity of the double salt at 86.0% *RH*, the deliquescence of the salt mixture is complete.

The crystallization pathway of a thecotrichite efflorescence enriched in CH_3COO^- and NO_3^- is depicted in Figure 5. The molar ratio of $\text{CH}_3\text{COO}^-/\text{Cl}^-/\text{NO}_3^-$ in the corresponding solution E_2 is 3.3/1/2.4. The course of the saturated solution composition during crystallization is shown in the phase diagram, depicted as inset in Figure 4. Solution E_2 is saturated with respect to $\text{Ca}_2(\text{CH}_3\text{COO})_3(\text{NO}_3) \cdot 2\text{H}_2\text{O}$ at $RH_{\text{cr}} = 86.3\%$. Further evaporation causes continuous crystallization until saturation with thecotrichite is reached at the univariant coexistence line of both solids at 76.0% *RH*. The evaporation pathway continues with $\text{Ca}_2(\text{CH}_3\text{COO})_3(\text{NO}_3) \cdot 2\text{H}_2\text{O}$ dissolution and thecotrichite precipitation as described before. In this case however, due to the excess of nitrate, the composition of the saturated solution moves along the coexistence line into the direction of the nitrate corner of the phase diagram

(see inset in Figure 5). Finally, the solution is also saturated with $\text{Ca}(\text{NO}_3)_2 \cdot 4\text{H}_2\text{O}$ at 49.0% *RH* which is the crystallization endpoint. The dry salt mixture consists of 89.1% w/w thecotrichite, 5.4% w/w $\text{Ca}(\text{NO}_3)_2 \cdot 4\text{H}_2\text{O}$ and 5.5% w/w $\text{Ca}_2(\text{CH}_3\text{COO})_3(\text{NO}_3) \cdot 2\text{H}_2\text{O}$. Hence, the mutual deliquescence humidity of this salt mixture is 49.0% *RH* and the deliquescence starts with the complete dissolution of $\text{Ca}(\text{NO}_3)_2 \cdot 4\text{H}_2\text{O}$. The further course of the deliquescence may be readily derived from Figure 4. Thecotrichite dissolution starts at 49.0% *RH* and is complete at 76.0% *RH*, while $\text{Ca}_2(\text{CH}_3\text{COO})_3(\text{NO}_3) \cdot 2\text{H}_2\text{O}$ crystallizes simultaneously. Above 76.0% *RH* starts the dissolution of the double salt which is complete at 86.3%.

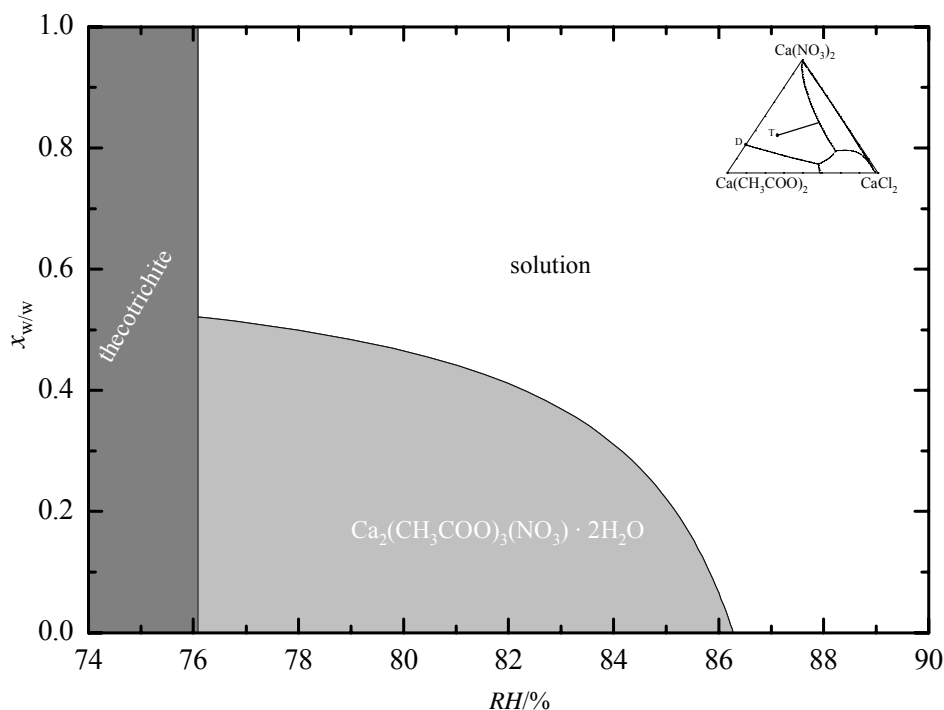


Figure 3: Crystallization and deliquescence pathway of pure thecotrichite in the quaternary phase diagram $\text{Ca}(\text{CH}_3\text{COO})_2\text{--CaCl}_2\text{--Ca}(\text{NO}_3)_2\text{--H}_2\text{O}$ at 25°C, expressed as weight fraction $x_{w/w}$ versus humidity. The inset shows the course of the saturated solution composition (solid line) in the triangular Jänecke projection.

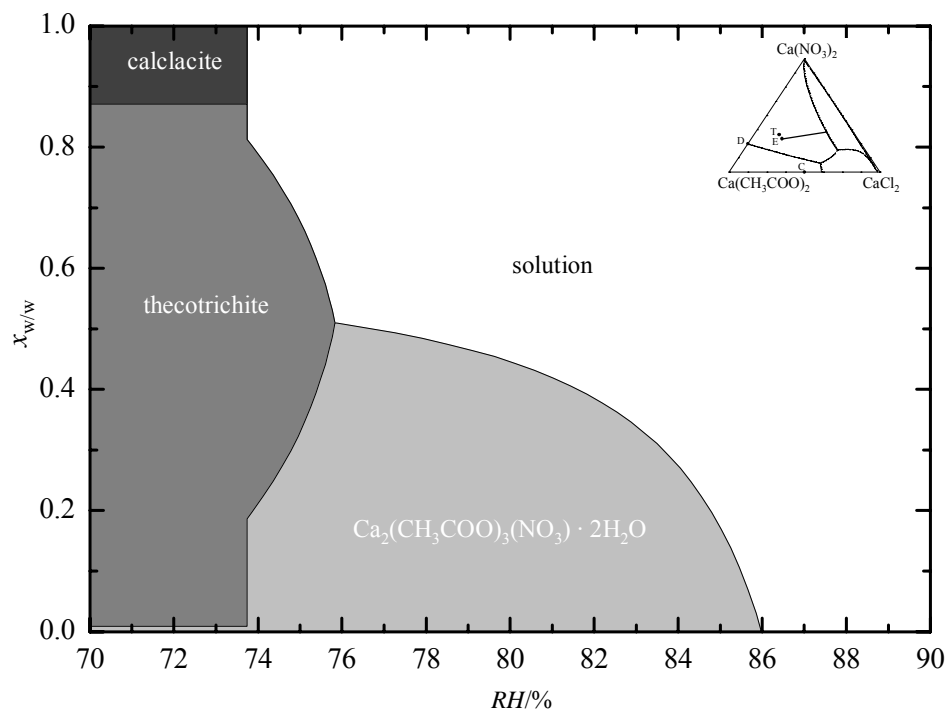


Figure 4: Crystallization and deliquescence pathway of synthetic sample E in the quaternary phase diagram $\text{Ca}(\text{CH}_3\text{COO})_2\text{--CaCl}_2\text{--Ca}(\text{NO}_3)_2\text{--H}_2\text{O}$ at 25°C , expressed as weight fraction $x_{w/w}$ versus humidity. The course of the saturated solution composition (solid line) is depicted as inset in the triangular Jänecke projection.

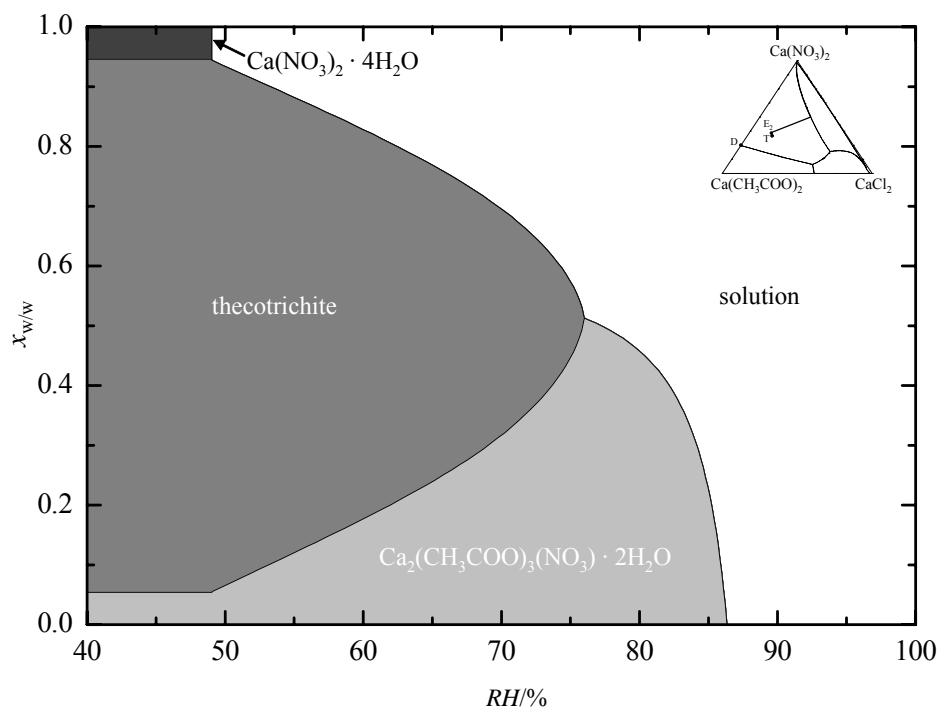


Figure 5: Crystallization and deliquescence pathway of an efflorescence E_2 in the quaternary phase diagram $\text{Ca}(\text{CH}_3\text{COO})_2\text{--CaCl}_2\text{--Ca}(\text{NO}_3)_2\text{--H}_2\text{O}$ at 25°C , expressed as weight fraction $x_{w/w}$ versus humidity. The course of the saturated solution (solid line) is depicted as inset in the triangular Jänecke projection.

8.3.3 Humidity controlled X-ray diffraction

The results of the in situ XRD investigation of the deliquescence reaction at different relative humidities are summarized in Table 3. The RH-XRD measurements confirmed deliquescence pathways inasmuch as the dissolution of thecotrichite was accompanied by $\text{Ca}_2(\text{CH}_3\text{COO})_3(\text{NO}_3) \cdot 2\text{H}_2\text{O}$ crystallization (see Table 3). Due to missing JCPD standards, $\text{Ca}_2(\text{CH}_3\text{COO})_3(\text{NO}_3) \cdot 2\text{H}_2\text{O}$ was identified by comparison with a powder pattern calculated from structural data [8] of the double salt. Thecotrichite was identified as described before.

The humidities at which thecotrichite or $\text{Ca}_2(\text{CH}_3\text{COO})_3(\text{NO}_3) \cdot 2\text{H}_2\text{O}$ dissolve completely are of particular interest. It was therefore attempted to use the same extrapolation technique that was used in a previous study [9] to determine deliquescence and hydration humidities of single salts. This extrapolation technique is based on an exponential relation between the relative humidity during the reaction and the total reaction time t_c :

$$RH = A \cdot \exp(B/t_c) \quad (5)$$

Linearization of Equation (1) yields the following expression:

$$\ln RH = \ln A + B/t_c \quad (6)$$

where B is the slope and $\ln A$ is the intercept. According to the GIBBS phase rule a crystalline solid and its saturated solution can coexist indefinitely at equilibrium. Therefore, the reaction time t_c for the complete deliquescence approaches infinity as the relative humidity approaches the equilibrium value, i.e. RH_{del} in the case of a deliquescence reaction. This forms the basis for the extrapolation technique for the determination of equilibrium humidities as applied in the previous work. Extrapolation to $1/t_c = 0$, i.e. t_c equal to infinity, then yields the desired deliquescence humidity as $\ln A = \ln RH_{\text{del}}$.

The coexistence of a congruently soluble salt with the saturated solution of its own composition represents a thermodynamically stable state. In contrast, the coexistence of an incongruently soluble salt with the saturated solution of its own composition is a metastable state. For example, a solution saturated with thecotrichite is supersaturated with respect to $\text{Ca}_2(\text{CH}_3\text{COO})_3(\text{NO}_3) \cdot 2\text{H}_2\text{O}$. Hence, thecotrichite cannot coexist indefinitely with its saturated solution and the dissolution of the salt leads to a consecutive reaction, i.e. the precipitation of $\text{Ca}_2(\text{CH}_3\text{COO})_3(\text{NO}_3) \cdot 2\text{H}_2\text{O}$. As discussed before, however, thecotrichite can coexist in stable equilibrium with a saturated solution and two additional solid phases at the

mutual deliquescence humidity RH_{mdel} , i.e. $\text{Ca}_2(\text{CH}_3\text{COO})_3(\text{NO}_3) \cdot 2\text{H}_2\text{O}$ and calclacite in the case of mixture composition E. Furthermore thecotrichite can coexist indefinitely in equilibrium with a saturated solution and crystalline $\text{Ca}_2(\text{CH}_3\text{COO})_3(\text{NO}_3) \cdot 2\text{H}_2\text{O}$ at the crystallization humidity of thecotrichite. The determination of the mutual deliquescence humidity of the salt mixture E was impossible, because calclacite could not be detected in the XRD pattern of sample E. Hence, the total reaction time for the calclacite dissolution could not be measured. However, thecotrichite peaks can be unambiguously identified in the XRD patterns offering the possibility to use the extrapolation technique for the determination of its crystallization humidity.

The complete reaction times t_c for the complete dissolution of thecotrichite were determined using successively recorded RH-XRD patterns. As an example, XRD patterns measured during the deliquescence of thecotrichite at 80% RH are depicted in Figure 6. In this experiment, a sample of about 100 mg of the synthetic thecotrichite was placed in the humidity chamber at 80.0% RH at the reaction time $t = 0$. Subsequently, XRD patterns were recorded every hour. In the initial XRD pattern only peaks of thecotrichite are present and no significant changes were observed during the initial three hours. First peaks of the product phase $\text{Ca}_2(\text{CH}_3\text{COO})_3(\text{NO}_3) \cdot 2\text{H}_2\text{O}$ were noticeable after 7 h (see Figure 6) and the subsequent patterns revealed the presence of both phases. Major thecotrichite peaks are still detectable in the XRD pattern collected at 16.0–16.4 h. Complete absence of the peaks was visually detected in the pattern recorded from 17.0–17.4 h. Subsequently, no further changes could be detected in the XRD patterns over a time period of 60 h. Hence, the thecotrichite dissolution reaction was complete after 16.4–17.0 h, i.e. corresponding to a total reaction time $t_c = 16.7 \pm 0.3$ h where the uncertainty reflects the limited time resolution of the XRD measurements. Due to the difficulties in the unambiguous detection of the complete disappearance of a peak in the XRD patterns the true uncertainty is somewhat larger. A maximum error of ± 1 h in the determination of t_c is estimated for the reactions studied in the present work. The total reaction times t_c of the thecotrichite dissolution were determined for each experimental humidity by visual detection of the complete absence of thecotrichite peaks in the XRD pattern as described before. The results are listed in Table 3.

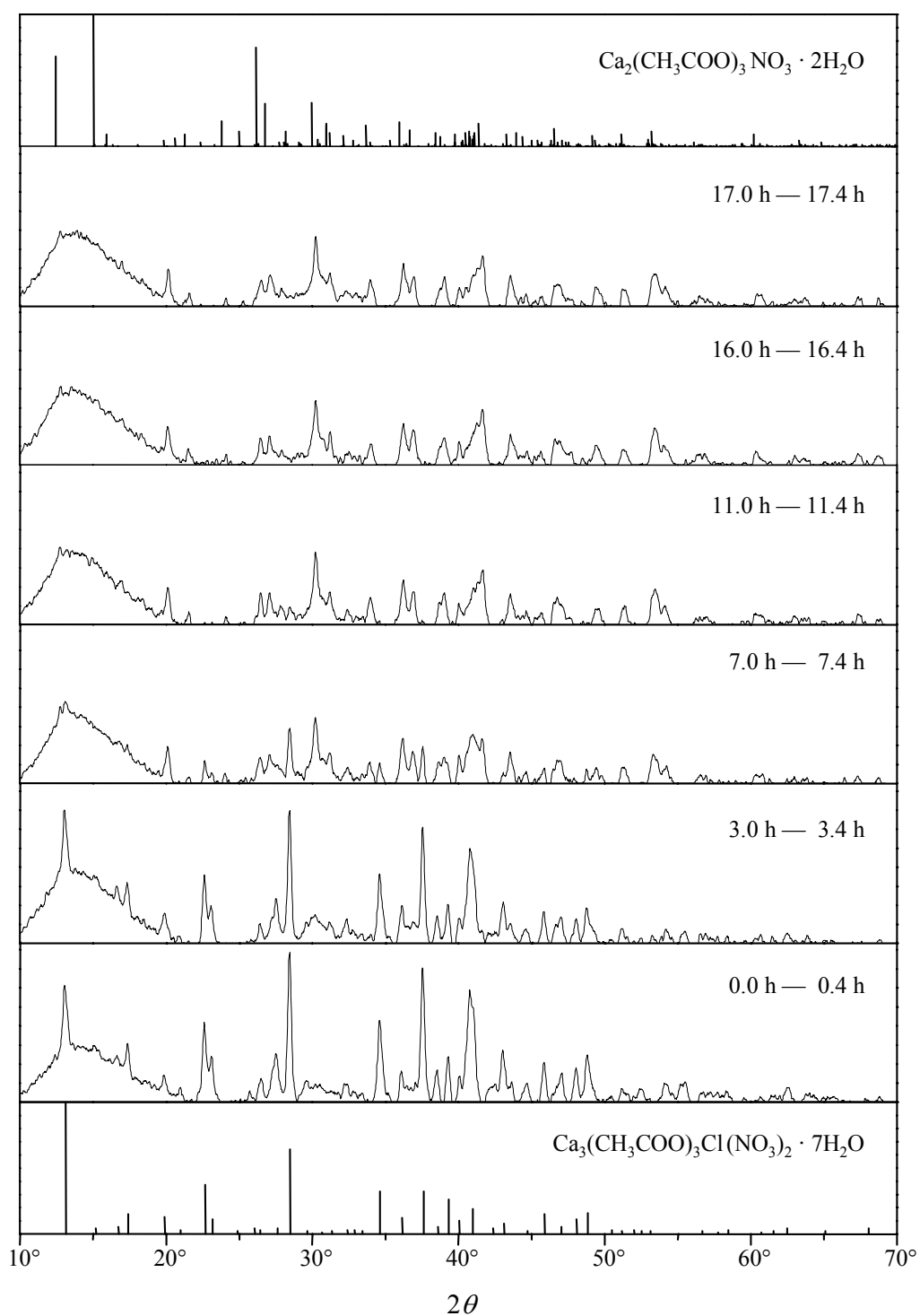


Figure 6: Evolution of the XRD patterns of $\text{Ca}_3(\text{CH}_3\text{COO})_3\text{Cl}(\text{NO}_3)_2 \cdot 7\text{H}_2\text{O}$ and $\text{Ca}_2(\text{CH}_3\text{COO})_3(\text{NO}_3) \cdot 2\text{H}_2\text{O}$ during the deliquescence reaction at 25°C and 80.0% RH.

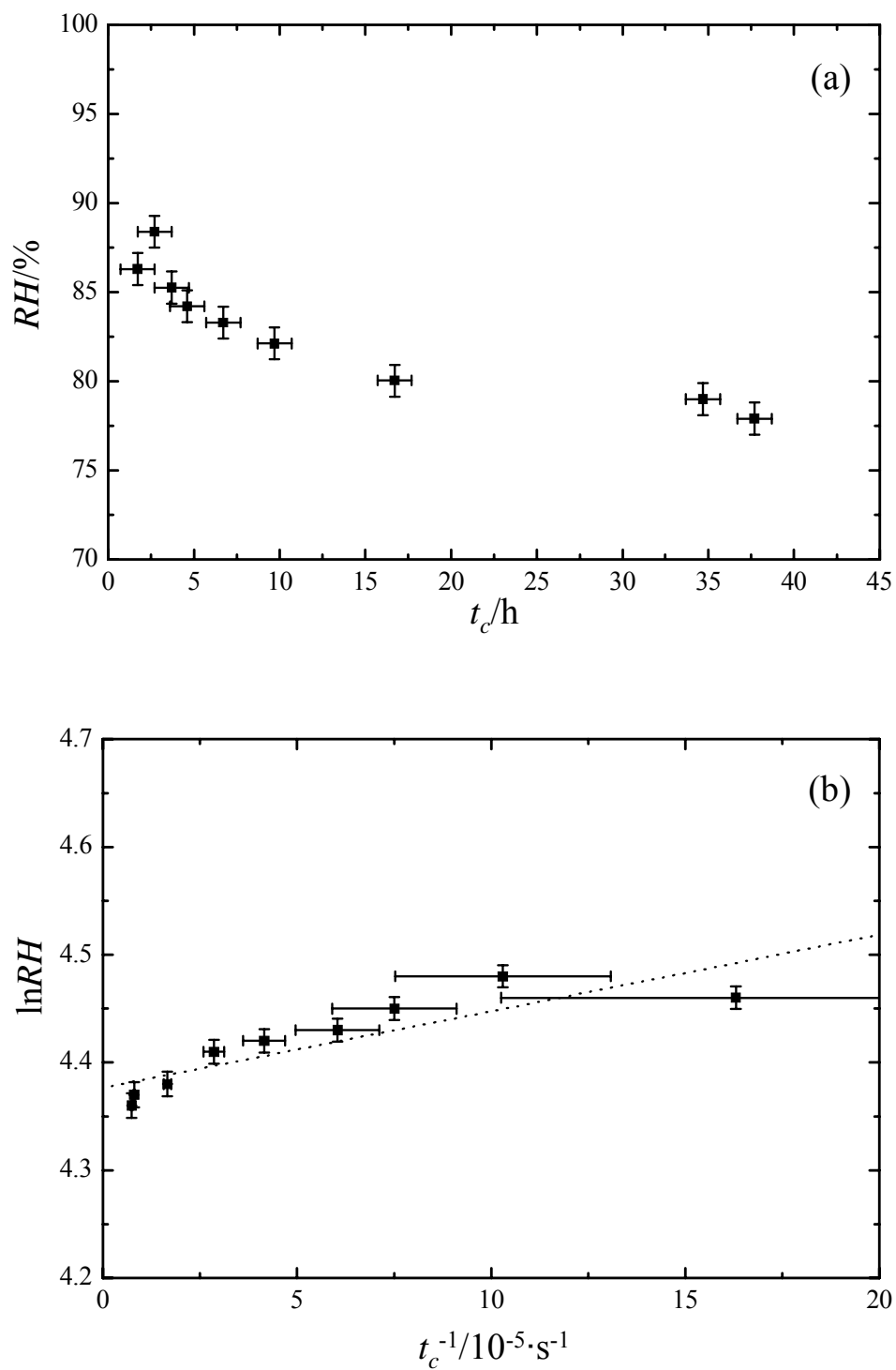


Figure 7: Plot of RH vs. t_c (a) and $\ln RH$ vs. t_c^{-1} (b) of the thecotrichite dissolution at 25°C; vertical error bars correspond to the uncertainty of the RH measurements (one standard deviation on either side), horizontal error bars reflect the maximum uncertainty in the determination of t_c from the XRD patterns. Linear regression is drawn as dotted line.

The course of RH versus t_c and $\ln RH$ versus t_c^{-1} is depicted in Figure 7. Obviously, there are significant deviations from the linear relation of Eq. (6) represented by the dotted regression line. In the case of a single salt, the deliquescence rate is affected by two processes: (1) the dissolution of the solid phase in the solution film that is formed initially and (2) the transfer of water vapor from the surrounding atmosphere. These influences yield the exponential relation between RH versus t_c , i.e. Eqs. (5) and (6). In the case of the thecotrichite dissolution, the relation is distorted by additional processes, the dissolution of calclacite and the crystallization of the double salt $\text{Ca}_2(\text{CH}_3\text{COO})_3(\text{NO}_3) \cdot 2\text{H}_2\text{O}$. Obviously, the crystallization humidity of thecotrichite cannot be determined by extrapolation. During the deliquescence process of sample E, the double salt $\text{Ca}_2(\text{CH}_3\text{COO})_3(\text{NO}_3) \cdot 2\text{H}_2\text{O}$ is initially formed but later redissolves (see Figure 4). Therefore, the determination of the equilibrium humidity by using the extrapolation technique was improper, because it proved to be quite difficult to determine the time t_0 at which the dissolution of $\text{Ca}_2(\text{CH}_3\text{COO})_3(\text{NO}_3) \cdot 2\text{H}_2\text{O}$ starts.

Table 3: Results of the humidity controlled X-ray measurements with increasing humidity at 25°C.

$RH/\%$	Thecotrichite	$\text{Ca}_2(\text{CH}_3\text{COO})_3(\text{NO}_3) \cdot 2\text{H}_2\text{O}$	
	t_c/h	formation	dissolution
73.7	— ⁽¹⁾	—	—
74.8	incomplete	—	—
76.9	incomplete	—	—
77.9	37.7	+ ⁽²⁾	—
79.0	31.7	+	—
80.0	16.7	+	—
82.1	9.7	+	—
83.3	6.7	+	—
84.2	4.7	+	—
85.4	3.7	+	—
86.5	1.7	+	—
88.6	2.7	+	+

(1) no reaction

(2) reaction observed

Despite of these problems, the results summarized in Table 3 still offer valuable clues on the dissolution and crystallization behavior of thecotrichite and $\text{Ca}_2(\text{CH}_3\text{COO})_3(\text{NO}_3) \cdot 2\text{H}_2\text{O}$. No deliquescence could be observed in RH-XRD at 73.7% *RH*, while a sudden increase in *RH* to 76.9% resulted in a significant diminution of the thecotrichite peak intensities. However, the crystallization of $\text{Ca}_2(\text{CH}_3\text{COO})_3(\text{NO}_3) \cdot 2\text{H}_2\text{O}$ could not be detected within 63 h. A comparison of the initial XRD pattern with the pattern after 65 h is depicted in Figure 8. At higher humidity, in the range from 77.9% to 88.6% *RH*, both the complete dissolution of thecotrichite and the formation of the double salt could be detected.

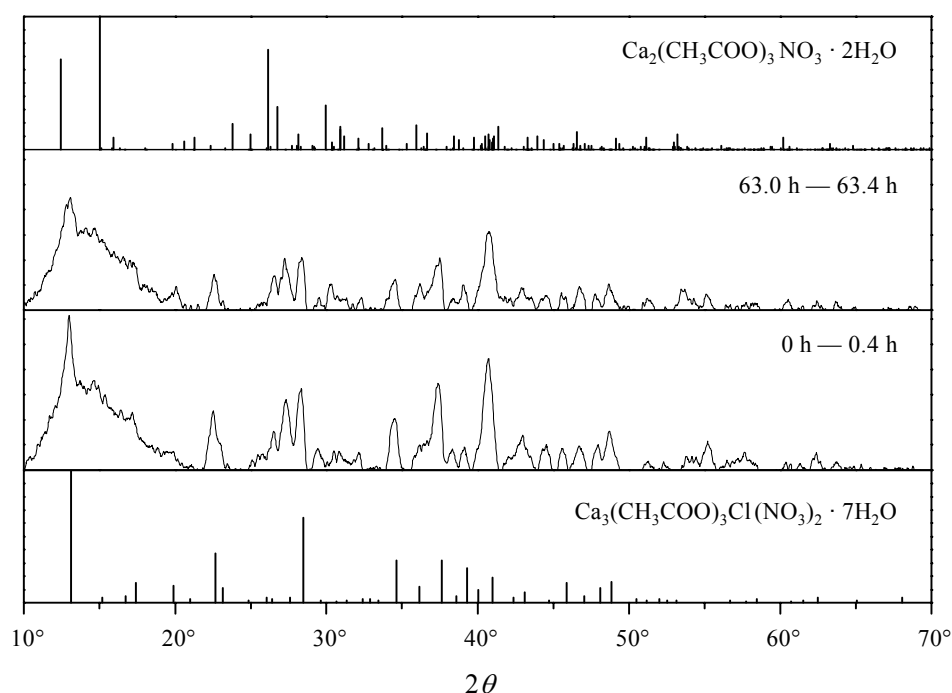


Figure 8: Dissolution of thecotrichite in the synthetic sample at 76.9%*RH* and 25°C.

The complete dissolution of $\text{Ca}_2(\text{CH}_3\text{COO})_3(\text{NO}_3) \cdot 2\text{H}_2\text{O}$ was observed at 86.5 % and 88.4% *RH* but did not occur within 70 h at 85.4% *RH*. Taking the average of the highest humidity at which complete dissolution was not observed and the lowest humidity at which complete dissolution of the double salt occurred yields $RH_{\text{cr}} = 86.0 \pm 0.5\%$ for the crystallization humidity, i.e. the lowest relative humidity at which the salt mixture E remains completely dissolved. Considering the additional error caused by the measurement uncertainty of the humidity sensor in the RH-XRD instrument, a maximum error of $\pm 1.4\%$ *RH* is estimated for the crystallization humidity of $\text{Ca}_2(\text{CH}_3\text{COO})_3(\text{NO}_3) \cdot 2\text{H}_2\text{O}$.

The RH-XRD observations of the crystallization pathway of a solution of composition E during a continuous decrease in *RH* are summarized in Table 4 and compared to the model predictions. Crystallization experiments during decreasing relative humidity revealed slightly different results than the XRD observations during the deliquescence of the salt mixture at increasing *RH*. In agreement with the model predictions, $\text{Ca}_2(\text{CH}_3\text{COO})_3(\text{NO}_3) \cdot 2\text{H}_2\text{O}$ was identified as sole solid phase at 76.9%–74.8% *RH*, whilst both phases, thecotrichite and $\text{Ca}_2(\text{CH}_3\text{COO})_3(\text{NO}_3) \cdot 2\text{H}_2\text{O}$, were detected at 73.7% *RH*. The measurements during decreasing *RH* also confirm the predicted redissolution of $\text{Ca}_2(\text{CH}_3\text{COO})_3(\text{NO}_3) \cdot 2\text{H}_2\text{O}$ below 73.7% *RH*, i.e. the double salt was no longer detectable at 72.7% *RH*. The crystallization of thecotrichite however, was observed at a lower *RH* than predicted by the model, i.e. the continuous crystallization of thecotrichite below 75.8% *RH* was not observed in the XRD measurements.

The results of the XRD observations during the deliquescence of the salt mixture are also compared to the model predictions in Table 4. There is a very good qualitative agreement at relative humidities above 77.9%. In particular, the endpoint of the deliquescence process, i.e. the experimental crystallization humidity of $RH_{\text{cr}} = 86.0 \pm 1.4\%$ for the double salt $\text{Ca}_2(\text{CH}_3\text{COO})_3(\text{NO}_3) \cdot 2\text{H}_2\text{O}$ agrees nicely with the calculated value. At lower *RH* however, deviations of the XRD observations from the model predictions are obvious. In contrast to the model predictions, only one solid phase, thecotrichite, could be detected between 73.7% and 76.9% *RH*. On the one hand, the deviations of the XRD results from the model predictions are related to the very limited sensitivity of the XRD technique. For instance, the very small amount of the double salt $\text{Ca}_2(\text{CH}_3\text{COO})_3(\text{NO}_3) \cdot 2\text{H}_2\text{O}$ in the dry salt mixture of only 1.3% w/w is clearly below the detection limit of the XRD method. Obviously however, the method also fails to detect calclacite in the dry salt mixture, although the concentration should be sufficient to allow its detection. Other deviations of the observed reaction pathways from the model predictions reflect kinetic influences. Approaching equilibrium from the high humidity side, i.e. in the experiments at decreasing *RH*, the observed phase transitions occur at somewhat lower relative humidities than expected. For example, thecotrichite was only observed at 73.7% *RH* by XRD but should be already present at 74.8% (see Table 4). Most likely, this behavior is due to a certain degree of supersaturation that is required for nucleation and growth to occur. Such a behavior is well known from experiments with levitated droplets which can form highly supersaturated solutions before a solid crystallizes out [10].

Table 4: Calculated solid phases and final observed solid phase of the RH-XRD measurements at 25°C.

<i>RH</i> /%	predicted solid phases	observed solid phases	
		with increasing <i>RH</i>	with decreasing <i>RH</i>
40.0	calc/th/tri ⁽¹⁾	th	th
72.7	calc/th/tri	n.a. ⁽²⁾	th
73.7	calc/th/tri	th	th/tri
74.8	th/tri	th	tri
75.9	tri	n.a.	tri
76.9	tri	th	tri
77.9	tri	tri	n.a.
79.0	tri	tri	n.a.
80.0	tri	tri	n.a.
82.1	tri	tri	n.a.
83.3	tri	tri	n.a.
84.2	tri	tri	n.a.
85.4	tri	tri	n.a.
>86.0	solution	solution	n.a.

(1) th: $\text{Ca}_3(\text{CH}_3\text{COO})_3\text{Cl}(\text{NO}_3)_2 \cdot 7\text{H}_2\text{O}$, tri: $\text{Ca}_2(\text{CH}_3\text{COO})_3(\text{NO}_3) \cdot 2\text{H}_2\text{O}$, calc: $\text{Ca}(\text{CH}_3\text{COO})\text{Cl} \cdot 5\text{H}_2\text{O}$

(2) not analyzed

Approaching equilibrium from below, i.e. in the experiments with increasing *RH*, there appears to be a tendency to overestimate the equilibrium humidities compared to the model predictions. For example, the dissolution of thecotrichite should be complete at 76.9% but the salt was still detected in the mixture at this *RH*. For a deliquescence reaction, two possible explanations might be considered: (1) condensation of water vapor on the crystalline solids might require a certain degree of supersaturation of the vapor phase, or, (2) the dissolution of the solid in the liquid film that is initially formed requires sufficient undersaturation of the solution to proceed with appreciable rate. The situation is more complicated in the intermediate range of the deliquescence process where one solid, thecotrichite, dissolves while a second solid, $\text{Ca}_2(\text{CH}_3\text{COO})_3(\text{NO}_3) \cdot 2\text{H}_2\text{O}$, crystallizes out. In this case, the overall kinetics is influenced by the rates of two consecutive processes. The rates of the two reactions are both affected by the relative humidity. It is difficult to predict the combined influence on the overall rate. However, the XRD measurements indicate that both processes, the

dissolution of thecotrichite and the subsequent crystallization of $\text{Ca}_2(\text{CH}_3\text{COO})_3(\text{NO}_3) \cdot 2\text{H}_2\text{O}$, are affected by reaction kinetics. Obviously, the conditions of the RH-XRD experiments in the present work were not sufficient to entirely avoid kinetic influences during the observed phase transitions reactions. Nonetheless, the qualitative agreement of the experimental results and the model calculations is considered reasonable. This is an important result as under real conditions at buildings or in the museum environment these processes will be affected by the same kinetic influences. In particular, the deliquescence of sample E under non-equilibrium conditions has important implications. It follows from mass balance considerations that the deliquescence of sample E, i.e. the complete dissolution of calclacite and $\text{Ca}_2(\text{CH}_3\text{COO})_3(\text{NO}_3) \cdot 2\text{H}_2\text{O}$ and the partial dissolution of thecotrichite, always leads to a solution that is supersaturated with respect to $\text{Ca}_2(\text{CH}_3\text{COO})_3(\text{NO}_3) \cdot 2\text{H}_2\text{O}$. This situation is quite similar to the deliquescence of $\text{MgSO}_4 \cdot \text{H}_2\text{O}$ discussed in detail in Chapter 5. The deliquescence of $\text{MgSO}_4 \cdot \text{H}_2\text{O}$ yields a solution supersaturated with respect to $\text{MgSO}_4 \cdot 6\text{H}_2\text{O}$. In agreement with theoretical considerations [11] it was observed that the crystallization of $\text{MgSO}_4 \cdot 6\text{H}_2\text{O}$ from supersaturated solution generates stress in the pore space resulting in considerable deformations of glass frits (cf. Chapter 5). Similar behavior has to be expected for the crystallization of the double salt $\text{Ca}_2(\text{CH}_3\text{COO})_3(\text{NO}_3) \cdot 2\text{H}_2\text{O}$ from supersaturated solutions and it is concluded that the deliquescence of thecotrichite efflorescences has to be considered as a potential damage process in porous materials

8.4 CONCLUSIONS

The crystallization pathways of three salt mixture compositions, containing thecotrichite, were derived from the phase diagram as typical examples of thecotrichite efflorescences on museum objects. The model parameters presented in Chapter 7 were used to calculate the equilibrium humidities of the saturated solutions. The mutual deliquescence humidity of pure thecotrichite is 76.1% *RH*, at this humidity simultaneous crystallization of $\text{Ca}_2(\text{CH}_3\text{COO})_3(\text{NO}_3) \cdot 2\text{H}_2\text{O}$ occurs. The crystallization humidity at which complete dissolution of $\text{Ca}_2(\text{CH}_3\text{COO})_3(\text{NO}_3) \cdot 2\text{H}_2\text{O}$ occurs is 86.3% *RH*. The crystallization humidity of mixed efflorescences containing thecotrichite varies within the stability field of thecotrichite depending on the nature and the amount of the impurities. Dissolution of thecotrichite with simultaneous crystallization of $\text{Ca}_2(\text{CH}_3\text{COO})_3(\text{NO}_3) \cdot 2\text{H}_2\text{O}$ do not occur at a specific value but rather across a range of relative humidities along the coexistence line of

thecotrichite and $\text{Ca}_2(\text{CH}_3\text{COO})_3(\text{NO}_3) \cdot 2\text{H}_2\text{O}$. The lower limit of this range is the mutual deliquescence humidity, which is also strongly affected by the nature and the amount of the impurities. The upper limit of this critical RH range is only slightly affected by the presence of impurities and is equal to the crystallization humidity of the respective salt mixture.

The RH-XRD measurements revealed, that the deliquescence kinetics of incongruently soluble salts such as thecotrichite is different from the deliquescence behavior of single salts. In this case, the application of the extrapolation technique that was successfully used for single salts in a previous study [9] was not possible. Nonetheless, dynamic RH-XRD measurements were successfully applied to determine the crystallization humidity of $\text{Ca}_2(\text{CH}_3\text{COO})_3(\text{NO}_3) \cdot 2\text{H}_2\text{O}$. The very good agreement of the value of $RH_{\text{cr}} = 86.0 \pm 1.4\%$ obtained for its complete dissolution with the calculated equilibrium humidity confirms the accuracy of the model parameters described in Chapter 7. Due to the detection limits of the X-ray powder diffraction method and the uncertainty of the humidity measurements was a precise determination of the mutual deliquescence humidity and the crystallization humidity of thecotrichite not possible. Nonetheless, it was found that the qualitative crystallization and deliquescence behavior agrees generally with the calculated crystallization pathway.

It was shown that the crystallization proceeds in accordance with the calculated crystallization pathway, i.e. thecotrichite crystallize with simultaneous dissolution of the double salt $\text{Ca}_2(\text{CH}_3\text{COO})_3(\text{NO}_3) \cdot 2\text{H}_2\text{O}$ under conditions of decreasing humidity. In contrast, it was predicted by model calculations and confirmed by experiment that thecotrichite dissolution and simultaneous crystallization of $\text{Ca}_2(\text{CH}_3\text{COO})_3(\text{NO}_3) \cdot 2\text{H}_2\text{O}$ are induced by increasing the relative humidity above 73.7%. It was further shown that supersaturated solutions of $\text{Ca}_2(\text{CH}_3\text{COO})_3(\text{NO}_3) \cdot 2\text{H}_2\text{O}$ are formed during this deliquescence process. This is an important result as crystals growing in pores can only generate pressure if they are in contact with a solution of sufficient supersaturation. The situation is quite similar to the deliquescence of $\text{MgSO}_4 \cdot \text{H}_2\text{O}$ yielding a solution supersaturated with respect to $\text{MgSO}_4 \cdot 6\text{H}_2\text{O}$. This supersaturation was sufficient to generate stress in a porous glass frits as discussed in detail in Chapter 5.

Besides thecotrichite and calclacite there exist many incongruently soluble double salts in the complex salt systems that are typically found in salt contaminated building materials. Among other salts, darapskite, $\text{Na}_3\text{SO}_4\text{NO}_3 \cdot \text{H}_2\text{O}$, glaserite, $\text{Na}_2\text{K}_6(\text{SO}_4)_4$, and astrakanite,

$\text{Na}_2\text{Mg}(\text{SO}_4)_2 \cdot 4\text{H}_2\text{O}$ are well known examples. The deliquescence of these salts also leads to the formation of supersaturated solutions. Therefore, the deliquescence of these salts might be considered as an important damage process and further investigations are required to assess their relevance for the deterioration of building materials.

8.5 REFERENCES

- [1] GIBSON L.T., COOKSEY B.G., LITTLEJOHN D., TENNENT N.H., Characterisation of an unusual crystalline efflorescence on an Egyptian limestone relief, *Anal. Chim. Acta* **1997**, 337, 151–164.
- [2] LINNOW K., HALSBERGHE L., STEIGER M., Analysis of calcium acetate efflorescences formed on ceramic tiles in a museum environment, *J. Cult. Her.* **2007**, doi:10.1016/j.culher.2006.09.004
- [3] GIBSON L.T., COOKSEY B.G., LITTLEJOHN D., LINNOW K., STEIGER M., TENNENT, N.H., The mode of formation of thecotrichite, a widespread calcium acetate chloride nitrate efflorescence. *Stud. Conserv.* **2005**, 50, 284–294.
- [4] LINNOW K., ZEUNERT A., STEIGER M., Investigation of sodium sulfate phase transitions in a porous material using humidity- and temperature-controlled X-ray diffraction, *Anal. Chem.* **2006**, 13, 4683–4689.
- [5] GREENSPAN L., Humidity fixed points of binary saturated aqueous solutions, *J. Res. Nat. Bur. Stand.* **1977**, 81A, 89–96.
- [6] GIBSON L.T., COOKSEY B.G., LITTLEJOHN D., TENNENT N.H., Investigation of the composition of a unique efflorescence on calcareous museum artifacts, *Anal. Chim. Acta* **1997**, 337, 253–264.
- [7] KLAUE B., Charakterisierung und Quantifizierung kristalliner Phasen in urbanen Aerosolen unter besonderer Berücksichtigung der Hygroskopizität sekundärer Ammoniumsalze, Dissertation, Fachbereich Chemie, Universität Hamburg **2001**.
- [8] COOKSEY B.G., GIBSON L.T., KENNEDY A.R., LITTLEJOHN D., STEWART L., TENNENT N.H., Dicalcium triacetate nitrate dehydrate, *Acta Cryst.* **1999**, C55, 324–326.
- [9] LINNOW K., STEIGER M., Determination of equilibrium humidities using temperature- and humidity-controlled X-ray diffraction (RH-XRD), *Anal. Chim. Acta.* **2007**, 583, 197–201.
- [10] TANG I. N., Thermodynamic and optical properties of mixed-salt aerosols of atmospheric importance, *J. Geophys. Res.* **1997**, 102, 1883–1893.
- [11] STEIGER M., Crystal growth in porous materials: I. The crystallization pressure of large crystals, *J. Crystal Growth* **2005**, 282, 455–469.

Chapter 9

Summary: Salt damage in porous materials

It is widely accepted that phase transitions of salts are the major cause of damage to porous materials such as stone, brick and mortar. Stress is generated in these materials by crystals growing from supersaturated solutions (crystallization pressure) and during hydration reactions (hydration pressure). In order to understand the underlying processes, the experimental observation of phase transition reactions within pores and their thermodynamic modeling are highly desirable. In the present thesis X-ray diffractometry under controlled conditions of relative humidity (RH) and temperature (RH-XRD) was applied for the in situ investigation of such reactions. The Pitzer ion interaction model was used to construct the phase diagrams and to predict appropriate experimental conditions.

RH-XRD measurements were carried out with bulk samples of salts and within the confined pore spaces of a porous material. Glass frits of different pore sizes were selected as porous substrates, because the amorphous glass frits did not interfere with the X-ray patterns of the salt phases. The median pore sizes of the selected glass frits are typical for many building materials such as natural stone and brick. The sample preparation procedure of the loaded glass frits including impregnation with salt solution and subsequent freeze-drying yielded different mass fractions for different porosity classes depending on the pore size and the characterization of loaded glass frits with scanning electron microscopy revealed that a homogeneous salt distribution in the porous substrates was not always achieved. Due to the limited penetration depth of the X-rays in the glass frits only a layer close to the surface of the substrate can be observed. For Cu K α -radiation and the substrate used in this work, it can be estimated from the absorption law that the penetration of the X-rays for different Bragg angles θ would hardly exceed about 100–200 μm . However, this is not a severe restriction for the suitability of RH-XRD measurements in porous materials in general, because visible damage of porous material is often located in a narrow zone close to the surface. The typical damage forms observed at buildings are blistering, powdering and granular disintegration leading to a gradual loss of the surface. This damage is caused by crystal growth in pores very close to the surface. Neither the preparation of the loaded glass frits nor the limited penetration depth of X-rays poses any particular problems in the observation of equilibrium humidities of confined crystals. However, restrictions had to be considered when using RH-XRD for kinetic measurements; the measurements in glass frits were not directly comparable to bulk sample measurements.

Using RH-XRD the hydration of $\text{Na}_2\text{SO}_4(\text{V})$ and the deliquescence of $\text{Na}_2\text{SO}_4 \cdot 10\text{H}_2\text{O}$ were observed on quartz fiber filters, as non porous environment, and within the pore space of glass frits with different sizes (nominal pore sizes of 1.0–1.6 μm and 10–16 μm). Both, the complete hydration of $\text{Na}_2\text{SO}_4(\text{V})$ and the deliquescence of $\text{Na}_2\text{SO}_4 \cdot 10\text{H}_2\text{O}$, were observed at the expected equilibrium humidities (RH_{eq}) within the stated experimental uncertainty of $\pm 2.5\% RH$. The filter samples and glass frits did not reveal any significant differences in the equilibrium humidities of the hydration and deliquescence reactions. It was found that the transition $\text{Na}_2\text{SO}_4(\text{III})$ – $\text{Na}_2\text{SO}_4(\text{V})$ and the hydration of $\text{Na}_2\text{SO}_4(\text{V})$ proceed as real solid state reactions. The crystallization of $\text{Na}_2\text{SO}_4 \cdot 10\text{H}_2\text{O}$ from solution did not take place even at very low RH , neither on the quartz fiber filter nor in the glass frits. The direct crystallization of $\text{Na}_2\text{SO}_4(\text{V})$ occurred instead at humidities far below the equilibrium humidities of the two solids. Crystallization was observed at even lower humidities in the glass frit than on the quartz fiber filter. Since no influence of the confinement in the pores on the thermodynamic properties of $\text{Na}_2\text{SO}_4(\text{V})$ and $\text{Na}_2\text{SO}_4 \cdot 10\text{H}_2\text{O}$ was noticed during the hydration and deliquescence experiments, it is concluded that the delayed crystallization is caused by inhibited nucleation kinetics leading to highly supersaturated solutions. This is an important result as crystals growing in pores can only generate pressure if they are in contact with a solution of sufficient supersaturation.

The uncertainty of the humidity measurements, limited by the absolute accuracy of the capacitive humidity sensor used, was not considered satisfactory to determine equilibrium humidities with sufficient accuracy. To improve the uncertainty a new extrapolation procedure was adopted and validated by determination of the well known equilibrium humidities of the deliquescence of NaCl and $\text{Ca}(\text{NO}_3)_2 \cdot 4\text{H}_2\text{O}$ and the hydration $\text{Ca}(\text{NO}_3)_2$ – $\text{Ca}(\text{NO}_3)_2 \cdot 2\text{H}_2\text{O}$. The procedure is based on the fact that reaction rates decrease as equilibrium is approached and the rate goes to zero at equilibrium. Hence, the equilibrium humidity of a reaction induced by a sudden increase in RH can be determined by extrapolation from rate measurements at different relative humidities. The extrapolation procedure yielded precise and accurate equilibrium humidities determined in bulk samples with a maximum error of $\pm 0.7\% RH$.

The same extrapolation method was also applied to the NaCl deliquescence in glass frits with different pore sizes. The extrapolated equilibrium humidities show, in agreement with theoretical considerations, that the deliquescence humidity of NaCl crystals of about 1–3 μm

in size is neither affected by crystal size nor by the confinement in the pore space of glass frits with median pore diameters in the range of 1.4–70 μm . In contrast to the equilibrium thermodynamics, the kinetic measurements revealed that reaction rates might be affected by pore size, crystal size and sample mass. Nonetheless, the ambient humidity has the strongest influence on the reaction rate. The deliquescence of NaCl in the pore space close to the surface of a porous substrate proceeds on a time scale of a few hours. Since the measurements were all carried out at comparably low relative humidity ($< 80\%$) even shorter reaction times are to be expected at high *RH*. This implies that the dynamics of deliquescence–crystallization cycles in building materials is strongly affected by both frequency and amplitude of the ambient humidity variation. Quite short-term variation of ambient relative humidity, e.g. typical daily fluctuations, might induce damaging deliquescence–crystallization cycles within the pore space of building materials.

The hydration of $\text{MgSO}_4 \cdot \text{H}_2\text{O}$ (kieserite) was observed by RH-XRD within the confined space of a glass frit (median pore radius 6 μm) at different relative humidities and 25°C. Hydration of $\text{MgSO}_4 \cdot \text{H}_2\text{O}$ and formation of $\text{MgSO}_4 \cdot 6\text{H}_2\text{O}$ proceeds slowly and is incomplete at humidities below 60% *RH*. In contrast, rapid and complete hydration is observed at humidities above 60% *RH*. Actually, the heptahydrate $\text{MgSO}_4 \cdot 7\text{H}_2\text{O}$ is the stable solid phase at humidities above 51% *RH*. However, the direct hydration of $\text{MgSO}_4 \cdot \text{H}_2\text{O}$ to $\text{MgSO}_4 \cdot 7\text{H}_2\text{O}$ did not take place, most likely the reaction is kinetically hindered. $\text{MgSO}_4 \cdot 7\text{H}_2\text{O}$ was only formed by the hydration of $\text{MgSO}_4 \cdot 6\text{H}_2\text{O}$ at 75% *RH*. The reaction pathway of the $\text{MgSO}_4 \cdot \text{H}_2\text{O}$ hydration and $\text{MgSO}_4 \cdot 6\text{H}_2\text{O}$ formation was deduced from the phase diagram of the stable phases $\text{MgSO}_4 \cdot \text{H}_2\text{O}$, $\text{MgSO}_4 \cdot 6\text{H}_2\text{O}$ and $\text{MgSO}_4 \cdot 7\text{H}_2\text{O}$ at climatic conditions between 0°C–80°C and 0%–100% *RH*. The phase diagram, constructed using the Pitzer ion interaction model, revealed a metastable deliquescence point of $\text{MgSO}_4 \cdot \text{H}_2\text{O}$ at 60% *RH* and 25°C. At lower relative humidities the hydration proceeds as a true solid state reaction and generated stress is best treated as a hydration pressure. Though not yet fully understood, it appears plausible that the formation of a barrier product layer of $\text{MgSO}_4 \cdot 6\text{H}_2\text{O}$ prevents the complete hydration of a bulk kieserite crystal. In addition, due to the considerable volume expansion during the hydration in the confined spaces of the porous glass filters, the accessibility of $\text{MgSO}_4 \cdot \text{H}_2\text{O}$ to the water vapor may be continuously reduced in the course of the reaction. At humidities above the deliquescence humidity, the deliquescence of $\text{MgSO}_4 \cdot \text{H}_2\text{O}$ leads to a very concentrated MgSO_4 solution. The maximum

possible concentration is given by the solubility of $\text{MgSO}_4 \cdot \text{H}_2\text{O}$, i.e. $m_{\text{sat}} = 6 \text{ mol} \cdot \text{kg}^{-1}$ at 25°C , which is far supersaturated with respect to the less soluble $\text{MgSO}_4 \cdot 6\text{H}_2\text{O}$ ($m_{\text{sat}} = 3.7 \text{ mol} \cdot \text{kg}^{-1}$ at 25°C). In this case, the hydration proceeds as a two-step reaction, involving the dissolution of kieserite followed by the rapid crystallization of $\text{MgSO}_4 \cdot 6\text{H}_2\text{O}$ and generated stress is best treated as crystallization pressure.

The investigation of the kieserite hydration in the present work was embedded in the project ‘Salze im Porenraum’ (funded by Deutsche Forschungsgemeinschaft, DFG). The collaborators in this project carried out additional measurements during the hydration reaction. Electronic speckle pattern interferometric measurements (ESPI) were carried out at Oldenburg University (G. Gülker, A. El Jarad, Department of Physics) to detect deformation of the porous substrates during crystal growth. Scanning electron microscopic investigations after cryo-fixation of samples (Cryo-SEM) were carried out at the Institute of Materials Science Bremen (H. Juling, IWT Bremen). Changes in the mechanical response of the glass frit measured by ESPI confirmed the action of hydration pressure at low humidities and crystallization pressure at high humidities. The pronounced increase of the strain rate at about 60% *RH* and the presence of liquid films on and directly beneath the surface, observed by Cryo-SEM, at high *RH* verified that there are two different reaction pathways for the kieserite hydration as discussed before.

Not only the hydration of $\text{MgSO}_4 \cdot \text{H}_2\text{O}$ and $\text{MgSO}_4 \cdot 6\text{H}_2\text{O}$ was observed below the corresponding deliquescence humidity, but also the hydration of $\text{Na}_2\text{SO}_4(\text{V})$ and the phase transition $\text{Na}_2\text{SO}_4(\text{III})\text{--}\text{Na}_2\text{SO}_4(\text{V})$ occurred below the deliquescence humidities of $\text{Na}_2\text{SO}_4(\text{V})$ and $\text{Na}_2\text{SO}_4(\text{III})$, respectively. It is concluded that these reactions proceed without intermediate formation of a solution phase. Nonetheless, the direct hydration in the solid state must involve an amorphous interface in the reacting solid between the reactant (e.g. $\text{MgSO}_4 \cdot \text{H}_2\text{O}$) and the recrystallized product (e.g. $\text{MgSO}_4 \cdot 6\text{H}_2\text{O}$). Preferably, the size of this reaction zone is very small such that an X-ray amorphous intermediate phase cannot be detected by XRD and the present investigations do not provide further insight into the nature of the reaction zone.

Salt crystallization not only is a major cause of damage in building materials but is also frequently observed as a major deterioration mechanism of porous museum objects. Apart from chlorides, nitrates and sulfates that are the main constituents of the salt systems typically

found in building materials, acetates have been identified as a major constituent in salt efflorescences grown on museum objects. Acetate is mainly present in the form of different double salts and the triple compound thecotrichite, $\text{Ca}_3(\text{CH}_3\text{COO})_3\text{Cl}(\text{NO}_3)_2 \cdot 7\text{H}_2\text{O}$. Thecotrichite plays a prominent role on porous objects in museum environments. It is generally accepted that the deposition of acetic acid vapor from the museum environment is the major source of acetate enrichment in calcareous or ceramic artifacts. The clarification of the mode of formation of thecotrichite and other acetate containing salts and their behavior in porous substrates was another major objective of the present thesis. In an analytical study surface efflorescences on seriously damaged Dutch tiles of glazed ceramics of the collection of the Stedelijke Musea in Kortrijk, Belgium, were analyzed and the composition of the remaining salt mixture in the tiles are determined. It turned out that the acetate was nearly exclusively present in the efflorescences, while there remained a large reservoir of a hygroscopic salt mixture in the tiles largely consisting of calcium chloride and nitrate. To improve the understanding of the formation of the various acetate containing phases requires the phase diagram of the quaternary thecotrichite system.

To construct the phase diagram of the $\text{Ca}(\text{CH}_3\text{COO})_2\text{--CaCl}_2\text{--Ca}(\text{NO}_3)_2\text{--H}_2\text{O}$ system the semi empirical Pitzer ion interaction model was used. The treatment of the quaternary thecotrichite system requires experimental data for the three ternary subsystems $\text{CaCl}_2\text{--Ca}(\text{NO}_3)_2\text{--H}_2\text{O}$, $\text{Ca}(\text{CH}_3\text{COO})_2\text{--CaCl}_2\text{--H}_2\text{O}$ and $\text{Ca}(\text{CH}_3\text{COO})_2\text{--Ca}(\text{NO}_3)_2\text{--H}_2\text{O}$. Due to the lack of available experimental data for the ternary system $\text{Ca}(\text{CH}_3\text{COO})_2\text{--Ca}(\text{NO}_3)_2\text{--H}_2\text{O}$ new solubility measurements were carried out. The data were used to parameterize the Pitzer model and to determine the equilibrium constants of thecotrichite and the double salt $\text{Ca}_2(\text{CH}_3\text{COO})_3(\text{NO}_3) \cdot 2\text{H}_2\text{O}$. The interaction parameters and the equilibrium constants of the respective solid phases then allowed for the calculation of the molalities and water activities of the saturated solutions of each possible composition.

A lot of information on the crystallization properties can be readily derived from the phase diagram. The thecotrichite stability field in the quaternary phase diagram extends over a strikingly broad range of $\text{Cl}^-/\text{NO}_3^-$ ratios, hence, thecotrichite formation is thermodynamically favored over a broad composition range. This explains the ubiquitous occurrence of the triple salt in different museums all over the world. In contrast, acetate deposition leads to the formation of the double salt calclacite, $\text{Ca}(\text{CH}_3\text{COO})\text{Cl} \cdot 5\text{H}_2\text{O}$, only at very high $\text{Cl}^-/\text{NO}_3^-$ ratios >0.96 . Similarly, the formation of $\text{Ca}_2(\text{CH}_3\text{COO})_3(\text{NO}_3) \cdot 2\text{H}_2\text{O}$ only occurs at

extremely small $\text{Cl}^-/\text{NO}_3^-$ ratios <0.008 . Hence, thecotrichite is the most commonly occurring efflorescence on calcareous museum objects contaminated with both chloride and nitrate. Furthermore, the phase diagram was used to discuss the possibilities of preventive conservation of salt contaminated ceramics in typical museum environments.

Finally, the deliquescence of the incongruently soluble compound thecotrichite was investigated using both, model simulations and RH-XRD. The equilibrium crystallization pathway of a solution with composition equal to the composition of typical thecotrichite efflorescences were calculated using the Pitzer model parameters. The measured crystallization pathway is in reasonable qualitative accordance with the predicted pathway. In contrast, crystallize $\text{Ca}_2(\text{CH}_3\text{COO})_3(\text{NO}_3) \cdot 2\text{H}_2\text{O}$ delayed under conditions of increasing *RH* during the deliquescence process of the salt mixture, i.e. at humidities above the calculated equilibrium humidity. It is concluded from mass balance considerations that the situation includes the formation of supersaturated solutions. This is an important result as crystals growing in pores can only generate pressure if they are in contact with a solution of sufficient supersaturation.

In conclusion, the in-situ RH-XRD investigations carried out in this work provide a significant contribution to a better understanding of salt weathering phenomena. Damaging phase transition reactions were successfully observed within the confined spaces of a porous material for the first time. Finally, the conditions for damaging phase transition reactions of single salts and salt mixtures, which are relevant to the deterioration of building materials or museum artifacts, were determined.

Appendix

Safety data sheet

Chemical	R-Phrase	S-Phrase	Hazard symbol
CaNO ₃ · 4H ₂ O	8-36		[O] [Xi]
CaCl ₂ · 6H ₂ O	36	22-24	[Xi]
CH ₃ COOH (100%)	10-35	23.2-26-45	[C]
CH ₃ OCH ₃	11-36-66-67	9-16-26	[F] [Xi]
LiCl	22-36/38		[Xn]
C ₁₀ H ₁₆ N ₂ O ₈	36-52/53	61	[Xi]
AgNO ₃	34-50/53	26-45-60-61	[C] [N]
Na ₂ CO ₃	36	22-26	[Xi]
(CH ₃) ₂ C ₆ H ₃ OH	24/25-34-51/53	26-36/37/39-45-61	[T] [N]
H ₂ SO ₄ (98%)	35	S 26-30-45	[C]
KNO ₃	8	16-41	[O]
H ₃ PO ₄ (87%)	34	26-36/37/39-45	[C]

CURRICULUM VITAE

Personal Information

Kirsten Linnow
Born 12.12.1964 in Hamburg, Germany
Unwed, 1 child (born 19.06.1996)

Education

Since 07/2000	Doctoral dissertation at the University of Hamburg
10/1998–05/2000	Study of chemistry at the University of Hamburg Degree: Diplom-Chemikerin
04/1996–09/1998	Parental leave
04/1991–03/1996	Study of chemistry at the University of Hamburg
10/1983–10/1986	Apprenticeship Unilever Forschungsgesellschaft mbH, Hamburg Degree: Chemical laboratory worker
06/1983	Gymnasium Bornbrook, Hamburg Degree: General qualification for university entrance (Abitur)

Professional Career

10/2003–06/2006	Research assistant at the University Hamburg DFG funded research projects
10/2000–09/2003	Teaching assistant at the University Hamburg within „Freies Praktikum in anorganischer und analytischer Chemie“
07/2000–09/2000	Research assistant at the University Hamburg DFG funded research project
10/1986–03/1991	Chemical laboratory assistant at the University Hamburg Institut für Anorganische Angewandte Chemie

Publications

Journals

Haupt O.; Linnow K.; Harmel R.; Schäfer, C.; Dannecker W.;
Qualitative X-Ray fluorescence analysis of emitted aerosol particles from incineration plants
sampled on quartz fibre filters.
X-Ray Spectrometry **1997**, 26, 79-84.

Gibson L.T., Cooksey B.G., Littlejohn D., Linnow K., Steiger M., Tennent, N.H.,
The mode of formation of thecotrichite, a widespread calcium acetate chloride nitrate
efflorescence.
Studies in Conservation **2005**, 50, 284-294.

Linnow K., Zeunert A., Steiger M.,
Investigation of sodium sulfate phase transitions in a porous material using humidity- and
temperature-controlled X-ray diffraction.
Analytical Chemistry **2006**, 13, 4683-4689.

Linnow K., Halsberghe L., Steiger M.,
Analysis of calcium acetate efflorescences formed on ceramic tiles in a museum environment.
Journal of Cultural Heritage **2007**, 8, 44–52.

Linnow K., Steiger M.,
Determination of equilibrium humidities using temperature and humidity controlled X-ray
diffraction (RH-XRD).
Analytica Chimica Acta **2007**, 583, 197–201.

Linnow K., Jüling H., Steiger M.,
Investigation of NaCl deliquescence in porous substrates using RH-XRD.
Environmental Geology **2007**, 52, 317–327.

Steiger M., Linnow K., Jüling H., Gülker G., El Jarad A., Brüggerhoff S., Kirchner D.,
Hydration of $\text{MgSO}_4 \cdot \text{H}_2\text{O}$ and generation of stress in porous materials. Journal of Crystal
Growth and Design **2007**, doi: 10.1021/cg060688c .

Conference Proceedings

Jüling H., Kirchner D., Brüggerhoff S., Linnow K., Steiger M., El Jarad A., Gülker G.,
Salt Damage of Porous Materials: A Combined Theoretical and Experimental Approach In:
D. Kwiatkowski, R. Löfvendahl (eds.): Proceedings of the 10th International Congress on
Deterioration and Conservation of Stone, ICOMOS, Stockholm 2004, 187–194.

Poster

Linnow K., Halsberghe L., Steiger M.,
Thecotrichite on salt contaminated ceramics, IAQ 5th meeting of the Indoor Air Pollution
Working Group, Norwich 2003.